



This work is protected by copyright and other intellectual property rights and duplication or sale of all or part is not permitted, except that material may be duplicated by you for research, private study, criticism/review or educational purposes. Electronic or print copies are for your own personal, non-commercial use and shall not be passed to any other individual. No quotation may be published without proper acknowledgement. For any other use, or to quote extensively from the work, permission must be obtained from the copyright holder/s.

**Experimental studies of hydrated
analogue materials of relevance to
Solar System bodies using
synchrotron radiation**

Emmal Safi

Doctor of Philosophy in Physics

School of Chemical and Physical Sciences, University of Keele.

March 2018

Abstract

Synchrotron X-ray powder diffraction on beamline I11 at the Diamond Light Source is used to study the in situ formation of CO₂/CH₄ clathrates. Frozen aqueous salt solutions were subjected to gas pressures between 5–26 bar and thermally cycled in the temperature range 90–270 K. This was done to replicate the likely sub-surface ocean compositions and pressures found on Europa, Enceladus and Titan and the Martian cryosphere. By using varying composition and concentration of the salt solutions we measure their inhibiting effect on clathrate formation, and in some cases find that the salts can affect the clathrate structure.

Synchrotron X-ray powder diffraction and in situ Raman spectroscopy are used to observe the change in structure of epsomite as it is cycled through a range of temperatures replicating diurnal and seasonal changes on the Martian surface. We find no evidence to support a low temperature phase of epsomite which would be the more prevalent form on colder surfaces.

Results are presented on the study of in situ synchrotron X-ray powder diffraction on meridianiite formation. A slow cooling rate was applied to the sample using a cold cell on I11's Long Duration Experiment facility; in situ cooling experiments were also performed on I11s time-resolved facility. Large ice crystals which then break into smaller particles as meridianiite forms were observed and the implications for ice rheology are discussed. A sample simulating Europa's ocean composition was also investigated in the same Long Duration Experiment. It is shown that meridianiite seemingly prevents gypsum forming at low temperatures, which has implications for organic material beneath the surface of Europa.

Acknowledgements

Firstly, I would like to express my utmost gratitude to my supervisor Professor Nye Evans for his unfailing support, patience and confidence throughout the duration of my research. He has allowed me the freedom to explore my own ideas whilst providing guidance and criticisms to ensure that my research was carried out professionally and completed on time.

In the same spirit, I would like to thank my Diamond supervisor Dr. Stephen Thompson for his assistance, support and encouragement. I would also like to thank Dr. Sarah Day for her invaluable help with TOPAS and, along with Dr. Annabelle Baker and Dr. Claire Murray, for providing technical support during beamtime at Diamond. I would also like to acknowledge Professor Hilary Kennedy and Dr. Benjamin Butler for providing some of the data for chapter 9. I would also like to thank Keele University and the Diamond Light Source for providing the funding for this project.

Thanks also to my office colleagues at Keele for creating an environment which was both enjoyable and broadening and made it a pleasure to work and learn there. Particular thanks goes to Jacqueline for all the fun and her friendship.

My deepest thanks must go to my family for their love and support. Especially my parents, who have taught me from an early age the value of education.

Contents

Abstract	iii
Acknowledgements	iv
1 Introduction	1
1.1 Overview	1
1.2 Research Objectives	5
1.3 Thesis Outline	6
2 Background	7
2.1 Clathrate Hydrates	7
2.1.1 Clathrate hydrates in the Solar System	8
2.1.1.1 Clathrate hydrates on Enceladus	8
2.1.1.2 Clathrate hydrates on Europa	12
2.1.1.3 Clathrate hydrates on Mars	14
2.1.1.4 Clathrate hydrates on Titan	20
2.2 Clathrate Hydrate Inhibitors	25
2.2.1 Electrolyte Inhibitors	25
2.3 Hydrated Sulphates in the Solar System	26
2.3.1 Hydrated Sulphates on Mars	26
2.3.2 Epsomite ($\text{MgSO}_4 \cdot 7\text{H}_2\text{O}$, MS7)	30
2.3.3 Meridianiite ($\text{MgSO}_4 \cdot 11\text{H}_2\text{O}$, MS11)	35
3 The theory of X-ray diffraction	42
3.1 Introduction	42
3.2 Synchrotron radiation	42
3.3 X-ray diffraction	44
3.3.1 Laue theory	45
3.3.2 Bragg's theory	47
3.3.3 Scherrer equation	50
3.4 X-ray powder diffraction	52
3.4.1 Analysing X-ray powder diffraction data	55
3.4.1.1 Qualitative analysis	55
3.4.1.2 Quantitative analysis	56
Rietveld refinement	56
Pawely and LeBail refinement	59
3.5 Raman spectroscopy	60
4 Experimental methods	62
4.1 Introduction	62
4.1.1 Diamond Light Source	62
4.1.2 Beamline I11	63

4.1.3	The Long Duration Experiment (LDE) Facility	65
4.1.3.1	The Cold Cell	71
4.2	Sample Preparation	71
4.2.1	Preparation of Saline Solutions for Clathrate Formation	71
4.2.2	Preparation of Epsomite Sample	73
4.2.3	Preparation of Meridianiite Sample	74
4.2.4	Loading Capillaries	74
4.2.5	The High Pressure Gas Cell	76
4.2.6	Data Collection	79
5	Properties of CO₂ clathrate hydrates formed in the presence of MgSO₄ solutions with implications for icy moons	80
5.1	Introduction	80
5.1.1	Clathrate Buoyancy in Ocean-Ice Environments	80
5.1.2	Effect of Ice and Ocean Salinity on Clathrate Dissociation	81
5.2	Experimental Work	83
5.3	Results	84
5.3.1	Arrhenius Curve and Inhibiting Effects on Clathrate Formation	86
5.3.2	Thermal Expansion	87
5.3.3	Density	92
5.3.4	Weight percentage of clathrate, Ih, and Ic ice	92
5.4	Discussion	94
5.4.1	Inhibiting effect of MgSO ₄ on Clathrate formation	94
5.4.2	Thermal Expansion	96
5.4.3	Clathrate Density and Buoyancy	97
5.4.4	The nature of the ice	99
5.5	Conclusion	99
6	Effects of ice polymorphs and chloride salts on clathrate hydrate evolution in the Martian cryosphere	101
6.1	Introduction	101
6.2	Experimental work	102
6.3	Results	104
6.3.1	Weight percentage of clathrate, Ih and Ic ice	104
6.3.1.1	10 g CaCl ₂ solution at 10 and 20 bar CO ₂	104
6.3.1.2	2 g MgCl ₂ solution at 10 bar CO ₂	106
6.3.1.3	6 g NaCl solution at 10 bar CO ₂	107
6.4	Discussion	107
6.4.1	The role of ice polymorphs	107
6.4.2	Implications for the Martian cryosphere	112
6.5	Conclusions	114
7	Does clathrate dissociation replenish Titan's atmospheric methane?116	

7.1	Introduction	116
7.2	Experimental work	118
7.3	Results	119
7.3.1	Thermal expansion	121
7.3.2	Density	125
7.3.3	Weight percentage of clathrate, Ih, Ic and $(\text{NH}_4)_2\text{SO}_4$	132
7.4	Discussion	135
7.4.1	Thermal Expansion	135
7.4.2	Buoyancy and density of CH_4 clathrates	136
7.4.3	Effects of ice and $(\text{NH}_4)_2\text{SO}_4$ on Titan's crust and ocean	138
7.5	Conclusion	139
8	The behaviour of epsomite at temperatures relevant to Solar System bodies	140
8.1	Hydrated sulphates on Mars	140
8.2	Hydrated sulphates on Europa	141
8.3	Hydrated sulphates on Ganymede	141
8.4	Hydrated sulphates on Callisto	142
8.5	Experimental	142
8.6	Results and Discussion	145
8.6.1	Laboratory work on epsomite	145
8.6.2	Thermal expansion of epsomite	153
8.7	Conclusion	156
9	A slow cooling study of hydrated minerals using the LDE	161
9.1	Introduction	161
9.2	Experimental	162
9.3	Results and discussion	163
9.4	Conclusion	166
9.5	LDE studies of the ocean composition on Europa	172
9.5.1	Introduction	172
9.5.2	Experimental set-up and results	174
9.5.3	Discussion	186
9.5.4	Conclusion	190
10	Conclusions and future work	192
10.1	Astrophysical implications of forming clathrate in saline solutions	193
10.2	Effects of ice polymorphs on clathrate dissociation	194
10.3	Behaviour of hydrated minerals on planetary bodies	195
10.4	Future work	196
10.4.1	Low pressure clathrate formation	196
10.4.2	Nature of ice	197
10.4.3	Meridianiite	197

10.4.4 Sulphur bearing materials on Europa	198
Bibliography	200
A Publication List	213
A.1 Peer-reviewed journal papers	213
A.2 Submitted journal papers	213
A.3 Journal papers in preparation	213
B List of abbreviations and acronyms	215

List of Figures

2.1	Various structures of clathrate hydrates. (a) structure I (sI), (b) structure II (sII) and (c) structure H (sH) (Momma et al. 2011).	8
2.2	sI clathrate encasing a gas molecule (https://ps.uci.edu).	9
2.3	Plume emanating from Enceladus' South Polar region (credit: Cassini imaging Team, JPL, ESA, NASA).	10
2.4	Internal structure of Europa (http://explanet.info/Chapter09.htm).	13
2.5	Recurring Slope Lineae on the Martian surface taken by the HiRISE camera (http://dovesipuoparlarediognicosa.blogspot.co.uk/2015/09/lanasa-conferma-su-marte-lacqua-ce.html).	17
2.6	Internal structure of Titan https://www.nasa.gov/mission	21
2.7	Phase diagram of ice (http://www1.lsbu.ac.uk)	24
2.8	Equilibrium binary phase diagram of the system $\text{MgSO}_4\text{-H}_2\text{O}$; MS7=epsomite, MS12=dodcahydrate, MS6=hexahydrate, and MS1=kieserite (Fortes et al. 2006).	27
2.9	The structure of epsomite (Fortes et al. 2006).	31
2.10	Raman spectra obtained from epsomite; (a) shows the stretching vibrational mode while (b) shows the bending vibrational mode of structural water in epsomite taken at temperatures and pressures relevant to Earth and Mars. The vertical dashed lines show the central positions of the peaks (Wang et al. 2013).	32
2.11	Raman spectra obtained from epsomite; (a) shows the H_2O vibrational mode and (b) shows the symmetric-stretching vibrational mode of $[\text{SO}_4]^{2-}$ for low temperature epsomite (denoted LT-7w), room temperature epsomite (denoted RT-7w), meridianiite (denoted 11w) and hexahydrate (denoted 6w) (Wang et al. 2011).	33
2.12	XRD pattern obtained from epsomite; (a) shows epsomite at the 2θ range of $14^\circ\text{-}45^\circ$ and (b) shows epsomite at the 2θ range $14^\circ\text{-}25^\circ$, the temperature of the LT-7w corresponds to dry ice (-78.5°C) (Wang et al. 2011).	34
2.13	Infrared spectra of hexahydrate, $\text{MgSO}_4\cdot 6\text{H}_2\text{O}$, and bloedite ($\text{Na}_2\text{Mg}(\text{SO}_4)_2\cdot\text{H}_2\text{O}$) at room temperature and pressure and at 120 K (Dalton et al. 2005).	36
2.14	Meridianiite at 250 K (https://crystallography365.wordpress.com)	38
2.15	XRD pattern obtained from meridianiite after a series of repeated scans, (Freeman et al. 2007).	40
2.16	Raman spectra obtained from meridianiite, where w denotes waters of hydration (Freeman et al. 2007).	41

3.1	Increase of brilliance as a result of better collimation and smaller source size going from a classical X-ray source to second and third generation synchrotron sources (Kunz 2001).	43
3.2	Diffraction from a lattice row along the x -axis. The incident and diffracted beams are at angles α_0 and α_n to the row respectively (Hammond 2009).	46
3.3	Three Laue cones representing the directions of the diffracted beams from a lattice row along the x -axis with $0\lambda(n_x = 0)$, $1\lambda(n_x = 1)$ and $2\lambda(n_x = 2)$ path differences (Hammond 2009).	46
3.4	An X-ray beam is incident onto the plane and partially reflected, while the transmitted beam is then incident on the next plane and reflected in the same way (Hammond 2009).	48
3.5	Bragg's law expressed in vector notation (Hammond 2009).	49
3.6	Explanation of the reciprocal lattice. (a) shows three sets of crystallographic planes in the lattice. (b) The normals of these planes originate from a common origin. (c) The reciprocal lattice vectors define the crystal planes and their d -spacing (Hammond 2009).	49
3.7	Diffraction pattern of a single crystal (from http://prism.mit.edu/xray).	53
3.8	Diffraction pattern of a polycrystallite, http://prism.mit.edu/xray	53
3.9	The formation of Debye-Scherrer cones (from http://prism.mit.edu/xray).	54
4.1	Ariel view of DLS (http://www.diamond.ac.uk).	63
4.2	Schematic layout of the hutches and control cabins around beamline I11 (Murray et al. 2017).	64
4.3	Diffractometer on I11.	66
4.4	Schematic layout of experimental components and equipment in EH2 (Murray et al. 2017). The dashed black line running through the centre of the area detectors represents the X-ray beam.	68
4.5	Layout of experimental components and equipment in EH2 (Murray et al. 2017).	69
4.6	Cold cell situated in EH2 (Murray et al. 2017).	72
4.7	Brass holders loaded onto the diffractometer on I11.	75
4.8	High pressure gas cell (Day et al. 2015).	77
4.9	Sapphire capillary mounted onto the high pressure cell loaded onto the diffractometer on I11.	78

5.1	Rietveld refinements of the MS10.5 solution at a 10 bar CO ₂ pressure experimental data. From top-bottom: 90 K, 180 K, 245 K. The experimental data are shown in black, the calculated fit in red, and the residuals in grey below. All dominant peaks are labelled where C = clathrate peaks and I = hexagonal ice peaks. The larger residuals for some of the ice peaks are due to poor powder averaging due to the way the ice freezes inside the cell (preferred orientation) and the restricted cell rocking angle used to compensate for this during measurement.	85
5.2	Arrhenius curve for CO ₂ clathrate hydrates in MS10.5 and MS3.1 solutions (black points, red curve) compared with the Arrhenius curve for CO ₂ clathrate hydrates in pure water (Miller 1961, blue curve).	86
5.3	The temperature dependency of the lattice parameters of CO ₂ clathrate hydrates formed in solutions of MS10.5 and MS3.1 at various pressures. From top-bottom: MS10.5 at 5 bar, MS10.5 at 10 bar and MS3.1 at 20 bar. For ease of presentation blue symbols represent values obtained during cooling and red values obtained during heating.	88
5.4	The thermal expansion coefficient for CO ₂ clathrate hydrates formed in solutions of MS10.5 and MS3.1 derived from the polynomial fits. H = Heating and C = Cooling.	89
5.5	Dependence of density on temperature. From top-bottom: MS10.5 at 5 bar, MS10.5 at 10 bar and MS3.1 at 20 bar. Symbols/colours as per Fig. 5.3.	93
5.6	Weighted percentage (wt%) curves for solutions. From top-bottom: MS10.5 at 5 bar, MS10.5 at 10 bar and MS3.1 at 20 bar. Symbols/colours as per Fig. 5.3.	95
6.1	Pawley whole pattern refinements of the CaCl ₂ solution at 10 bar CO ₂ pressure experimental data. From top to bottom: 90 K, 180 K, 290 K. The experimental data are shown in black, the calculated fit in red, and the residuals in grey below. All dominant peaks are labelled where C = clathrate peaks and I = ice peaks. The larger residuals for some of the ice peaks are due to poor powder averaging based on the way the ice freezes inside the cell (preferred orientation) and the restricted cell rocking angle used to compensate for this during measurement.	105
6.2	wt% for clathrates formed in the presence of 10 g CaCl ₂ solution at 10 and 20 bar CO ₂ pressure. The black line represents the transitions from 10 to 20 bar CO ₂ pressure. Black triangles: clathrates; blue circles: Ih ice; green squares: Ic ice. See text for details.	108
6.3	wt% for clathrates formed in the presence of 2 g MgCl ₂ solution at 10 bar CO ₂ pressure. Symbols/colours as per Figs 6.2. See text for details.	109
6.4	wt% for clathrates formed in the presence of 6 g NaCl solution at 10 bar CO ₂ pressure. Symbols/colours as per Figs 6.2. See text for details.	110

7.1	The internal structure of Titan, after Fortes et al. (2007). “AS” in the crust (Layer 4) is ammonium sulphate.	117
7.2	Pawely whole pattern refinements of the experimental data for 15 wt% ammonium sulphate solution at a 26 bar CH ₄ pressure. From top-bottom: 90 K, 170 K, 270 K. The experimental data are shown in black, the calculated fit in red, and the residuals in grey below. All prominent peaks are labelled where C = clathrate peaks and I = hexagonal ice peaks; blue vertical bars are (NH ₄) ₂ SO ₄ peaks. The larger residuals for some of the ice peaks are due to poor powder averaging due to the way the ice freezes inside the cell (preferred orientation) and the restricted cell rocking angle used to compensate for this during measurement. The error bars in these plots are smaller than the plotted points.	120
7.3	Temperature dependence of the lattice parameters of CH ₄ clathrate hydrates formed in a solution of 10 wt% ammonium sulphate at 26 bar pressure. From top-bottom: cycle 1, cycle 2 and cycle 3. “(1)” and “(2)” indicate that the cooling was performed first, followed by heating. The black squares are experimental data from Shpakov et al. (1998). For ease of presentation blue symbols represent values obtained during cooling and red values obtained during heating. The error bars in these plots are smaller than the plotted points.	126
7.4	Temperature dependence of the lattice parameters of CH ₄ clathrate hydrates formed in a solution of 15 wt% ammonium sulphate at 26 bar pressure. From top-bottom: cycle 1 and cycle 2. “(1)” and “(2)” indicate that the cooling was performed first, followed by heating. The black squares are experimental data from Shpakov et al. (1998). For ease of presentation blue symbols represent values obtained during cooling and red values obtained during heating. The error bars in these plots are smaller than the plotted points.	127
7.5	Density curves for the 10 wt% solution. From top-bottom: cycle 1, cycle 2, and cycle 3 at 26 bar. Colours are as per Fig. 7.3. The error bars in these plots are smaller than the plotted points.	128
7.6	Density curves for the 15 wt% solution. From top-bottom: cycle 1 and cycle 2 at 26 bar. Colours are as per Fig. 7.3. The error bars in these plots are smaller than the plotted points.	129
7.7	The density of supercooled H ₂ O as a function of temperature, (Clegg & Wexler 2011).	131
7.8	Weighted percentage (wt%) curves for the 10 wt% solution. From top-bottom: cycle 1, cycle 2, and cycle 3 at 26 bar. Triangles: clathrates; circles: Ih ice; squares: Ic ice. Colours are as per Fig. 7.3, except in the case of the black squares which represent (NH ₄) ₂ SO ₄ precipitate on cooling. The error bars in these plots are smaller than the plotted points.	133

7.9	Weighted percentage (wt%) curves for the 15 wt% solution. From top–bottom: cycle 1 and cycle 2 at 26 bar. Triangles: clathrates; circles: Ih ice; squares: Ic ice. Colours are as per Fig. 7.8, except in the case of the green squares which represent $(\text{NH}_4)_2\text{SO}_4$ precipitate on heating. The error bars in these plots are smaller than the plotted points.	134
8.1	Experimental set–up of the in situ Raman measurements.	144
8.2	XRD pattern of epsomite. Between each successive pattern there is a temperature step of 10 K. RT is room temperature.	146
8.3	Zoomed pattern of XRD pattern of epsomite ($5^\circ < 2\theta < 30^\circ$). Between each successive pattern there is a temperature step of 10 K. RT is room temperature.	147
8.4	Zoomed pattern of XRD pattern of epsomite ($19^\circ < 2\theta < 26^\circ$). Between each successive pattern there is a temperature step of 10 K. RT is room temperature.	148
8.5	Zoomed pattern of XRD pattern of epsomite ($7.7^\circ < 2\theta < 11^\circ$). Between each successive pattern there is a temperature step of 10 K. RT is room temperature.	149
8.6	Zoomed pattern of XRD pattern of epsomite ($14^\circ < 2\theta < 19.3^\circ$). Between each successive pattern there is a temperature step of 10 K. RT is room temperature.	150
8.7	Raman pattern obtained from epsomite. Between each successive pattern there is a temperature step of 10 K. RT is room temperature.	151
8.8	Zoomed hydration band of Raman obtained from epsomite. Between each successive pattern there is a temperature step of 10 K.	152
8.9	Pawley whole pattern refinement of the experimental data. The experimental are shown in blue, the calculated fit in red and the residuals in grey below.	155
8.10	Thermal expansion curves of epsomite along the a –axis.	157
8.11	Thermal expansion curves of epsomite along the b –axis.	158
8.12	Thermal expansion curves of epsomite along the c –axis.	159
8.13	Volumetric expansion of epsomite.	160
9.1	Meridianiite data collection from the LDE.	164
9.2	Evolution of ice and MS11 in the first 7 weeks of data collection on the LDE.	165
9.3	Evolution of ice and MS11 from week 7 to 13 of data collection on the LDE.	167
9.4	Changes in ice peaks after thermal cycling of the LDE sample.	168
9.5	Evolution of ice peaks as MS11 forms.	169
9.6	Ice forming on outside of the cell as base temperature on the LDE is reached.	170

9.7	Zoomed in ice peaks formed in in-situ time-resolved experiment in EH1. Ice peaks are broadening indicating disintegration of the ice as MS11 forms.	171
9.8	Modelled changes in solution composition and associated mineral precipitates based on the output of the thermodynamic model FREZCHEM (Courtesy of Benjamin Butler).	175
9.9	Evolution of epsomite during the LDE experimental run.	179
9.10	Evolution of meridianiite during the LDE experimental run.	180
9.11	Evolution of gypsum during the LDE experimental run.	181
9.12	Comparison of the evolution of meridianiite versus gypsum during the LDE experimental run.	182
9.13	Comparison of the evolution of gypsum versus epsomite during the LDE experimental run.	183
9.14	Comparison of the evolution of meridianiite versus epsomite during the LDE experimental run.	184

List of Tables

2.1	Mass of water per kg of hydrated sulphate (Chou & Seal 2007).	38
4.1	Types of salts and their corresponding concentrations and densities present during clathrate formation/dissociation.	73
5.1	Concentration, temperature range, pressure, density of salt solutions.	83
5.2	Coefficients of the polynomial expression for describing lattice constants of CO ₂ clathrate hydrates formed in the MS10.5 and MS3.1 solutions.	90
6.1	Concentration, temperature range and pressure of the salt solutions used in this work. Concentrations were chosen to match those found by landers and rovers on the Martian surface (Gough et al. 2016).	102
7.1	Concentration, temperature range and pressure of the salt solutions used in this work.	118
7.2	Polynomial coefficients of the polynomial expression describing lattice parameters of CH ₄ clathrates formed in 10 and 15 wt% ammonium sulphate solutions during heating.	122
7.3	Polynomial coefficients of the polynomial expression describing lattice parameters of CH ₄ clathrates formed in 10 and 15 wt% ammonium sulphate solutions during cooling.	123
7.4	Clathrate formation temperatures (K) during individual cycles for the salt solutions indicated.	124
7.5	Clathrate dissociation temperatures (K) during individual cycles for the salt solutions indicated.	124
8.1	Coefficients of a_0 , a_1 and a_2 for each axis and the volumetric expansion, obtained from fitting Eq.(8.1).	154
9.1	Initial composition of sample used to model mineral precipitates on Europa.	174
9.2	Initial lattice parameters used in Pawely refinement.	176
9.3	The values of the coefficient m , the constant c and the correlation coefficient, R for the results obtained from the LDE experimental run for days 0–190.	177
9.4	The values of the coefficient m , the constant c and the correlation coefficient, R for the results obtained from the LDE experimental run for days 331–443.	185
9.5	Mineral precipitation temperatures obtained from calculations by Zolotov & Shock (2001).	187

1 Introduction

1.1 Overview

One of the most complex problems that remains unanswered is the question of the origin of life. In the Solar System, Earth is the only body confirmed to harbour life. The Earth formed approximately 4.6 billion years ago with micro-organisms emerging in the first 3.5 billion (Cottin et al. 2017). This period is known as the “the Hadean” era where the surface of Earth was molten and contained lava and active volcanoes; life is thought to have formed once this surface had solidified, implying it has the ability to form even in the most extreme environments and not to merely spread. Indeed, a group of microbes known as extremophiles can survive high radiation environments, such as those in the near surface ice of comets, or on the surfaces of Europa and Enceladus. They are also thought to be capable of surviving in the seafloor deep beneath the icy crusts of these satellites (Pikuta & Hoover 2007). Therefore, the fact that these microbes can form in such extreme environments suggests that they have the ability to adapt to these conditions, leading to the possibility that life may also be present on other bodies within our Solar System.

The presence of water is thought to be essential for the formation of life. The elements that compose water molecules, hydrogen and oxygen, are some of the most abundant elements in the universe. Markers of water can be seen in giant molecular clouds (Downes & Genzel 1980), in material that represents newborn planetary systems (Hogerheijde et al. 2011), and in the atmospheres of giant planets orbiting other stars (de Mooij et al. 2012). Dust grains originate from stellar outflows and it was established many years ago that their surfaces act as catalysts in the production of water (Oort & van de Hulst 1946). Molecular clouds provide cold dense regions where it is possible for the surface of dust grains to become blanketed in ice, the main constituent of which is water (Gibb et al. 2004). However due to the low density of the interstellar medium, most extra-terrestrial water either takes the form of vapour or ice mantles which stick

to interstellar dust grains.

There are, however, icy bodies within the Solar System thought to contain liquid water beneath their surfaces. The interiors and atmospheres of both Jupiter and Saturn are thought to contain a significant amount of liquid water (Bergin et al. 2000; Helled & Guillot 2013; Helled & Lunine 2014), and their satellites have an abundance of water ice. It is thought that both Europa and Enceladus have a liquid water sub-surface ocean in contact with mineral-rich rock. This suggests that they may have the three essential ingredients for life: liquid water, elements for biological processes, and sources of energy that could be used by micro-organisms. NASA's Cassini mission has shown Enceladus is an active satellite of icy geysers. Recently there have been suggestions that it may also have ongoing hydrothermal activity on its ocean floor, which is potentially suitable for living organisms (Hsu et al. 2015). Titan has been explored by the Cassini-Huygens mission (NASA and ESA) with the Huygens probe that landed on its surface in 2005. The mission suggested the presence of a significant quantity of organic material and large reservoirs of methane, ethane and propane (Mousis et al. 2014).

NASA spacecraft have returned data suggesting that Mars once had water on its surface. The Curiosity Mars Rover revealed an ancient streambed that once existed in an environment that may have supported life. More recently, ground-based telescopes were able to estimate the quantity of water that Mars has lost over its history. It was found that Mars had an adequate amount of liquid water to form an ocean the size of approximately half of its northern hemisphere. It is clear some of this water has been lost to the Martian polar ice caps and to below the surface. It is also thought that much of the early Martian atmosphere was removed by charged particles that originate from the Sun, hence causing the planet to dry out (Jakosky et al. 2015).

The conditions present beneath the surfaces of these icy bodies are ideal for clathrate formation (low temperatures and high pressures). Clathrates are cage-like structures composed of water molecules bonded together via hydrogen bonds. Situated inside these cages are guest gas molecules and the type of clathrate structure depends on the gas present (see Section 2.1 for details on the various structures of clathrates).

One of the motivations for investigating the behaviour and properties of various

clathrate structures in relation to their presence in the Solar System is that they are thought to support life (Prieto-Ballesteros & Muñoz-Iglesias 2014). The presence of clathrates is related to (bio)geochemistry of terrestrial environments due to

1. their sensitivity to pressure and temperature changes;
2. their potential to release nutrients (NO_2^- , NO_3^- , SO_4^{2-});
3. their ability to alter physical and chemical conditions such as pH and salinity by dissociating;
4. their formation mechanism being an exothermic reaction and therefore can contribute to providing the correct environment in which micro-organisms can thrive.

These same points can also be assumed to apply to extra-terrestrial environments (Prieto-Ballesteros & Muñoz-Iglesias 2014).

Water ice and CO_2 have been detected on the surface of Enceladus in the plume emanating from its south polar region. With the exception of CO_2 , the gases observed in the plume (e.g. CH_4 , N_2) are known to have poor solubility in water, therefore the presence of clathrates are inferred. In this way, due to the trapping of the gases within the clathrate structures and their subsequent dissociation, the presence of CO_2 and other gases can be explained (Porco et al. 2006). CO_2 is also present in large quantities in the Martian atmosphere and condenses seasonally at high latitudes in large amounts. Mars has a cryosphere of thickness 0–9 km at equator and 10–22 km at the poles (Clifford et al. 2010) and presents suitable conditions for clathrate formation (Mousis et al. 2013). Mars also presents chaotic terrain features on its surface such as collapsed craters and floods, which are representative of clathrate dissociation (Hoffman 2000; Baker 2009). Clathrates are also thought to be responsible for replenishing CH_4 in the atmosphere of Titan (Fortes et al. 2007). It is thought that CH_4 is present in the sub-surface ocean on Titan which provides suitable conditions for clathrate formation. It is suggested that these clathrates rise to the surface, where they dissociate and release CH_4 into the atmosphere.

Despite the observational evidence on the presence of clathrates throughout the Solar System, there is a lack of experimental studies, and therefore data, present in current literature. Therefore, information on clathrate properties and behaviour on planetary bodies is lacking. Many of the studies at present are based on theoretical modelling (e.g. Fortes et al. (2007); Thomas et al. (2007); Mousis et al. (2011); Bouquet et al. (2015)) and of the experimental studies a majority are based on forming clathrates in pure water (e.g. Tse (1987); Dartois et al. (2012); Ambuehl & Elwood Madden (2014); Johnson et al. (2017)). It is a well known fact that salts depress the freezing point of water, implying that they could also depress the formation and dissociation temperatures of clathrates. Therefore, it is of fundamental importance to carry out experimental investigations of clathrates in the presence of saline solutions in order to provide realistic data on extra-terrestrial clathrates which can be applied to the oceans of Europa, Enceladus and Titan and the surface of Mars. This could therefore shed light on the geology of these bodies and hence provide information on their environments and potential for harbouring life.

The presence of hydrated minerals on the surface of planetary bodies is also thought to support the presence of life due to their large water content. This thesis will focus on the two highest hydrated magnesium sulphate minerals, epsomite ($\text{MgSO}_4 \cdot 7\text{H}_2\text{O}$) and meridianiite ($\text{MgSO}_4 \cdot 11\text{H}_2\text{O}$). Epsomite is the thermodynamically stable hydrated phase (Vaniman et al. 2004), however when low temperatures are reached ($< -2^\circ\text{C}$) meridianiite begins to form instead. Due to its stability at low temperature, meridianiite is thought to be the most stable hydrated magnesium sulphate salt present on the surfaces of Mars and Europa (Peterson & Wang 2006; Muñoz-Iglesias et al. 2014), and therefore could be one of the main source of water on the surface of Mars. In addition, the presence of mineral precipitates could affect ice rheology due to their size and distribution. When aqueous solutions containing NaCl , MgCl_2 and CaCl_2 , which are some of the main salts found in terrestrial oceans, are frozen the result is a highly concentrated brine. Indeed, it has been shown that minerals that precipitate from ice-brine environments remain trapped within pores of the ice rather than sinking to the ocean floor (Light et al. 2003). Therefore, understanding the

mineral precipitation from highly concentrated brines is important in enabling us to comprehend processes such as hydrological activity on Mars and core–ocean–ice crust interactions on Enceladus and Europa. Furthermore, understanding low temperature mineral precipitation could prove equally important in aiding our understanding of low temperature biogenic interactions, as it is possible that brines could play an important role for putative life on Mars, Europa, Enceladus and potentially other icy bodies in our Solar System.

1.2 Research Objectives

Due to its unique physical properties, water in both liquid and solid form has played a crucial role in many global and astrophysical processes. This research project investigates the formation of, interactions with, and alterations of, minerals and related materials in various natural environments with, and by, water in its different states. The objective of this PhD will therefore be to investigate the role of water in its different forms in shaping the geology of planetary bodies.

The objectives will be met by

1. using synchrotron radiation structure–probing techniques, primarily X–ray powder diffraction, at Diamond light Source (DLS)¹;
2. exploiting the newly constructed Long Duration Experiment (LDE) facility at DLS. This will allow water–solid interactions to be explored over a wide range of conditions of low and high temperatures (90–300 K) and timescales of seconds to minutes and hours through to months. This will enable the distinction between thermodynamic and kinetics driven processes occurring in astrophysical environments to be made.

¹For acronyms and abbreviations see Appendix B.

1.3 Thesis Outline

This thesis is composed of a total of 10 chapters. Chapter 1 (this introductory chapter) gives an introduction and context for the research followed by the research objectives. Chapter 2 gives a literature review of clathrate hydrates on various Solar System bodies and the inhibiting affect of different salts on the freezing point of clathrates and ice. Chapter 2 also gives an introduction to the hydrated sulphates found on planetary bodies and an example of some experiments done previously on these hydrated minerals. Chapter 3 discusses the theory behind the experimental methods used during this research project, primarily X-ray powder diffraction, and the quantitative and qualitative methods used to analyse the experimental data. Chapter 4 provides the technical details on the experimental facilities used to collect the data for this project and also discusses sample preparation, and individual tools used to create realistic astrophysical environments to which samples could be subjected. The following 5 chapters explain the results and conclusions of the experimental work. Chapters 5, 6 and 7 present results on the in-situ formation of clathrate hydrates in the presence of various salt solutions with relevance to Enceladus and Europa, Mars and Titan respectively. These chapters discuss the effect that the various salts have on clathrate formation and dissociation temperature, thermal expansion, density and the resulting solution composition. They also discuss various ice polymorphs formed and their effect on clathrate hydrate dynamics. Chapter 8 begins by briefly discussing the planetary bodies thought to contain hydrated sulphates, then goes on to present and discuss results on the effect of temperature on the structure of epsomite. Chapter 9 presents results on the slow cooling of merdianiite and a saline solution representative of Europa's ocean composition using the LDE. The final chapter, chapter 10, presents the overall conclusion of the research work in this thesis and identifies the future work that could be carried out as a continuation from the results presented in chapters 5–9.

2 Background

2.1 Clathrate Hydrates

Clathrates were discovered in 1810 by Humphry Davy (Davy 1811). They are formed at high pressures and low temperatures, and are cage-like structures in which water molecules bonded via hydrogen bonds can encase guest molecules.

The type of guest molecule that can be trapped within a clathrate depends on the clathrate structure, of which three are currently known: sI, sII and sH (Sloan & Koh 2007) (see Figs. 2.1 and 2.2). sI clathrates form a cubic structure with space group Pm-3n. They are composed of two cage types: the smaller 5^{12} (12 pentagonal faces) and the larger $5^{12}6^2$ (12 pentagonal faces and 2 hexagonal faces). sI clathrates are constructed of two small cages for every six larger ones, and host relatively large molecules such as CO_2 and CH_4 . sII also form cubic structures and are composed of sixteen small 5^{12} cages and eight large $5^{12}6^4$ cages; sII clathrates typically host smaller molecules such as O_2 and N_2 . The least common clathrate hydrate, sH, is composed of one large cage, three smaller cages and two medium $4^45^66^3$ cages. sH clathrates form hexagonal structures and usually require two types of guest species in order to remain stable. Recently a new structure of clathrate has been proposed (Huang et al. 2016); this type of clathrate (structure III) is predicted to have a cubic structure and be composed of two large $8^66^84^{12}$ and six small 8^24^8 cages.

On Earth clathrates can be found naturally on the seabed, in ocean sediments, and in deep lake sediments. Methane can potentially be trapped in clathrate structures, which makes them a significant potential energy resource. Clathrates have a strong tendency to form in pipelines and stick to the pipe wall, therefore blocking the pipeline. Once formed, they can be dissociated by increasing the temperature and/or decreasing the pressure. However, even under these conditions, the dissociation process is slow. Therefore, preventing hydrate formation is a key problem for gas and oil pipelines.

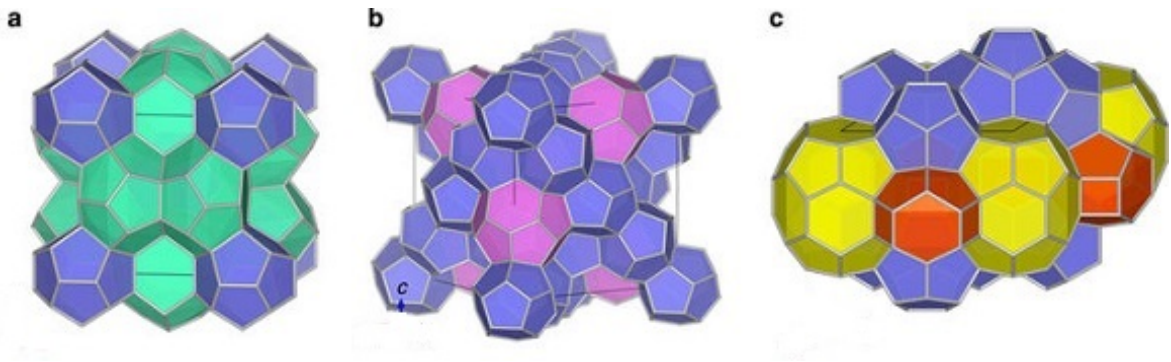


Figure 2.1: Various structures of clathrate hydrates. (a) structure I (sI), (b) structure II (sII) and (c) structure H (sH) (Momma et al. 2011).

2.1.1 Clathrate hydrates in the Solar System

The conditions on icy Solar System bodies such as Enceladus, Europa, Mars and comets have long been considered as potential for clathrate formation (Max & Clifford 2000; Prieto-Ballesteros et al. 2005; Marboeuf et al. 2010; Bouquet et al. 2015). Clathrates are leading candidates for the storage of gases such as CH_4 and CO_2 in the Solar System (Prieto-Ballesteros et al. 2005; Mousis et al. 2015; Bouquet et al. 2015); therefore understanding the kinetics and thermodynamics of clathrate hydrates under planetary conditions is important.

2.1.1.1 Clathrate hydrates on Enceladus

It has been confirmed that water ice and CO_2 are present on the surface of Saturn's satellite, Enceladus (Matson et al. 2013). Among the gases present in the plumes emanating from the satellite's surface (Waite et al. 2006) are CO_2 , CH_4 and N_2 all of which have poor solubility in water (except for CO_2). Therefore the presence of these gases in the plumes is suggestive of their trapping in the form of clathrate hydrates, with subsequent release due to their dissociation (Bouquet et al. 2015). An image of

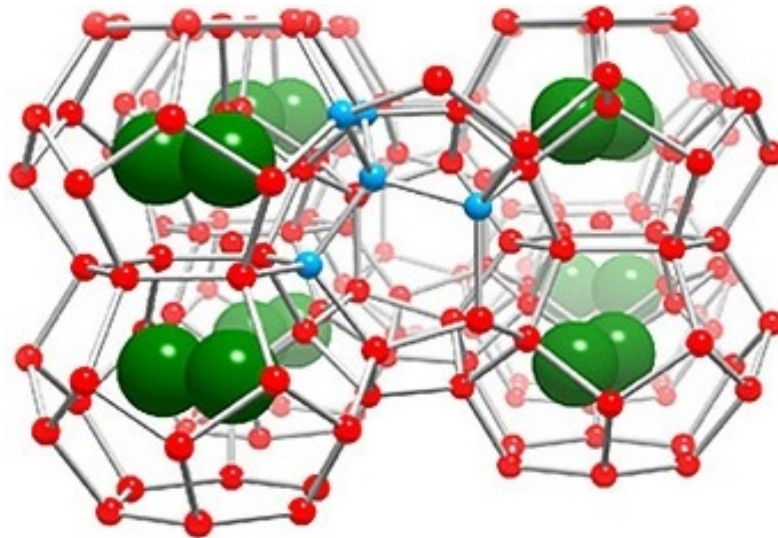


Figure 2.2: sI clathrate encasing a gas molecule (<https://ps.uci.edu>).

the plume on Enceladus' South Polar region is shown in Fig. 2.3. It is not clear as to the origin of the plumes seen by the Cassini spacecraft on the surface of Enceladus. Measurements of gravity fluctuations in the vicinity of Enceladus taken by Cassini indicate that there is an underground sea of liquid water at the satellite's South Pole, and this may be the origin of the vapour plumes seen at its surface. Alternatively the plumes could be due to the heating of ice which could cause the dissociation of clathrate hydrates (Kieffer et al. 2006). However, Fortes (2007) used a clathrate xenolith model to explain the formation of the plumes on Enceladus' surface. They suggested that fluids pass through the ice shell, where clathrates which lie along fractures and grain boundaries metasomatise the mantle; that is there is a change in the composition of rock as a result of the introduction or removal of chemical constituents. Clathrates are then trapped in the rising cryomagmas as xenoliths. These are subsequently carried upwards where they dissociate, releasing their enclosed gas and forming the plumes.

The plumes of Enceladus are composed mostly of water ice and vapour with traces of CO_2 , CH_4 and N_2 gas (Fortes 2007). If it is assumed that the reservoir that

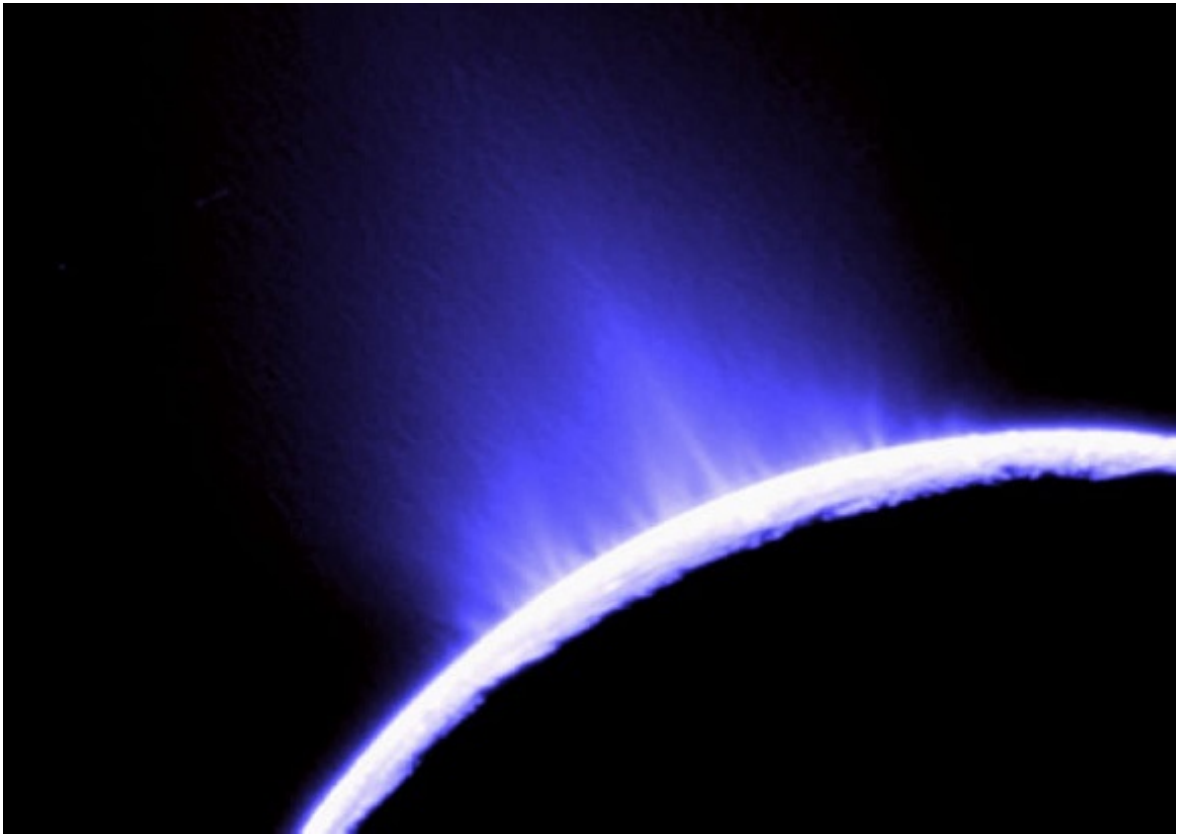


Figure 2.3: Plume emanating from Enceladus' South Polar region (credit: Cassini imaging Team, JPL, ESA, NASA).

produces the plumes is composed primarily of water, then it can be said that the plumes originate from chambers of liquid water at 273K (Porco et al. 2006); this is known as the “Cold Faithful” model. However, Waite et al. (2006) suggests that the composition of the plume represents the composition of the surface at the location of out-gassing, which means that the trace gases must also be taken into account. The plume composition as measured by the Cassini Ion and Neutral Mass Spectrometer (INMS) (Waite et al. 2006), and reported by Fortes (2007), is $\text{H}_2\text{O}=91\pm 3\%$, $\text{CO}_2 = 3.2\pm 0.6\%$ and $\text{CH}_4 = 1.6\pm 0.4\%$; these abundances are all at least a magnitude larger than the solubility of these molecules in the reservoir (with the exception of CO_2).

Conversely the ability of these gases to dissolve in clathrate hydrates is significant (Waite et al. 2006). It is suggested by Kieffer et al. (2006) that the plume comes about from the fracturing of the ice cap, hence exposing the clathrates to conditions close to that of a vacuum. This causes the clathrates to decompose violently, producing the plumes. The ice cap reseals after a period of time and original conditions are restored. This is known as the “Frigid Faithful” model. However, Fortes (2007) notes some weaknesses in the “Frigid Faithful” model. The mechanism implies that, in any fracture region, there will be plumes emanating from the fractures; this is not the case. Also there is some difficulty in understanding how fractures can penetrate through kilometres of crust and not become partially filled with debris. In addition it is also not well understood how a fracture can remain active when the clathrates have been removed after de-gassing.

Kieffer et al. (2006) did not propose an origin for their clathrate reservoir, however Fortes (2007) states that there are only two possible scenarios. The first is that the clathrates are primordial and condensed ex situ from the proto-Saturnian nebula; this case implies that the clathrates should contain noble gases, as it is thought that these gases are in abundance in the proto-Saturnian nebula (Niemann et al. 2005). The second, preferred, case is that the clathrates are formed in situ by the hydrothermal activity at the rock-ice interface. Fortes (2007) puts forward an alternative scenario for the origins of the plumes: the “Frothy Faithful” model. He assumes that the cryovolcanic melts are propagated to the surface and they entrain fragments of the

clathrate hydrate; these decompose at low pressure and add “fizz” to the magma to produce large vent eruption velocities. This model can explain the volatile abundances, the ice to vapour ratio in the plumes, and vent temperatures.

The trapping of gases by clathrates could also have a significant impact on Enceladus’ ocean composition, and hence on that of the plumes emitted in the South Polar Region (Bouquet et al. 2015). The enclathration of gases would lower the concentration of volatiles in the ocean to below that observed in the plumes; this would indicate that any clathrates formed would need to dissociate in order to replenish the volatile concentration of the plume. If this is not the case then the gas concentration would need to be restored by an alternative mechanism, such as hydrothermal activity (Bouquet et al. 2015).

2.1.1.2 Clathrate hydrates on Europa

The low temperatures and high pressures present in the icy crust (~ 5.3 MPa at 273 K; Bouquet et al. (2015)) and beneath the oceans (~ 3.6 – 4.2 MPa at 273 K; Bouquet et al. (2015)) of Jupiter’s satellite Europa make it an ideal location for the formation of clathrate hydrates. CO_2 and SO_2 are thought to be the guest molecules trapped within the clathrate cages as they have been detected on Europa (Prieto-Ballesteros et al. 2005). The internal structure of Europa is shown in Fig. 2.4.

There are two possible formation mechanisms of clathrates on Europa, as discussed by Prieto-Ballesteros et al. (2005). First, volatiles would be trapped by a floating ice shell in the ocean; in this case clathrate hydrates would be expected to form due to the interactions of the gases with the ice crust. Second, a more complicated formation mechanism for clathrates involving the gas-phase and gas-solid chemical reactions; this could be related to Europa’s complex formation.

The final salt concentration of the oceans on Europa is the deciding factor of the sinking or floating of clathrates. There should be a marked variation in the clathrates formed in the oceans compared to the clathrates formed in the ice shell. In the latter case the clathrates formed would be via metamorphism (change of the geological

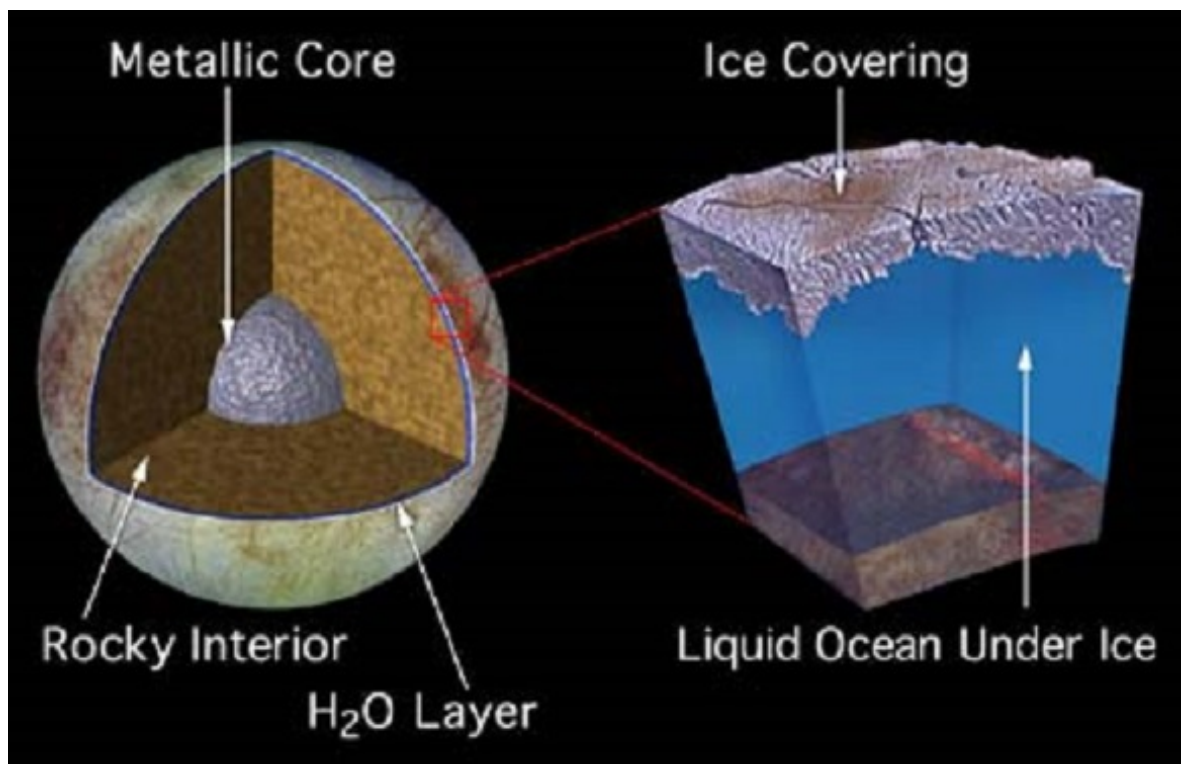


Figure 2.4: Internal structure of Europa (<http://explanet.info/Chapter09.htm>).

texture) of the water ice, while the clathrates formed in the ocean would be igneous minerals as they crystallise from the aqueous cryomagma.

Muñoz-Iglesias et al. (2014) have investigated the formation and dissociation of CO₂ clathrate hydrates in a H₂O-MgSO₄-CO₂ system using Raman spectroscopy. This was done at room temperature, which is much higher than the temperature range found on Europa, therefore does not replicate the appropriate conditions in which clathrate hydrates would form on the satellite. They found that CO₂ clathrates and MgSO₄ mineral hydrates could both co-exist on the satellite. Additionally, they found that the amount of CO₂ clathrate formed in comparison to ice varied despite being produced under the same experimental conditions. This was attributed to high meta-stability of CO₂.

2.1.1.3 Clathrate hydrates on Mars

Early in its history, Mars is believed to have possessed a planetary inventory of water equal to a global equivalent layer $\sim 0.5 - 1$ km deep (Carr 1986, 1996). Although some of this inventory has been replenished by H₂O exsolution from magmas (Craddock & Greeley 2009), since the Late Hesperian $\sim 15\%$ of the original inventory is thought to have been lost to space (Vaille et al. 2010), with a so far unquantified amount believed to have been further taken up in the formation of hydrated minerals.

Of the water remaining today $\sim 90 - 95\%$ is believed to reside in two thermally distinct subsurface reservoirs (Carr 1986, 1996):

1. as ice in the cryosphere (a permanently frozen near-surface region); and
2. as groundwater located deeper in the crust, where radiogenic heating is thought to have increased lithospheric temperatures above freezing (Fanale 1976; Rossbacher & Judson 1981; Kuzmin 1983; Clifford 1993; Carr 1996; Clifford & Parker 2001).

The average thickness of the cryosphere likely varies from 0–9 km at the equator, to $\sim 10 - 22$ km at the poles (Clifford et al. 2010). As well as being significant in

the hydrological and mineralogical evolution of the Martian crust, these sub-surface regions may also provide a potential means of survival for any putative life forms in sub-surface habitats, where they would have been isolated from the effects of oxidants, climate change and large, surface-sterilising impacts (Onstott et al. 2006; Wadsworth & Cockell 2017).

Within the cryosphere (at depths down to a few kilometres) and in the near sub-surface (depths down to a few metres), conditions are also suitable for the existence of clathrate hydrates (Mousis et al. 2013). The pressure below the present-day Martian surface is dominated by the lithostatic pressure which, assuming the surface is predominantly tholeiitic basalt, is given by $P_{\text{lith}} \simeq 11 [h/100 \text{ m}] \text{ bar}$ at depth h , (McSween et al. 2009). Had the atmospheric pressure in the past been higher ($\simeq 2 \text{ bar}$ as suggested by Chassefière et al. (2013)) the pressure at depth h would have been correspondingly enhanced in Mars' past such that historic clathrate formation at depth could have extended much deeper than present day conditions might suggest.

Under present day conditions, the lowest and highest surface temperatures in the South Polar Region are 150 K and 303 K (Mousis et al. 2013). Calculations suggest that, under these conditions, CO_2 clathrates should be stable at the coldest temperature and unstable at the highest surface temperature and, therefore, likely to dissociate. In order for Martian clathrates to remain stable throughout the Martian year they would need to be buried at a depth of at least 1.1 m (Mousis et al. 2013).

The thermodynamic stability field of clathrates on Mars extends to different depths in different regions. According to models, at the equator it reaches to within the top 15 m of the surface and extends to a depth of 3–5 km, while at the poles it reaches the surface and extends down to depths of 8–13 km (Chastain & Chevrier 2007; Ambuehl & Elwood Madden 2014); this implies that a large reservoir of CO_2 hydrate is available. CO_2 is believed to be present in large quantities at depth (Mousis et al. 2013). In Nature, ice is rarely composed of pure water and will contain volatiles prior to clathrate formation. Ambuehl & Elwood Madden (2014) suggest that the presence of volatiles will affect the clathrate formation and dissociation processes and therefore the ice caps and frozen lakes, or oceans, preserved as permafrost on the planet.

Some geomorphic features on the surface of Mars are attributed to the dissociation of clathrates. For example, certain observed chaotic terrain is the result of a collapsed cratered region due to the removal of surface material that may include clathrates (Baker 2009). The dissociation of CO₂ clathrates is thought to be one of the causes of floods on the Martian surface (Hoffman 2000). Understanding the dissociation of hydrates can lead to better understanding of how the release of CO₂ from permafrost and polar caps is influenced by seasonal temperature changes, seismic events, landslides, pore water salinity changes, impacts and changes in obliquity (Ambuehl & Elwood Madden 2014).

Salinity is an important factor to consider in the context of the Martian surface as it depresses the freezing point of water (Sloan & Koh 2007; Safi et al. 2017). Soil samples collected by landers and rovers at various locations show similar chlorine concentrations of between 0.2–1 wt% (Gough et al. 2016). It is thought that these salts were produced from the interactions of volcanic gases with mafic surface material (Rieder et al. 1997). Widespread surface deposits consistent with the presence of chloride-bearing material were detected by the Mars Odyssey Thermal Emission Imaging System (Osterloo et al. 2008). Due to the fact that chlorides form highly soluble salts, their high content in the Martian regolith is somewhat surprising and could possibly be due to the dispersal of early brine, or the wind dispersal of dried evaporite dust (Burt & Knauth 2003).

Since eutectic¹ magma compositions are known to be common on Earth, eutectic brine compositions may occur at shallow depths in the Martian sub-surface region (Burt & Knauth 2003). Studies on the thermodynamic and chemical stability of salts on Mars have shown MgCl₂, CaCl₂ and LiCl, are likely to occur, with the freezing point of the brines being as low as 210 K (Burt & Knauth 2003).

In fact MgCl₂ and CaCl₂ are thought to be the most fitting salts responsible for the Recurring Slope Lineae (RSL, narrow low-reflectance features) on the Martian surface which are thought to be due to the transient flow of brines (see Fig. 2.5). In

¹Mixture of two or more components in such proportion that their combined melting point is the lowest attainable

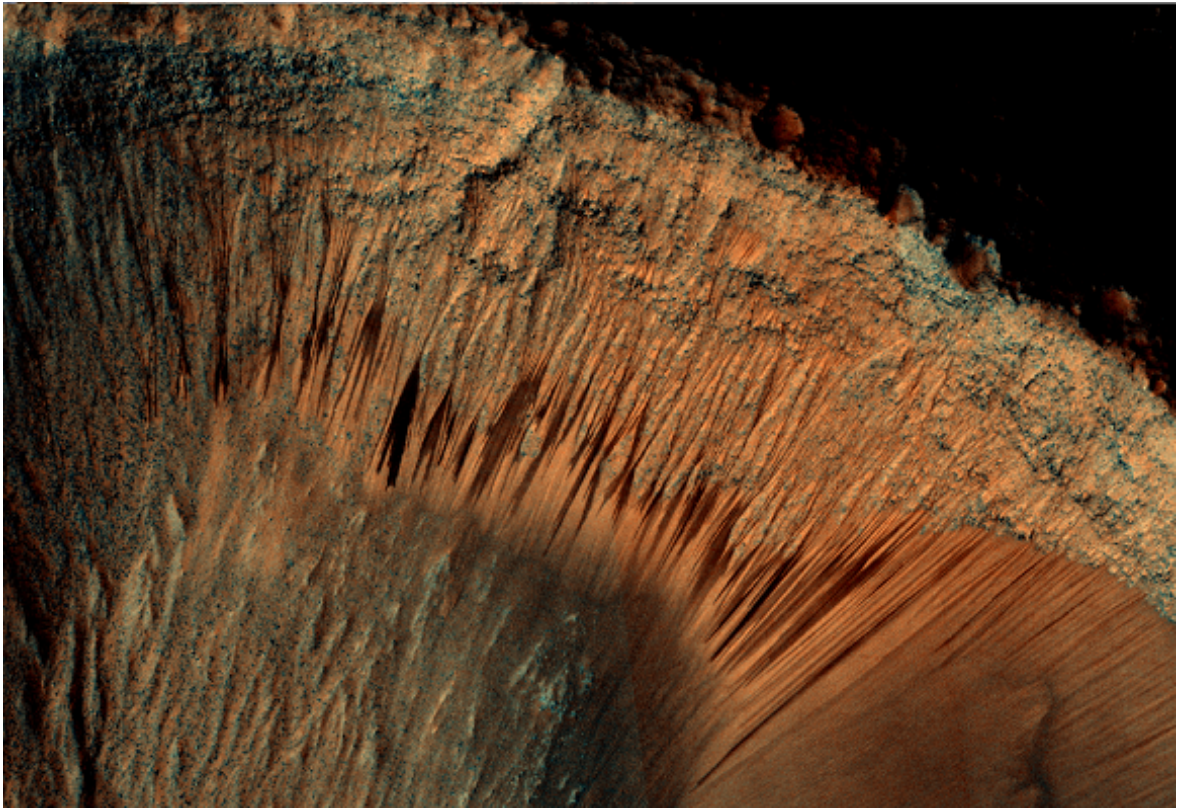


Figure 2.5: Recurring Slope Lineae on the Martian surface taken by the HiRISE camera (<http://dovesipuoparlarediognicosa.blogspot.co.uk/2015/09/la-nasa-conferma-su-marte-lacqua-ce.html>).

some cases (e.g. the Palikir crater, located in the southern highlands) the RSL are too narrow to have been caused by liquid water and instead, are attributed to hydrated mineral (Ojha et al. 2015). RSL extend downwards on steep, warm slopes; they appear every Martian year when temperatures reach 250–300 K and fade out the brines freeze in “winter” (Ojha et al. 2015). The seasonality of the observed RSL formation is consistent with the seasonality of the melting of ice caused by these salts (Gough et al. 2016). Adding salts such as MgCl_2 or CaCl_2 , lowers the freezing point of water, but only by a few degrees (Burt & Knauth 2003).

The inhibition of clathrate formation within briny solutions will cause a shift in the clathrate stability zone. This could potentially change the structure of clathrates by altering how gas molecules occupy the cages (Sloan & Koh 2007). However, the presence of clathrates in the Martian cryosphere is thought to be primarily constrained by temperature and pressure conditions at the relevant depths where the cryosphere ends (Mousis et al. 2013). Indeed, due to low pressures and temperatures on the present day surface, water cannot be stable in its liquid form. However if salts are added to liquid water the triple point is depressed, therefore enabling liquids to be stable at lower temperatures and pressures (Elwood Madden & Bodnar 2002). Due to their density and fluid nature, brines which occur in the regolith on Mars should lie between an upper ice layer and lower salt layer (Burt & Knauth 2003).

Elwood Madden & Bodnar (2002) carried out geochemical thermal modelling to predict the Martian brine composition. They found that a chloride ion brine could be a stable fluid at low temperatures (~ 250 K), while a sulphate ion brine, however, has low solubility at these lower temperatures, so that it will become saturated and precipitate out, leaving chloride as the dominant liquid phase ion.

The goal of the Phoenix Lander mission was to determine if the northern polar regions on Mars were capable of sustaining life and, as water is considered essential for life, a prime objective was to determine if liquid water was present at the landing site (Renno et al. 2009). It is thought that a top layer of regolith protects an under-layer of near-surface ice from high temperatures and sublimation (Renno et al. 2009). At the Phoenix landing site there are areas of disturbed and undisturbed regolith. The disturbed areas arise from the thrusters on the Phoenix lander, which removed surface material (Mehta et al. 2011). In both disturbed and undisturbed areas, Renno et al. (2009) gave theoretical and observational evidence for liquid brines. There is evidence that soft water ice found in the undisturbed areas is in fact frozen brine (Martínez & Renno 2013). Previously it was suggested by Mellon et al. (2004) that the pure water ice could have been of low density, but Martínez & Renno (2013) argued that the trenches dug by the robotic arm on the Phoenix lander contain white material which could not be a consequence of the sublimation of pure water ice. Instead, the

proposal by Renno et al. (2009) that this material could be salt crystals left behind after the sublimation of frozen brine seem more likely. Indeed, perchlorates have been discovered at the site of the Phoenix Lander (Hecht et al. 2009), suggesting that salts are present in both disturbed and undisturbed regions around the landing site (Hecht et al. 2009).

The numerous albedo features – showing bright or dark contrast with adjacent regions – observed on the surface are significant on Mars as it has been hypothesised that they originate from processes such as seepage of liquid brines from the shallow sub-surface (Renno et al. 2009). Dark spots with dark albedo features have been observed on polar dunes in both the southern and northern-hemisphere regions (Martínez & Renno 2013), and water ice has been observed on them (Kereszturi et al. 2011). The spots are darkest at the centre and have a brighter zone on their edges, often referred to as “bright halos”; it is at the centres of these spots where liquid brines form (Martínez et al. 2012). Flow-like features originating from the dark spots flow downwards and are located on the dune ridges. The generally accepted cause of these dark spots and flow-like features is gas-venting from the sub-surface (Kieffer 2007). Martínez & Renno (2013) propose that the decrease, and subsequent increase, in albedo as the surface temperature increases is caused by brine formation followed by subsequent/later freezing. They also show that the formation and presence of brines is consistent with the temperatures measured by the Thermal Emission Spectrometer and the Thermal Emission Imaging System aboard the Mars Global Surveyor. However, flow-like features could also be a result of ephemeral water migration in the form of liquid brines and under-cooled liquid interfacial water (Kereszturi et al. 2011). Furthermore, sub-surface melt water can also be invoked to account for the growth of the flow-like features on the Martian surface, as the brine can form from salts in contact with sub-surface water (Möhlmann 2010).

2.1.1.4 Clathrate hydrates on Titan

In general the structure of Titan is a rocky core overlain by an ice-rich mantle (Fortes et al. 2007). A sub-surface ocean and ice-rich crust are also possible, depending on the pressure and temperature conditions at the time of formation and at present. The internal structure of Titan is shown in Fig. 2.6.

The methane found in Titan's atmosphere is likely to have formed in the protosolar nebula. The theory is that methane was produced through serpentinisation — processes whereby rock is changed, with the addition of water into the crystal structure of the minerals found within the rock — which took place in the interior (Mousis et al. 2009). However, this theory was later invalidated by the methane D/H ratio measurements (Mousis et al. 2009). Due to photochemistry, by solar UV, the amount of methane currently present in the atmosphere of Titan would vanish in a time span of 10-100 Myr (Choukroun et al. 2010). This implies that there must be a replenishing source on the satellite's surface, or a reservoir that involves the release of methane.

Methane in Titan's atmosphere could have also originated from comets. Cometary material would have fallen onto the satellite's surface whereupon the methane is released due to the release of heat energy on impact (Choukroun et al. 2010). Indeed high impact rates were expected on Titan between its formation and the late heavy bombardment period which could have contributed to the satellite's methane content (Choukroun et al. 2010). However, despite this, the rate of impacts since then has significantly reduced, and looking at data from the Cassini Radar observations an overall age of Titan's surface is given as 0.1–1 Gyrs (Lorenz et al. 2007). In addition to this, if comets were responsible for the atmospheric methane, they would have brought large amounts of CO, which is inconsistent with the low abundance of the gas that is observed on the present day Titan (Bellucci et al. 2009). Therefore from this, it is unlikely that comets are the cause of the atmospheric methane on Titan.

Taking all this into consideration, the most probable source of methane is located deep in Titan's interior (see Fig, 2.6), either in a liquid state or as clathrate hydrates (Choukroun et al. 2010). The boiling point of pure methane is between 110–130 K,

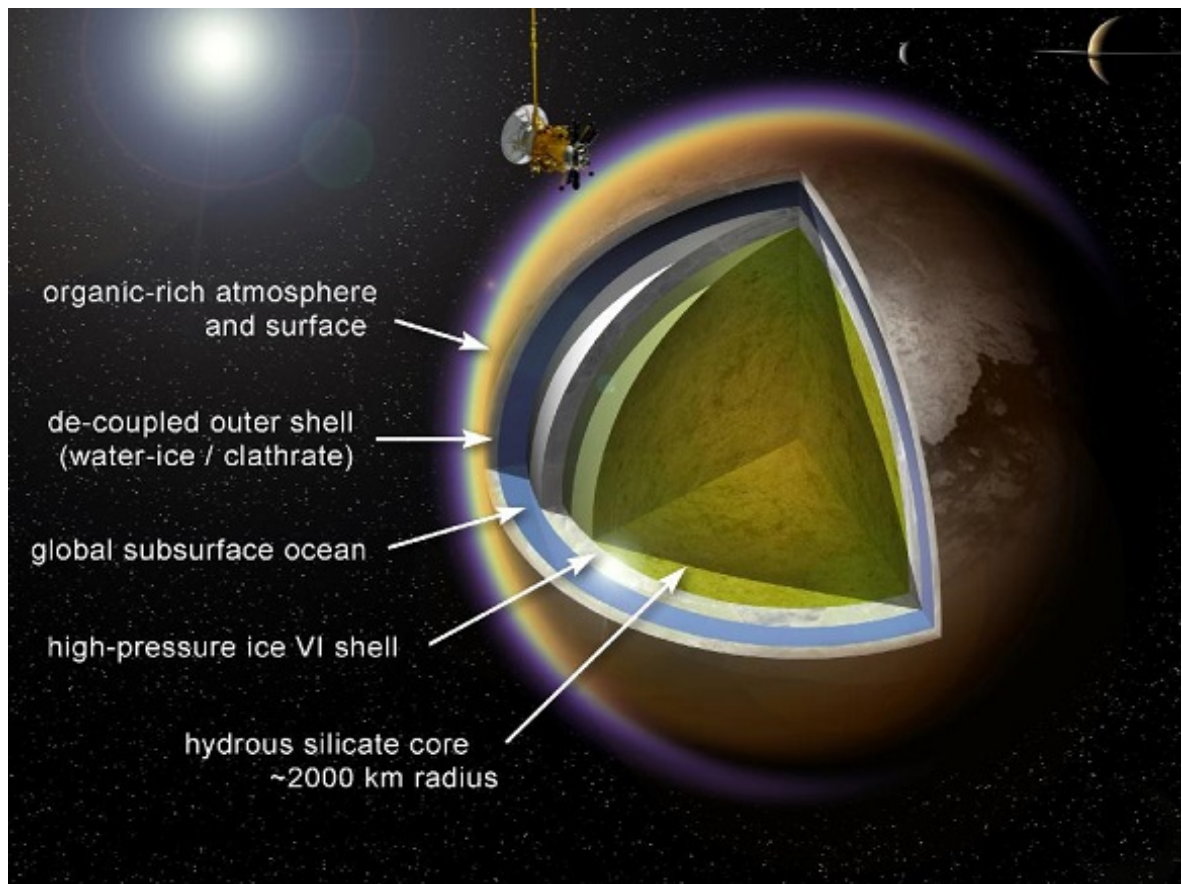


Figure 2.6: Internal structure of Titan (https://www.nasa.gov/mission_pages/cassini/multimedia/titan20120223L.html).

which depending on the pressure conditions, is a temperature that can be reached at shallow depths on Titan. Therefore, this restricts the possibility of methane existing in the regolith of this satellite (Choukroun et al. 2010).

Titan's atmosphere is thought to be largely influenced by methane clathrates. If Titan had a 100 km thick surface that was of high strength, and contained methane clathrates of low thermal conductivity, then its interior would have to be significantly warmer than is expected. The satellite's upper atmosphere is thought to have a max-

imum methane abundance of 1.4% (Choukroun et al. 2010). Once the troposphere is reached the abundance of methane increases and close to the surface the concentration reaches 5% (Choukroun et al. 2010).

Tobie et al. (2006) suggested that methane in the atmosphere originated from the dissociation of clathrates. Experiments have shown that methane clathrate formation under Titan's proto-core is feasible and that they would ascend to the outer liquid layer. Due to their large stability field, clathrates are thought to have stored methane at depth on Titan since its early history. This therefore could make their dissociation difficult and implies that they may be an unlikely source of methane on Titan unless there is a source for intense warming at shallow depths. Sudden reservoir decomposition and/or chemical interactions with an inhibitor of clathrates favours the dissociation of methane clathrates (Choukroun et al. 2010).

Cryovolcanism has long been inferred to occur on icy satellites (Lewis 1971). Also, surface features which may have resulted from cryovolcanism on Titan have been identified by the Cassini spacecraft (Nelson et al. 2009; Choukroun et al. 2010). These features are still a matter of debate in the literature; however the most accepted source is the emission of material from the interior of the satellite. Evidence in the atmosphere lead to the same conclusion (Choukroun et al. 2010). In addition to ammonia, ammonium sulphate and methanol have been suggested to be present on Titan (Choukroun et al. 2010). The presence of ^{40}Ar in the atmosphere suggests that some material has come from the interior of the satellite as this atom is produced from the radioactive decay of ^{40}K (Niemann et al. 2005). Another factor that contributes to this conclusion is that the ratio of $^{40}\text{Ar}/\text{N}_2$, as measured by the Gas Chromatography and Mass Spectrometer (GCMS), indicates that N_2 is not primordial but comes from the conversion of ammonia by photochemistry (Atreya et al. 1978). Collectively this information leads to the conclusions that 1) out-gassing is currently an active process on Titan or that it was once, and 2) ammonia is likely involved in the formation and/or destabilising of the materials that are emitted from the surface and/or atmosphere of Titan (Choukroun et al. 2010).

A surprising feature in Titan's atmosphere is the lack of xenon and krypton.

Mousis et al. (2009) proposed a model that suggests these gases are trapped in clathrate hydrates formed in the protosolar nebula. This model theorises that Xe and Kr are trapped in the methane-dominated clathrates that went on to form the building blocks of Titan. In this scenario Ar sublimated due to the pressure and temperature conditions in Saturn’s subnebula.

Thomas et al. (2007) and Mousis et al. (2011) both suggest an alternative scenario for the depletion of these noble gases that also involves clathrates. They propose that originally there were large amounts of Kr and Xe present in Titan’s atmosphere and that they were trapped in methane- and nitrogen-dominated clathrates formed from the crystalline ice on the satellite’s surface.

To explain the deficiency of CO, N₂, Ar, and Kr on Titan it was proposed by Alibert & Mousis (2007) that Titan was formed in the subnebula, which is thought to have been warm enough to at least partly de-volatilise the planetismals captured from the Solar nebula. Due to the warm conditions of the subnebula, this would cause the de-volatilisation of CO, N₂, Ar, and Kr, whose clathration temperatures are low, while H₂O, NH₃, H₂S, CO₂, Xe, and CH₄ would stay in the solids. This scenario, however, could not explain effectively enough the observed deficiencies of noble gases in the atmosphere of Titan, as we would expect that Xe would remain trapped in planetismals (Alibert & Mousis 2007).

Titan is thought to have NH₃ included in its sub-surface oceans of liquid water. The relationship between the dissociation temperature of the clathrates and the concentration of ammonia is not well established (Choukroun et al. 2010). The work of Tobie et al. (2006) has estimated the decrease in the dissociation temperature by transposing the effect of ammonia on the melting curve of ices. They find that the presence of ammonia likely increases the dissociation of clathrates. However the experimental constraints are lacking to robustly quantify this effect.

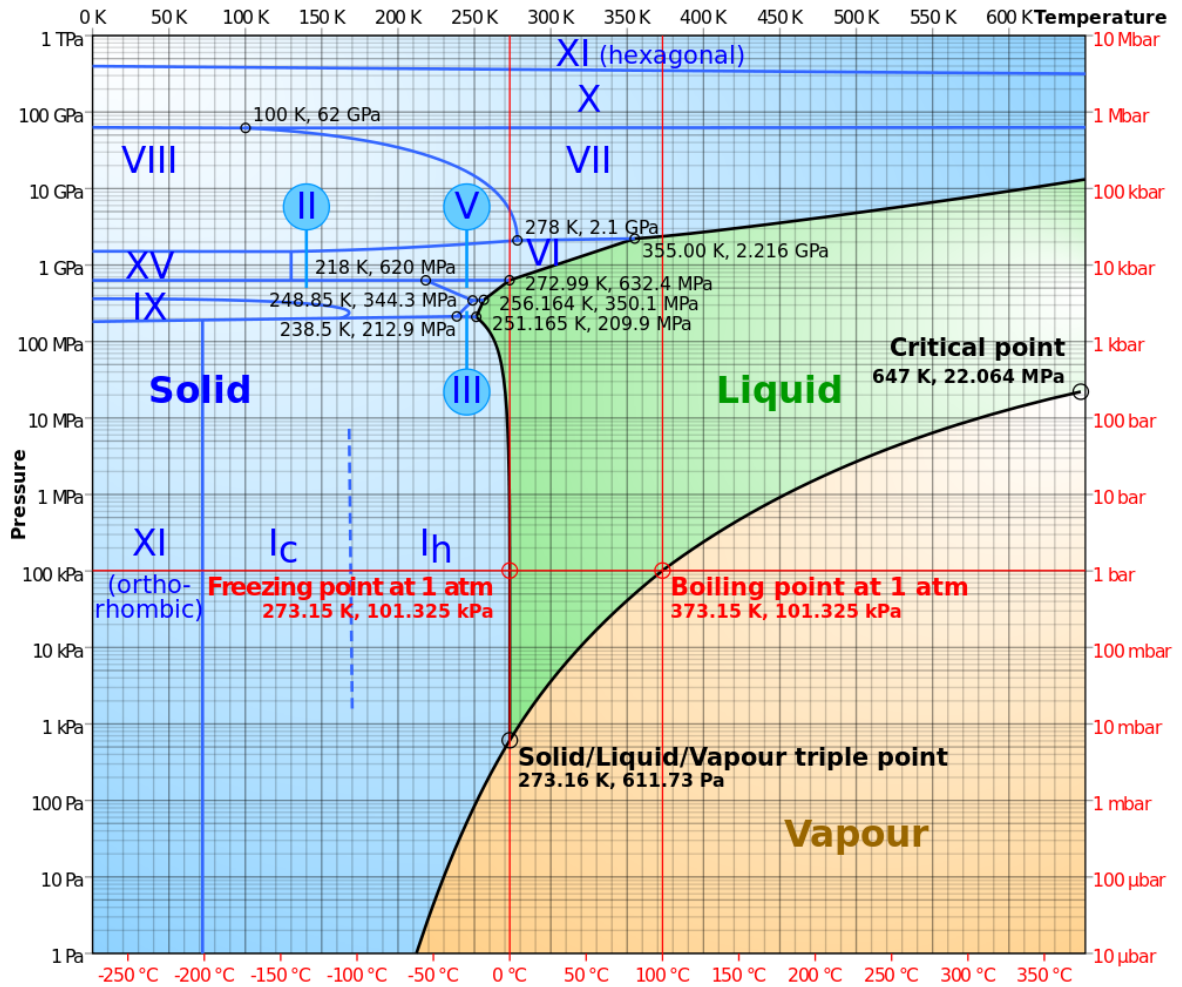


Figure 2.7: Phase diagram of ice (<http://www.iii.lv/ice/?lang=lv>).

2.2 Clathrate Hydrate Inhibitors

2.2.1 Electrolyte Inhibitors

It is well known that electrolytes have an inhibiting effect on the formation of clathrate hydrates (Sabil 2009); however this effect is not well documented in the current literature, particularly experimentally. The inhibition effect is caused by the ions in the electrolyte solution lowering the solubility of the gas, hence lowering the activity of the water, resulting in the clathrate hydrates forming at lower temperatures relative to their development in pure water (Duan & Sun 2006). Also, the presence of inhibitors impedes the water molecules from forming hydrogen bonds (Sabil 2009), adding a further obstacle to clathrate formation.

The best electrolyte inhibitors will exhibit maximum charge and minimum radius (Makogon 1997) and, while less is known about magnesium electrolyte solutions (e.g. MgCl_2 and MgSO_4), they do exhibit an inhibiting effect that is stronger than calcium or sodium electrolyte solutions (Sabil 2009). The smaller ionic size of magnesium increases the surface charge density, and so attracts more water molecules, thus decreasing the activity of water (Sabil 2009).

There is also another effect, called the freezing point depression, where the freezing point of a liquid is lowered due to the presence of a foreign molecule in the solution. This arises due to the colligative properties² of water. The only property of the molecule that effects the freezing point depression is the number of ions in the molecules, i.e. MgCl_2 and CaCl_2 have the same effect on the freezing point depression, while NaCl has a weaker effect. This could have an effect on the ice phase formation before the clathrate is formed.

Dholabhai et al. (1996) performed experiments on CO_2 gas hydrates in solutions that contained the electrolytes KCl , NaCl , or CaCl_2 and methanol. From this work they concluded that, in the presence of methanol, the electrolyte NaCl acts as a stronger

²Properties of solutions that depend on the ratio of the number of solute particles to the number of solvent molecules in solution, and not to the type of chemical species present.

inhibitor than CaCl_2 . Also Sun et al. (2001) studied the equilibrium data for organic molecules in aqueous solutions of ethylene glycol and NaCl or CaCl_2 ; they found that CaCl_2 was a stronger inhibitor than the ethylene glycol but a weaker one than NaCl on a mass basis.

2.3 Hydrated Sulphates in the Solar System

2.3.1 Hydrated Sulphates on Mars

Hydrated magnesium sulphates such as kieserite ($\text{MgSO}_4 \cdot \text{H}_2\text{O}$), hexahydrate ($\text{MgSO}_4 \cdot 6\text{H}_2\text{O}$), epsomite ($\text{MgSO}_4 \cdot 7\text{H}_2\text{O}$) and meridianiite ($\text{MgSO}_4 \cdot 11\text{H}_2\text{O}$), may be significant sources of water on the surface of planetary bodies (Dalton et al. 2005) (see Fig. 2.8, which shows the phase diagram of the system $\text{MgSO}_4\text{-H}_2\text{O}$). On Mars, meridianiite is thought to be the most abundant hydrated sulphate and is therefore important in studies of the Martian water cycle. However, the other hydrated phases mentioned above may also be present and therefore must also be discussed. These minerals are suggested to have formed from brine solutions beneath the surface of Mars, or formed elsewhere and carried by the wind (Peterson & Wang 2006).

A variety of instruments both on the Martian surface and in orbit provide the evidence for these hydrated sulphates. Thermal emission spectra of outcrops show the presence of 15–35 vol% of mineral sulphates (Christensen et al. 2004). Mossbauer spectra show evidence for the mineral jarosite ($\text{KFe}_3^{+3}(\text{OH})_6(\text{SO}_4)_2$) being present (Klingelhöfer et al. 2004). Additionally, kieserite and gypsum ($\text{CaSO}_4 \cdot 2\text{H}_2\text{O}$) (Langevin et al. 2005) have also been identified by the Visible and Infrared Atmospheric Spectrometer (OMEGA)/Mars Express instrument on the Terra Meridiani landing site, and on other areas on the Martian surface. The equatorial regions of Mars also contain an abundance of water-equivalent hydrogen; this abundance has been proposed to be a consequence of the presence of epsomite and hexahydrate (Feldman et al. 2004).

A majority of data related to Martian studies originate from remotely sensed

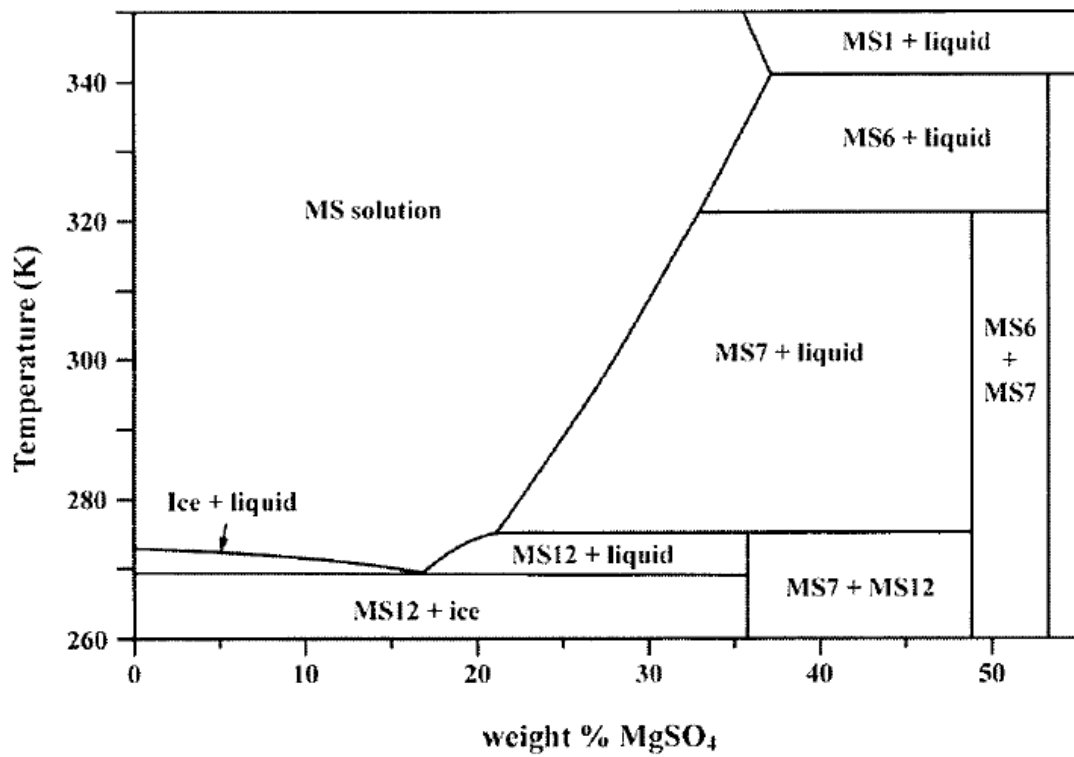


Figure 2.8: Equilibrium binary phase diagram of the system MgSO₄-H₂O; MS7=epsomite, MS12=dodcahydrate, MS6=hexahydrate, and MS1=kieserite (Fortes et al. 2006).

spectroscopic data from satellites, spectroscopic data from landers or rovers, and meteorites thought to have originated from Mars itself (Chou & Seal 2007). The data from these studies give little information related to the mineralogy and mineral chemistry of Mars' surface; this instead is inferred in the context of known phase relations, which are based on the bulk geochemical data from the regolith on the surface of the planet. This information can also be gained from the temperature and relative humidity (RH) changes of the surface of the planet due to seasonal changes.

Large amounts of hydrogen have been found in areas on the Martian equator. It is not clear where this hydrogen originates, however there are several possibilities: 1) buried water ice (Clifford 1998), 2) water molecules adsorbed on the surface of soil grains (Tokano 2003), 3) structural OH and interlayer H₂O in clays, 4) water from cations in zeolites and 5) structural OH and H₂O in hydrated salts (Clark 1998; Vaniman et al. 2004).

The Mars Express Rover and the Compact Reconnaissance Imaging Spectrometer for Mars (CRISM) on the Mars Reconnaissance orbiter discovered hydrated magnesium sulphates and phyllosilicates (sheet silicates) (Bibring et al. 2007; Murchie et al. 2009). The results from other exploration rovers give better analyses of the ground composition as these rovers studied sub-surface materials. For example the outcrops on walls of impact craters (Clark et al. 2005) and the sub-surface regolith in trenches (Haskin et al. 2005) were investigated by the rovers and hydrated Fe³⁺, magnesium-, and calcium-sulphates were found.

Looking at the water content of the phyllosilicates we see that the maximum abundance of OH and H₂O is between 5–21 wt%, which implies that their water content on Mars would have to be unrealistically high (>50 wt%) to accommodate the amount of water detected (Wang et al. 2013). In contrast the maximum abundance of OH and H₂O in hydrated sulphates is much higher, in the range of 21–62 wt%, which means a lower abundance of these hydrated sulphates in near surface rocks (<1m) is needed to be present in order to accommodate the observed water on Mars (Wang et al. 2013).

Magnesium sulphates are thought to form from weathering and evaporation processes (King et al. 2004). According to Feldman et al. (2004) hexahydrate is metastable

at temperatures below 284 K, therefore any stable reaction below 284 K would have to occur between kieserite and epsomite (see Fig. 2.8). However, work by Vaniman et al. (2004) shows the possibility of hexahydrite being the dominant hydrated magnesium sulphate phase at conditions relevant to Mars, despite it being metastable. Vaniman et al. (2004) also suggests that it is possible for hexahydrite to form and linger as epsomite decomposes to kieserite. Epsomite, compared to hexahydrite, is stable in the Medusae Fossae and is unstable in a small region in the Arabia Terra (Feldman et al. 2004). Indeed, magnesium sulphates are thought to be also present at the Gusev crater (Peterson & Wang 2006). Feldman et al. (2004) also note that any hydrated phase of magnesium sulphate is more stable than anhydrous magnesium sulphate under Martian conditions.

Feldman et al. (2004) show that epsomite and hexahydrite could be major contributing factors to our understanding of the physical structure and composition of the soil on the surface of Mars if magnesium sulphate is present in large enough quantities. Also, where epsomite and hexahydrite are not stable, then kieserite would be, and could contribute instead to the water-equivalent hydrogen (WEH) reservoir. As noted by Feldman et al. (2004) the latter could be consistent with that fact that a contribution of 10% anhydrous magnesium sulphate as kieserite to WEH (1.5%), added to the contribution of adsorbed water (0.5%) on the grains in regolith, could account for the minimum abundance of WEH present at equatorial latitudes. Feldman et al. (2004) also note, however, that this water could also be accounted for with or without kieserite from amorphous hydrated sulphates, jarsite, gypsum and other hydrated phases. In addition to this, it is possible that the amount of magnesium sulphate present varies with location near the equator, and most of that present is amorphous with an inadequately defined hydration state between epsomite and kieserite (Feldman et al. 2004). In comparison, epsomite appears to be relatively stable where WEH is abundant close to the Martian equator.

Magnesium sulphate salts are able to act as a source or a sink of water during diurnal cycles. This is due to their ability to be stable and metastable in various hydration and dehydration reactions, and these reactions are rapid under ambient terrestrial

surface conditions at least (Chipera et al. 2005). Consequently there have been many studies over recent decades on the significant role that magnesium sulphates play in the water cycle on Mars, with each study confirming their critical role (Clark 1993; Gendrin et al. 2005; Wang et al. 2006). In addition, if we take hydrated calcium sulphate phases, the extremes in hydration states are gypsum ($\text{CaSO}_4 \cdot 2\text{H}_2\text{O}$) and anhydrite (CaSO_4), which have a relatively small difference of 0.27 kg of H_2O per kg of CaSO_4 compared to the difference in water content of the extremes of the hydrated magnesium sulphates.

2.3.2 Epsomite ($\text{MgSO}_4 \cdot 7\text{H}_2\text{O}$, MS7)

Epsomite is one of the most common naturally occurring terrestrial hydrated sulphates, and it is also believed to be one of the only minerals to occur on Earth as a thermodynamically stable mineral (Vaniman et al. 2004). It is stable when in contact with a saturated solution in the temperature range 275–320 K; it has also been observed to be abundant in the Martian regolith. The structure of epsomite was resolved using neutron and X-ray diffraction (XRD); it consists of a sulphate ion tetrahedron and a $\text{Mg}(\text{H}_2\text{O})_6$ ion octahedron, which are linked together with hydrogen bonds. The seventh water molecule is not linked via hydrogen bonds to the magnesium but resides in a “void” in the structure. The structure of this compound is shown in Fig. 2.9.

There has been an interest in the structure and behaviour of hydrated sulphates at varying temperatures over recent years due to their significance and presence on Mars. Wang et al. (2013) show the structure of the stretching and vibrational modes of water in epsomite. They varied the temperature and pressure of the sample and then conducted Raman spectroscopy; their results are shown in Fig. 2.10.

These results clearly illustrate the effects of the temperature and pressure changes on the hydration band in epsomite; this particular point was not taken note of by Wang et al. (2013), however in a separate earlier experiment by Wang et al. (2011) this effect received significant scrutiny. Wang et al. (2011) conducted 30 systematic experiments at -10 C using RH levels between 13–98% and up to 33,288 hours of reaction time with hydrous magnesium sulphates, namely epsomite ($\text{MgSO}_4 \cdot 7\text{H}_2\text{O}$), starkeyite

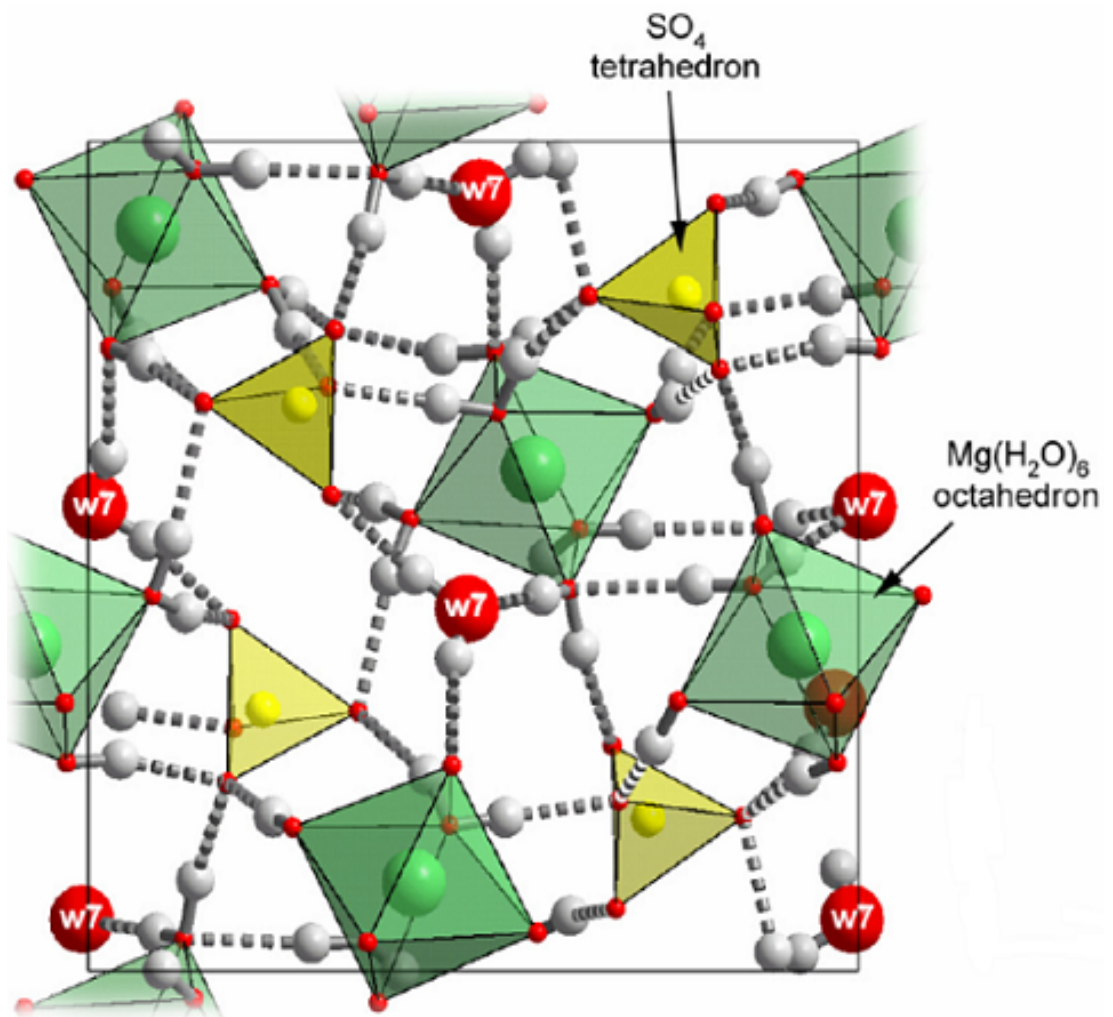


Figure 2.9: The structure of epsomite (Fortes et al. 2006).

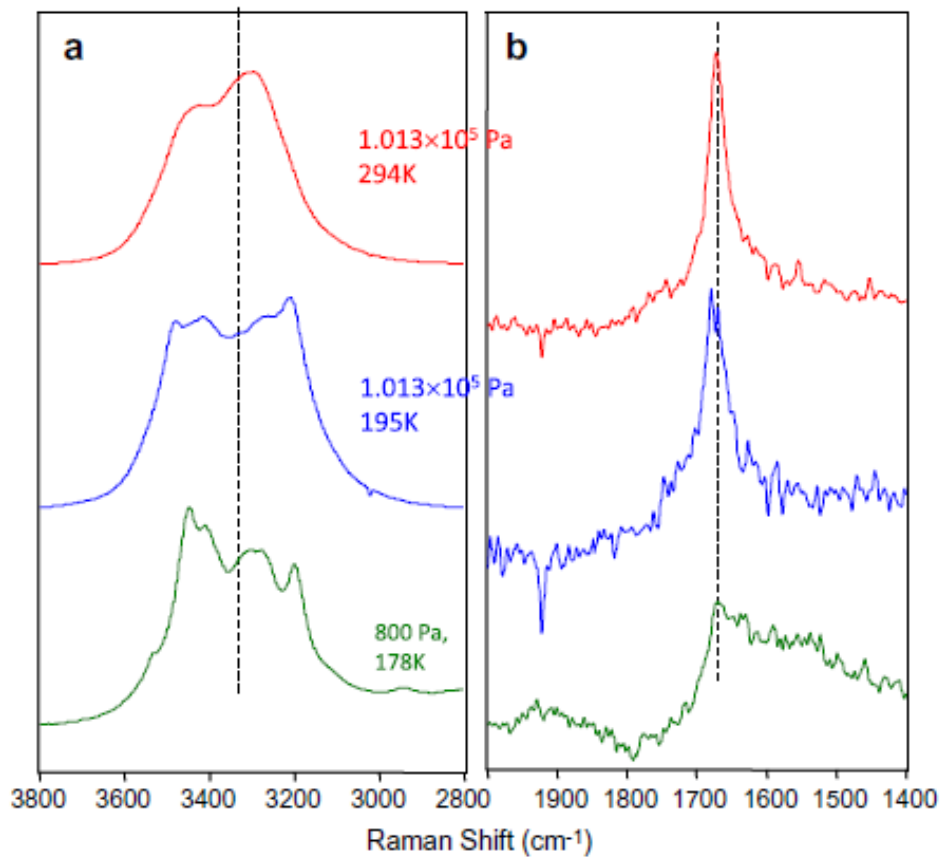


Figure 2.10: Raman spectra obtained from epsomite; (a) shows the stretching vibrational mode while (b) shows the bending vibrational mode of structural water in epsomite taken at temperatures and pressures relevant to Earth and Mars. The vertical dashed lines show the central positions of the peaks (Wang et al. 2013).

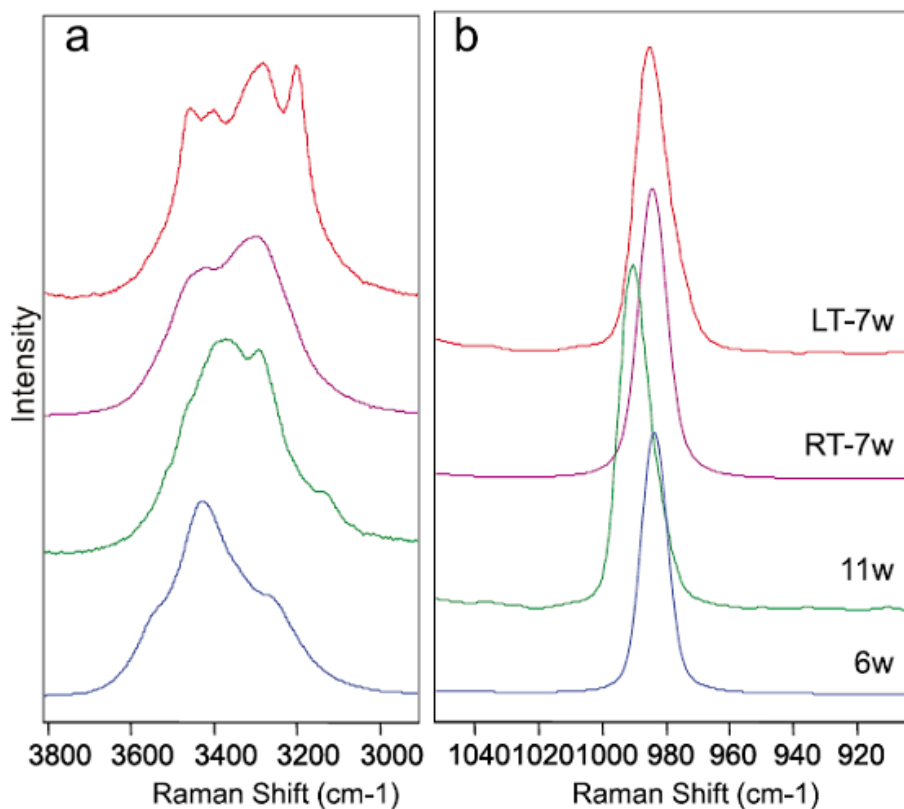


Figure 2.11: Raman spectra obtained from epsomite; (a) shows the H₂O vibrational mode and (b) shows the symmetric-stretching vibrational mode of [SO₄]²⁻ for low temperature epsomite (denoted LT-7w), room temperature epsomite (denoted RT-7w), meridianiite (denoted 11w) and hexahydrate (denoted 6w) (Wang et al. 2011).

(MgSO₄·4H₂O), monohydrate (MgSO₄·H₂O), amorphous (MgSO₄·2H₂O) and meridianiite (MgSO₄·11H₂O) (see Wang et al. (2011) for details of sample and experimental conditions). The results they obtained for epsomite are shown in Fig. 2.11.

Wang et al. (2011) included hexahydrate and meridianiite in the spectra to eliminate the possibility that epsomite could have dehydrated to hexahydrate (where 6w denotes the presence of 6 waters of hydration) or rehydrated to meridianiite (where 11w denoted the presence of 11 waters of hydration). Wang et al. (2011) conclude from

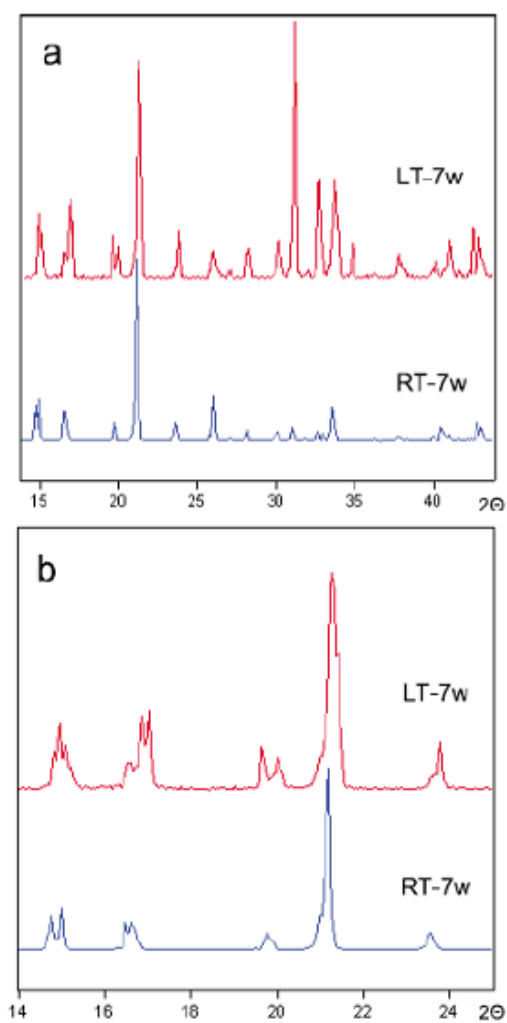


Figure 2.12: XRD pattern obtained from epsomite; (a) shows epsomite at the 2θ range of 14°-45° and (b) shows epsomite at the 2θ range 14°-25°, the temperature of the LT-7w corresponds to dry ice (-78.5°C) (Wang et al. 2011).

Figs. 2.10 and 2.11 that epsomite has a low-temperature phase due to what they think is the appearance of additional peaks on Raman spectra when the mineral is cooled to lower temperatures, and the splitting of the peaks on the XRD data (shown in Fig. 2.12) at lower temperatures. Conversely, Dalton et al. (2005) took measurements of various hydrated salts' reflectance spectra. The reflectance spectra they obtained for some of their samples at room temperature are shown in Fig. 2.13. Dalton et al. (2005) come to a different conclusion to that of Wang et al. (2011). Hydrated salts show spectral behaviour due to the vibrational modes of the waters of hydration. The fundamental vibrational modes of water come from the symmetric and asymmetric O-H stretching and the symmetric H-O-H bending mode. Hydrogen bonding creates strong intermolecular coupling between the vibrational modes and so many of the spectral features are not caused by single oscillations. Different overtones and combinations of the mentioned modes overlap and produce broad absorption features. However, when cryogenic temperatures are reached the crystal structure changes due to thermal effects and this, along with lower available energy, causes the spectral features to become more distinct. From this Dalton et al. (2005) conclude that the sharpness of the peaks at lower temperatures is due to reduced intermolecular coupling between the water molecules, which causes them to become more isolated from each other; this in turn causes the individual minor absorption peaks to overlap less and become more distinct.

2.3.3 Meridianiite ($\text{MgSO}_4 \cdot 11\text{H}_2\text{O}$, MS11)

Meridianiite, rather than epsomite, is the hydrated magnesium sulphate that is generally expected to be in equilibrium with either ice or brine below the surface of Mars (Peterson & Wang 2006). Currently the equatorial regions of Mars have low humidity conditions, implying that any meridianiite present would dehydrate into kieserite and be spread across the Martian surface by wind.

MS11 was first discovered in central British Columbia on the surface of ponds that had frozen. The ponds had been formed between 1920 and 1972, when magnesium

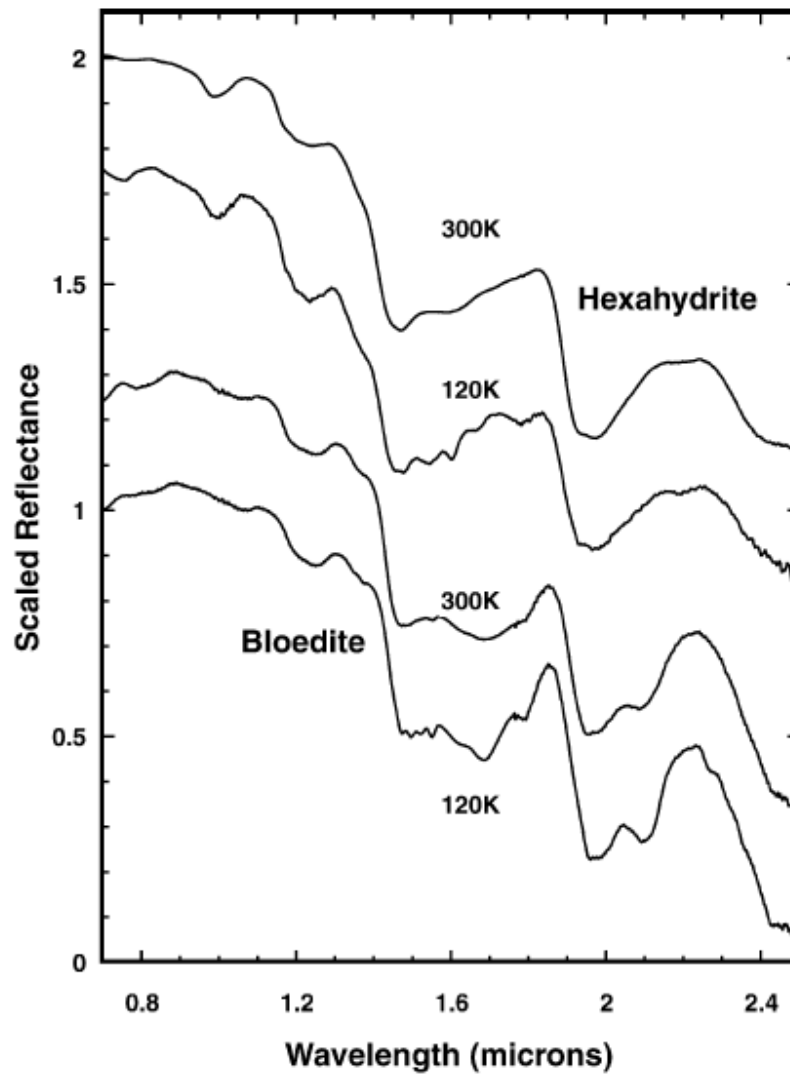


Figure 2.13: Infrared spectra of hexahydrate, $\text{MgSO}_4 \cdot 6\text{H}_2\text{O}$, and bloedite ($\text{Na}_2\text{Mg}(\text{SO}_4)_2 \cdot \text{H}_2\text{O}$) at room temperature and pressure and at 120 K (Dalton et al. 2005).

sulphate was mined from evaporite deposits (Peterson et al. 2007). MS11 was formed as it crystallised out when a solution that contained magnesium sulphate evaporated below 2°C. The name meridianiite was chosen for this mineral to reflect the site (Meridiani Planum, a Martian plain located 2 degrees south of the equator) on Mars in which the Mars Exploration Rover (MER) Opportunity discovered crystal moulds in sedimentary rock that are thought to be the result of minerals (most likely MS11) that have since dehydrated or dissolved (Peterson et al. 2007). Others have suggested that sulphates may form in a different manner in the Meridiani region, implying that sulphur dioxide could react with water-bearing vapours in volcanic ash accumulations (Culka et al. 2014).

Meridianiite was first reported as a new type of low temperature hydrated Mg sulphate phase by Peterson & Wang (2006) (the structure of meridianiite at 250 K is shown in Fig. 2.14); they carried out a structural refinement using single crystal XRD from which they deduced that the crystal moulds in outcrops at the Meridiani site could suggest the melting of eleven waters of hydration. Meridianiite is thought to be the main water source on Mars, and plays a crucial role in the water cycle on the planet, particularly in the low latitude regions where ice is less common or absent from the regolith through dehydration and hydration reactions (Grindrod et al. 2008). Chou & Seal (2007) gives the amount of water present in 1 kg of each hydrated magnesium-sulphate phase, which are summarised in the Table. 2.1. Magnesium sulphate salts are thought to occur from the combined weathering and evaporation on the planet (Chou & Seal 2007). Studies on the stability of the $\text{MgSO}_4\text{-H}_2\text{O}$ system predict that it could undergo cycling between its various phases during the Martian day, however due to slow hydration reactions it is difficult to accurately predict the phase transitions occurring in the day.

Peterson & Wang (2006) performed an experiment in which meridianiite was formed from a solution of 30 wt% $\text{MgSO}_4\cdot 7\text{H}_2\text{O}$ (epsomite) and 70 wt% H_2O . This solution was placed in a Petri dish and left for a few days in temperatures in the range -0.3°C to -2.3°C . They found that $\text{MgSO}_4\cdot 7\text{H}_2\text{O}$ formed after 24 hours and meridianiite followed after 48 hours; also they state that at a temperature above 2°C

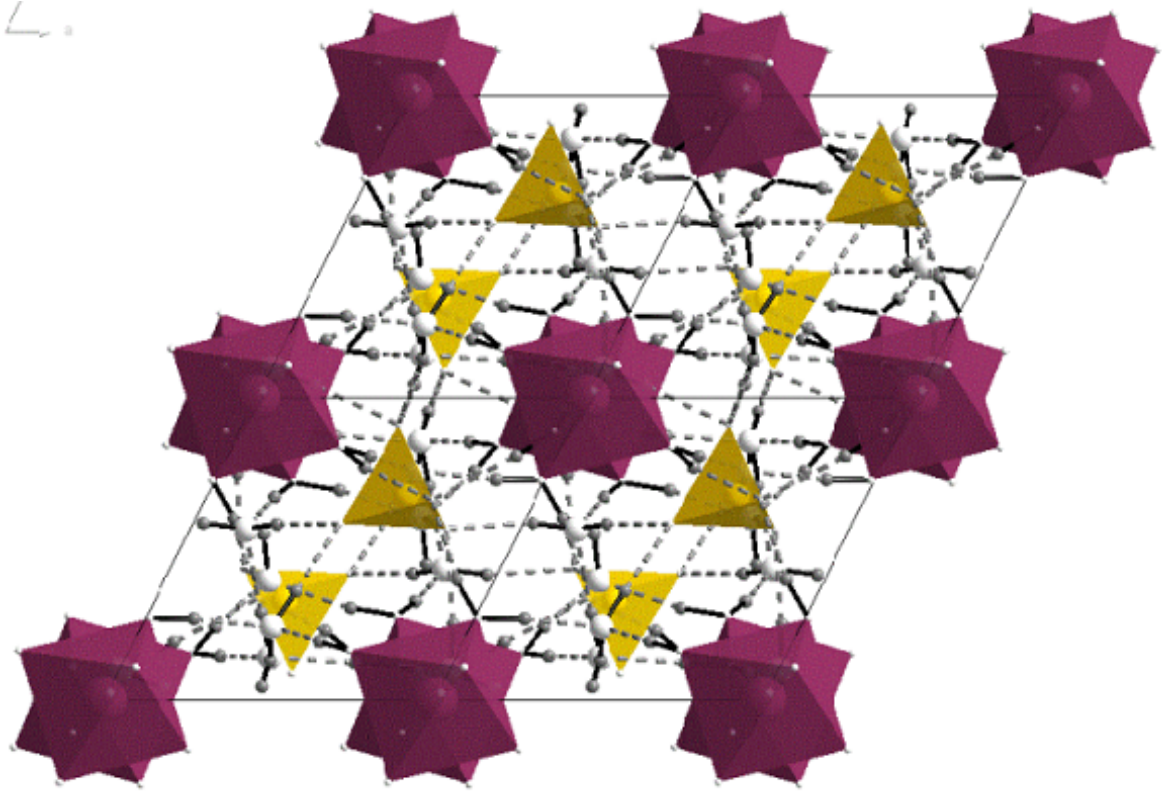


Figure 2.14: The structure of Meridianiite at 250 K. Mg is maroon, sulphate is yellow, oxygen is white and hydrogen is grey (<https://crystallography365.wordpress.com/2014/07/30/an-earth-and-mars-mineral-meridianiite-mgso4-11h2o/>).

Table 2.1: Mass of water per kg of hydrated sulphate (Chou & Seal 2007).

Hydrated magnesium sulphate	Water present g/kg
Kieserite	0.15
Starkeyite	0.60
Hexahydrate	0.90
Epsomite	1.05
Meridianiite	1.80

the meridianiite melts back to epsomite, also producing significant amounts of water.

The goal of the Freeman et al. (2007) experiment was also to produce meridianiite. They prepared their samples using epsomite and water in the mass ratio of 7:3; this ratio produced approximately 12.9 waters of hydration which can be accounted for by evaporation that could occur during preparation. The epsomite was first ground so that the particle sizes were less than $150\mu\text{m}$; this was to ensure the particles dissolved in the water. The solution was placed in petri dishes with one dish being placed in a freezer with a temperature of -5°C and the other dish was placed in freezer with a temperature of -15°C . After a few days meridianiite formed in both dishes below. Figs. 2.15 and 2.16 show the XRD pattern and Raman spectra that they obtained.

The XRD pattern in Fig. 2.15c is of epsomite. The diffraction pattern of the initial phase (Fig. 2.15a) is different to that of epsomite. It has the strongest peaks at 2θ values of 15.8° , 18.1° , 18.3° , 26.2° , 29.9° , 30.1° , 31.0° , and 31.2° . These positions are in agreement with the peak positions of the XRD pattern obtained by Peterson & Wang (2006), based on their refinement for $\text{MgSO}_4 \cdot 11\text{D}_2\text{O}$.

Fig. 2.16 compares the hydration band of meridianiite (11w) with that of epsomite (7w) and starkeyite (4w). Spectra from epsomite and starkeyite are shown with two crystal orientations. Freeman et al. (2007) states this comparison confirms the specificity of the spectral peaks of meridianiite, not being an orientation effect. The sub-peak feature indicate that all eleven water molecules have distinct crystallographic sites in meridianiite.

Taking into consideration phase equilibria, meridianiite would be, in the absence of ice, the most likely source of water on the Martian surface.

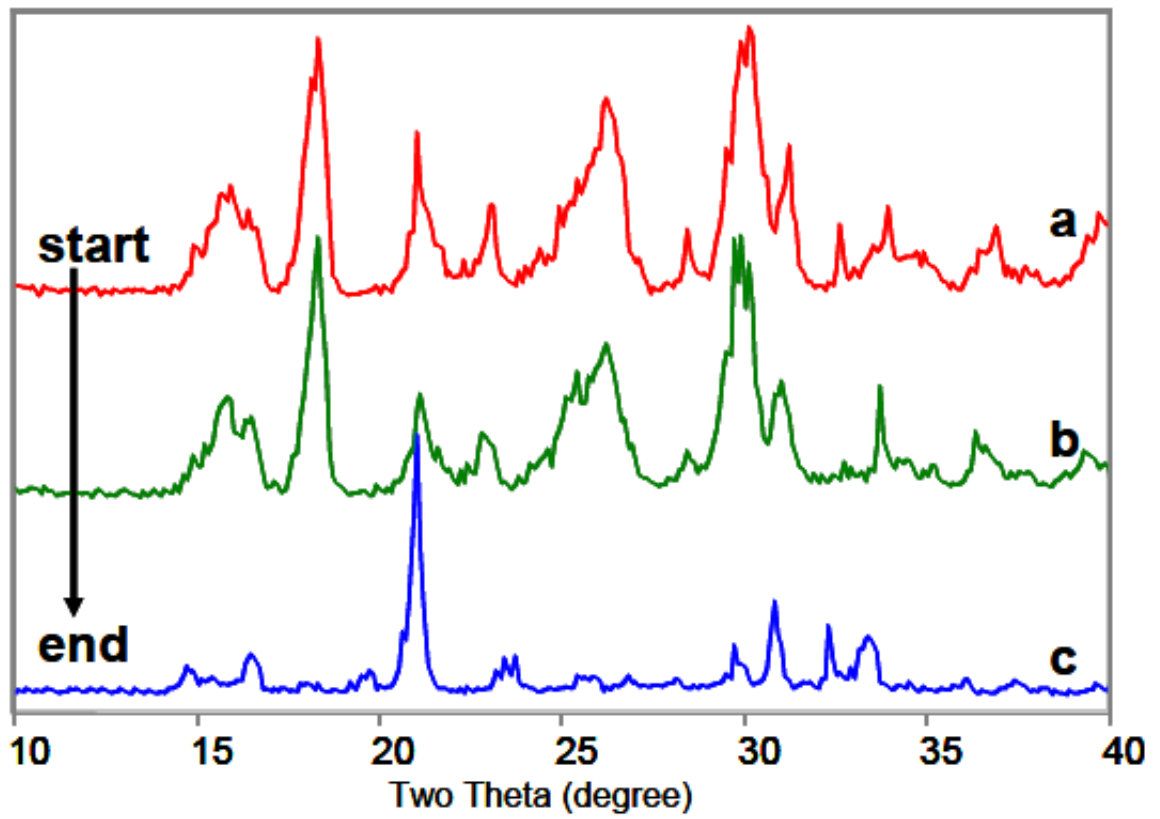


Figure 2.15: XRD pattern obtained from meridianiite after a series of repeated scans, (Freeman et al. 2007).

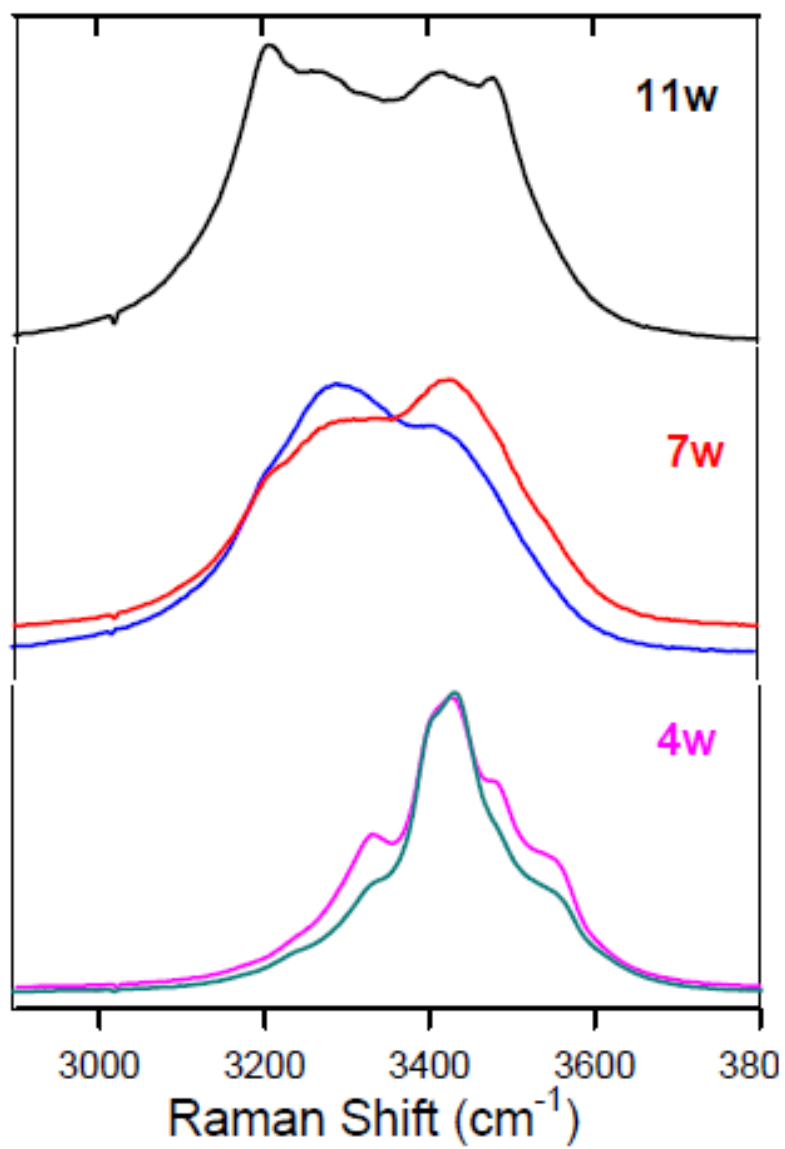


Figure 2.16: Raman spectra obtained from meridianiite, where w denotes waters of hydration (Freeman et al. 2007).

3 The theory of X-ray diffraction

3.1 Introduction

All work presented in this thesis is based on data collected from experiments at the Diamond Light Source (DLS), a third generation synchrotron facility situated in Oxfordshire, UK. This chapter discusses the theory behind the methods used at DLS, including X-ray diffraction and more specifically, powder diffraction. A complementary method also used during data collection, Raman spectroscopy, is also discussed. Additionally, this chapter explains the analysing tools utilised and the theory behind these tools.

3.2 Synchrotron radiation

Synchrotron radiation was first observed by Elder et al. (1947). High energy electrons subjected to accelerations should emit electromagnetic radiation (Elder et al. 1947). In a classical sense, all charged particles moving in a curved path or accelerated in a straight-line path will emit electromagnetic radiation. Synchrotrons use the magnetic fields of bending magnets to curve path of charged particles. In the storage ring of DLS, the electrons have energies of 3 GeV and are guided around the ring via these bending magnets, which connect a number of straight segments in the synchrotron.

DLS is a third generation synchrotron facility. Third generation facilities began operating in the 1990s, and now there are more than 50 in operation worldwide (Bildersback et al. 2005). Until 1975, synchrotron radiation was used almost exclusively for elementary particle physics experiments (Kunz 2001). During this time, the experiments in various research fields demonstrated the advantages of this type of radiation source and it was realised that it could do even better if the machines built as X-ray

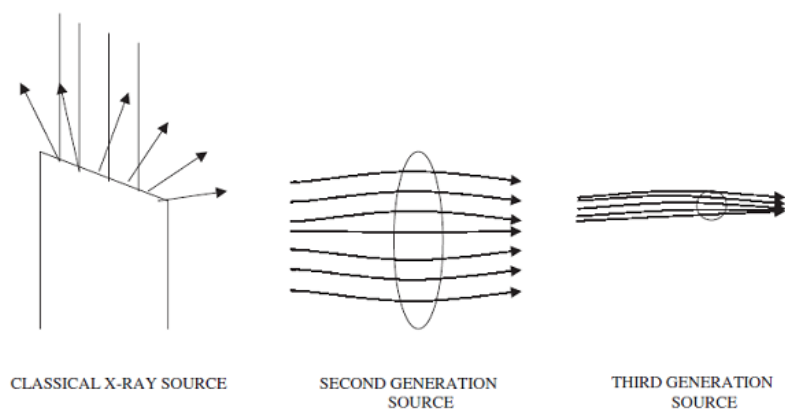


Figure 3.1: Increase of brilliance as a result of better collimation and smaller source size going from a classical X-ray source to second and third generation synchrotron sources (Kunz 2001).

sources. This led to the idea of third generation sources¹. Over the past century the brilliance of these sources has increased - this is shown in Fig. 3.1.

These synchrotrons use insertion devices as opposed to bending magnets to guide charged particles around the storage ring. Insertion devices enable the path of electrons to oscillate by producing alternating magnetic fields, this in turn produces synchrotron radiation. The properties of synchrotron radiation depend on the period and amplitude of the oscillations, hence allowing the radiation to be tailored to different individual experiments.

There are many advantages of using synchrotron radiation as opposed to a standard source:

1. has a brilliance that is more than a billion times higher than a laboratory source. This enables a more detailed image of the material under study to be obtained;

¹Second generation sources were machines built for particle physics, handed over to the synchrotron radiation community.

2. higher energy beams to penetrate deeper into matter;
3. smaller wavelengths, therefore we can study smaller features (e.g. molecular bonds and nanoscale objects);
4. depending on the insertion device, the radiation can either be linear or circularly polarised;
5. cover a larger wavelength range from infrared (10^4 \AA) to hard X-rays (10^{-1} \AA);
6. they have higher brightness allowing faster data collection due to higher photon flux on the sample and detector.

3.3 X-ray diffraction

X-rays were first discovered in 1895 by Wilhelm Rontgen while working on cathode rays in various types of evacuated glass tubes at the University of Wurzburg, Germany (Stanton 1896). They are photons with energies of a few keV and have wavelengths comparable to atomic spacings ($\sim 1 \text{ \AA}$).

Diffraction occurs when incident radiation strikes a crystal structure and is constructively and destructively scattered by atomic electrons. If the wavelength of the radiation is similar to that of the atomic spacing in the crystal, then a set of well-defined beams arranged in characteristic geometry occurs. This is known as a diffraction pattern. Individual materials have their own unique diffraction patterns which can be likened to the human finger print - no two materials have the same pattern, therefore this is an excellent technique to use when identifying new or unknown materials. The positions and intensities of the diffracted beams depend on the arrangement of atoms in space and, particularly in the case of X-rays, the atomic number of the atoms. Therefore, the positions and intensities of the diffracted beams can give us information on the arrangement of atoms in the crystal and their chemical nature.

X-rays are used when investigating crystal structures of materials as they provide a non-destructive method to study the material. The depth which can be studied depends on the energy of the incident X-rays and the electron density of the sample material. Other than X-rays, only neutron and electron scattering can provide information on the crystal structure of a material.

3.3.1 Laue theory

The idea that crystals could be used as a diffraction grating for X-rays was proposed in 1912 by Paul Peter Ewald and Max von Laue. Ewald had proposed a resonator model of crystals, however this model could not be confirmed using visible light, since the wavelength is much larger than the spacing between the resonators. von Laue suggested using electromagnetic radiation which had the shorter wavelengths needed to observe such small spacings. He suggested X-rays may have a wavelength comparable to the unit-cell spacing in crystals. von Laue shone a beam of X-rays through a copper sulphate crystal and measured its diffraction on a photographic plate. The plate showed a large number of well-defined spots arranged in a pattern of intersecting circles around the spot produced by the central beam. von Laue developed a law that connected the scattering angle and the size and orientation of the unit-cell spacings in the crystal.

To explain X-ray diffraction, von Laue considered a crystal to be composed of rows of atoms of spacing a along the x -axis, of spacing b along the y -axis and of spacing c along the z -axis. First consider the condition for constructive interference for waves scattered from the x -axis; for this all that is considered is the path difference of waves scattered from adjacent rows of atoms, as shown in Fig. 3.2.

For constructive interference, the path difference (AB-CD), must be a whole number of wavelengths:

$$(\text{AB-CD})_x = a(\cos \alpha_n - \cos \alpha_0) = n_x \lambda \quad (3.1)$$

where α_n and α_0 are the angles between the diffracted and incident beams, respectively, and n_x is an integer representing the order of diffraction and a is the atom spacing along

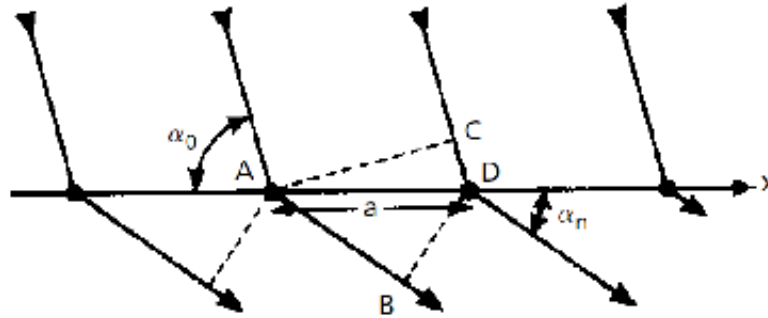


Figure 3.2: Diffraction from a lattice row along the x -axis. The incident and diffracted beams are at angles α_0 and α_n to the row respectively (Hammond 2009).

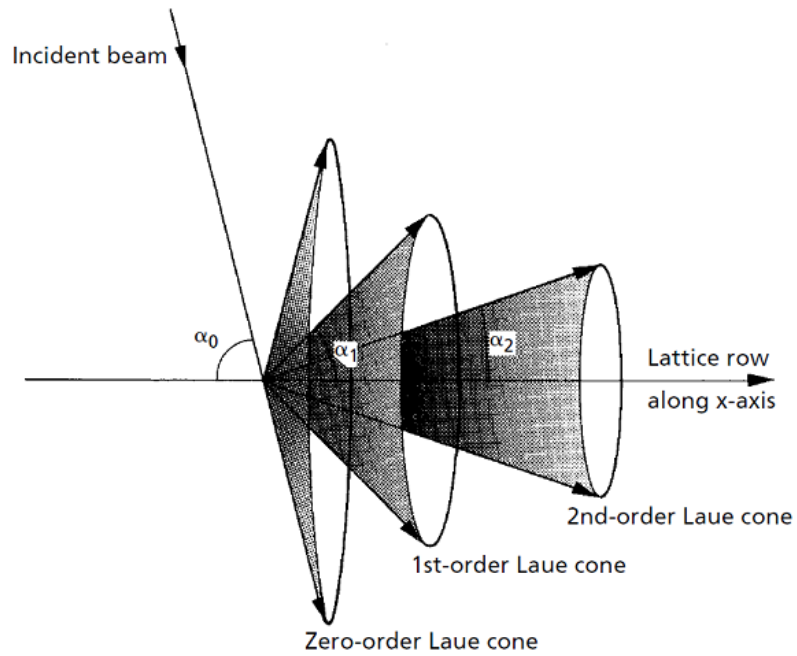


Figure 3.3: Three Laue cones representing the directions of the diffracted beams from a lattice row along the x -axis with 0λ ($n_x = 0$), 1λ ($n_x = 1$) and 2λ ($n_x = 2$) path differences (Hammond 2009).

the x -axis.

Fig. 3.2 shows the diffracted beam at angle α_n below the atom row. However, the same path difference is obtained if the diffracted beam lies in the plane at angle α_n above the atom row or out of the plane at angle α_n to the atom row. Therefore all the diffracted beams with the same path difference occur at the same angle to the atom row, i.e. the diffracted beams of the same order all lie on the surface of a cone called a Laue cone. This is shown in Fig. 3.3. Therefore, this analysis can be extended to the y -axis:

$$(\text{AB-CD})_y = b(\cos \alpha_n - \cos \alpha_0) = n_y \lambda \quad (3.2)$$

and z -axis:

$$(\text{AB-CD})_z = c(\cos \alpha_n - \cos \alpha_0) = n_z \lambda \quad (3.3)$$

For constructive interference to occur from all three atom rows, all three Laue equations must be satisfied simultaneously.

3.3.2 Bragg's theory

In 1912-1913, after von Laue's revolutionary research, William Lawrence Bragg developed Bragg's law (Bragg & Bragg 1913), which connects the observed scattering with reflections from evenly spaced planes within the crystal.

Laue's analysis is in effect an extension of the idea of a diffraction grating to three dimensions. A disadvantage of his work is that to calculate the directions of the diffracted beams, a total of six angles, three lattice spacings and three integers need to be determined. Bragg, however, developed a simpler method by which to explain the theory of diffraction. He considered crystals as being made of parallel planes from which X-rays are reflected, known as crystallographic planes and described by Miller indices, hkl . This is shown in Fig. 3.4, from which Bragg's law can be derived.

The path difference between the reflected rays in Fig. 3.4 is:

$$(\text{AB+BC}) = (d_{hkl} \sin \theta + d_{hkl} \sin \theta) = 2d_{hkl} \sin \theta \quad (3.4)$$

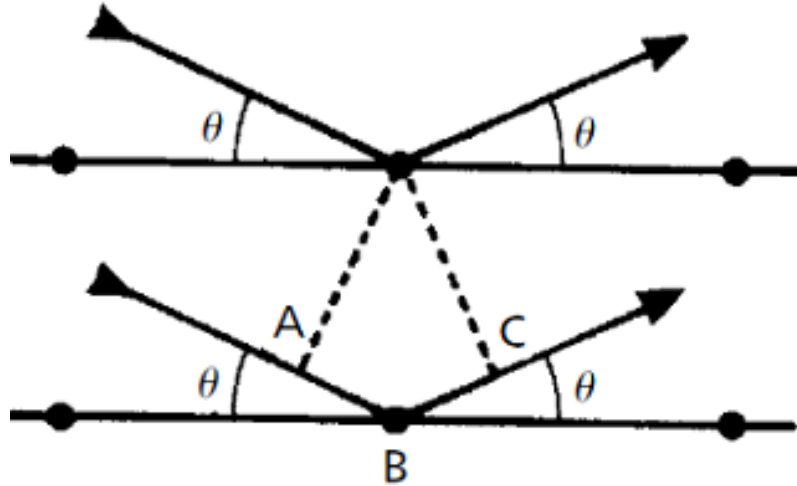


Figure 3.4: An X-ray beam is incident onto the plane and partially reflected, while the transmitted beam is then incident on the next plane and reflected in the same way (Hammond 2009).

where d_{hkl} is the interplanar spacing, and θ is the angle of reflection. If the path difference is a whole number of wavelengths then constructive interference occurs, which would increase the intensity of the X-rays and a strong feature known as a Bragg peak will occur in the diffraction pattern. This results in Bragg's law:

$$n\lambda = 2d_{hkl} \sin \theta \quad (3.5)$$

An important point to note is that Bragg's law is independent of the positions of the atoms in the planes, it only depends on the spacing between the planes. It follows that the path difference between the rays scattered by atoms in the same plane is zero i.e. they interfere constructively. This is only the case when the angle of incidence to the plane equals the angle of reflection. Also Bragg's law is only represented in two dimensions; the incident and diffracted beams all lie in a plane.

Vector notation can also be used to express Bragg's law, Fig. 3.5 shows this. \mathbf{s} and

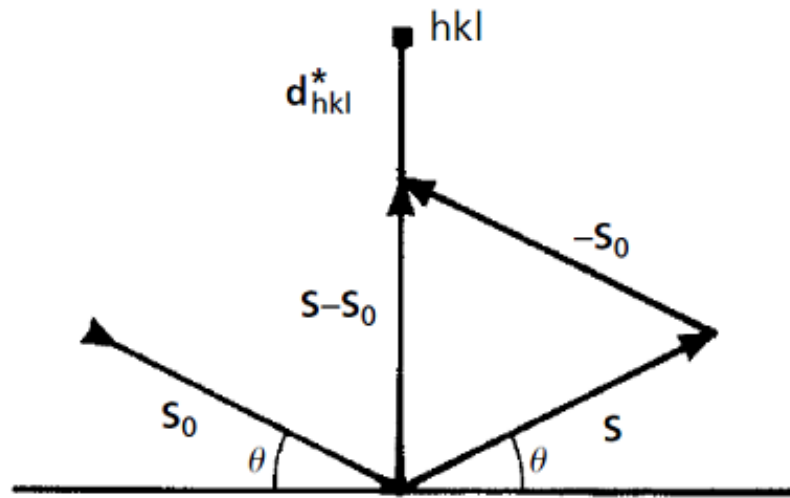


Figure 3.5: Bragg's law expressed in vector notation (Hammond 2009).

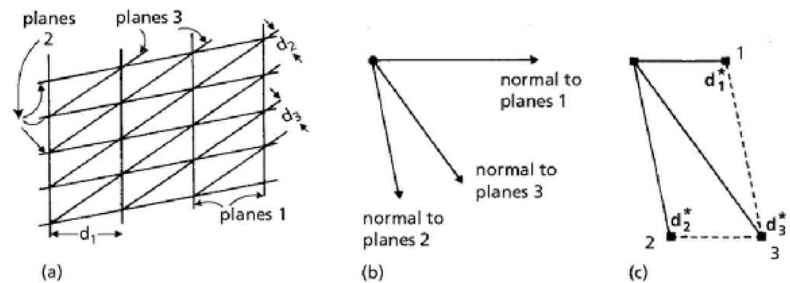


Figure 3.6: Explanation of the reciprocal lattice. (a) shows three sets of crystallographic planes in the lattice. (b) The normals of these planes originate from a common origin. (c) The reciprocal lattice vectors define the crystal planes and their d -spacing (Hammond 2009).

\mathbf{s}_0 are unit vectors in the direction of the diffracted and incident beams respectively. Therefore the vector $(\mathbf{s} - \mathbf{s}_0)$ is parallel to the reciprocal lattice vector of the reflecting planes, d_{hkl}^* . From Fig. 3.5 $(\mathbf{s} - \mathbf{s}_0) = 2\sin\theta$ and knowing that $d_{hkl}^* = 1/d_{hkl}$, we can find that their ratio is λ . Therefore:

$$\frac{(\mathbf{s} - \mathbf{s}_0)}{\lambda} = d_{hkl}^* \quad (3.6)$$

3.3.3 Scherrer equation

The Scherrer equation relates the size of crystallites in a solid to the broadening of a peak in a diffraction pattern. The Bragg equation suggests that, for an ideal crystal, a diffraction peak is a mathematically narrow line because of successive cancellation due to 100% destructive interference between X-ray waves scattered from successive layers. However, due to the following points the Bragg reflections have a width:

1. reflections from individual layers remove intensity from the remaining penetrating wave, so that complete cancellation is not quite achieved between layers;
2. in real crystals the lattice planes may not be perfectly arranged (i.e. they are disordered) and atoms also move slightly so they are not so well defined, depending on temperature or strain, further reducing the cancellation;
3. real crystallites have a finite size, so that the number of layers contributing to the cancellation is finite;
4. the incoming radiation is not 100% monochromatic, so there is a spread in the available Bragg angle and therefore exciting diffraction from particles that are close to, but not actually in, the nominal Bragg condition;
5. the angular divergence of the incident beam means that different photons are also hitting the sample at different Bragg angles and again exciting diffraction from particles that are close to, but not actually in, the nominal Bragg condition;

6. the resolution of the measuring device also has an intrinsic width.

Beamline I11 at DLS (see Chapter 4 for details) has a very high energy resolution monochromator (i.e. very low dispersion in wavelength). It also has an undulator source which gives a very low divergent (i.e. highly parallel) beam and Multi-Analysing crystals (MACs) which have analyser crystals meaning high resolution and collimation can be achieved. These, combined together, produce diffraction peaks whose width comes entirely from the sample (note does not apply to the position sensitive detector (PSD) or long duration experiment (LDE) data due to absence of collimation).

From points 1–4 above, the main contribution to peak broadening from well-ordered crystals is 4. Therefore, when peaks begin to broaden out, it is due to one of the following:

1. strain broadening given by the Wilson formula:

$$B = 4E \tan(\theta) \quad (3.7)$$

where E is the microstrain (dimensionless) and usually assumed to be proportional to the square root of the dislocation density. Unless a sample is massively strained by a sudden shock, usually a subtle and progressive effect;

2. particle size broadening given by the Scherrer equation:

$$B = \frac{K\lambda}{T \cos(\theta)} \quad (3.8)$$

where T is the crystallite size and K a dimensionless shape factor;

3. the material becoming more and more disordered. Eventually the difference between a material that is comprised of nano-particles, or one that is comprised of large amorphous particles cannot be determined from the diffraction pattern alone.

The latter point 3 comes down to understanding what the Scherrer equation actually is. The Scherrer equation was originally derived for cubic systems and is a

measure of the length over which successive lattice planes are parallel. The limit of this length is due to the physical finite particle size, or because after this distance, either disorder begins to set in, or the planes deviate away from parallel stacking. In amorphous materials, therefore, this correlation length is very short, i.e. nano-scale. Thus the Scherrer equation describes the length over which the Bragg planes are ordered and can be considered a crystallite size. However, this crystallite size could either be a physical particle size, or a structural domain within a larger grain.

3.4 X-ray powder diffraction

From the description of Bragg's law, it is clear that a single crystal sample subjected to a synchrotron X-ray beam would produce only a single family of peaks in the resulting diffraction pattern. Hence, using a single crystal sample would produce only one Bragg feature in the diffraction pattern, this is shown in Fig. 3.7. Diffraction peaks are observed when the plane is correctly aligned allowing the perpendicular to the plane to bisect the incident and diffracted rays, shown in Fig. 3.7(a) and Fig. 3.7(c). Because the sample is only a single crystal, some planes are not correctly aligned to produce a diffraction peak and the perpendicular plane does not bisect the incident and diffracted rays, in this case only background is observed as shown in Fig. 3.7(b). To ensure a full pattern from single crystal diffraction the sample must be spun through all orientations so that all sets of planes obey Bragg's law. However, single crystal diffraction is an effective tool when determining the space group and structure of materials.

Conversely, as there are thousands of crystallites in a powder sample, all possible diffraction peaks should be observed, as shown in Fig. 3.8. Within the powder only a small fraction of crystallites will have a particular set of planes in the correct orientation to produce diffraction peaks. However powder diffraction assumes that for every set of planes there are an equal number of crystallites which are able to diffract and that there is a large sample of crystallites. A small sample quantity could cause problems as it limits the number of crystallites that can contribute to the end pattern. Therefore

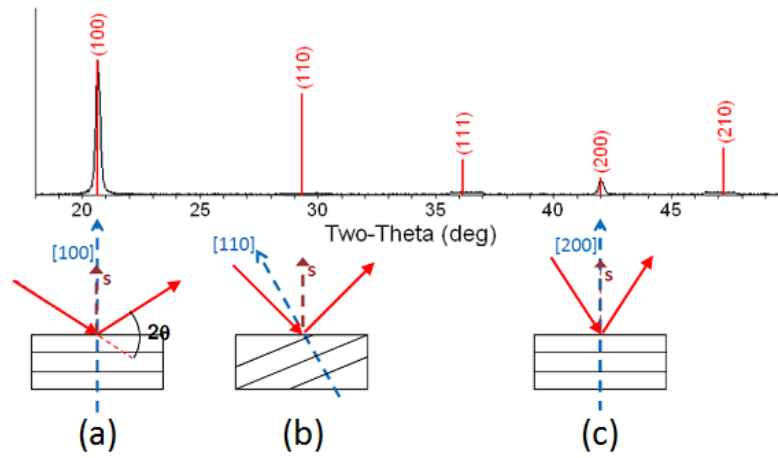


Figure 3.7: Diffraction pattern of a single crystal (from <http://prism.mit.edu/xray>).

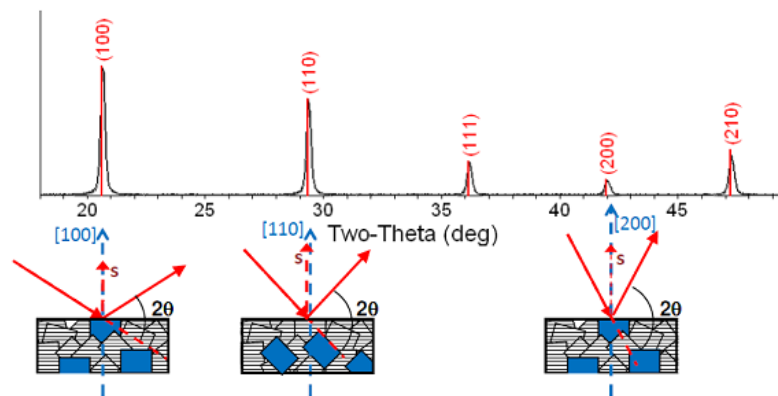


Figure 3.8: Diffraction pattern of a polycrystallite, <http://prism.mit.edu/xray>.

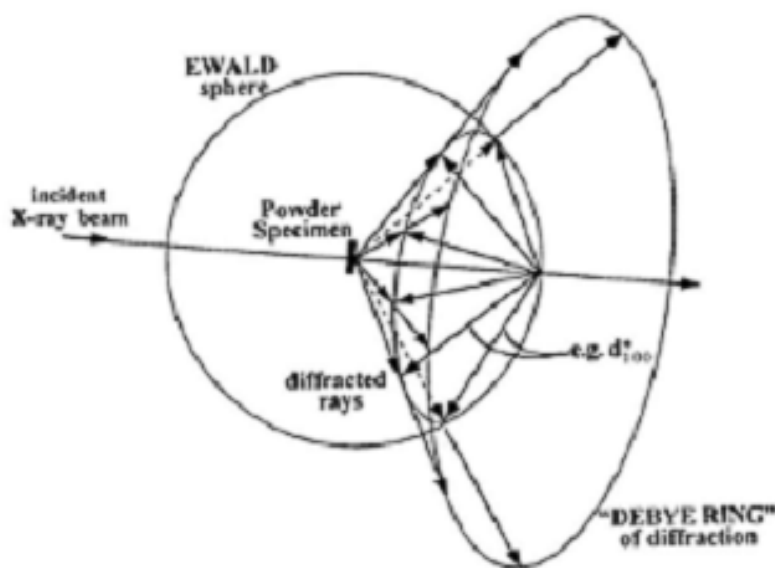


Figure 3.9: The formation of Debye–Scherrer cones (from <http://prism.mit.edu/xray>).

having a larger sample will help to ensure that a relevant number of grains contribute to the final diffraction pattern. Additionally, spinning the sample will also cause a larger fraction of crystallites to contribute.

When a powder sample is subjected to X-rays, the X-rays are scattered around the sample in a sphere and a cone shape is produced from the sample to the detector called a Debye–Scherrer cone, as shown in Fig. 3.9. Each cone is due to the scattering of X-rays from a single crystallite, therefore a powder sample will produce many Debye–Scherrer cones. A powder sample will create a series of concentric Debye–Scherrer cones due to individual lattice vectors having different length and magnitude values relating to the d -spacing of each set of planes, hence causing the radius of each reciprocal lattice sphere to be different.

Two types of area detector can be placed in line with the incident beam to record these Debye–Scherrer cones: a 1D or 2D detector. With a 2D detector the cones appear as concentric rings (Debye–Scherrer rings) which have a radius proportional to the 2θ

angle. Alternatively, and more commonly, 1D detectors are used. These detectors can only record diffraction patterns on one plane, thus they effectively show a thin slice of the pattern.

When using powder diffraction it is very easy to detect preferred orientation. This phenomenon occurs when the sample is not randomly orientated, and can be detected as the Debye–Scherrer rings would have varying intensity along the rings and the intensity would not be uniformly distributed. This can be accounted for by rotating the sample during data collection to allow for random orientation of the planes.

3.4.1 Analysing X-ray powder diffraction data

3.4.1.1 Qualitative analysis

Powder diffraction is fundamental when attempting to determine the structure of crystalline materials. All materials can be identified from their diffraction as these are unique to individual materials. In the case where two materials are present within the same sample then the resulting diffraction pattern is the sum of the individual ones.

When attempting to identify diffraction patterns of an unknown material (or indeed, trying to find the diffraction pattern of a known material) it is possible to refer to an online database. There are two databases that have been used for the work in this thesis; Crystallography Open Database (COD; (Grazulis et al. 2009)) and the International Centre for Diffraction Data (ICDD; (Fawcett et al. 2005)). However, in some cases, it could be extremely time-consuming and tedious to manually compare experimental patterns to those found on the databases, this is when using a search-match software can be useful. For this work the search-match software Match! (Crystal Impact 2003) was utilised. This software enables the comparison of peak positions and intensities of experimental data to a large database with over forty thousand reference patterns.

However, despite the presence of these computer resources, sometimes they may not be enough to provide a definitive conclusion to the identity of the material in

question. In some cases, materials may have very similar diffraction patterns which are hard to distinguish, and the pattern suggested by software as being the best match for the experimental data may actually not be correct. Also, experimental data can sometimes have peaks present which do not appear in the selected reference pattern. This could either be due to the presence of multiple phases and/or materials in the sample or a low quality/resolution of the reference pattern compare to the experimental data.

All samples used to collect data for the work in this thesis are placed into capillaries before being exposed to X-rays. These capillaries are made from either sapphire, quartz or borosilicate, all of which also have their own unique powder diffraction pattern. Therefore, sometimes it is possible that the diffraction pattern of the sample collected in a sum of the patterns from the material and the capillary, which means there will be peaks present in the pattern that would not be found on a reference pattern. Therefore, in order to obtain a reliable pattern from the sample, a X-ray diffraction pattern of an empty capillary to be used during the experiment is taken. This can then be compared to the resulting experimental diffraction pattern so only the features from the sample are being analysed. This can be done via plotting software, of which this thesis uses Gnuplot (Williams & Kelley 2015). This plotting software enables the user to compare diffraction patterns and look for changing features and intensities of peaks; it can also help in determining changes in peak widths. This will help in deciding which peaks/patterns require further analysis.

3.4.1.2 Quantitative analysis

Rietveld refinement Once the sample has been identified via its powder diffraction pattern, a quantitative analysis of the material can be made; this can be done using Rietveld refinement (Rietveld 1969). The Rietveld method refines pre-selected parameters and attempts to minimise the difference between the obtained experimental pattern and a model pattern based on the theoretical crystal structure and instrumental parameters i.e. the calculated pattern. To do this the Rietveld method uses a

least-squares piece-wise linear interpolation procedure to improve the agreement between the experimental and calculated fits. In this thesis Rietveld refinement of all data is done using the TOPAS Academic profile analysis program (Coelho 2007). Rietveld is a full profile fitting refinement – it refines lattice parameters and space groups to constrain peak positions and the crystal structure constrains peak intensities.

For Rietveld refinement, a structural model must first be determined by inputting information such as atomic positions, unit cell parameters, occupancy, displacement parameters and space-groups of the relevant material. Using this model a diffraction profile can be determined which produces information on the intensity of each Bragg peak:

$$I_{\text{obs}(\text{hkl})} = Sj_{\text{hkl}}L_{\text{hkl}}P_{\text{hkl}}A_{\text{hkl}}F_{\text{hkl}}^2 \quad (3.9)$$

where S is the scale factor, L , P and A are the Lorentz, polarisation, and absorption correction factors respectively, j is the multiplicity factor which is dependent on the crystal symmetry, and F_{hkl}^2 is the atomic structure factor. However, to increase detail and be able to distinguish between overlapping Bragg peaks, Rietveld introduced a new method whereby a more detailed model is produced by calculating intensity on a step by step basis by taking into account the peak shape function:

$$y_{c,i} = y_{b,i} \sum_{k=k1}^{k2} G_{\text{hkl},i} I_{\text{obs}} \quad (3.10)$$

This equation calculates the intensity $y_{c,i}$ of any point, i , across a specific 2θ range. Here, $y_{b,i}$ is the background intensity at any point, i . $k1$ and $k2$ represent the Bragg reflections contributing to point i and $G_{\text{hkl},i}$ is the peak profile function describing how the intensity of a Bragg peak, $I_{\text{obs}(\text{hkl})}$ is distributed over a range 2θ .

Rietveld refinement minimises the intensity at every i th point within the pattern. This is done by minimising the following function:

$$\sum_i (1/\sigma^2[y_{o,i}], y_{c,i}(y_{c,i} - y_{o,i})^2) \quad (3.11)$$

where $y_{o,i}$ is the observed intensity at every i th point, and $\sigma^2[y_{o,i}]$ is the square of the standard uncertainty for $y_{o,i}$.

When complete, the refinement produces a plot with three profiles which include the experimental data, the refined best fit and a residual profile (the difference between the experimental and refined profiles). This resultant plot allows us to make a visual analysis of the data by comparing the fitted and residual profiles to the experimental data, hence allowing us to decide how to make the refinement better (if need be). As well as visually, TOPAS enables us to determine how good the fit is numerically by calculating agreement indices, or R -factors. The first is the weighted profile R -factor and is calculated using the following equation:

$$R_{wp} = \left[\frac{\sum_i \omega_i (y_{c,i} - y_{o,i})^2}{\sum_i \omega_i (y_{o,i})^2} \right]^{1/2} \times 100\% \quad (3.12)$$

If the R_{wp} value is below 10% then the fit is generally considered to be good. However, there are other factors that need to be taken into account, meaning the R_{wp} is low but this is not due to a good refinement, an example is the contribution of background to the fit. For the R_{wp} value to be a true representation of a good fit then the background intensity must be subtracted from $y_{o,i}$. If not, and the background is included in the refinement, then a significant part of $y_{o,i}$ will be due to background contributions, which will result in a deceptively low R_{wp} value.

The second R -factor is the expected R -factor, R_{exp} , and is defined as:

$$R_{exp} = \left[\frac{N}{\sum_i \omega_i (y_{o,i})^2} \right]^{1/2} \quad (3.13)$$

where N represents the number of steps used in the refinement. R_{exp} is the statistically expected R -factor and defines the quality of the raw experimental data, therefore R_{wp} should be of a similar value to R_{exp} . Finally, TOPAS can also calculate a goodness of fit parameter (GoF), χ^2 :

$$\chi^2 = \left(\frac{1}{N} \right) \sum_i \omega_i (y_{c,i} - y_{o,i})^2 \quad (3.14)$$

which represents the ratio of the R -factors and in this case N is the number of degrees of freedom. Consequently χ^2 can also be defined as:

$$\chi^2 = \left(\frac{R_{wp}}{R_{exp}} \right)^2 \quad (3.15)$$

$\chi^2 \approx 1$ in the case of a good fit.

Despite their intended use, these parameters should not be the sole determining factor when it comes to deciding how well the refinement fits the experimental data. Crystallographic parameters as well as visual interpretation should also be taken into consideration to ensure a realistic fit. In addition to providing fitting parameters, the Rietveld method, when used on a mixed sample, can indicate the weight percent (wt%) of each phase present:

$$wt\%_1 = \frac{S_1\rho_1}{\sum_n S_n\rho_n} \quad (3.16)$$

where n represents each individual phase and S_n is the refined scale factor on which the calculation is based.

Pawley and LeBail refinement Pawley and LeBail software refinements use the Rietveld method. Rietveld refinement refers to refining a structural model, while Pawley/LeBail refers to refining unit cell parameters, however all are least squares methods and do in fact use Rietveld least square procedure.

Before a Rietveld refinement can be performed for a powder pattern on an unknown material, the unit cell type must be identified, an hkl index has to be assigned to each peak and, the unit cell (lattice) must be calculated or refined using the intensities. This last is done by whole pattern least squares fitting/refining using, for example, the Pawley method. The Pawley method assumes that the angle dispersive powder diffraction pattern can be described by a small number of parameters, i.e. the intensity for each hkl reflection, unit cell parameters, 2θ instrumental zero error and peak width and peak shape parameters. This method does work well in cases where none of the peaks in the pattern are overlapped, however an artificial correlation in peak intensities can be introduced if two or more peaks are closely overlapped. This can cause the least squares calculation to become unstable and/or not converge. Additionally, the Pawley method is computationally expensive as it can take up significant memory space.

Lebail took a different approach by not treating the intensities as least squares re-

finable parameters (Le Bail 2005). Instead, they are initially set to a uniform value and then treated as calculated values as if derived from a model. Application of Rietveld's procedure for partitioning the observed profile points between calculated profiles leads to a set of "calculated observed" intensity values. These are then used instead of a structural model for the least-squares fitting of the diffraction profile, and the whole process iterated. Since intensities are not refined, less memory is used and programs can run faster, however these provide less of an issue with modern computer technology.

Pawley and LeBail thus basically perform the same function. However, both can struggle in certain cases (e.g. with severely overlapped peaks), and both should return similar results, but in some case one method can perform better than the other. Originally, whole pattern decomposition was set out to provide a set of hkl intensities for structure solution, however if the structure is already known, then Pawley/LeBail can be used to refine the the diffraction pattern.

3.5 Raman spectroscopy

Raman spectroscopy is used as it can give complementary information on the structure of materials when used in conjunction with X-ray powder diffraction.

X-rays interact with electrons; it can reveal the reciprocal space by diffraction and is suited to determining the crystal structures of materials. Raman spectroscopy uses radiation with long wavelengths which can interact with atoms, molecules or ions therefore revealing information on the vibration frequencies of system by scattering.

When light is scattered by a material, most of it is an elastic process (Rayleigh scattering) and the total energy of the system remains the same. However, a small percentage of the scattered light is an inelastic process, therefore it has a different energy from the incident light. This inelastic scattering of light was predicted theoretically by Adolf Smekal 1923 and first observed experimentally by Chandrasekhara Venkata Raman in 1928 (Raman 1928).

The incident light interacts with the material and distorts the cloud of electrons

around the nucleus of an atom and forms a “virtual state which is unstable. The photon is re-radiated as scattered light. Rayleigh scattering is when a ground state electron is excited and subsequently falls back to the original ground level. There is no energy change, therefore Rayleigh scattered light has the same energy as incident light. Raman scattering can be classified as two types: Stokes Raman scattering and anti-Stokes Raman scattering. With Stokes Raman scattering an electron is excited from the ground state and falls to a vibrational level. This causes the molecule to absorb energy and hence Stokes Raman scattered light has less energy than the incident light. Anti-Stokes Raman involves an electron being excited from the vibrational level to the ground state. It there is an energy transfer to the scattered photon therefore anti-Stokes Raman scattered light has more energy than the incident light.

Rayleigh scattering is the dominant form of scattering, as with Raman scattering, only one in every 10^6 – 10^8 photons are scattered. The ratio of Stokes Raman and anti-Stokes Raman scattering is dependent on the number of various states of the molecule. The Raman scattering intensity is defined by the following equation:

$$I_{\text{Raman}} = KI_L(v_0 - v_i)^4 \left(\frac{d\alpha}{dQ} \right)^2 \quad (3.17)$$

where v_0 is the wavenumber of the monochromatic radiation beam from the laser source, v_i is the wavenumber of the i th vibrational mode of the molecule, K is a constant based on experimental parameters, I_L is the power of the incident laser, and $d\alpha/dQ$ is the change in polarizability, α , with respect to the normal coordinate of vibration, Q .

4 Experimental methods

4.1 Introduction

Many materials naturally occur, or are manufactured, in powdered or polycrystalline states, therefore X-ray powder diffraction beamlines are of high importance scientifically; consequently they are available at many synchrotron facilities around the world. These beamlines allow for the delivery of bright, intense and collimated X-ray beams, and therefore high quality data that could not otherwise be obtained using, for example, a conventional laboratory source can be collected.

All the experimental work presented in this thesis was conducted at the Diamond Light Source (DLS) which is a third generation synchrotron facility. The beam brightness (and therefore resolution of the data) is increased by the presence of insertion devices, hence allowing for the possibility of advances in quality and nature of the data obtained.

4.1.1 Diamond Light Source

DLS is situated at Harwell Science and Innovation Campus in Oxfordshire. It was opened in 2007 to replace the previous synchrotron source at the Daresbury laboratory. It measures half a kilometre in circumference, and produces high intensity beams of X-rays, infrared and ultraviolet radiation. An aerial view of DLS is shown in Fig. 4.1.

An electron gun is used to generate high energy electrons (3 GeV) which are then fired into a series of three particle accelerators; these are the linear accelerator (linac), the booster synchrotron, and the storage ring. The booster synchrotron and the linac are used to accelerate the electrons so that they reach speeds close that of light. The electrons then reach the storage ring. This ring is not an actual circle but a polygon with 48 straight sections joined by 48 bending magnets. It is the bending



Figure 4.1: Ariel view of DLS (<http://www.diamond.ac.uk>).

magnets or insertion devices¹ which direct the electrons in a circular path around the storage ring. The result is the production of highly focused, intense synchrotron radiation in the direction of each beamline. To ensure a supply of constant current beam on each beamline, the stored beam is topped-up with electrons every six hundred seconds. Additionally, the storage ring is kept under vacuum conditions (pressure of 7.9×10^{-10} mbar) to reduce the scattering due to electron collisions with air molecules to a minimum.

4.1.2 Beamline I11

DLS has many beamlines, each with their own specific use. This work utilises the capabilities of beamline I11 which is a high resolution X-ray powder diffraction beamline (Thompson et al. 2009; Thompson et al. 2011). I11 is composed of three hutches; 1) the

¹These are periodic magnetic structures that produce forward-directed synchrotron radiation by allowing a stored beam to wiggle, or undulate, as it passes through the device.

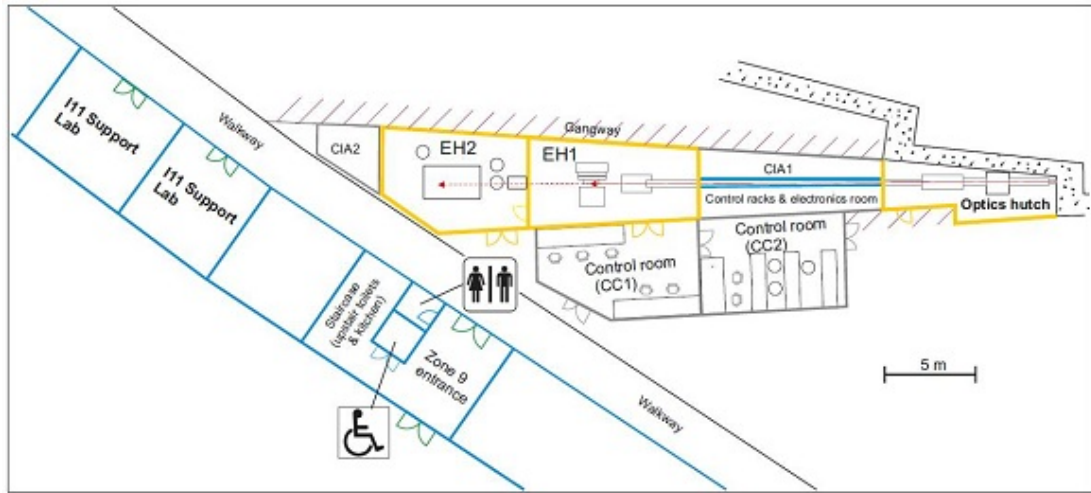


Figure 4.2: Schematic layout of the hutches and control cabins around beamline I11 (Murray et al. 2017).

optics hutch, 2) Experimental hutch 1 (EH1) and 3) Experimental hutch 2 (EH2) which houses the Long Duration Experiment (LDE); this is discussed in the next section. The optics hutch implements a three slit system; beam diagnostics, monochromator and the harmonic rejection mirrors. A schematic layout of I11 is shown in Fig. 4.2.

The X-ray source on I11 originates from an in-vacuum undulator, which is located in the main storage ring of the synchrotron. The undulator holds an array of 90 permanent magnets with a period length of 22 m, which produces X-rays in the range of 5–30 keV. However the best incident flux obtained is between 11–20 keV, therefore the optimal energy of the beamline is generally set at 15 keV. This energy corresponds to wavelengths of approximately 0.826\AA to 3 d.p.; however an accuracy of 6 d.p. can be obtained by calibrating against a certified silicon reference powder, NIST SRM640c. A calibration of the wavelength is performed at the beginning of each new experiment.

The optics hutch is approximately 4 m high, 10 m long, and 2.5 m wide with walls made from steel and lead. The main components are 1) water cooled primary slits, 2) double-crystal-monochromator (DCM), 3) double bounce harmonic rejection

mirrors (HRM), 4) two sets of monochromatic slits and 5) an embedded intensity monitor I_o comprising a thin 45° Kapton scattering foil and scintillation counter. The heat load on the DCM crystals is reduced using a closed-circuit liquid nitrogen cooling system incorporating a cryo-cooler reservoir which allow samples to maintain a constant temperature.

The purity of the monochromatic beam is essential and to maintain this HRM are located downstream of the DCM; this is also a double bounce device which ensures a fixed-height geometry.

EH1 is also constructed from lead and steel panels; it is located in adjacent to the optics hutch, with dimensions 9.7 m in length, 5.0 and 9.3 m in width at its ends and is 4.0 m high. The main component of this experimental hutch is the heavy duty diffractometer which has three concentric circles making up the rotary stages (θ -, 2θ - and δ -circle, see Fig. 4.3). The circles are located on a base composed of granite which has motorised xyz , movement allowing the instrument to be accurately aligned with the centre of rotation of the X-ray beam.

The hutch also contains a 200-sample carousel and a robotic arm which allows for efficient and automatic change of samples on the diffractometer.

The diffractometer has two different detectors (see Fig. 4.3): the Multi-Analysing Crystal (MAC) detector and the Position Sensitive Detector (PSD). For high resolution data the 2θ circle scans positive angles using the MAC detector, the disadvantage of this is that it takes longer to gather the data compared to the PSD. The PSD is a time-resolved detector and measurements are taken using the δ -circle.

4.1.3 The Long Duration Experiment (LDE) Facility

The Long Duration Facility (Murray et al. 2017) is the first of its kind whereby users are granted months and even years (as opposed to days and weeks) to expose their samples to in-situ environments (e.g. cryogenic systems, incubators, heating stages, climate simulators and high pressure gas cells) over long periods of time, and observe the changes in the properties and behaviour of various types of materials. Measurements

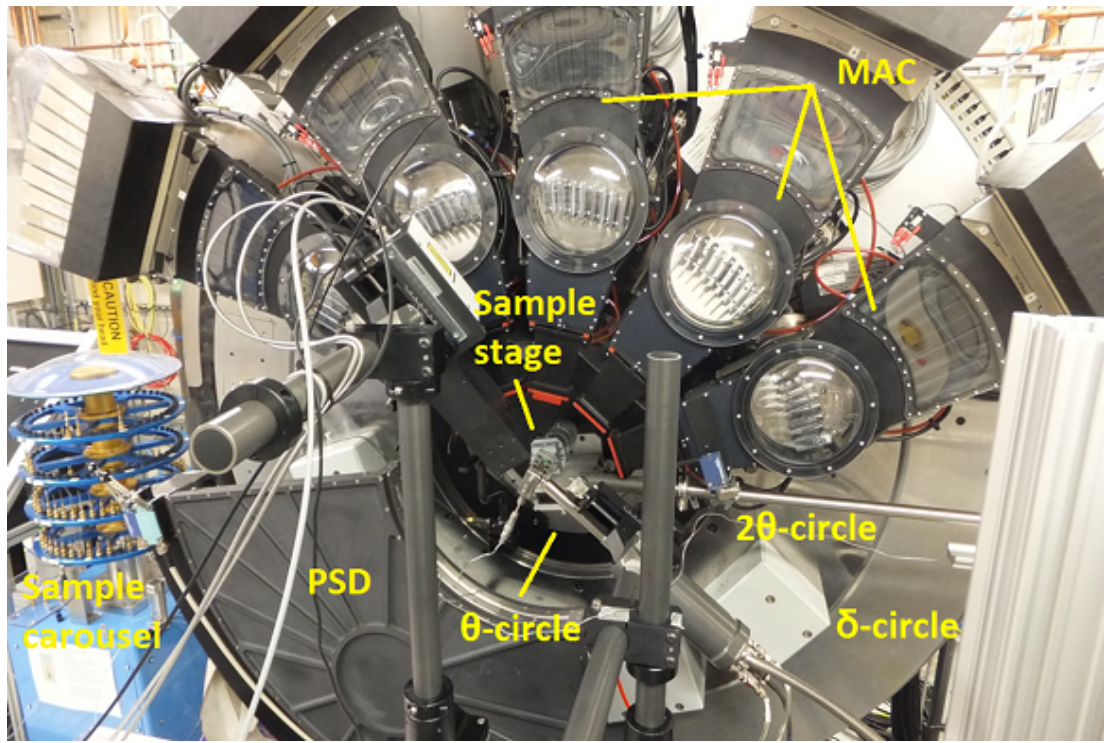


Figure 4.3: Diffractometer on I11.

on the LDE are taken weekly and users are able to observe the long term changes in their samples as they are likely to occur in their natural environments. Particular areas that might benefit from experiments on this facility are: studies of crystallisation, mineral evolution, seasonal effects, gas storage, fuel cells, corrosion science, and thermal and electrical power cycling. This projects uses the LDE to look at the geochemical processes in cold aqueous environments such as those found on planets such as Mars and planetary satellites like Europa and Enceladus.

The LDE complements the existing high resolution and fast time resolved facilities on I11. It is located in the third hutch on I11 (EH2) and more laboratory space has also been constructed (see Fig. 4.2). EH2 houses a large sample table on which the experiments are mounted and which can periodically move samples in and out of the X-ray beam. A motorised stage can drive a pixium area detector, which records the diffraction patterns. The experiments on the LDE, once set up, are left to run with automatically programmed data collection. Cryogenic systems, incubators, heating stages, climate simulators and high pressure gas cells can be used with the LDE to create the sample environments that the experiments require.

A pixium digital area detector (RF4343, Thales) was chosen to log the 2D powder diffraction patterns. This was due to its large active area (430×430 mm) and columnar crystalline CsI scintillator array which is capable of high-energy detections. Here X-rays are converted to visible light which is detected by an amorphous silicon photodiode array (Murray et al. 2017). The active area contains 2880×2880 pixels, each of which is $148 \mu\text{m} \times 148 \mu\text{m}$. The signal is processed before being written to a 2D file of 16 bit depth resolution (Murray et al. 2017).

Using the LDE, good quality, 2D diffraction patterns can be collected. These 2D diffraction patterns are produced indirectly by the direct capture of whole Debye-Scherrer (powder) ring (Murray et al. 2017). The resolution of these rings is lower ($\delta d/d \simeq 10^{-3} - 10^{-4}$ where d represents the lattice parameter) than those attained via slower angle dispersive or angle scanning measurements. A whole ring pattern is achieved as opposed to small portions of the Debye-Scherrer rings, which is what is obtained when using the slower processes. However, the main aim of the LDE is to record

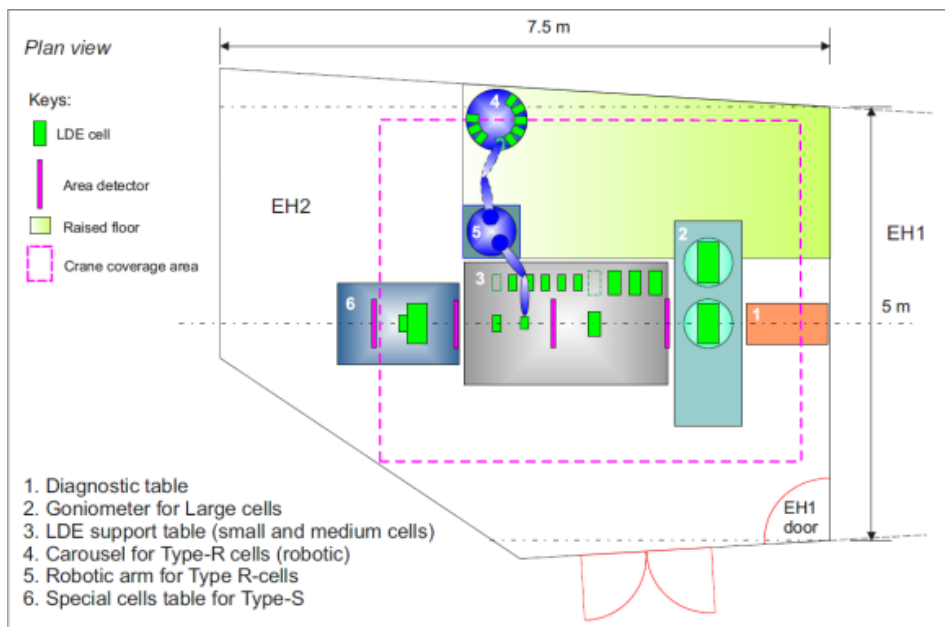


Figure 4.4: Schematic layout of experimental components and equipment in EH2 (Murray et al. 2017). The dashed black line running through the centre of the area detectors represents the X-ray beam.

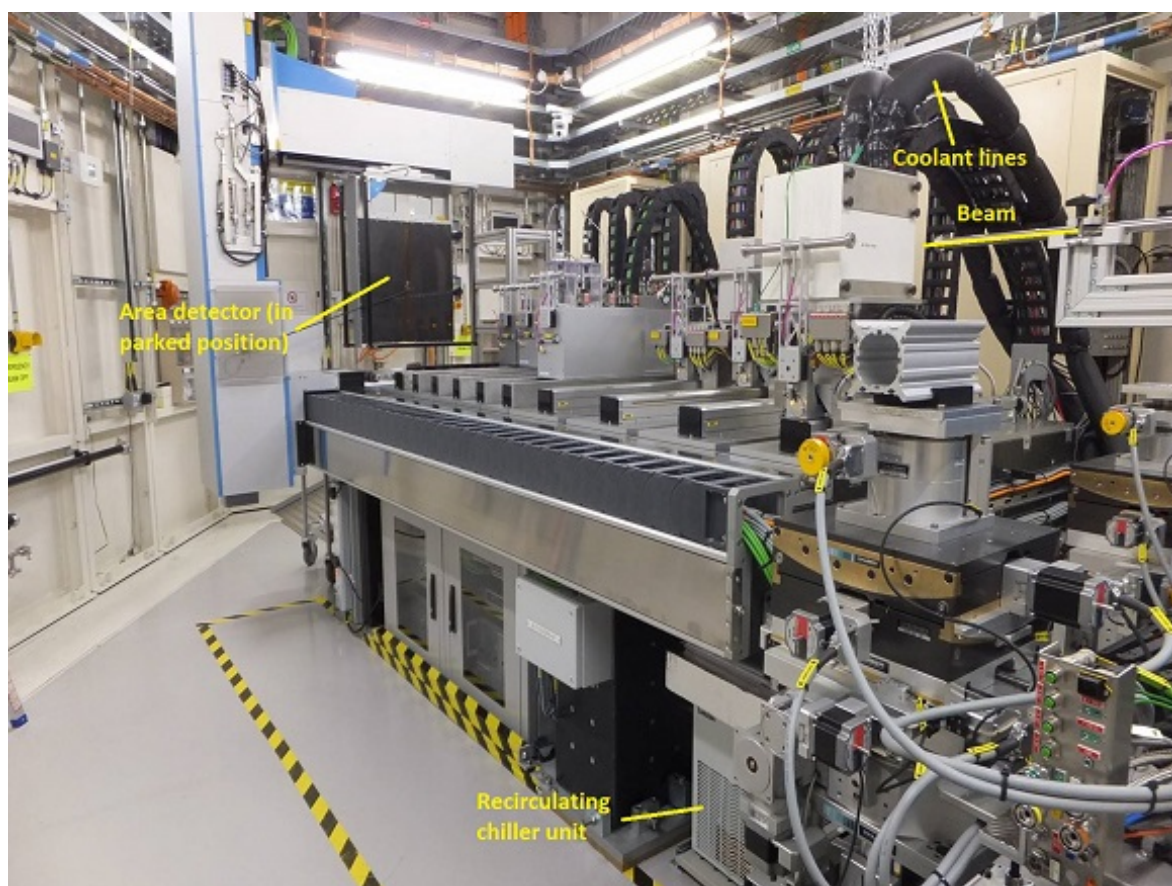


Figure 4.5: Layout of experimental components and equipment in EH2 (Murray et al. 2017).

phase development rather than high-quality resolution, therefore a lower resolution measurement is sufficient for most cycling and processing experiments (Murray et al. 2017).

A schematic of EH2 is shown in Fig. 4.4. At the beginning of experiments the sample cells are loaded onto a motorised stage at its parked position. The detector is attached to a large frame and is also motorised, therefore can move along the sample table and can travel along the beam. The operation sequence of the LDE is as follows (Murray et al. 2017):

1. the first sample cell crosses the sample table into the beam;
2. the distance at which the detector is able to view the cell is determined and the detector moves to that position;
3. data collection commences;
4. the cell moves back to its parked position and the detector withdraws.

There can be more than one sample cell present, in which case this process is repeated.

The acquisition of the LDE data is achieved via the Generic Data Acquisition system (GDA). The collection of whole powder diffraction patterns is outlined in Murray et al. (2017) and is summarised below:

1. the X-ray shutter is closed and all cells are moved from their parked to zero positions to provide a low background beam path;
2. the sample stage is moved to its in-beam position for calibration. The calibrate for the LDE is a CeO_2 sample as a opposed to a silicon standard as used in EH1;
3. the detector is moved to the sample-detector distance and the dark current is calibrated without the beam;
4. the hutch shutter is opened and the calibrated diffraction patterns are collected for a particular exposure-time;

5. using lattice parameters the calibrated data are automatically fitted. The calibrated data are integrated and the wavelength and detector distance are refined;
6. the sample stage is moved to the sample position and data are collected for a particular exposure time;
7. the refined wavelength and detector distance are used to integrate the collected sample data, which are converted to intensity vs 2θ .

4.1.3.1 The Cold Cell

The cold cell was designed with the aim of studying mineral precipitation in cold aqueous environments; it can hold up to five samples at any one time (Murray et al. 2017). The samples are loaded into chambers with dimensions 5 mm deep \times 25 mm diameter. The cell itself is composed of a copper block in which a coolant is circulated. The beam enters and leaves the sample compartments via diamond windows. A thermally insulated body with kapton windows houses the sample blocks. The temperature of the cell is managed using a Lauda chiller with an antifreeze–water mixture (Murray et al. 2017). Fig. 4.6 shows the set–up of the cold cell in EH2.

4.2 Sample Preparation

4.2.1 Preparation of Saline Solutions for Clathrate Formation

The saline solutions that are used in order to produce clathrate hydrates are prepared in the laboratory. These solutions are used so that we are able to simulate the in–situ conditions in which clathrates form in astrophysical oceans, such as those on Enceladus and Europa. Various salts are used in different quantities, and are mixed with deionised (18.2 M Ω) water. These are then loaded into capillaries and mounted onto a high pressure gas cell.

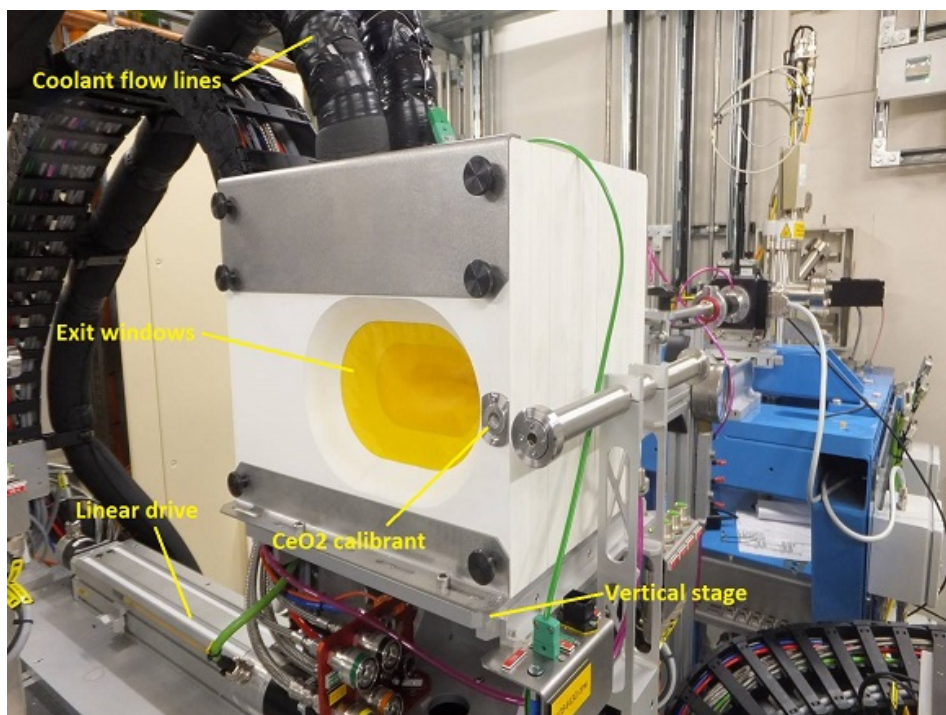


Figure 4.6: Cold cell situated in EH2 (Murray et al. 2017).

Table 4.1: Types of salts and their corresponding concentrations and densities present during clathrate formation/dissociation.

Salt	Concentration (g/kg H ₂ O)	Density of Solution (kg/m ³)
MgSO ₄	5	1.016 ± 0.001
	20	1.016 ± 0.001
MgCl ₂	2	N/A
CaCl ₂	10	N/A
(NH ₄) ₂ SO ₄	100	1.055 ± 0.001
	150	1.076 ± 0.001

The solutions are prepared by simply grinding the chosen salt into a fine powder using a pestle and mortar, measuring out the correct mass using a Mettler Toledo balance and then mixing with a specific volume of deionised water using measuring cylinders. The concentrations and types of salt used in the prepared solutions are shown in Table 4.1.

In order to determine information on the buoyancy of clathrates in extra-terrestrial oceans (see Table 4.1) we must know their density relative to the solutions in which they were formed, therefore the densities of each sulphate salt solution listed in Table 4.1 were measured. The bulk densities of the starting solutions were measured using a 1000µm PhysioCare concept Eppendorf Reference pipette to gather a precise volume of solution and weighed using a Mettler Toledo balance at room temperature. The densities of the solutions are given in Table 4.1.

4.2.2 Preparation of Epsomite Sample

A sample of commercially sourced reagent grade MgSO₄ hexahydrate (Sigma Aldrich) was lightly ground in a pestle and mortar. The epsomite (MgSO₄·7H₂O, MS7) powder was then scooped up using the open end of a 0.7 mm internal diameter borosilicate glass capillary which was vibrated so that an even filling of the capillary was achieved. The sample was then sealed in a brass holder (see next section for information on brass

holders) and mounted onto the diffractometer.

4.2.3 Preparation of Meridianiite Sample

Meridianiite ($\text{MgSO}_4 \cdot 11\text{H}_2\text{O}$ MS11) was first prepared by mixing a solution of deionised water with epsomite in the weight percent ratio 7:3 respectively. The epsomite was ground to a fine white powder using a pestle and mortar to ensure that the epsomite dissolved completely in the water. The mixture was placed in a petri dish and left overnight in a laboratory freezer at -30°C . The resulting meridianiite that was formed could be scraped to form a powder; however upon transportation the powder became a “slurry” that proved extremely difficult to load into the capillaries, as the samples were highly viscous due to their high water content. While it is possible to create powdered meridianiite in cold rooms, physical phase separation during freezing of meridianiite, water and other hydrated magnesium sulphate phases results in an uncertain capillary content and, as mentioned, there is a possibility that melting will occur during transportation and mounting which leads to an uncertain wt%.

Due to the difficulty encountered when trying to produce MS11 ex-situ (i.e. outside the capillaries) and then subsequently attempting to load the mineral, an alternative pathway was required. A simple ageing technique was adapted whereby a small quantity of ultra-fine grained epsomite powder is loaded into the capillaries followed by deionised water. These capillaries are then left for a few days at room temperature in order for the epsomite to dissolve into the water. By varying the length of the capillary that the epsomite powder occupies, the wt% of solution can be controlled.

4.2.4 Loading Capillaries

There are two methods for loading samples onto the diffractometer on I11: 1) flat-plate sample holders, where a thin sample layer on a flat disc is subjected to incident beam at a specific angle to the surface, and 2) using thin capillaries in which samples are loaded. This work utilises the thin capillaries as our samples can readily be loaded into

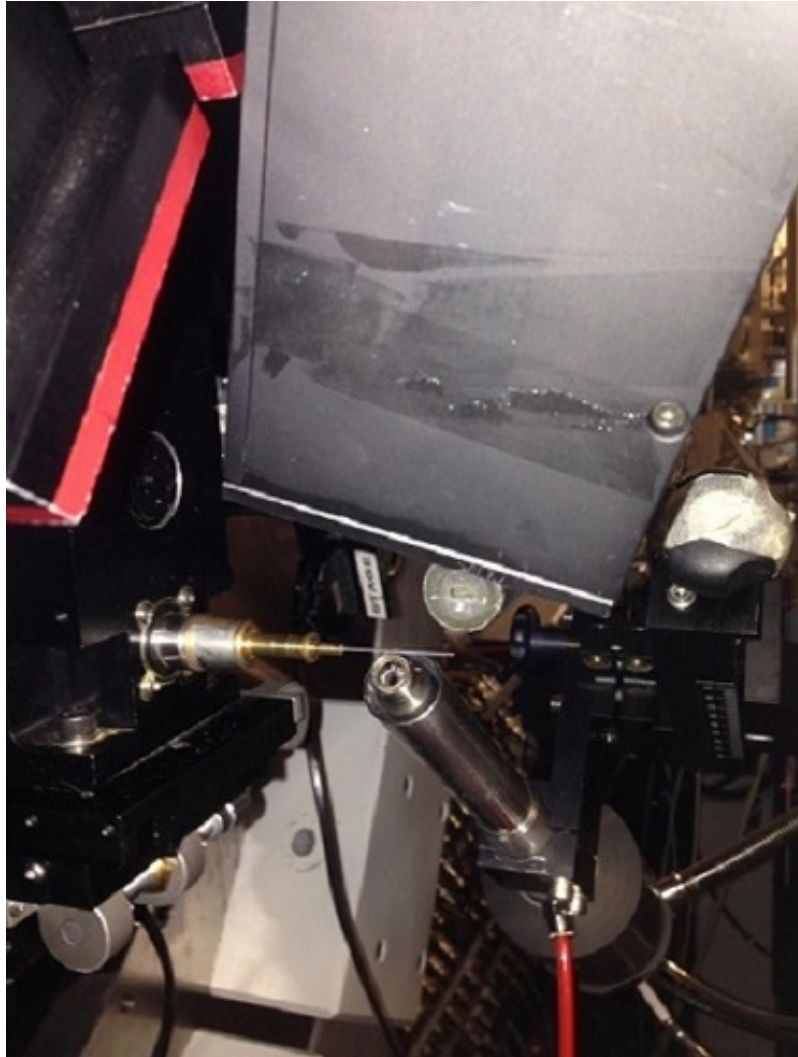


Figure 4.7: Brass holders loaded onto the diffractometer on I11.

them and they provide good powder-averaging if the capillaries are spun during data collection.

Capillaries used on the beamline are available in different internal diameters and materials. The internal diameters range from 0.3mm to 1mm; the smaller the diameter the better the resolution of the diffraction pattern produced, as focusing to a smaller size increases the X-ray flux density at the crystal. The type of capillary used depends on the temperature and pressure ranges of the experiment. Borosilicate capillaries are stable at the lower temperature range below 973 K. Alternatively quartz capillaries can be used up to a relatively higher temperature, 1873 K. The use of sapphire capillaries is pressure-dependent; these capillaries should be used if the sample is to be subjected to pressures of more than 50 bar.

Depending on the experiment being carried out, the capillaries can be loaded onto the diffractometer in different ways. For the experiments described here we use brass holders and a high pressure gas cell.

Brass holders are used when mounting capillaries containing epsomite and mercurianite samples onto the diffractometer (see Fig. 4.7). The holders are made to fit the capillaries and should be approximately 0.1–0.2 mm larger than the actual capillaries so that they can accommodate them; if they are too tight then the capillaries could fracture and the sample will leak out. When fitting the capillary into the brass holder it is important to ensure that approximately 3/4 of the capillary is protruding from the holder. The capillary is then inserted into the brass holder, the open end cut off and sealed using superglue which ensures the capillary stays in place before screwing the holder into the brass base.

4.2.5 The High Pressure Gas Cell

A high pressure cell is used when loading the capillaries containing samples used to produce clathrate hydrates as these structures are most stable at higher pressures and therefore easier to form. The high pressure sample cell employs 1/16" Swagelok fitting, mounted into a stainless steel body with bracing supports and can withstand pressures

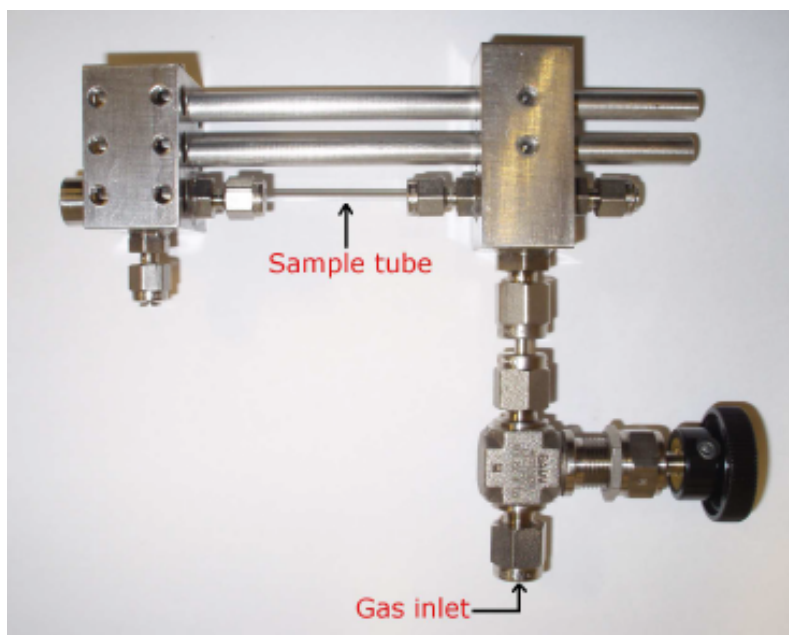


Figure 4.8: High pressure gas cell (Day et al. 2015).

of up to 100 bar (see Fig. 4.8). The cell itself is mounted onto the central circle of the diffractometer via a goniometer mount which allows for sample alignment; a gas inlet allows gas from a pressure panel to flow into the sample.

As mentioned sapphire capillaries (0.8 mm internal diameter) are used for these samples as clathrates require high pressures to form. The capillaries are cut to size and both ends are open. The sample is injected into the capillaries using a syringe and then both ends are sealed using cotton wool and vespel ferrules drilled to match the diameter of the capillary. The capillary is then screwed onto the cell and mounted onto the diffractometer (see Fig. 4.9).

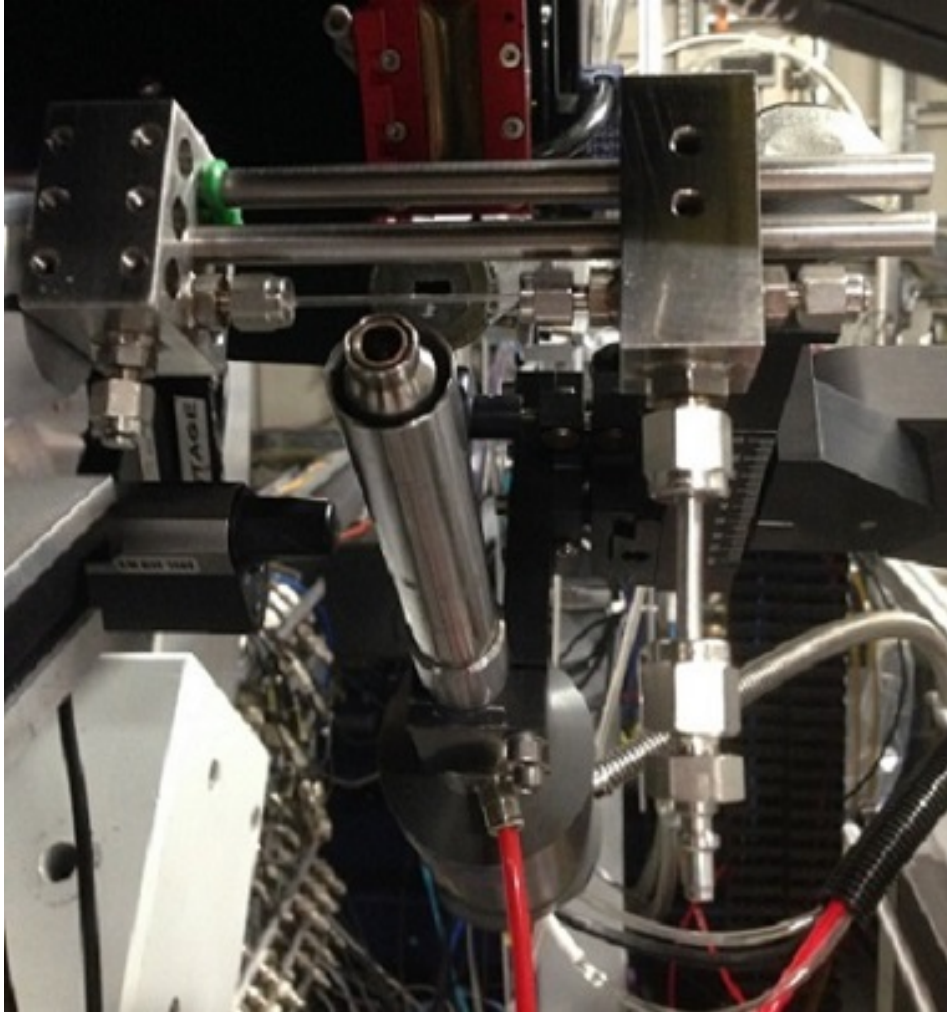


Figure 4.9: Sapphire capillary mounted onto the high pressure cell loaded onto the diffractometer on I11.

4.2.6 Data Collection

The collection and plotting of data used on both I11 and the LDE are both controlled by GDA. This software enables control of all forms of data acquisition i.e. remote movement of the sample stages and tables and Cryostream. The software uses a scripting language called Jython; this allows beamline users to write scripts that allow the almost automated running of the beamline.

Before any data can be collected the wavelength must be calibrated. This is done using a silicon (111) standard and performing a high resolution scan for approximately 30 minutes using the MAC detectors. The position of the Bragg reflections are needed to calculate the exact wavelength of the X-ray beam. This can be done using Bragg's law, and knowing the d -spacing of each of the hkl planes. The final wavelength value will have an accuracy of six-decimal places. It is good practice to take one measurement of an empty capillary at the beginning of every new experiment, and when the experimental set-up is significantly altered. The pattern that the empty capillary produces can be subtracted from all the data patterns collected, and therefore users can be sure that only the features of the sample in question are taken into account.

5 Properties of CO₂ clathrate hydrates formed in the presence of MgSO₄ solutions with implications for icy moons

This chapter presents results of a study focussed on forming CO₂ clathrates in the presence of magnesium sulphate salt solutions and the effect that these solution have on their thermal expansion and density. The effect of pressure on clathrates is also investigated. Results are also presented on the inhibiting effect of these salt solution on CO₂ clathrate formation and dissociation temperatures. This work has been published in Safi et al. (2017).

5.1 Introduction

5.1.1 Clathrate Buoyancy in Ocean-Ice Environments

The density of clathrates is a significant factor in determining their fate: if their density is higher than that of the oceans in which they are formed, they sink to the ocean floor; if lower, they rise to the ice/ocean interface. If their destination is the ocean floor then they might be dissociated by heat produced from hydrothermal activity; if however they ascend then a clathrate layer would be present at the interface between the ice and ocean surface.

Bouquet et al. (2015) calculated the density of clathrates assuming fully filled cages and a volatile composition based on Enceladus' plume. They found densities of 1.04 g cm^{-3} and 0.97 g cm^{-3} for sI and sII clathrates respectively; when comparing these to their computed ocean densities they deduced that sII clathrates should be buoyant and therefore likely to ascend; however they were unable to arrive at a conclusion regarding the sI clathrates, as there was significant uncertainty regarding the ocean's salinity and because the clathrate density was too close to that of the ocean itself. Clathrate ascension would however, enable them to play a part in the formation of

the plumes, as their dissociation would increase pressure conditions at the site of the plume's origin (Bouquet et al. 2015).

Prieto-Ballesteros et al. (2005) evaluated the stability and calculated the density of several types of clathrates thought to be found in the crust and ocean of Europa using thermal models for the crust. They found SO_2 , CH_4 , H_2S and CO_2 clathrates should all be stable in most regions of the crust, and deduced that CH_4 , H_2S and CO_2 clathrates should float in an eutectic ocean composition of $\text{MgSO}_4\text{-H}_2\text{O}$, but that SO_2 clathrates would sink. However the sinking and floating capabilities of various hydrates will also likely depend on the salinity of the ocean since this will affect their buoyancy.

Mousis et al. (2013) investigated clathrates in Lake Vostok (Antarctica) using a statistical thermodynamic model. They assumed temperatures of 276 K and pressures of 35 MPa and found that Xe, Kr, Ar and CH_4 should be depleted in the lake, while CO_2 should be enriched compared to its atmospheric abundance. They also found that air clathrates should float as they are less dense than liquid water. However, air clathrates have not been observed on the surface of the ice above the lake (Siegert et al. 2000). To account for this McKay et al. (2003) suggested that large amounts of CO_2 are also trapped within the clathrates, increasing their relative density.

Clathrates have been found to form in the Sea of Okhotsk (Pacific Ocean); Takeya et al. (2006) used X-Ray powder diffraction to study their crystal structures and thermal properties. They found that four samples from four different locations each had sI clathrates encaging CH_4 and a small amount of CO_2 . The small amount of encaged CO_2 is consistent with the suggestions of McKay et al. (2003) that a large amount of trapped CO_2 is necessary for clathrates to sink.

5.1.2 Effect of Ice and Ocean Salinity on Clathrate Dissociation

It is likely that the type of ice present during the formation of clathrates also has an effect on their dissociation. Using neutron diffraction Falenty et al. (2011) studied the dissociation of CO_2 clathrates in pure water ice between 170–190 K, with special

attention paid to the polymorph of ice formed. They found that below 160 K cubic ice (Ic) was the more stable phase, while between 160–190 K Ic transforms to the more thermodynamically stable hexagonal ice (Ih). Falenty et al. (2011) concluded that, due to Ic forming with smaller crystallite sizes compared to Ih, it could provide an additional pathway for the escaped gas molecules originating from clathrate structures, therefore supporting their dissociation.

An important factor when considering clathrate dissociation is ocean salinity. It is well known that saline solutions depress the freezing point of water (e.g. Duan & Sun 2006) and would suggest that the temperatures at which clathrates form and dissociate within the oceans on planets and satellites will also be lower. Miller (1961) showed how clathrate dissociation is affected by temperature and pressure conditions in pure water. However, when comparing the results obtained by Miller with the more recent theoretical results obtained by Bouquet et al. (2015) for saline solutions, there is a significant difference, suggesting that increased salinity may indeed lower the temperature at which clathrates are able to form.

In this chapter we use synchrotron X-ray powder diffraction (SXRPD) to investigate the thermal and physical properties of CO₂ clathrate hydrates produced from weak aqueous solutions of MgSO₄ under conditions relevant to objects such as Enceladus (whose salinity is 8 g/kg H₂O, Zolotov 2007) and Europa (salinity 10 g/kg H₂O; Hand & Chyba 2007). We replicate possible thermal variations due to seasonal and tidal changes, ocean depth and salt concentration and observe the formation and dissociation conditions of CO₂ clathrate hydrates. The SXRPD provides information about the temperature-dependence of clathrate densities and hence their ability to rise or sink in the oceans in which they are formed. We also investigate clathrate dissociation kinetics and the influence of the different polymorphs of ice.

Table 5.1: Concentration, temperature range, pressure, density of salt solutions.

Concentration	wt%	Temperature	Pressure	Density
g MS7/kg H ₂ O	MgSO ₄ /kg H ₂ O	range (± 5) (K)	(bar)	(g cm ⁻³)
20	10.5 (MS10.5)	90.1 – 225.0	5.00 \pm 0.01	1.016 \pm 0.001
20	10.5 (MS10.5)	90.0 – 240.0	10.00 \pm 0.01	1.016 \pm 0.001
5	3.1 (MS3.1)	89.9 – 245.0	20.00 \pm 0.01	1.003 \pm 0.001

5.2 Experimental Work

In this work we use an epsomite (MgSO₄·7H₂O) salt solution, with concentrations similar to those detected by the Cassini Ion and Neutral Mass Spectrometer (INMS) instrument (Waite et al. 2004), to form the ice and CO₂ clathrate system. The concentrations, densities and the temperature and pressure ranges used, are summarised in Table 5.1. In the table the concentration of MgSO₄·7H₂O has also been converted to concentration of MgSO₄ per kg water, allowing for the contribution that the waters of hydration make to the achieved concentrations. Thus in the following we refer to 20 g MgSO₄·7H₂O/1kg H₂O as MS10.5, and 5g MgSO₄·7H₂O/1kg H₂O as MS3.1.

SXRPD data were collected using beamline I11 at the Diamond Light Source (Thompson et al. 2009). The X-ray wavelength was 0.826220 Å, calibrated against NIST SRM640c standard Si powder; the beam size at the sample was 2.5 mm (horizontal) \times 0.8 mm (vertical). The high pressure gas cell and the procedure used to form clathrates have been described previously by Day et al. (2015). In brief, a 0.8 mm diameter single-crystal sapphire tube is filled with solution and sealed into the gas cell which is then mounted onto the central circle of the beamline’s concentric three circle diffractometer and cooled using a liquid nitrogen Oxford Cryosystems 700+ cryostream, with temperature stability ± 0.1 K and a ramp rate of 360K/h. Once frozen at ~ 240 K, CO₂ gas is admitted to the cell at the chosen pressure and a fast position sensitive detector (Thompson et al. 2011) is used to collect in situ powder diffraction data as the temperature is slowly raised. During this time ice and clathrate formation is si-

multaneously observed. We then continue to increase the temperature until both the clathrate and ice are lost, whereupon the temperature ramp is reversed and the cell is cooled once more. Depending on pressure and solution composition, either pure-phase clathrates or an ice-clathrate mix is formed. Using this “second cycle” technique provides increased clathrate formation (see discussion in Day et al. 2015). For the present work we then cycled the temperature between 250 K and 90 K using the Cryostream to replicate diurnal and tidal variations with applied CO₂ pressures between 5–20 bar. Dissociation temperatures and pressures were determined by holding the sample at constant pressure and gradually increasing the temperature in 5 K temperature steps until there were no peaks discernible in the X-ray diffraction pattern.

5.3 Results

The SXRPD patterns were analysed via Rietveld structure refinement, using TOPAS refinement software (Coelho 2007) and previously published clathrate atom positions and lattice parameters (Udachin et al. 2001) as starting values. Published atom positions and lattice parameters (Fortes et al. 2007) for Ih and Ic were similarly used. From the refinements, the lattice parameter, a , at each temperature step were obtained and hence the thermal expansion and density of the cubic clathrate structures were derived. As an example, Fig. 5.1 shows a comparison of the SXRPD patterns for Ih, Ic and CO₂ clathrates formed in the MS10.5 solution at a CO₂ pressure of 10 bar. The presence of the clathrates at 90 K and 180 K is evident from the formation of multiple features at 14°-19°, 21.4°, 23°-24°, 24.6° and 25.2° 2θ (Day et al. 2015). During fitting, the lattice parameters of Ih were initially set to 4.497479 Å for the a -axis and 7.322382 Å for the c -axis (Fortes et al. 2007); the lattice parameter for Ic was initially set to 6.36 Å and for clathrates to 11.893 Å (Motoi 1968; Udachin et al. 2001). The space groups of sI clathrate, Ih and Ic are Pm-3n, P63/mmc and Fd3m respectively. Values for the background subtracted fitting agreement parameter, R'_{wp} , between the calculated and experimental diffraction data (see McCusker et al. 1999, for further details) excluding

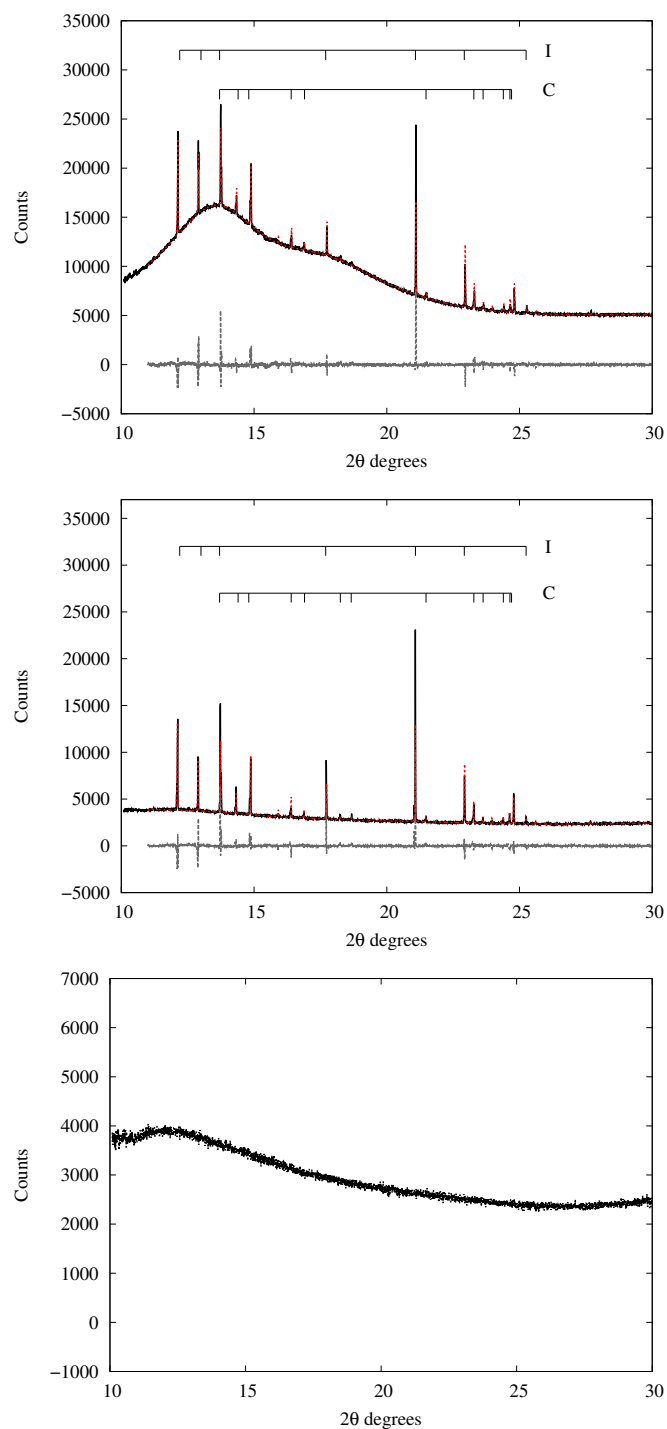


Figure 5.1: Rietveld refinements of the MS10.5 solution at a 10 bar CO_2 pressure experimental data. From top-bottom: 90 K, 180 K, 245 K. The experimental data are shown in black, the calculated fit in red, and the residuals in grey below. All dominant peaks are labelled where C = clathrate peaks and I = hexagonal ice peaks. The larger residuals for some of the ice peaks are due to poor powder averaging due to the way the ice freezes inside the cell (preferred orientation) and the restricted cell rocking angle used to compensate for this during measurement.

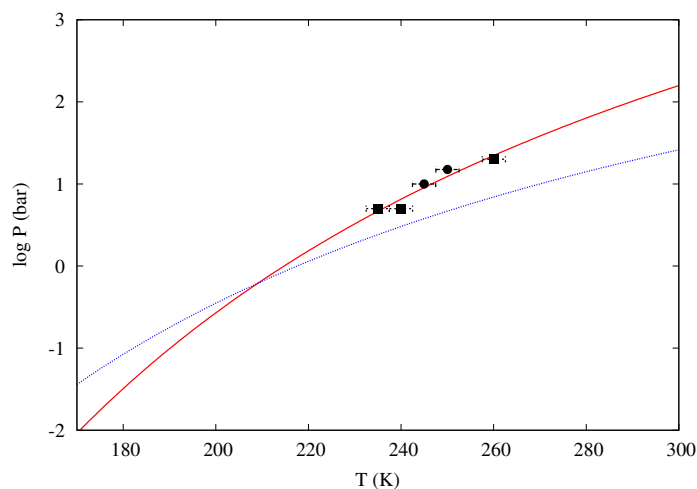


Figure 5.2: Arrhenius curve for CO_2 clathrate hydrates in MS10.5 and MS3.1 solutions (black points, red curve) compared with the Arrhenius curve for CO_2 clathrate hydrates in pure water (Miller 1961, blue curve).

the ice peaks from the refinement, were 30.71% and 27.95% for the structures formed at 90 K and 180 K respectively. The associated error in the lattice parameter was typically $\pm 0.001 \text{ \AA}$.

The bulk densities of the MgSO_4 starting solutions were measured using a $1000 \mu\text{m}$ PhysioCare concept Eppendorf Reference pipette to gather a precise volume of solution and weighed using a Mettler Toledo balance at room temperature. The solution densities are given in Table 5.1.

5.3.1 Arrhenius Curve and Inhibiting Effects on Clathrate Formation

Fig. 5.2 compares the dissociation temperatures and pressures for the CO_2 clathrates formed in the MS10.5 and MS3.1 solutions to those reported by Miller (1961) for pure water. We have fitted the data for the MS10.5 and MS3.1 solutions, for which we have

dissociation temperatures at four pressures, to a function of the form (cf. Miller 1961)

$$\log_{10} P = -\frac{\alpha}{T} + \beta , \quad (5.1)$$

where T is in K, P is in bar, and α and β are constants to be determined. While we recognise the limited amount of available data to determine the two parameters α and β , we find $\alpha = 1661 \pm 292$ K and $\beta = 7.74 \pm 1.19$. These values may be compared with those given by Miller (1961) for CO₂ clathrates in pure water: $\alpha = 1121.0$ K and $\beta = 5.1524$; the measurements by Miller (1961) are based on measurements in the temperature range 175–232K. Our data confirms likely the inhibiting effect by lowering the temperature at which they dissociate at a given pressure over the temperature range 235–260 K.

5.3.2 Thermal Expansion

The thermal expansion of clathrate hydrates is an important property that enables us to understand their physical behaviour in greater depth. For example, it has been suggested that the increase in thermal expansion could be due to greater anharmonicity in the crystal lattice (Tse 1987) such that the larger thermal expansion of clathrates compared to hexagonal ice could be due to interactions between the guest molecule and host structure (Shpakov et al. 1998).

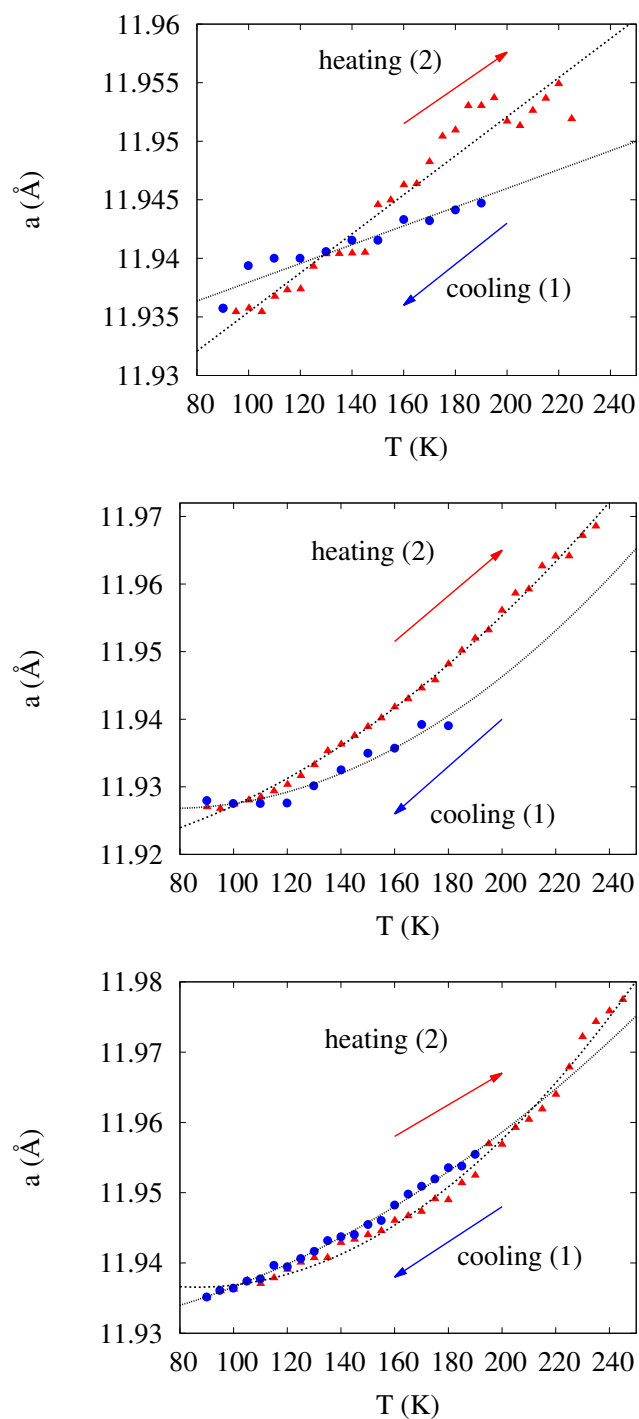


Figure 5.3: The temperature dependency of the lattice parameters of CO₂ clathrate hydrates formed in solutions of MS10.5 and MS3.1 at various pressures. From top-bottom: MS10.5 at 5 bar, MS10.5 at 10 bar and MS3.1 at 20 bar. For ease of presentation blue symbols represent values obtained during cooling and red values obtained during heating.

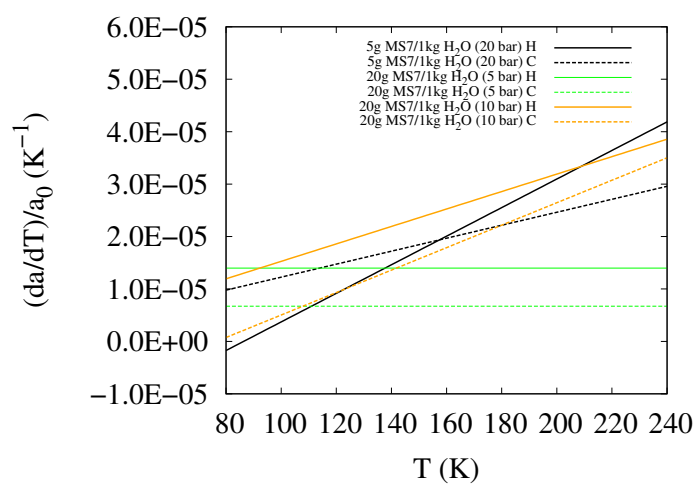


Figure 5.4: The thermal expansion coefficient for CO₂ clathrate hydrates formed in solutions of MS10.5 and MS3.1 derived from the polynomial fits. H = Heating and C = Cooling.

Table 5.2: Coefficients of the polynomial expression for describing lattice constants of CO₂ clathrate hydrates formed in the MS10.5 and MS3.1 solutions.

Solution	Heating			Cooling		
	a_0 (Å)	a_1 (10^{-5} Å K ⁻¹)	a_2 (10^{-7} Å K ⁻²)	a_0 (Å)	a_1 (10^{-5} Å K ⁻¹)	a_2 (10^{-7} Å K ⁻²)
20g MS7/1kg H ₂ O (5 bar) {10.5 g MgSO ₄ /kg H ₂ O}	11.9187 ±0.0014	16.6710 ±0.8611	— —	11.9299 ±0.0011	8.0139 ±0.8213	— —
20g MS7/1kg H ₂ O (10 bar) {10.5 g MgSO ₄ /kg H ₂ O}	11.9189 ±0.0021	-1.6416 ±2.6850	9.9181 ±0.8200	11.9343 ±0.0090	-19.5623 ±13.7700	12.7815 ±5.0770
5g MS7/1kg H ₂ O (20 bar) {3.1 g MgSO ₄ /kg H ₂ O}	11.9487 ±0.0028	-28.1259 ±3.4900	16.2818 ±1.0340	11.9294 ±0.0023	0.1446 ±3.3950	7.3817 ±1.2070

Fig. 5.3 shows the dependence of the clathrate lattice parameter on temperature at three pressure-composition combinations. We have used a polynomial approach to describe the temperature dependency of the lattice parameter, using the function:

$$a = a_0 + a_1T + a_2T^2 . \quad (5.2)$$

Although apparently small, the second order term was found to improve the fit to our experimental data for the higher pressures. Table 5.2 gives the values of the coefficients a_0 , a_1 , a_2 , obtained by fitting Eq. (5.2) to the data.

The MS10.5 solution at a CO₂ pressure of 10 bar was cycled once and clathrates appeared at 185 ± 2.5 K on cooling from 250 K. It seems evident from Fig. 5.3 that the expansion of the clathrate on heating does not follow the behaviour on cooling: there is hysteresis in that the cooling and heating seem not to be reversible. The MS10.5 solution at a CO₂ pressure of 5 bar shows a greater degree of hysteresis compared to the 10 bar solution; it too was thermally cycled and, on cooling, clathrates appeared at 195 ± 2.5 K. Similarly, the MS3.1 solution at a CO₂ pressure of 20 bar was also cycled once, with clathrates appearing at 247.5 ± 2.5 K when cooled from 250 K. This solution shows a significantly lower degree of hysteresis compared to the solutions at 5 and 10 bar CO₂ pressure. The difference in behaviour between heating and cooling may be related to differing levels of bonding disorder within the clathrate phase (see discussion in Section 5.4).

The coefficient of thermal expansion at constant pressure is defined in the usual way as $[(da/dT)/a_0]_P$. In the simplest case, the expansion has a linear dependence on temperature and the coefficient of expansion is a_1 , which is itself independent of temperature. The coefficients of thermal expansion are plotted as a function of temperature in Fig. 5.4; they exhibit strong pressure dependency. Those CO₂ clathrates formed at the lower pressure of 5 bar display a purely linear expansion, while those formed at higher pressure show more complex behaviour. Since higher pressures result in higher cage occupancy (Hansen et al. 2016), our results imply that the occupancy of the cages may influence the thermal expansion of clathrates. This is discussed further

in Section 5.4.

5.3.3 Density

The density, ρ , of a clathrate depends on the lattice parameter, the mass of its water molecules, the mass of the guest molecule and the cage occupancy; it is calculated as follows (Prieto-Ballesteros et al. 2005):

$$\rho = \frac{(M_{\text{CO}_2} (6\theta_1 + 2\theta_2) + 46M_{\text{H}_2\text{O}})}{a^3} . \quad (5.3)$$

here M_{CO_2} and $M_{\text{H}_2\text{O}}$ are the masses of the CO_2 guest and water molecules respectively, and θ_1 and θ_2 are the fractional occupancies of the large and small cages respectively. Raman data for CO_2 clathrates formed at 20 bar in pure water (Day et al. 2015) indicated that only the large clathrate cages are occupied by CO_2 (see also Ratcliffe & Ripmeester 1986); for the time being, we assume in the following that this is also the case for clathrates formed in the presence of MgSO_4 and that therefore $\theta_1 = 1$ and $\theta_2 = 0$. The dependence of the clathrate densities on temperature, calculated using Eq. (5.3) are shown in Fig. 5.5. As with the lattice parameter hysteresis shown in Fig. 5.3, the obtained densities vary with composition and on whether the clathrate is being heated or cooled. We discuss this further in Section 5.4.3 below and also consider the effect of fractional occupancy of the cages.

5.3.4 Weight percentage of clathrate, Ih, and Ic ice

From the relative contribution of each phase to the overall intensity of features in the powder pattern we can obtain the relative fraction by weight of each crystalline component present in the sample under study. These are shown in Fig. 5.6 as a function of temperature for the MS10.5 (at 5 and 10 bar CO_2) and MS3.1 (20 bar CO_2). It is immediately evident that the proportion of Ic formed in all three samples is small (typically $< 5\%$), even at 90 K.

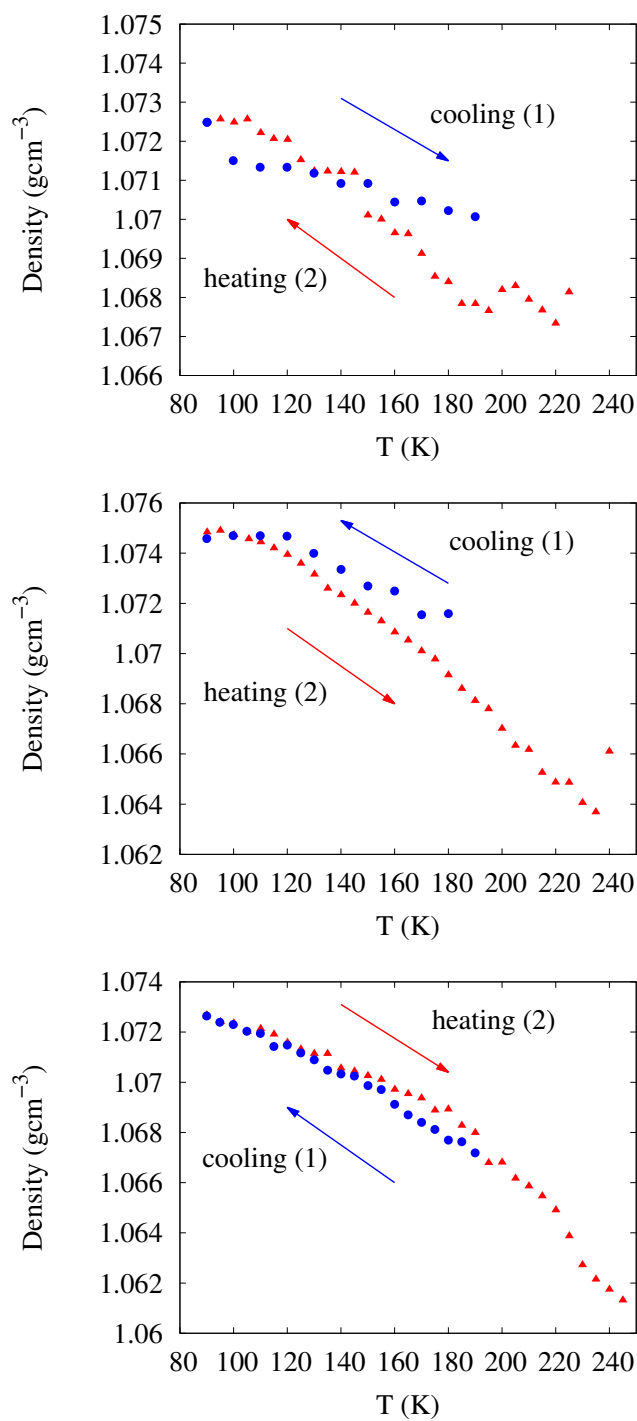


Figure 5.5: Dependence of density on temperature. From top-bottom: MS10.5 at 5 bar, MS10.5 at 10 bar and MS3.1 at 20 bar. Symbols/colours as per Fig. 5.3.

The dissociation of clathrates below the freezing point of water results in gas and water ice (Falenty et al. 2011). Some studies have found that water molecules from dissociated clathrates do not crystallise into the hexagonal ice phase, but rather the cubic phase (Kuhs et al. 2004) which is a lower temperature phase of ice stable below 160 K (Falenty et al. 2011), implying that it should be the most common form found on icy satellites. However, the implication of Fig. 5.6 is that the proportion of Ic resulting from clathrate dissociation in saline environments may in fact be very low.

Fig. 5.6 also shows that the relative composition predominantly depends on pressure and salt concentration. The MS3.1 solution at a CO₂ pressure of 20 bar is the lowest concentration and highest pressure sample and contains the highest proportion of clathrates. The other two samples have the same salt concentration but are at lower pressures (5 and 10 bar) and consequently show lower proportions of clathrate. However, in all three samples, the composition of Ic is similar and always less than 5%; this is discussed further in Section 5.4.4.

5.4 Discussion

5.4.1 Inhibiting effect of MgSO₄ on Clathrate formation

Sodium chloride (NaCl) and calcium chloride (CaCl₂) electrolyte solutions have been extensively studied as these are some of the major components of terrestrial seawater and rocks, and their inhibiting effect is well known: they decrease the dissociation temperature of clathrates by approximately 5 K in concentrations of 10% by weight of solution, and by more than 10 K close to the eutectic solution composition (17% by weight (Prieto-Ballesteros et al. 2005)). In situ studies of clathrate hydrates formed in chloride solutions are reported in Chapter 6 (Safi et al. 2018).

Prieto-Ballesteros et al. (2005) observed a decrease in the crystallisation temperature of clathrates due to the presence of magnesium. However, the inhibiting effect of the dissolved magnesium in their experiment was small, amounting to about 2 K at

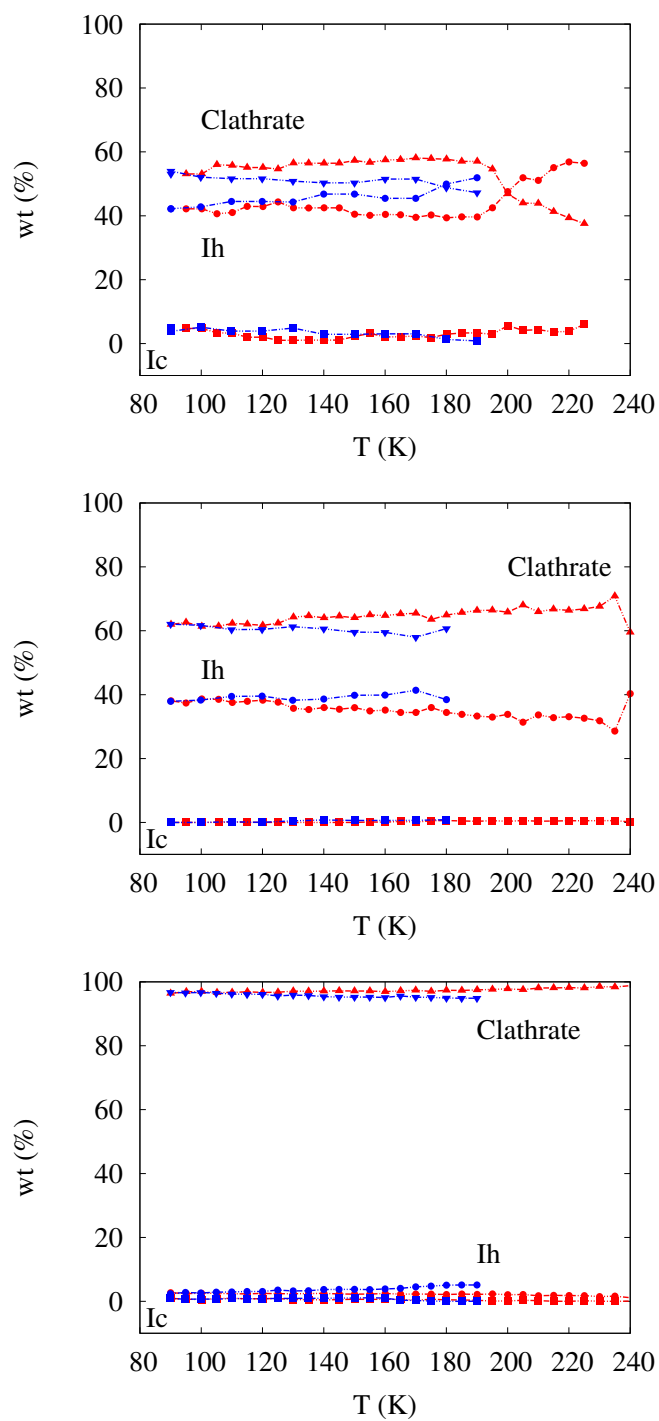


Figure 5.6: Weighted percentage (wt%) curves for solutions. From top-bottom: MS10.5 at 5 bar, MS10.5 at 10 bar and MS3.1 at 20 bar. Symbols/colours as per Fig. 5.3.

17% MgCl_2 . Also noted by Prieto-Ballesteros et al. (2005) is that the salt depresses the freezing point of water by approximately 4 K, and so a larger temperature difference between ice melting and clathrate dissociation is observed in the eutectic salt system. A similar trend was reported earlier by Kang et al. (1998) who found that, as they increased the concentration of MgCl_2 , the amount of hydrate formed at a particular pressure becomes less.

Fig. 5.6 shows that there is a larger difference in the wt% of clathrates, during both heating and cooling for the samples at a CO_2 pressure of 10 and 20 bar compared to the samples at 5 and 10 bar. This could be due to the fact that the solutions subjected to 5 and 10 bar CO_2 contain 20 g of epsomite per kg water and the solution subjected to a 20 bar CO_2 pressure contains 5 g of epsomite per kg water, i.e. the epsomite is acting as a clathrate inhibitor. This is further suggested in Fig. 5.2 where we compare our clathrate dissociation temperatures with the Arrhenius curve given by Miller (1961) which, as discussed in Section 5.3.1, shows that clathrates formed in the salt solution dissociate at lower temperatures.

5.4.2 Thermal Expansion

A surprising feature of the thermal expansion behaviour (Fig. 5.3) is the apparent hysteresis in the dependence of a on T depending on whether the sample is being cooled or heated. The variation of a with T for the MS3.1 solution at a CO_2 pressure of 20 bar is almost reversible, with little difference between the cooling and heating curves. However for the MS10.5 solution at a CO_2 pressure of 10 bar we begin to see a distinct difference between cooling and heating, while for the MS10.5 solution at a CO_2 pressure of 5 bar the difference is very noticeable. The increase in hysteresis with decreasing pressure may be due to two contributing factors:

1. clathrate stability is greater at higher pressures and therefore thermal cycling has a lesser effect;
2. when clathrates form, the amount of water present in solution decreases; the ab-

sorption and desorption of water from solution has previously been attributed to stress hysteresis (Soh et al. 2007). We suggest that, during clathrate formation, the ice-phase water molecules that form the clathrate cages might shift in position and form hydrogen bonds with liquid-phase water molecules originating from the fluid inclusions/channels rich in Mg and SO_4 ions that result from the eutectic freezing out of the pure-phase water ice. This displacement would cause adjacent water molecules from the surrounding cages to break hydrogen bonds, hence altering neighbouring cages (Shin et al. 2012). This effect should be strongest in those samples with the highest concentration of epsomite, as is indeed observed. This may also be related to our observation (see Section 5.4.4) that the clathrate structure may play a role in stabilising the Ih ice phase over the Ic phase.

Furthermore, at higher pressures the cage occupancy is higher and could result in an increase of the lattice parameters by several thousandth of an Å (Hansen et al. 2016). Indeed, Hansen et al. found that CO_2 molecules situated in the small cages expand the clathrate lattice at higher temperatures. Despite the fact that we have assumed $\theta_1 = 1$ and $\theta_2 = 0$, it is a possibility that the clathrates formed at higher pressures have a value of $\theta_2 \neq 0$ which, according to Fig 5.4, is what our experimental data are suggesting as the thermal coefficient of expansion for the samples at the higher pressure exhibit a steeper gradient.

5.4.3 Clathrate Density and Buoyancy

The variation of clathrate density with temperature (see Fig. 5.5) has implications for the sinking or rising capabilities of the clathrates in planetary oceans. According to our results the general implication is that the clathrate density is higher at lower temperatures and lower at higher temperatures, implying they have a greater probability of sinking at lower temperatures and of floating at higher temperatures. However, this will also depend on the salinity of the ocean in question.

The MS3.1 and MS10.5 solutions used in this experiment can be used to approximate the salinity of the oceans on Enceladus and Europa which have salinities of 8 and 10 g/kg H₂O respectively (Zolotov 2007; Hand & Chyba 2007). If we compare our clathrate densities at various temperatures with that of the solutions in which they were formed, we see that both the measured solution densities are much lower than the CO₂ clathrate density (i.e. 1.003 g cm⁻³ and 1.016 g cm⁻³ for MS3.1 and MS10.5 solutions respectively), irrespective of the temperature and pressure conditions, suggesting the clathrates would always sink. Indeed, this is also true if we assume θ_2 is between 0.625–0.688 (keeping $\theta_1 = 1$) which are the values Hansen et al. (2016) obtained from their experimental investigation. Therefore the sinking of clathrates is the likely scenario for both Enceladus and Europa.

For CO₂ clathrates to float in an ocean whose salinity is close to Enceladus' and Europa's they would need lower guest molecule occupancy. From Eq. (5.3 the clathrates formed in the MS3.1 solution at a CO₂ pressure of 20 bar would require the larger cages to be 73% filled, while the MS10.5 solutions at CO₂ pressures of 5 and 10 bar would need the larger cages to be 78% and 77% filled respectively (assuming $\theta_2 = 0$). As mentioned, pressure directly affects the clathrate cage occupancy in that occupancy (and hence density) is greater at increased pressure. A consequence of this would be that clathrates formed deeper in an ocean would have a higher occupancy and would therefore have a greater probability of sinking.

Our results also suggest that if CO₂ clathrates were to form at the base of a floating ice shell (e.g. Europa; Prieto-Ballesteros et al. 2005), they too should sink and transport encased gases to the bottom of the ocean floor. If, on the other hand, the ocean was of eutectic composition of MgSO₄ (17 wt%, as suggested for Europa by Prieto-Ballesteros et al. 2005), the ocean density would be 1.19 g cm⁻³, implying the CO₂ clathrates would in fact float; this would cause fracturing and gravitational collapse of the terrain due to rapid release of gas (Prieto-Ballesteros et al. 2005).

The effect of pressure on density can be seen in Fig. 5.5. If we compare both the MS10.5 solutions at CO₂ pressures of 5 and 10 bar, we see that the sample subjected to 5 bar CO₂ pressure has a lower density from 95 K to 195 K on heating. From 195 K

onwards the sample subjected to a CO₂ pressure of 10 bar produces the lowest density clathrates. However, considering the cooling curves in Fig. 5.5, the MS10.5 solution at a CO₂ pressure of 10 bar has the highest density throughout the entire cooling process. For most of the heating curves and all of the cooling curves in Fig. 5.5 our results are consistent with the conclusion that higher pressure environments produce clathrates with higher densities and which are therefore less buoyant.

5.4.4 The nature of the ice

Ic is the most common polymorph of ice at temperatures below 160 K; therefore investigation into the nature of the ice phase that coexists with clathrates is especially significant in the context of cold extra-terrestrial environments as it would impact on the interpretation of remotely sensed data and our understanding of the physical processing and conditions in these environments (Falenty et al. 2011). Above 240 K water crystallises into the thermodynamically favoured Ih phase, the rate of change of Ih to Ic being highest between 200 K – 190 K, while below ~ 160 K Ic is the stable phase (Falenty et al. 2011).

Despite being thermodynamically favourable at low temperature, our data show that the wt% of Ic is never more than about 5%, even at 90 K (see Fig. 5.6) and it may be that the clathrate structure preferentially stabilises the Ih phase over the Ic phase. However, it is also possible that, at low temperatures, the rate of transformation is slow and, given sufficient time, all of the Ih would eventually transform to Ic.

5.5 Conclusion

By the use of in situ synchrotron X-ray powder diffraction we have studied the formation, dissociation and thermal expansion properties of CO₂ clathrate hydrates formed in MgSO₄ salt solutions at salinities, temperatures and pressures representative of the likely conditions on icy moons such as Europa and Encelladus. Specifically, we have:

1. found the dissociation temperatures and pressures of CO₂ clathrate hydrates formed in a salt solution containing epsomite (MgSO₄·7H₂O) and that the salt solution inhibits clathrate formation.
2. computed the density of these clathrates at different temperatures and pressures and compared this to the density of the solution in which they were formed. While it was found that the density of the clathrate depends on temperature and pressure (and hence local factors such as seasonal and tidal changes), when compared to the density of the salt solution they formed in they should in general sink, irrespective of the temperature and pressure.
3. investigated the polymorphs of the associated ice phases. We report the dominance of Ih throughout the experiment despite the expectation of Ic being the thermodynamically stable polymorph at lower temperatures. This may be due to the salt solution inhibiting the Ih to Ic transformation, however further investigation into the thermodynamics and kinetics of ice in relation to clathrates is needed to confirm this.

These experimental observations demonstrate the importance of understanding the role played by salts, clathrates and ice on the surface geology and sub-surface oceans of icy Solar System bodies. As a gas transport mechanism the likely sinking of CO₂ clathrates formed in saline environments could make a significant contribution to ocean floor geochemistry on such objects.

6 Effects of ice polymorphs and chloride salts on clathrate hydrate evolution in the Martian cryosphere

This chapter presents results of an investigation focussed on forming CO₂ clathrates in the presence of chloride salt solutions and the effect that these solutions have on their dissociation and formation temperatures. Results are also presented on the effect that ice polymorphs have on the dissociation of clathrates. This work has been submitted for publication (Safi et al. 2018).

6.1 Introduction

A number of different experimental methods have been used to study the formation of hydrates at temperatures below the freezing point of water (Kawamura et al. 2002; Kuhs et al. 2006; Ambuehl & Elwood Madden 2014). These studies have shown that clathrates form in two stages. The first is a nucleation stage, in which gas and ice react at the surface of an ice particle and clathrate cages form rapidly. Here the ice particle size controls the rate of formation of the hydrate layer that subsequently surrounds the ice particle (Ambuehl & Elwood Madden 2014). The second stage is much slower and involves gas and/or water diffusing through the clathrate shell (Kawamura et al. 2002). While this is the generally accepted mechanism of clathrate formation, there are other influencing factors which are not well understood. For example, the so-called “memory effect”, whereby water which has either been previously frozen, or formed clathrates, seems to form clathrates more readily upon refreezing, increasing the rate of production (Takeya et al. 2006). In addition, since most studies relate to clathrate formation in pure water/ice, the effect that impurities, such as dissolved salts, have on both clathrate formation and subsequent behaviour is not fully understood.

We reported (Safi et al. 2017) on the formation of CO₂ clathrate in the presence

Table 6.1: Concentration, temperature range and pressure of the salt solutions used in this work. Concentrations were chosen to match those found by landers and rovers on the Martian surface (Gough et al. 2016).

Salt	Concentration g /kg H ₂ O	Temperature range (± 5) (K)	Pressure (bar)
MgCl ₂	2	90 – 242	10.0 \pm 0.1
CaCl ₂	10	90 – 193	10.0 \pm 0.1
CaCl ₂	10	200 – 268	20.0 \pm 0.1
NaCl	6	169 – 250	10.0 \pm 0.1

of MgSO₄, finding that the dissociation temperatures and pressures of CO₂ clathrate are depressed. We also found that clathrates would likely sink in oceans similar to those found on Enceladus and Europa. Furthermore we reported the dominance of hexagonal ice (Ih) throughout the experiment, despite the expectation of cubic ice (Ic) being the thermodynamically stable polymorph at lower temperatures. In this chapter we consider the effects that chlorides can have on both the ice and clathrate phases, and discuss our results within the context of the Martian cryosphere.

6.2 Experimental work

In this work aqueous solutions of MgCl₂, CaCl₂ and NaCl were used to form the ice and CO₂ clathrate hydrate system. The concentrations, temperature range and pressures used are summarised in Table 6.1. The salt concentrations used are the lower, mid and upper values detected by landers and rovers in all locations on the Martian surface (Gough et al. 2016). The temperatures used in this experiment include the range found at Mars’ polar ice caps (Falenty et al. 2011). The pressures used are representative of clathrates forming on, or very close to, the Martian surface.

In the experimental data reported below, we refer to an individual set of data showing either heating or cooling as a “run”; and “cycle” is used to refer to a set of

data that has undergone both heating and cooling successively. SXRPD data were collected using the fast position sensitive detector on beamline I11 at the Diamond Light Source (Thompson et al. 2009; Thompson et al. 2011), during nine 8-hour shifts. The incident X-ray wavelength was 0.825654 Å, calibrated against NIST SRM640c standard Si powder.

A high pressure gas cell was used to create the clathrates, details of which can be found in Day et al. (2015) along with the procedures used to form the clathrates, while information on the cycling techniques can be found in Safi et al. (2017) and Section 5.2. In short, an 0.8 mm diameter sapphire capillary was filled with the salt solution and loaded onto the gas cell which is subsequently loaded onto I11's diffractometer. Cooling is done using a liquid nitrogen cryostream with a temperature stability ± 0.1 K and a ramp rate of 360 K/h. Once the solution has frozen at ~ 240 K, CO₂ gas is admitted to the cell at 10 bar and the PSD is used to collect in situ SXRPD data as the temperature is decreased. Once ice and clathrate formation is observed the temperature is increased until the clathrate/ice peaks are lost. At this point the cell is cooled once more. This "second cycle" technique provides increased clathrate formation (see discussion in Day et al. (2015) and experimental section in Safi et al. (2017)). For the present work we then cycled the temperature between 250 K and 90 K. Dissociation temperatures were determined as per Section 5.2. Each SXRPD data-collection cycle, including the time allowed for the sample to come to equilibrium at each temperature step, took approximately 20 min.

The SXRPD patterns were analysed via Pawley whole structure refinement, using TOPAS refinement software (Coelho 2007). From the refinements the percentage of each phase present was determined at each temperature step during cycling, allowing the formation and dissociation temperatures of clathrates, Ih and Ic to be established.

6.3 Results

A typical example of a refinement is shown in Fig. 6.1 which shows a comparison of the SXRPD patterns for clathrates, Ih and Ic formed in the CaCl_2 salt solution at a CO_2 pressure of 10 bar. We found previously (Safi et al. 2017) that Ic also forms when forming clathrates in the presence of MgSO_4 salt solutions, despite being thermodynamically unfavourable. The presence of the clathrates at 90 K and 180 K is evident from the formation of multiple features at the 2θ positions stated in Section 5.3. The initial lattice parameters of clathrate, Ih and Ic are as stated in Section 5.3, as are the space groups. Excluding ice peaks from the refinement, the values for the weighted profile R_{wp} and background-corrected weighted profile R'_{wp} fitting agreement parameters between the calculated and experimental diffraction data for clathrate structures formed at 90 K and 180 K (see McCusker et al. 1999, for further details) were $R_{\text{wp}} = 6.07\%$ and 4.01% and $R'_{\text{wp}} = 21.70\%$ and 19.86% respectively.

6.3.1 Weight percentage of clathrate, Ih and Ic ice

From the relative contribution of each phase to the overall scattered intensity in the SXRPD pattern we can obtain the relative fraction by weight of each crystalline component present in the sample under study. These are shown in Figs 6.2, 6.3 and 6.4 as a function of temperature for the 10 g CaCl_2 solution at 10 and 20 bar CO_2 , the 2 g MgCl_2 solution at 10 bar CO_2 , and the 6 g NaCl solution at 10 bar CO_2 respectively and discussed in turn below.

6.3.1.1 10 g CaCl_2 solution at 10 and 20 bar CO_2

The 10 g CaCl_2 solution in Fig. 6.2 was thermally cycled two and a half times, with data analysis starting at ~ 175 K, beginning with heating (the first set of cooling data could not be used due to ice forming on the outside of the cell as a result of slight misalignment, which was corrected at the base temperature). Fig. 6.2 shows that, in

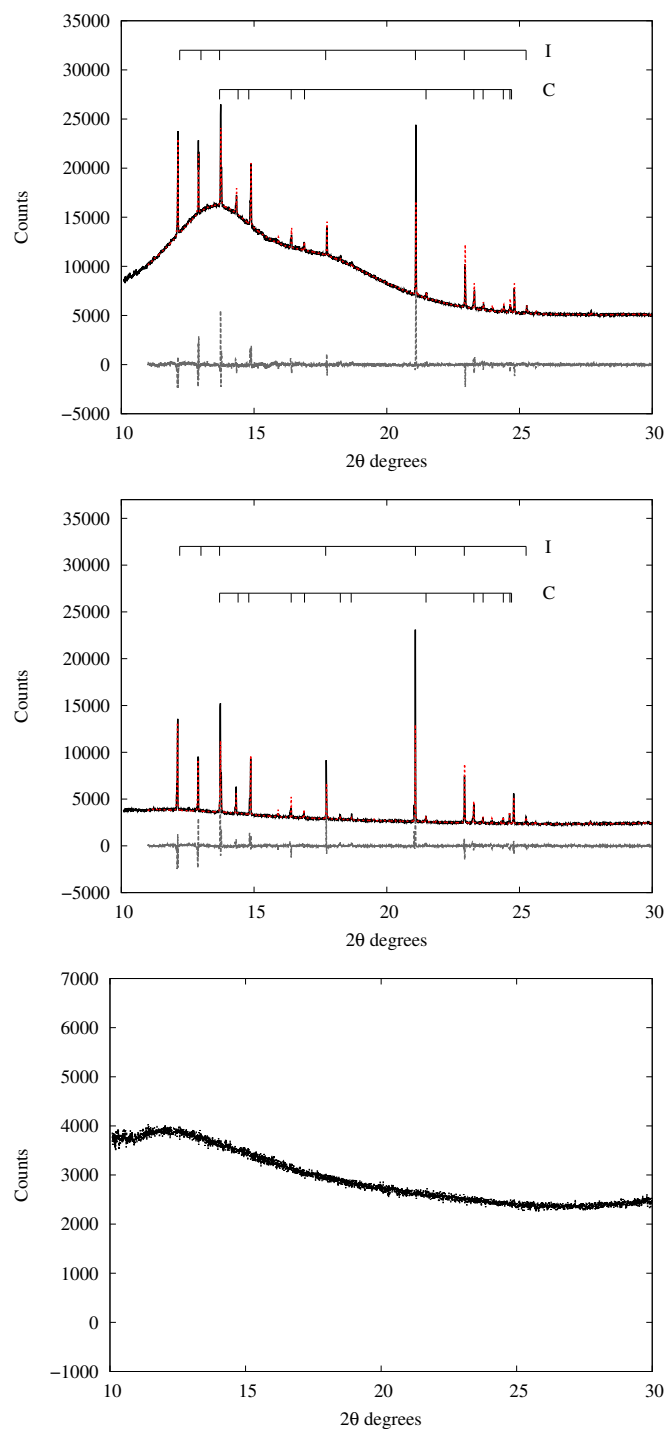


Figure 6.1: Pawley whole pattern refinements of the CaCl_2 solution at 10 bar CO_2 pressure experimental data. From top to bottom: 90 K, 180 K, 290 K. The experimental data are shown in black, the calculated fit in red, and the residuals in grey below. All dominant peaks are labelled where C = clathrate peaks and I = ice peaks. The larger residuals for some of the ice peaks are due to poor powder averaging based on the way the ice freezes inside the cell (preferred orientation) and the restricted cell rocking angle used to compensate for this during measurement.

the first cycle during heating, the percentage of clathrate present began at 0%, with the dominant phase being Ih. As the temperature increased the percentage of clathrate increased, while Ih decreased. At the end of heating in this cycle the relative fractions by weight of clathrate, Ih and Ic were approximately 40%, 55% and 5% respectively. During the subsequent cooling phase in cycle one and all of cycle two this percentage varied, with the percentage of Ih fluctuating between 40–75% and clathrate between 20–60%; the amount of Ic, after heating in the first cycle, essentially remained at 0%.

On heating in the third cycle, the relative fraction of each crystalline component continued to follow the same trend; however after reaching ~ 200 K the percentage of clathrate rapidly rose to 100% when 20 bar CO_2 pressure was applied, while Ih simultaneously decreased to 0%; during this time the percentage of Ic peaked at approximately 10%. This behaviour could not be investigated further due to the end of the beamtime allocation.

6.3.1.2 2 g MgCl_2 solution at 10 bar CO_2

Fig. 6.3 shows the relative fraction by weight of each component formed in the presence of the 2 g MgCl_2 solution. This solution started cooling at ~ 220 K and underwent two cycles, where clathrates were initially the dominant phase and continued to increase. Once ~ 180 K was reached Ih became the dominant phase. During this cooling process, the fraction of Ic remained close to zero. Heating in the first cycle showed that Ih continued to dominate with a wt% of $\sim 60\%$, while clathrate remained at $\sim 40\%$; again the fraction of Ic was negligible. This continued until approximately 230 K, where the fraction of Ih and clathrate were comparable.

During the second cycle of cooling, clathrate once again was the dominant phase, with a weight percent of 100%. This remained the case until the temperature reached ~ 180 K, at which point the fraction of clathrate decreased significantly, to $\sim 20\%$, while the fraction of Ih and Ic each increased to approximately 40%. This relative fraction by weight for each crystalline component remained the same during heating in cycle two.

6.3.1.3 6 g NaCl solution at 10 bar CO₂

Fig. 6.4 shows the relative fraction by weight of each crystalline component formed in the presence of the NaCl solution. This solution also underwent two cycles, beginning with cooling where the only crystalline phase present was clathrate. This continued to be the case down to approximately 170 K. Clathrates also remained the only crystalline phase during heating in the first cycle up to approximately 240 K where they dissociated.

During the second cycle of cooling Ih was the dominant crystalline phase, with a wt% of $\sim 80\%$, while clathrates were present with a wt% of $\sim 20\%$. As the temperature cooled to ~ 170 K Ih decreased to $\sim 70\%$, while clathrate increased to $\sim 30\%$. During heating in the second cycle Ih decreased even further to $\sim 60\%$ and clathrate increased to $\sim 40\%$. At approximately 230 K the weight percent of clathrate rapidly increased to $\sim 80\%$, while Ih decreased to $\sim 20\%$. During both cycles using NaCl as the salt solution we observed no Ic.

6.4 Discussion

6.4.1 The role of ice polymorphs

It is known that the polymorph of ice formed on the surface of a decaying clathrate provides different diffusion pathways for the gas molecule escaping the clathrate cages (Falenty et al. 2011). Ic provides an easier diffusion pathway due to the presence of a large number of grain boundaries and defective zones, hence promoting clathrate dissociation. Ih however, provides a more challenging route and, because it is the thermodynamically more stable phase, Ih inhibits clathrate dissociation (Falenty et al. 2011).

This phenomenon can be seen in Figs 6.2, 6.3 and 6.4. During the first run using CaCl₂ solution, there is a peak in the wt% of Ic at approximately 170 K; the wt% of Ic subsequently begins to decrease as the solution is heated. At ~ 170 K the

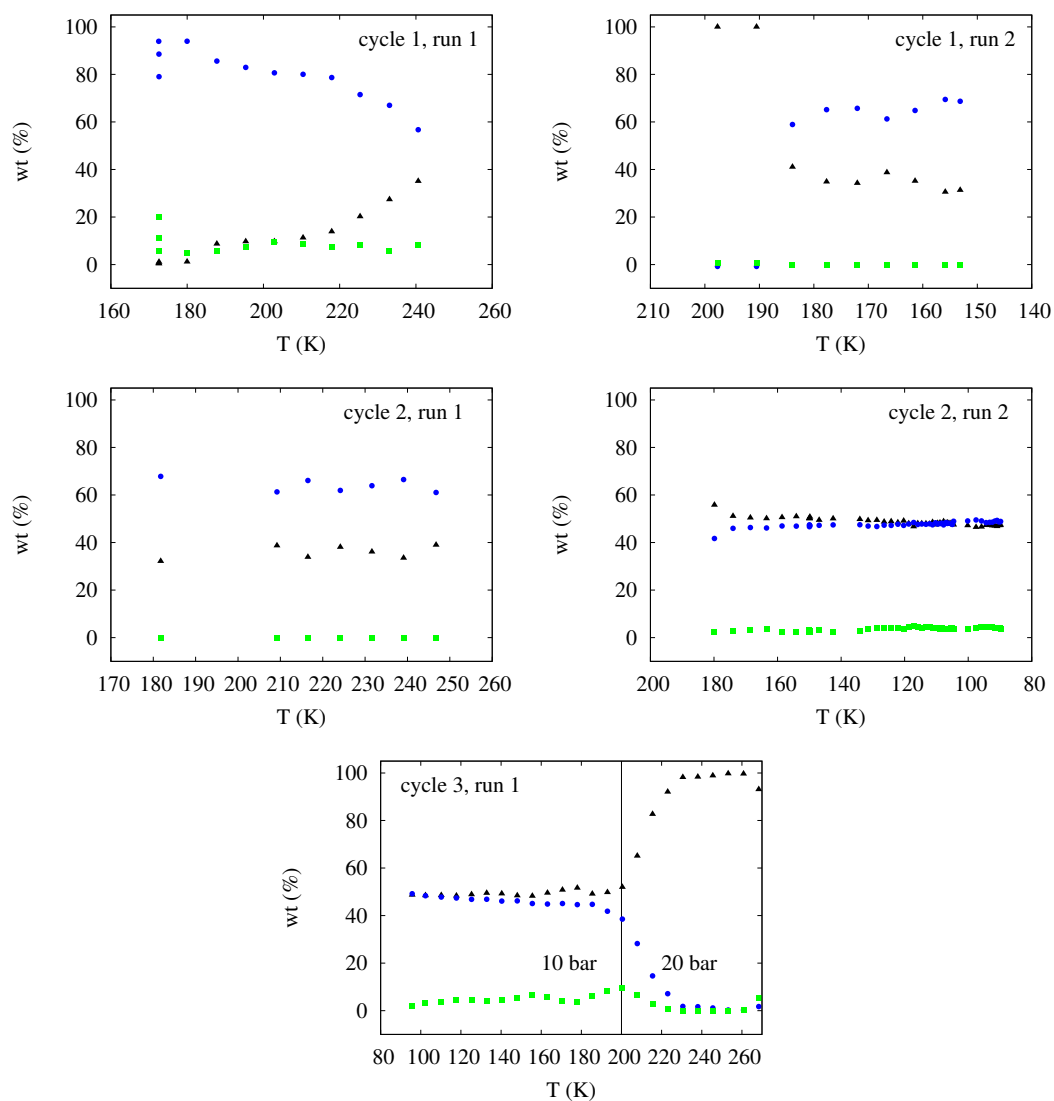


Figure 6.2: wt% for clathrates formed in the presence of 10 g CaCl₂ solution at 10 and 20 bar CO₂ pressure. The black line represents the transitions from 10 to 20 bar CO₂ pressure. Black triangles: clathrates; blue circles: Ih ice; green squares: Ic ice. See text for details.

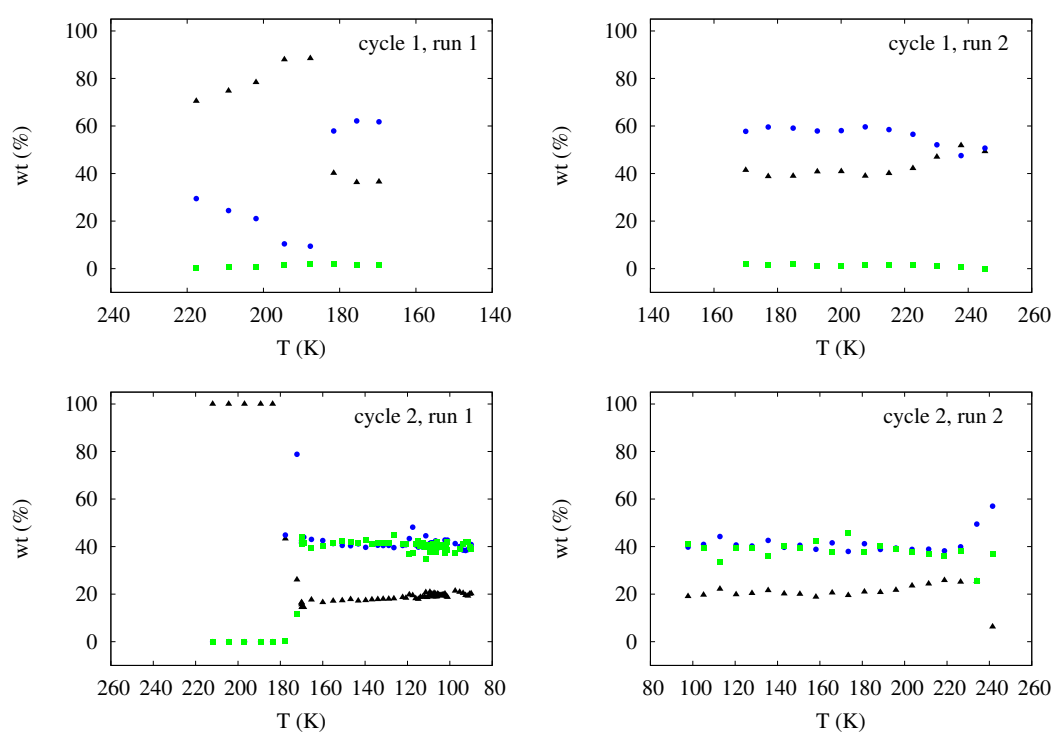


Figure 6.3: wt% for clathrates formed in the presence of 2 g MgCl_2 solution at 10 bar CO_2 pressure. Symbols/colours as per Figs 6.2. See text for details.

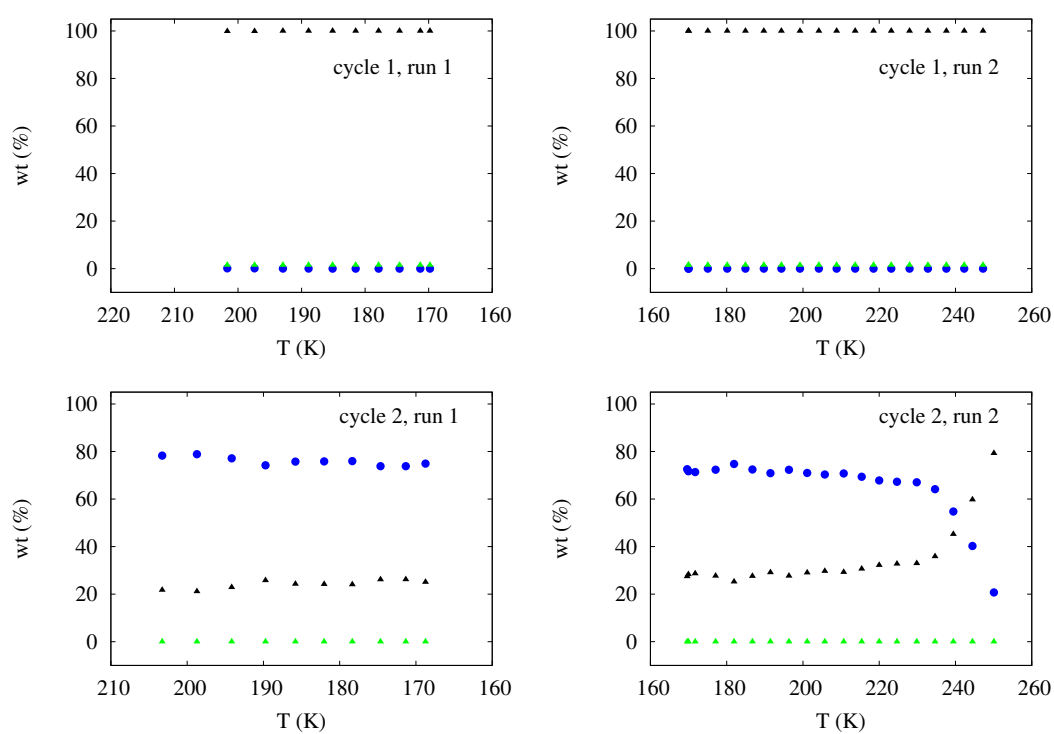


Figure 6.4: wt% for clathrates formed in the presence of 6 g NaCl solution at 10 bar CO₂ pressure. Symbols/colours as per Figs 6.2. See text for details.

amount of clathrate increases; this could be a consequence of the decrease in Ic and hence the removal of the easier pathway for clathrate dissociation as the solution is heated. For the remainder of the CaCl₂ run, the wt% of clathrate remains stable as the wt% of Ic is negligible. During the last run there is a significant increase in the wt% of clathrates which can be attributed to raising the CO₂ pressure to 20 bar. Clathrates are more stable at higher pressures (Sloan & Koh 2007) and raising the pressure by an additional 10 bar in the final run should cause an increase in the wt% of clathrates produced independent of the ice phases present.

The behaviour of the MgCl₂ solution can also be attributed to the presence of Ic and its ability to provide an easier pathway for clathrate dissociation. Interestingly, 170 K is ~10 K above the temperature of Ic formation (Falenty et al. 2011). This could imply that the presence of a salt in the solution affects the formation behaviour of the ice polymorphs. Mg has a larger inhibiting effect on ice and clathrate compared to Ca (Makogon 1997). Also, the best electrolyte inhibitors of ice/clathrate exhibit maximum charge and minimum radius. In this case due to both Mg and Ca ions having the same charge, it is likely to be the smaller size of the Mg which would cause it to have a larger inhibiting effect. The smaller ionic size increases the surface charge density, attracting more water molecules, therefore resulting in a decrease of water activity (Sabil 2009).

Similarly, where there is negligible wt% of Ic present, Fig. 6.4 shows that, during the experimental run using NaCl as the saline solution, the wt% of clathrate does not increase; it is either the dominant phase throughout the entire cycle (as seen in the first cycle) or is the dominant phase at the end of the cycle (as seen at the end of heating in the second cycle).

However, it is also possible the Ih and Ic formed during the experiment are in fact part of a single phase, ice I. It has been noted that the metastable form of ice I can be made through the decomposition of clathrate hydrates (Malkin et al. 2015). Ice I is thought to be composed of a combination of cubic and hexagonal stacking sequences and have a trigonal space group P3m1 (Malkin et al. 2015). Indeed, to the best of our knowledge, no experimentally obtained Ic reported in the literature produces a diffraction pattern that is fully representative of the theoretical Fd3m Ic

structure (Dowell et al. 1962; Mayer & Hallbrucker 1987; Kohl et al. 2000; Moore & Molinero 2011). This, unfortunately, means that any diffraction analysis of Ic would be limited by current methods (e.g. Rietveld profile analysis; Hansen et al. 2008) due to the presence of the hexagonal stacking faults (Murray & Bertram 2005). It is possible, therefore, that during our clathrate dissociation experiments, the ice phase is better described by ice I, which embodies certain aspects of both Ic and Ih. Hence our attempts to identify Ic at 160 K and below were unsuccessful and could explain why we were seemingly obtaining Ic at an increased freezing point of 170 K. Additionally, we employed a fast cooling ramp rate of 360K/hour during our experiment such that, potentially, separate Ic and Ih phases may not have been able to form, but rather the formation of a hybrid ice I phase was driven by the kinematics of fast cooling. Additionally, the ratio of Ih and Ic aspects in ice I may vary with temperature; this could explain the observation of Ic at approximately 170 K during our experiment.

From our current data, we are unable to distinguish between the two hypotheses for the nature and behaviour of ice in the presence of clathrates and salts, but our results suggest that the ice I phase could be the dominant ice phase whenever clathrates are formed in the presence of chlorides, hence leading to the conclusion that ice I could be the most dominant phase of ice present in the Martian cryosphere. Further work may offer the prospect of determining a suitable observational diagnostic, either remotely, or for data gathering by landers and rovers.

6.4.2 Implications for the Martian cryosphere

The temperature of the Martian polar and sub-polar surface ranges from 167.7–185 K (Falenty et al. 2011). These temperatures represent the transformation region in the H₂O phase diagram of Ic to Ih. It is thought both CaCl₂ and MgCl₂ (as well as Ca- and Mg- sulphates), along with sodium salts, are present in the Martian polar regions (Knauth & Burt 2002; Burt & Knauth 2003; Mousis et al. 2013). There is some debate as to whether calcium or sodium is the more dominant salt on the Martian surface, dependent on whether the salts are chlorides or sulphates. It has been noted

that the most stable sulphates on Mars are calcium and magnesium; however due to the fact that the atmosphere is CO₂-dominated, these salts would both be removed as insoluble carbonates (Knauth & Burt 2002). This leads to the conclusion that NaCl should be the major soluble salt present in the Martian brines exposed to the atmosphere (Knauth & Burt 2002). However, Burt & Knauth (2003) also state that the Martian regolith is basaltic in addition to being significantly reactive. Therefore basalt-brine reactions would have enriched the brine in calcium, with lesser amounts of sodium and magnesium once the brine is isolated from the atmosphere. This implies that partial melting and fractional crystallisation processes could lead to near-surface brines becoming eutectic and highly enriched in CaCl₂.

We have used the minimum concentration of chlorine ($\sim 0.2\%$, Gough et al. (2016)) thought to be present on Mars for our MgCl₂ solution, as this is one of the salts that is present to a lesser extent. Similarly, we have used the maximum concentration of chlorine ($\sim 1\%$, (Gough et al. 2016)) thought to be present on Mars for our CaCl₂ solution, due to its possible dominance on the Martian surface and we have used an intermediate concentration of chlorine ($\sim 0.6\%$, (Gough et al. 2016)) thought to be present on the Martian surface for our NaCl solution. Magnesium is the stronger inhibitor of ice and clathrate, yet we get a large wt% of Ic (and therefore a smaller wt% clathrate) during our cycles using this as the salt solution. Conversely, when using the weaker inhibitor CaCl₂ we obtain a smaller wt% of Ic and a larger wt% of clathrate. As discussed in the previous section, it seems that the type of salt present in the cryosphere of Mars is an influential factor when it comes to the polymorphs of ice formed and consequently on the formation of clathrate hydrates.

It could also be the case that chloride salts are not homogeneously distributed on the Martian surface. This could mean clathrates in one region could dissociate whilst remaining intact in another. Clathrate dissociation has been suggested as the mechanism behind the formation of seasonal methane plumes observed in various regions of Mars (Mumma et al. 2009). The plumes were observed in three regions over the Northern hemisphere; east of the Arabia Terra, the Nili Fossae region and in the south-east quadrant of the Syrtis Major. Each of these areas show evidence of ancient

ground ice or flowing water. The plumes were seen during the Martian summer and spring, suggesting the permafrost vaporises allowing the methane to escape into the atmosphere. Indeed, these plumes may be caused by the dissociation of clathrates as they encounter higher temperatures and lower pressures.

In our experiment we cycle the clathrates between approximately 90–270 K. The cycles do not allow us to draw a definitive conclusion on the effect thermal cycling has on the evolution of clathrates. Cycles performed using the CaCl_2 and NaCl salt solutions indicate repeated cycling may aid in clathrate formation. However, our results also seem to show that thermal cycling is detrimental for clathrates formation in the presence of MgCl_2 .

6.5 Conclusions

By the use of in situ SXRPD we have studied the effect that different polymorphs of ice have on the formation of clathrate hydrates in the presence of aqueous chloride solutions. Specifically, we have:

1. shown, for the first time, that clathrate hydrates can form in the cryosphere of Mars despite the presence of salts;
2. hypothesised that, during the formation of clathrates in our saline solutions, we could be forming ice I, which embodies structural aspects of both Ih and Ic as opposed to pure phase Ic. This would account for the negligible wt% of Ic even at temperatures of ~ 90 K where it should be the more stable form of ice. Also, we have observed features consistent with Ic at 170 K but have suggested that this could be due to the ratio of Ih and Ic aspects in ice I varying with temperature;
3. suggested that due to its possible stability during clathrate formation, ice I could be the dominant phase of ice within the Martian cryosphere
4. shown that despite the presence of saline solutions, a low-temperature phase

of ice does form in some cycles and its presence seems to provide an easier diffusion pathway for clathrate dissociation;

5. found that the types of salts used (and their inhibiting effect) seems to have a more significant impact on the ice formed and therefore clathrate formation than the concentration of the salt used.

These experimental observations demonstrate the importance of the role played by salts and, although we have focussed on the chloride concentrations typical for Mars, our results may be applicable to other Solar System bodies. Ligier et al. (2016), for example, have suggested that the salts present on the surface of Europa are possibly Mg-chlorides rather than Mg-sulphates. Future experiments focusing on the formation of clathrates and their interaction with various polymorphs of ice in the presence of salt solutions will be of fundamental importance to our understanding of planetary environments.

7 Does clathrate dissociation replenish Titan's atmospheric methane?

7.1 Introduction

In some of the earlier studies of the Titan environment, the focus was on the thermodynamic equilibrium of methane with reservoirs composed of mixtures of methane and ethane (Lunine et al. 1983). However, this global ocean hypothesis has been ruled out by ground-based radar and infrared observations of Titan's surface (Coustenis et al. 1995). From the Cassini spacecraft (Stofan et al. 2007) and the Huygens probe (Tomasko et al. 2005), it has been shown that there are in fact no extensive liquid hydrocarbon bodies, the lakes of the North and South Polar Regions being an exception.

Fortes et al. (2007) proposed an internal structure for Titan, shown in Fig. 7.1. They hypothesise that the rocky core consists of aqueous ammonium sulphate (Layer 1 in Fig. 7.1) along with a crust that is composed primarily of methane clathrate with small amounts of ice I, thought to be a mixture of hexagonal (Ih) and cubic (Ic) ice (Murray & Bertram 2005) (see Fig. 2.7 for details on the various phases of ice), and ammonium sulphate (Layer 4 in Fig. 7.1). An ocean consisting of aqueous ammonium sulphate has a freezing temperature of approximately 250 K which, compared to one composed of a mixture of water and ammonia, is significantly warmer (Layer 3 in Fig. 7.1).

However the current state of knowledge on the possibility of a warm sulphate-rich ocean on Titan is limited. Grindrod et al. (2008) model the thermal evolution of a sub-surface ocean consisting of aqueous ammonium sulphate. In all the models that they examined the ocean temperature did not fall below the high pressure eutectic in the binary $(\text{NH}_4)_2\text{SO}_4\text{-H}_2\text{O}$ system. Therefore they deduced that the only crystallisation product of this system would be ice and, as more ice is crystallised, the concentration of ammonium sulphate in the ocean would increase. This would lead to an increase in

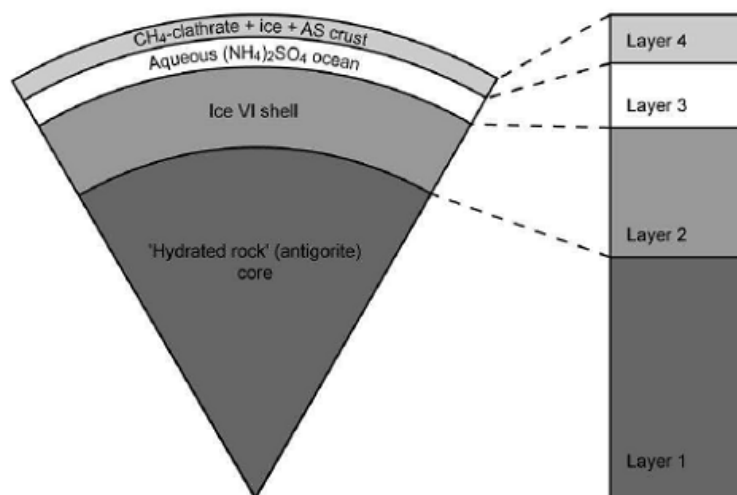


Figure 7.1: The internal structure of Titan, after Fortes et al. (2007). “AS” in the crust (Layer 4) is ammonium sulphate.

the density and viscosity of the ocean, which would need to be taken into consideration with any future study of sub-surface oceans on Titan. Finally, Grindrod et al. (2008) conclude that it is possible for a sub-surface ocean of ammonium sulphate to remain a liquid up until the present day.

Due to the high pressures (up to 1.25 GPa at the base of the ice VI shell, Layer 2 in Fig. 7.1) and low temperatures (down to 100 K) (Fortes et al. 2007) present on Titan, it is thought that a number of phases of H₂O are present and, due to their varying densities, are separated into different layers: the low pressure phase Ih, liquid water and high pressure polymorphs of ice V and ice VI (Choukroun et al. 2010). It is thought that the concentration of primordial ammonia on the icy fraction of the planetesimals that formed Titan is likely to be no more than 5 wt%, which is enough to still affect the internal structure and thermal profiles significantly.

Table 7.1: Concentration, temperature range and pressure of the salt solutions used in this work.

Salt	Concentration g /kg H ₂ O	Temperature range (K)	Pressure (bar)	Density (gcm ⁻³)
(NH ₄) ₂ SO ₄	100	90 – 270	26.0 ± 0.1	1.055
(NH ₄) ₂ SO ₄	150	90 – 270	26.0 ± 0.1	1.076

7.2 Experimental work

In this work an aqueous solution of (NH₄)₂SO₄ was used to form the ice and CH₄ clathrate hydrate system. The concentrations, temperature range and pressures used are summarised in Table 7.1. The salt concentrations used are those predicted by Fortes et al. (2007). For the first salt concentration used in our experiment, Fortes et al. (2007) considered a magma composition with a density equal to the bulk density of their model crust (1065 kgm³), which corresponds to a composition of 10.6 wt% (NH₄)₂SO₄. The second salt concentration used is based on the underlying liquid layer, which Fortes et al. (2007) suggests consists of a weak solution of ammonium sulphate (15 wt%). The pressure used is derived from the bulk density of the model crust (Fortes et al. 2007).

SXRPD data were collected as per in Chapters 5 and 6 during nine 8-hour shifts with an incident X-ray wavelength of 0.825905 Å. To summarise, a single-crystal sapphire capillary of diameter 0.8 mm was filled with the (NH₄)₂SO₄ solution. This is then mounted onto the beamline’s diffractometer, and cooled using a liquid nitrogen cryostream which has a temperature stability ±0.1 K and a ramp rate of 360 K/h. Once the solution has frozen at ~240 K, CH₄ gas is admitted to the cell at 1 bar and gradually increased to 26 bar in order to test for CH₄ gas leaks. The PSD is used to collect the in situ data as the temperature is decreased and subsequently increased. During this time ice and clathrate formation and dissociation is observed respectively. The temperature ramp is then reversed and the cell is cooled once more. This tech-

nique provides increased clathrate formation (see discussion in Day et al. (2015) and experimental section in Chapters 5 and 6). For the present the temperature is cycled between 270 K and 90 K. Dissociation temperatures were determined by holding the sample at constant pressure and gradually increasing the temperature in 2 K temperature steps until there were no peaks discernible in the X-ray diffraction pattern. Each SXRPD data-collection cycle together with equilibrium time at each temperature step, took approximately 20 min.

The SXRPD patterns were analysed via Pawley whole pattern refinement, using TOPAS refinement software (Coelho 2007). From the refinements the percentage of each phase present was determined at each temperature step during cycling, allowing the formation and dissociation temperatures of clathrates, Ih and Ic to be established.

7.3 Results

A typical example of a refinement is shown in Fig. 7.2 which shows a comparison of the SXRPD patterns for clathrates, Ih, Ic and $(\text{NH}_4)_2\text{SO}_4$ formed in the 15 wt% salt solution at a CH_4 pressure of 26 bar. The presence of the clathrates can be confirmed by the appearance of peaks in the 2θ positions (see Section 5.2) at 90 K and 170 K. During fitting, the lattice parameters of clathrate, Ih and Ic were as stated in Section 5.2, and for $(\text{NH}_4)_2\text{SO}_4$ they were initially set to 5.951 Å, 10.56 Å, and 7.729 Å for the a , b and c axes respectively. The space groups of sI clathrate, Ih and Ic are as stated in Section 5.2, and for $(\text{NH}_4)_2\text{SO}_4$ is Pmcn. Excluding ice peaks from the refinement, the values for R_{wp} and R'_{wp} (McCusker et al. 1999) fitting agreement parameters between the calculated and experimental diffraction data for clathrate structures formed at 90 K and 170 K were $R_{\text{wp}} = 6.92\%$ and 6.98% and $R'_{\text{wp}} = 18.66\%$ and 17.56% respectively. The associated error in the lattice parameter was typically ± 0.001 Å, leading to a typical error in the density measurements of ± 0.0001 gcm⁻³. The bulk densities of the initial $(\text{NH}_4)_2\text{SO}_4$ solutions were measured at room temperature as per Section 5.2. The solution densities are shown in Table. 7.1.

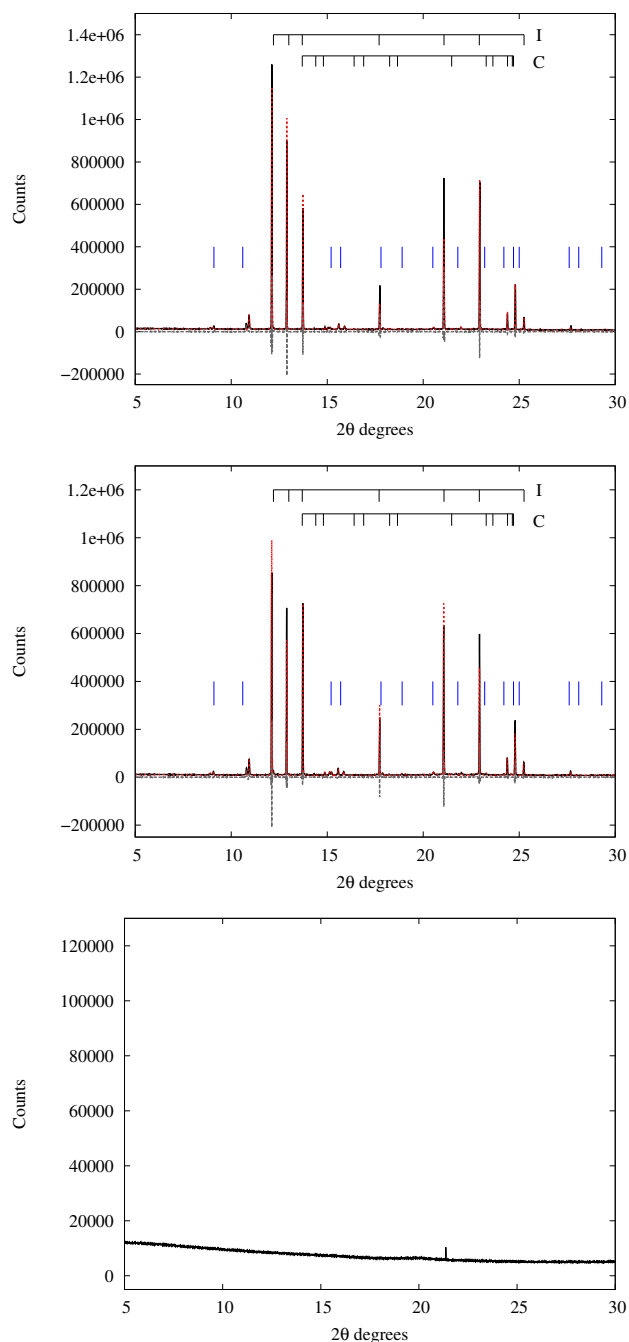


Figure 7.2: Pawley whole pattern refinements of the experimental data for 15 wt% ammonium sulphate solution at a 26 bar CH_4 pressure. From top-bottom: 90 K, 170 K, 270 K. The experimental data are shown in black, the calculated fit in red, and the residuals in grey below. All prominent peaks are labelled where C = clathrate peaks and I = hexagonal ice peaks; blue vertical bars are $(\text{NH}_4)_2\text{SO}_4$ peaks. The larger residuals for some of the ice peaks are due to poor powder averaging due to the way the ice freezes inside the cell (preferred orientation) and the restricted cell rocking angle used to compensate for this during measurement. The error bars in these plots are smaller than the plotted points.

7.3.1 Thermal expansion

As mentioned in Section 5.3.2, the thermal expansion is a property of materials which enables us to understand their physical behaviour. Therefore it is important for us to understand the thermal behaviour of clathrates if we are to better understand their behaviour in extreme environments, such as the sub-surface ocean on Titan.

Figs. 7.3 and 7.4 show the temperature dependence of the lattice parameters of clathrates formed in the presence of the 10 wt% and 15 wt% ammonium sulphate solutions respectively. There is a notable difference in the lattice parameters between heating and cooling in terms of the behaviour of the temperature dependency. To describe the expansion/contraction behaviour of clathrates during heating and cooling (except for the first cycle in Fig. 7.4, which exhibits neither linear nor quadratic behaviour) we have used the function:

$$a = a_0 + a_1 T + a_2 T^2. \quad (7.1)$$

Tables 7.2 and 7.3 give the values of the coefficients a_0 , a_1 , and a_2 obtained by fitting Eq.(7.1) to the data for heating and cooling respectively.

Table 7.2: Polynomial coefficients of the polynomial expression describing lattice parameters of CH₄ clathrates formed in 10 and 15 wt% ammonium sulphate solutions during heating.

Solution	Cycle	$a_0(\text{Å})$	$a_1(10^{-5}\text{ÅK}^{-1})$	$a_2(10^{-6}\text{ÅK}^{-2})$
10 wt% (NH ₄) ₂ SO ₄	1	11.9692 ±0.0229	-77.4107 ±26.4100	3.1745 ±0.7168
	2	11.8868 ±0.0036	26.6259 ±2.2440	- -
	3	11.9307 ±0.0038	-38.5044 ±5.1480	2.0114 ±0.1693
15 wt% (NH ₄) ₂ SO ₄	1	12.0116 ±0.0288	-131.4840 ±52.9000	9.4551 ±30.7200
	2	11.9631 ±0.0128	-62.2747 ±14.8800	2.6161 ±0.4082

Table 7.3: Polynomial coefficients of the polynomial expression describing lattice parameters of CH₄ clathrates formed in 10 and 15 wt% ammonium sulphate solutions during cooling.

Solution	Cycle	$a_0(\text{Å})$	$a_1(10^{-5} \text{ÅK}^{-1})$	$a_2(10^{-6} \text{ÅK}^{-2})$
10 wt% (NH ₄) ₂ SO ₄	1	11.8952 ±0.0011	26.2279 ±0.6918	- -
	2	11.8579 ±0.0042	46.7327 ±2.5880	- -
	3	11.8764 ±0.0032	40.6550 ±2.2240	- -
15 wt% (NH ₄) ₂ SO ₄	2	11.9365 ±0.0085	-24.2809 ±12.3200	1.4176 ±0.4286

Table 7.4: Clathrate formation temperatures (K) during individual cycles for the salt solutions indicated.

Salt	Cycle 1	Cycle 2	Cycle 3
10 wt% (NH ₄) ₂ SO ₄	214.5	199.5	194.5
	±2.5	±2.5	±2.5
15 wt% (NH ₄) ₂ SO ₄	–	199.5	–
	–	±2.5	–

Table 7.5: Clathrate dissociation temperatures (K) during individual cycles for the salt solutions indicated.

Salt	Cycle 1	Cycle 2	Cycle 3
10 wt% (NH ₄) ₂ SO ₄	254.1	220.5	210.1
	±1.0	±1.0	±1.0
15 wt% (NH ₄) ₂ SO ₄	258.2	250.2	–
	±1.0	±1.0	–

Clathrate formation temperatures for the 10 wt% and 15 wt% solutions are shown in Table. 7.4. These results indicate that once formed, clathrates are subsequently easier to form. However, once formed, the clathrates seem to also have decreasing dissociation temperature as indicated in Table. 7.5. Additionally, it is possible to note that clathrates, on cooling, seem to have larger lattice parameters than on heating, i.e. there is hysteresis showing that the heating and cooling are not reversible. These results are consistent with our earlier work on forming clathrates in the presence of MgSO₄ solutions (see (Safi et al. 2017) and Chapter 5) suggesting that the difference in behaviour is due to levels of bonding disorder within the clathrate phase.

Shpakov et al. (1998) calculated the variation of the unit cell lattice parameter of CH₄ clathrates formed in pure water with temperature at “zero pressure” (Shpakov et al. (1998) do not state their definition of zero pressure). Shpakov et al. (1998) fitted their experimental data with a quadratic and obtained the following expression for the

unit cell parameter as a function of temperature:

$$a(T) = 11.80 + 5.39 \times 10^{-5} T + 1.78 \times 10^{-6} T^2 \quad (7.2)$$

where $a(T)$ is in \AA . Eq. (7.2) is plotted in Figs. 7.3 and 7.4 in order to provide a comparison for the temperature dependency of CH_4 clathrate lattice parameters formed in the presence of $(\text{NH}_4)_2\text{SO}_4$ with those formed in pure water. It can clearly be seen that the lattice parameters of CH_4 clathrate formed in pure water are significantly lower than those formed in the presence of $(\text{NH}_4)_2\text{SO}_4$. However, it must also be noted that the clathrates formed in our experiment were under a CH_4 pressure of 26 bar, while those formed by Shpakov et al. (1998) were under “zero pressure”. This may be a contributing factor in the difference of lattice parameters.

7.3.2 Density

As mentioned in Section 5.3.3, the density of clathrates is dependent on the lattice parameter, a , the masses of the water and guest molecules and the cage occupancy. For CH_4 clathrates, it is calculated as follows:

$$\rho = \frac{(M_{\text{CH}_4} (6\theta_1 + 2\theta_2) + 46M_{\text{H}_2\text{O}})}{a^3} . \quad (7.3)$$

here M_{CH_4} and $M_{\text{H}_2\text{O}}$ are the masses of the CH_4 guest and water molecules respectively, and θ_1 and θ_2 are the fractional occupancies of the large and small cages respectively. We will assume, as in Section 5.3.3, that $\theta_1 = 1$ (Hansen et al. 2016) and $\theta_2 = 0$ (Day et al. 2015). The dependence of CH_4 clathrate densities on temperature, calculated using Eq.(7.3), are shown in Figs. 7.5 and 7.6. The density varies with temperature, and on whether the clathrates are being heated or cooled, as would be expected due to the hysteresis effect seen when plotting the temperature dependency of the lattice parameters in Figs. 7.3 and 7.4. This was also observed in the density results in Chapter 5.

Additionally, during the first heating cycle in Fig. 7.6, we see a distinctive behaviour exhibited in the clathrate density which cannot be described by a linear or

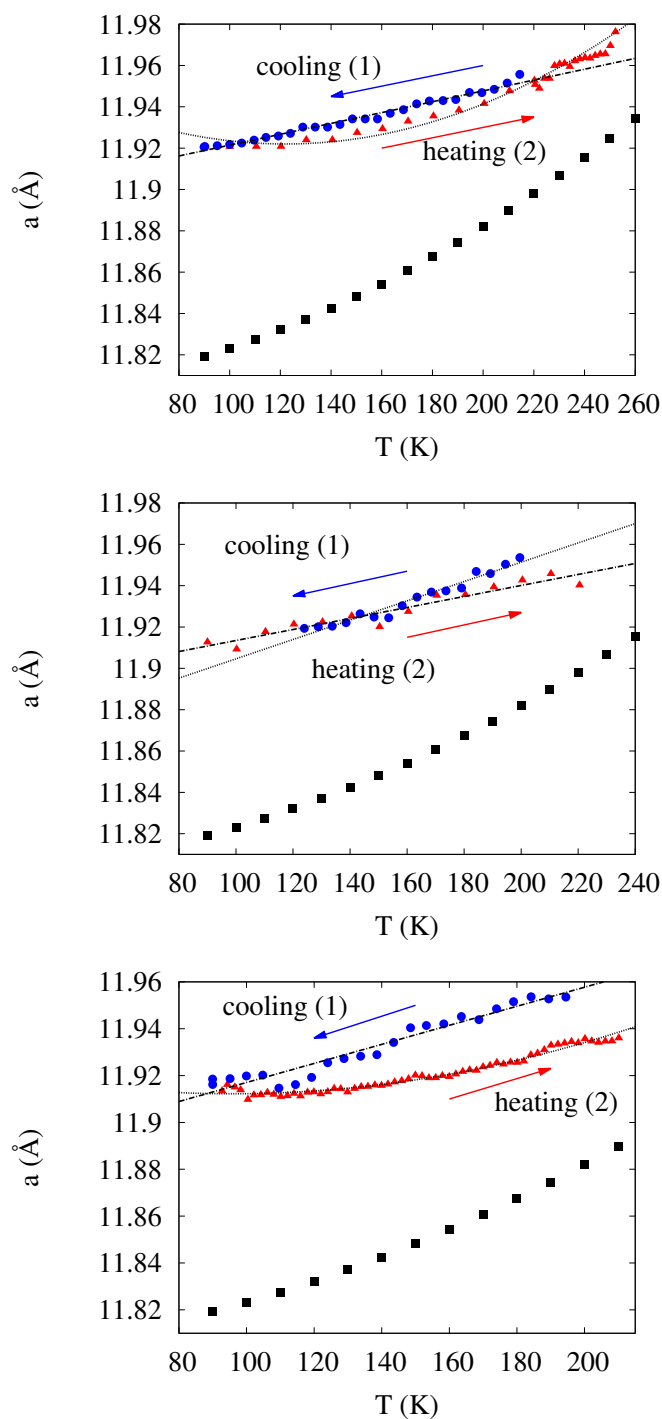


Figure 7.3: Temperature dependence of the lattice parameters of CH_4 clathrate hydrates formed in a solution of 10 wt% ammonium sulphate at 26 bar pressure. From top–bottom: cycle 1, cycle 2 and cycle 3. “(1)” and “(2)” indicate that the cooling was performed first, followed by heating. The black squares are experimental data from Shpakov et al. (1998). For ease of presentation blue symbols represent values obtained during cooling and red values obtained during heating. The error bars in these plots are smaller than the plotted points.

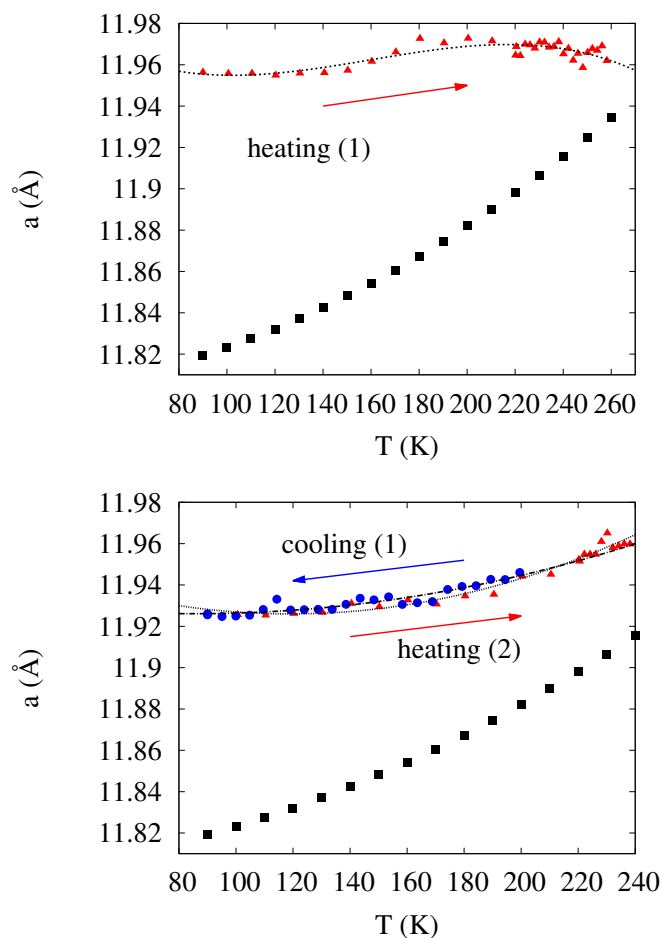


Figure 7.4: Temperature dependence of the lattice parameters of CH_4 clathrate hydrates formed in a solution of 15 wt% ammonium sulphate at 26 bar pressure. From top–bottom: cycle 1 and cycle 2. “(1)” and “(2)” indicate that the cooling was performed first, followed by heating. The black squares are experimental data from Shpakov et al. (1998). For ease of presentation blue symbols represent values obtained during cooling and red values obtained during heating. The error bars in these plots are smaller than the plotted points.

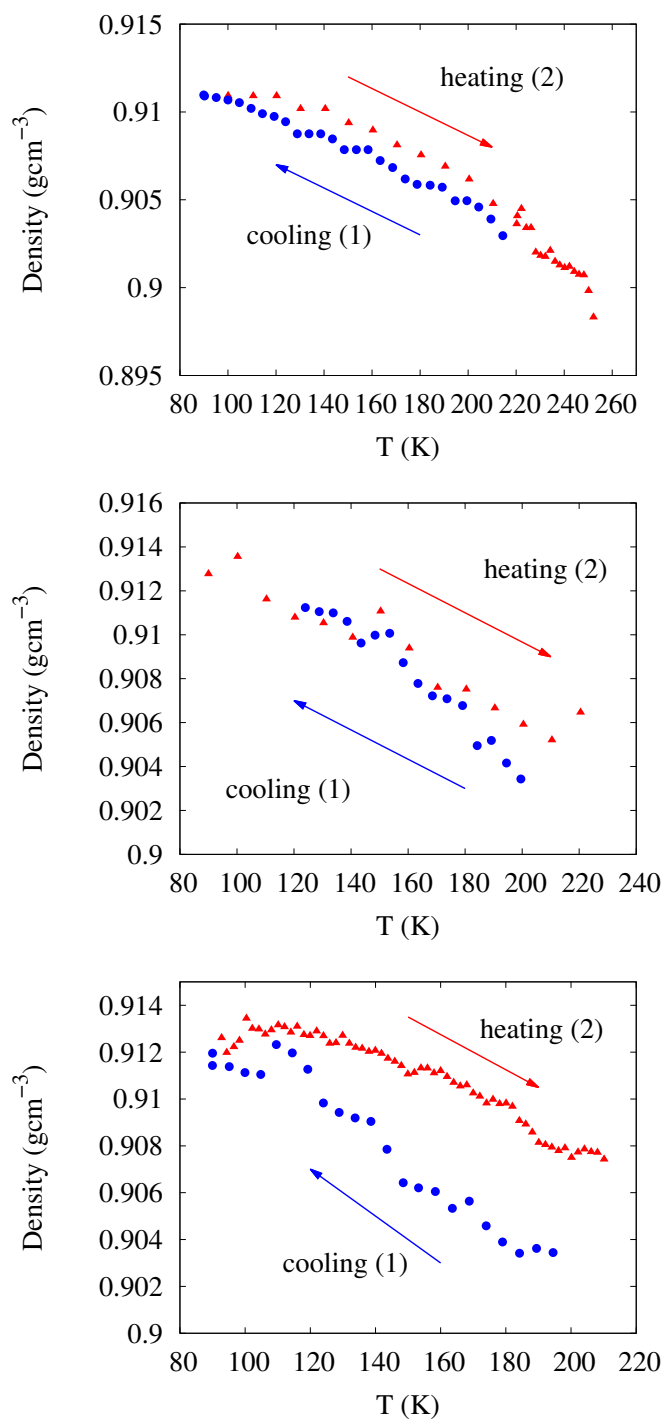


Figure 7.5: Density curves for the 10 wt% solution. From top–bottom: cycle 1, cycle 2, and cycle 3 at 26 bar. Colours are as per Fig. 7.3. The error bars in these plots are smaller than the plotted points.

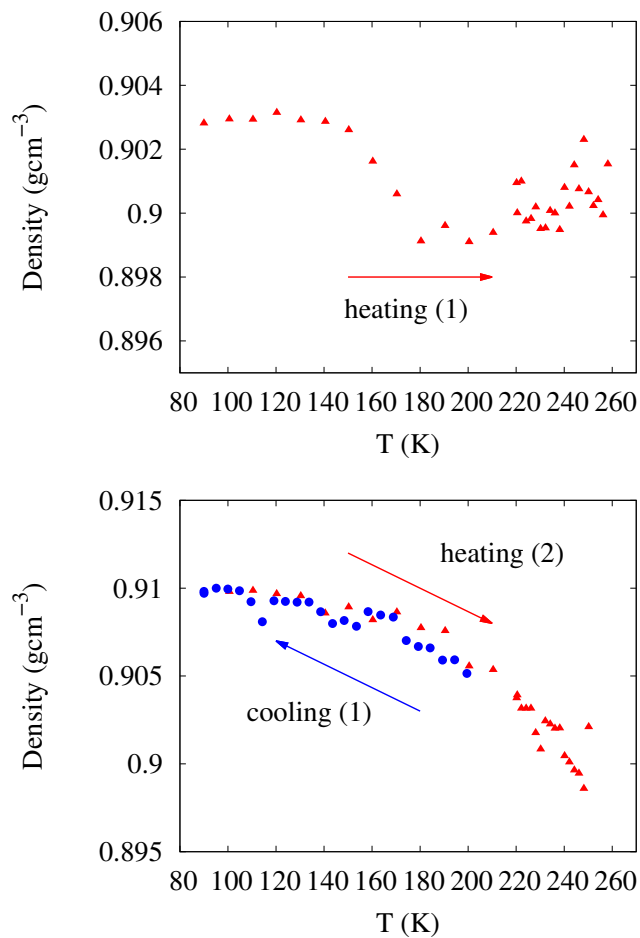


Figure 7.6: Density curves for the 15 wt% solution. From top–bottom: cycle 1 and cycle 2 at 26 bar. Colours are as per Fig. 7.3. The error bars in these plots are smaller than the plotted points.

quadratic fit. A similar behaviour is also exhibited by ice (see Fig. 7.7). The homogeneous nucleation temperature of pure ice occurs at ~ 235 K (Liu et al. 2007), and is where the densities of supercooled water and ice converge. The convergence of these densities arise due to the tetrahedrally arranged hydrogen bonding in water reaching its limit, i.e. two acceptor and two donor hydrogen bonds per water molecule, meaning no further decrease in density can be achieved unless an energetically infeasible stretching (or breaking) of the bonds occur. Therefore, liquid water can be divided into two forms: low and high-density. The density minimum has been proposed to lie at approximately 200 ± 5 K (Clegg & Wexler 2011), which is similar to the temperature at which the minimum occurs in Fig. 7.6. This minimum may be occurring in Fig. 7.6 as this solution was initially turbo-cooled to 90 K before the first heating cycle occurred. Indeed, it has been shown that supercooled salt solutions allow the existence of liquid water below eutectic temperatures (Toner et al. 2014), implying salt solutions may increase the duration of the liquid water/brine phase on icy bodies. Furthermore, a glassy state occurs when a solid phase (in this context, the salt) crystallises at a higher temperature forming a mixed glassy-crystalline solid (see Toner et al. (2014), who explore the effect of supercooling and its dependence on salt composition and concentration). They conclude that perchlorate solutions could stabilise liquid water on Mars at low temperatures in viscous and glassy states over diurnal timescales. This conclusion raises the possibility that this same scenario could occur on other icy planetary bodies, including Titan.

Additionally, Macfarlane (1986) notes that it is possible for ice to crystallise from a saline solution, continuously concentrating the remaining solution, until it transitions to glass, forming an ice-glass mixture. Therefore, pure glass, or a mixture of glass and crystalline solid, is able to form. This glassy state has been known to protect microorganisms from potentially damaging eutectic crystallisation (Toner et al. 2014). This is because microbes can enter a suspended animation state and be revitalised when warmed to their liquid state. Toner et al. (2014) also concludes that perchlorate glasses could preserve cellular structures on Mars, implying again that this could also have the same implications on other icy bodies including Titan.

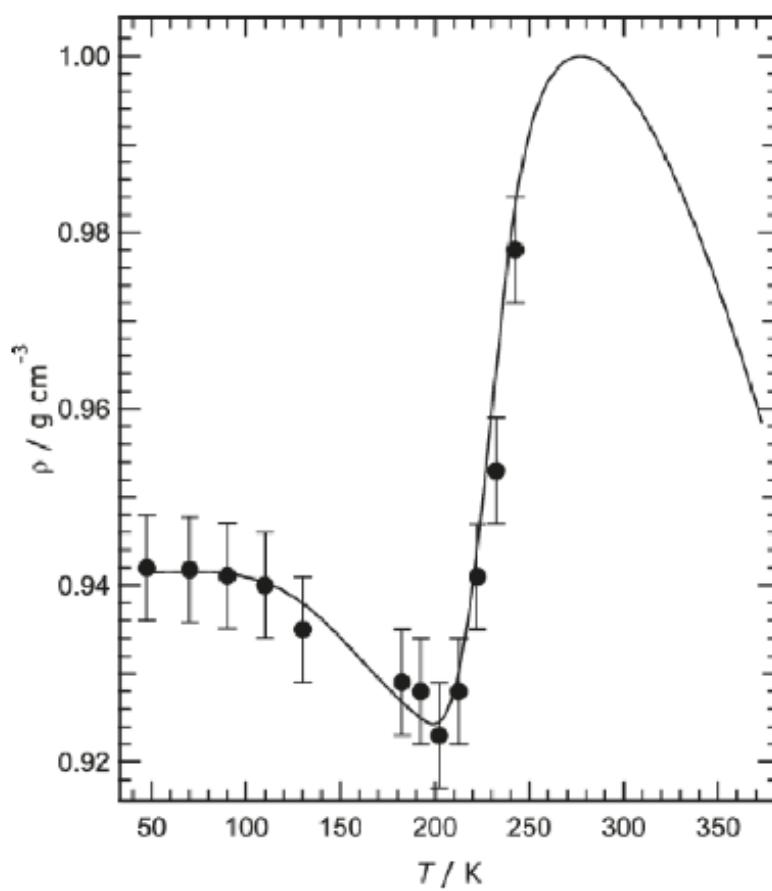


Figure 7.7: The density of supercooled H_2O as a function of temperature, (Clegg & Wexler 2011).

7.3.3 Weight percentage of clathrate, Ih, Ic and $(\text{NH}_4)_2\text{SO}_4$

As stated in Section 5.3.4, the relative contribution of each phase to the overall intensity of features in the powder pattern can give the relative fraction by weight of each crystalline component present in the sample under study. These relative weights are shown in Figs. 7.8 and 7.9 as a function of the temperature for clathrates, Ih, Ic and $(\text{NH}_4)_2\text{SO}_4$ formed in both the 10 wt% and 15 wt% $(\text{NH}_4)_2\text{SO}_4$ solutions.

From Fig. 7.8 it can be seen that no $(\text{NH}_4)_2\text{SO}_4$ forms during the first two cycles. It appears at approximately 160 K during cooling in the third cycle and disappears at approximately 120 K in the same cycle during cooling. However, Fig. 7.9 shows that $(\text{NH}_4)_2\text{SO}_4$ precipitate appears during the first heating cycle at 90 K and disappears at approximately 210 K, while it appears at approximately 170 K during the second cooling cycle and is present throughout thereafter. $(\text{NH}_4)_2\text{SO}_4$ disappears from the diffraction pattern at approximately 250 K during the second heating cycle.

Initially with the 10 wt% $(\text{NH}_4)_2\text{SO}_4$ solution in the first cooling cycle, the wt% of clathrate is 100%. This percentage quickly decreases to approximately 50%, while the percentage of Ih ice increases to approximately 50%. The wt% of Ic during the whole of cycle 1 (both for heating and cooling) never amounts to more than approximately 5%. During the second cycle using 10 wt% of $(\text{NH}_4)_2\text{SO}_4$ solution, the wt% of clathrates remains below 10% during both heating and cooling, with the wt% being slightly higher during the cooling run. Conversely, the wt% of Ih ice dominates this cycle and is never below approximately 65% during cooling and 90% during heating. During this second cycle we observe more Ic than during cycle 1, with its wt% reaching 30% at approximately 160 K. The wt% of clathrate and Ih in the third cycle are similar to those in the second cycle, with the wt% of clathrates reaching a maximum of approximately 25% and Ih a minimum of 60%; except on cooling at 90 K, where the wt% of clathrate reached 45% and Ih 50%. Ic was only present from 195–170 K during cooling in the third cycle, after which Ic was no longer discernible.

During the first heating cycle using the 15 wt% $(\text{NH}_4)_2\text{SO}_4$ solution, the wt% of clathrate remained between 10–20%, Ih between 40–70% and Ic 2–30%. At approxi-

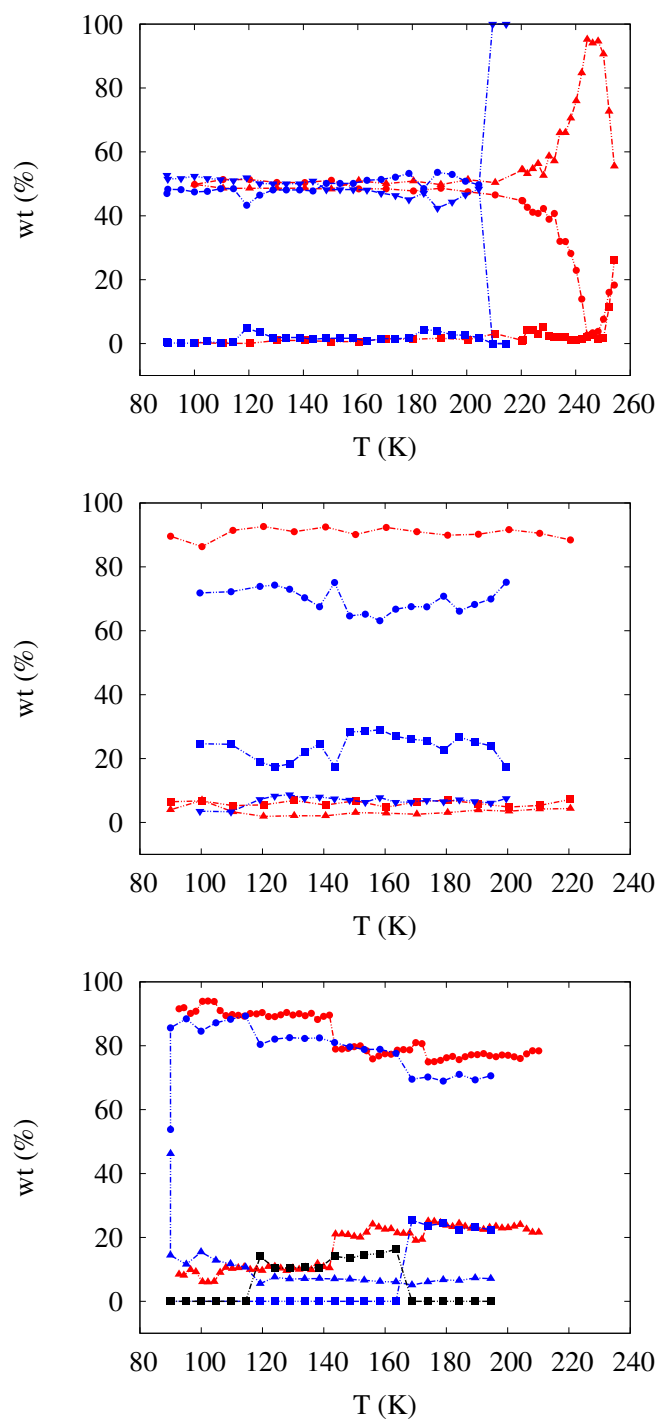


Figure 7.8: Weighted percentage (wt%) curves for the 10 wt% solution. From top–bottom: cycle 1, cycle 2, and cycle 3 at 26 bar. Triangles: clathrates; circles: Ih ice; squares: Ic ice. Colours are as per Fig. 7.3, except in the case of the black squares which represent (NH₄)₂SO₄ precipitate on cooling. The error bars in these plots are smaller than the plotted points.

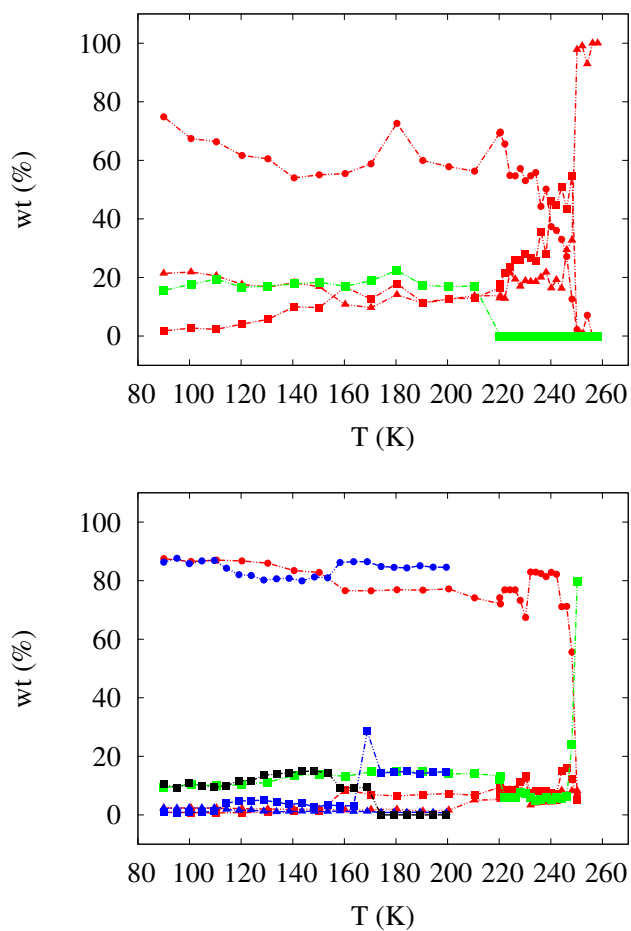


Figure 7.9: Weighted percentage (wt%) curves for the 15 wt% solution. From top–bottom: cycle 1 and cycle 2 at 26 bar. Triangles: clathrates; circles: Ih ice; squares: Ic ice. Colours are as per Fig. 7.8, except in the case of the green squares which represent $(\text{NH}_4)_2\text{SO}_4$ precipitate on heating. The error bars in these plots are smaller than the plotted points.

mately 245 K, Ih and Ic gradually began to disappear leaving clathrate as the dominant phase until it dissociated at approximately 260 K. During the second heating cycle the wt% of clathrate remained negligible, while Ih dominated the solution with a wt% between 80–90% and Ic between 0.5–30%. This remained the case during the second heating cycle using the 15 wt% $(\text{NH}_4)_2\text{SO}_4$ solution.

7.4 Discussion

7.4.1 Thermal Expansion

Figs. 7.3 and 7.4 show the behaviour of the clathrate lattice parameter with respect to temperature. A notable feature in these curves (particularly in Fig. 7.3) is the apparent hysteresis in the heating and cooling curves. This same observation was made in previous work (see Safi et al. (2017) and Section 5.3.2 of this thesis for details) where the saline solution used was composed of MgSO_4 . As explained in Section 5.3.2, the hysteresis could arise due to the ice-phase water molecules that form the clathrate cages shifting in position and forming hydrogen bonds with the liquid phase water molecules. This would cause adjacent water molecules from the surrounding clathrate cages to break hydrogen bonds and alter neighbouring cages. This would affect the elastic properties of the cages causing stress hysteresis, leading to the hysteresis we see in Figs. 7.3 and 7.4.

The degree of hysteresis we see in Figs. 7.3 and 7.4 compared to those in Safi et al. (2017) and Section 5.3.2 are not significantly different, except for cycle 3 in Fig. 7.3 where a greater degree of hysteresis is present. However, this can be attributed to the number of cycles the sample experienced, so that at this stage during the experiment, clathrates would have been exposed to the salt for a longer period of time, hence possibly causing further displacement to the ice and liquid phase water molecules. From this, it is possible to assume that salt concentration or type do not effect the hysteresis significantly. As mentioned, the salt used in Section 5.3.2 and Safi et al.

(2017) is MgSO_4 while in Figs. 7.3 and 7.4 it is $(\text{NH}_4)_2\text{SO}_4$. Despite using different salt solutions, the degree of hysteresis in the dependence of a on T does not differ significantly. The same can be said for the concentration of solutions used; using a higher or lower salt concentration does not seem to significantly affect the hysteresis between heating and cooling.

Eq.(7.2) is plotted in Figs. 7.3 and 7.4 in order to provide a comparison of the temperature dependency of clathrate lattice parameters formed in the presence of $(\text{NH}_4)_2\text{SO}_4$ under 26 bar CH_4 pressure to those formed in pure water under “zero pressure” (Shpakov et al. 1998); the difference in lattice parameters is plain to see. The clathrates formed under 26 bar CH_4 pressure clearly exhibit lattice parameters which are larger than those formed under “zero pressure”. This is due to the cage occupancy being larger at higher pressures, hence increasing the the lattice parameters. This would, in turn, have effect on the density and volume of clathrates, of which the implications are discussed below.

7.4.2 Buoyancy and density of CH_4 clathrates

The results shown in Figs. 7.5 and 7.6 show that the variation of density with temperature could have implications for the buoyancy of clathrates in Titan’s ocean. In general the results show that clathrate density is higher at lower temperatures, therefore implying that they would have a greater probability of sinking at lower temperatures, depending on ocean salinity. These results are consistent with those of Safi et al. (2017).

Fortes et al. (2007) propose a structure of Titan which includes a liquid layer of aqueous ammonium sulphate, and a heterogeneous shell of methane clathrate, ice Ih and solid ammonium sulphate (see Fig. 7.1). Fortes et al. (2007) argue that the contact between the ammonium sulphate cryomagma and the CH_4 clathrates in the crust allows some CH_4 to dissolve in the cryomagma, forming a “xenolith”. On rising to the clathrate decomposition depth (1.7 km, pressure 20 bar), the xenolith dissociates to ice and CH_4 gas, powering surface eruptions that penetrate several km into the

atmosphere, replenishing the atmospheric CH_4 . Therefore, outgassing of CH_4 occurs via “cryovolcanoes”: volcanoes that erupt volatiles like water and CH_4 rather than molten rock. The liquid layer of aqueous ammonium sulphate consists of a weak solution of ammonium sulphate of approximately 15 wt% (at a depth of 153 km), while the shell is thought to consist of a slightly weaker solution of ammonium sulphate of approximately 10 wt% (at a depth of 123 km; see Fig. 7.1). Therefore, the ammonium sulphate solutions used in this experiment can be used to replicate the salinity of the ocean and crust on Titan. If we compare the resulting clathrate densities in our temperature range with that of the solutions in which they were formed (see Section 7.3 and Table. 7.1), we find that both measured densities are higher than the CH_4 clathrate density irrespective of temperature, suggesting that CH_4 clathrates would always float. Indeed, this is also the case if we assume θ_2 is between 0.856–0.885 (with $\theta_1=1$), which are the values Hansen et al. (2016) obtained from their experimental investigation.

Another feature to note in Figs. 7.5 and 7.6 is that the density of CH_4 clathrates during heating seems to be larger than during cooling. The higher density could be attributed to the filling of the clathrate cages being greater during heating. This could be due to a larger time elapse from the beginning of the cycle compared to that of cooling, hence allowing the uptake of more CH_4 into the cages. If this is indeed the case it has implications for the buoyancy of clathrates in Titan’s crust and ocean. Once formed in the crust, the CH_4 clathrates may begin to rise to their decomposition depth. However an increase in cage occupancy during this time may cause them to become denser preventing the clathrates from reaching this depth, resulting in their sinking to the ocean floor. However, this scenario would not be able to occur if the salinity of the ocean and crust were as stated above (i.e. 15 wt% and 10 wt% respectively), even if we were to assume $\theta_1 = \theta_2=1$, i.e. full occupancy of the large and small cages. In order for a scenario to occur that involved the sinking of the CH_4 clathrates, the density of the ocean and crust would need to be $\sim 0.91 \text{ g cm}^{-3}$ or less; indeed Beuthe (2015) predicts a lower bound on the crust density on Titan could be 0.93 g cm^{-3} . Pressure is another factor that directly affects cage occupancy in that an increase in pressure can result in an increase in cage occupancy. This implies that clathrates formed at

greater depth have a larger occupancy, hence increasing their chance of sinking in the crust and ocean – this is however dependant on the ocean and crust salinity. Finally, if CH₄ clathrates were to sink in the crust/ocean of Titan, then the model put forward by Fortes et al. (2007), suggesting outgassing of CH₄ occurs via cryovolcanoes, could not be valid.

7.4.3 Effects of ice and (NH₄)₂SO₄ on Titan’s crust and ocean

As mentioned previously in Section 5.4.4, Ic ice is the most common polymorph of ice at low temperatures. Figs. 7.8 and 7.9 shows the composition of the 10 wt% and 15 wt% (NH₄)₂SO₄ solutions during the experiment. From Fig. 7.8 we can see that during the first cycle no Ic ice was formed, only Ih ice and clathrate are present in approximately equal quantity; the large increase in wt% of clathrate and decrease in wt% of Ih is due to the ice melting and leaving predominantly clathrate present before it also dissociates. However, during the second cooling cycle we see that Ic ice has formed; this is consistent with the hypothesis in Section 5.4.4 that the rate of transformation of Ih to Ic is slow at low temperatures. It should also be noted that, during this second cycle, the wt% of clathrate is extremely low; this is consistent with the hypothesis in Section 6.4.1 that Ic provides an easier diffusion pathway for clathrate dissociation. During the third cycle Ih is again the dominant phase present. Ic is also present during cooling, but decomposes as soon as (NH₄)₂SO₄ precipitates from solution. However, these results show that Ic seems to form at ~190 K, 30 K above the temperature it is expected to form. This is also consistent with the hypothesis in Section 6.4.1, that Ic could in fact be ice I. In general, the same pattern of behaviour can be observed in Fig. 7.9.

These results suggest that the low temperature phase of ice could cause the dissociation of clathrates to occur more readily in both the crust and ocean, before they rise to their decomposition depth of 1.7 km. Due to this, a “cycling” of clathrate formation and dissociation may occur where clathrates form; they begin to rise and dissociate to release CH₄ before they reach the surface, thus allowing more clathrates

to form and the process can repeat. Therefore, the presence of a low temperature phase of ice and $(\text{NH}_4)_2\text{SO}_4$ precipitate further decreases the chance that outgassing of CH_4 occurs via cryovolcanoes.

7.5 Conclusion

By the use of SXRPD we have investigated the formation, dissociation, buoyancy and thermal expansion properties of CH_4 clathrates formed in ammonium sulphate salt solutions. Using our results we have hypothesised that the atmospheric source of methane may not originate from outgassing via cryovolcanoes as previously suggested, due to the density of the clathrates compared to that of the ocean and crust. Additionally, we have shown that, in the presence of a low temperature phase of ice and/or ammonium sulphate precipitate, clathrates seem to dissociate more readily. This would further prevent the rising of clathrates to the surface of Titan, once again suggesting that cryovolcanoes may not be the source of atmospheric CH_4 .

These results emphasise the importance of the role played by salts and ice on clathrate formation and dissociation. Therefore, as clathrates are thought to be one of the leading candidates for the storage of gases on icy planetary bodies, these results further highlight the need of further experimental investigations to allow a more precise quantification of the effect of ice and salts on clathrate properties.

8 The behaviour of epsomite at temperatures relevant to Solar System bodies

In this chapter we present the results of a study focussed on the thermal cycling of epsomite at temperatures relevant to planetary environments; in particular we explore the structural and Raman spectroscopic behaviour of this hydrated sulphate. The experimental work completed in this chapter was done in conjunction with Dr. Stephen Thompson (DLS).

8.1 Hydrated sulphates on Mars

On Mars magnesium sulphates are thought to result from the reaction of basaltic material with sulphuric acid of volcanic origin (Tosca et al. 2005). Evidence for magnesium sulphate in Martian soils and rocks first came from the 1977 Viking landings (Clark & van Hart 1981; Clark 1993), and was later confirmed by the Pathfinder landers in 1997 (Rieder et al. 1997; Wänke et al. 2001) and the Mars Exploration Rovers Opportunity and Spirit in 2004 (Gellert et al. 2004; Rieder et al. 2004). Chemical analyses carried out during these missions pointed to magnesium sulphate being present in significant quantities. Indeed, from mineralogical modelling, Clark et al. (2005) suggested higher average abundances of about 18% w/w in the outcrops at Meridiani Planum.

Magnesium sulphate has various hydrated forms ($\text{MgSO}_4 \cdot n\text{H}_2\text{O}$, $n = 1..7$ and 11, see Fig. 2.8 in Section 2.3.1) and may account for a large fraction of water equivalent hydrogen observed near the Martian equator (Feldman et al. 2004). Kieserite was the first hydrated mineral to be considered (Baird et al. 1976), however the OMEGA and CRISM instruments on the Mars Express and Mars Reconnaissance Orbiter spacecraft showed data consistent with higher hydration states (e.g. epsomite and meridianiite) (Gendrin et al. 2005; Roach et al. 2009). The cold atmosphere on Mars, together with the limited diffusion between hydrated phases, suggests hydration states of buried

phases are likely to have been preserved.

8.2 Hydrated sulphates on Europa

Europa is subjected to a strong energy input from tidal flexing by Jupiter (Pappalardo et al. 1998), which causes the layers beneath the ice crust to melt, producing a liquid ocean, while the dissolution of the minerals that make up the core contribute to its saline composition. Evidence regarding the composition of the crust is limited, however near-infrared reflectance spectra for some surface regions collected by the Near Infrared Mapping Spectrometer (NIMS) instrument on the Galileo mission (Carlson et al. 1996) show highly distorted H₂O vibrational overtone bands suggestive of endogenic frozen salt mineral mixtures (e.g. epsomite, bloedite (MgSO₄Na₂SO₄·7H₂O), mirabilite, (Na₂SO₄·10H₂O) and natron (Na₂CO₃·10H₂O)). Models indicate salts such as MgSO₄ and Na₂SO₄ can be produced by low-temperature aqueous alteration of solar nebula material, as seen in Kargel et al. (2000) and is expected to lead to the formation of MgNaCa-sulphate rich material. Additionally, it should be noted that arguments, based on the likely composition of the subsurface ocean, suggesting the preferential formation of chlorinated phases over sulphates on Europas surface have also been made (Ligier et al. 2016).

8.3 Hydrated sulphates on Ganymede

NIMS data for Ganymede show almost identical spectral pattern to Europa, suggesting similar salt and sulphate compositions (McCord et al. 2001) consistent with a fluid layer just beneath the surface (Kivelson et al. 2000). Certain regions on Ganymede appear to have experienced severe surface disruptions similar to Europa, suggesting a MgSO₄-rich brine reached the surface at some point in the satellite's history (McCord et al. 2001).

8.4 Hydrated sulphates on Callisto

Callisto has dark, globally abundant, densely cratered plain features and is, in the geological sense, the least evolved of the Galilean satellites (Stephan et al. 2013). Its surface displays various impact features, similar to those on Ganymede, and are indicative of intense surface erosion and degradation. Similar crater features on Callisto and Ganymede suggest similar rheological properties and sub-surface layering. Although little is known about the internal structure of Callisto, the Galileo spacecraft detected large-scale features of magnetic field perturbations during the flyby. These features are consistent with induced magnetic dipoles. The observed magnetic field perturbations are those expected if Callisto was a perfectly conducting sphere. This response indicates a globally distributed, highly conducting, medium close to the surface of the satellite. This suggests the presence of a large liquid reservoir within the crust (Zimmer et al. 2000). This, therefore, indicates the possibility that hydrated sulphate materials may also exist on its surface.

As discussed in Section 1.3.2, epsomite is a mineral which has received significant scrutiny in terms of its behaviour when subjected to various temperatures. The fact that a low temperature phase of epsomite exists has been debated in the literature over the years (Dalton et al. 2005; Wang et al. 2011), however no definitive conclusion has been drawn. In this section we present our own results and conclusions on this topic, and discuss the possibility of the presence of a low temperature phase of epsomite.

8.5 Experimental

A sample of reagent grade $\text{MgSO}_4 \cdot 7\text{H}_2\text{O}$ (magnesium heptahydrate, Sigma Aldrich) was ground using a mortar and pestle, loaded into a 0.7 mm internal diameter borosilicate capillary, then sealed and mounted on the centre of beamline I11's 3-circle diffractometer. An Oxford Cryosystems (UK) 700+ liquid nitrogen Cryostream, with a temperature stability of ± 0.1 K, was used to subject the capillary to a mixture of dry air

and nitrogen vapour, allowing the sample to experience temperatures between 300 and 90 K with temperature steps of 10 K. At each temperature step thermal overshoot was between 2 K at higher temperatures and 1.1 K at lower (<160 K) temperatures. The sample experienced a ramp rate of 360 K/hour between temperature steps. Once a specific temperature had been reached, the sample was left for 2 minutes to equilibrate before data collection commenced. An X-ray wavelength of 0.825818\AA was used (calibrated against NIST SRM640c Si standard) and data were recorded using the beamline's PSD detector (Thompson et al. 2011). To account for the small gap between adjacent detector modules and to allow for high signal to noise, the detector was stepped from 2° to 4° 2θ in 0.25° steps, with 1 s exposures being collected at each position. These data were then summed at the end of each scan. Hence, SXPD data collection took 9 seconds at each temperature step. The data were subsequently analysed using the TOPAS software package.

The experimental set-up is shown in Fig. 8.1. The in situ Raman system comprises a 200 mW 532 nm laser, Raman probe super head (Horiba) mounted on a motorised linear drive stage located on a heavy duty motorised table adjacent to the diffractometer, also holding the Cryostream. The super head is connected via optical fibre to a Horiba iHR550 imaging spectrometer. A 600 g/mm grating was used in order to provide good resolution of solid state lines and a wide spectral range so data could be collected from 50 to 4000 cm^{-1} using two grating positions. The laser power was restricted to 80 mW which allowed for reduced heating to the sample, while simultaneously providing short collection times. Spectra were acquired as 5 accumulations at each grating position of 10 seconds each. Both SXPD and Raman data were collected on cooling.

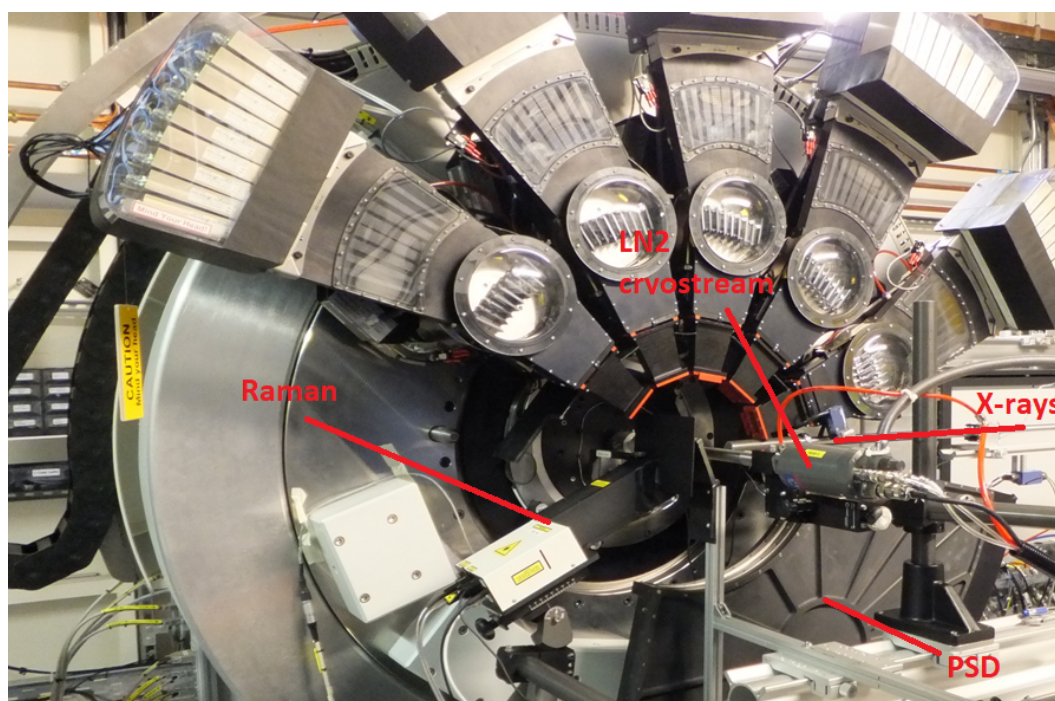


Figure 8.1: Experimental set-up of the in situ Raman measurements.

8.6 Results and Discussion

8.6.1 Laboratory work on epsomite

Figs. 8.2 to 8.6 show the XRD pattern obtained from the epsomite sample collected at 10 K intervals from room temperature (290 K) to 90 K; Fig. 8.2 is the complete XRD pattern, while Figs. 8.3 to 8.6 show zoomed in regions of the pattern. Inspection of Fig. 8.2 seems to indicate that nothing significant is occurring, however upon zooming into the peaks (Figs. 8.3 to 8.6), it is possible to see the peaks are splitting as the temperature decreases. Each successive pattern in Figs. 8.2 to 8.6 obtained from room temperature to 90 K is very similar to the previous one; if a new phase were being formed it is most likely that peaks would appear/disappear as the temperature is decreased. It is obvious from the pattern collected that this is not occurring, and that the peak splitting is an evolution. Furthermore, it is also possible to observe that the peaks in the XRD pattern of an existing phase are being shifted towards higher 2θ in Figs. 8.3 to 8.6 as the temperature is decreased, some more so than others. This general effect is due to the d -spacing in the crystals contracting as the temperature is lowered. The decreased d -spacing, according to Bragg's law, leads to a larger 2θ hence resulting in a shift of the peaks as seen in Figs. 8.4 to 8.6. The fact that some peaks show a greater shift than others is a possible indicator of the structural contraction being different for one or other of the lattice parameters. Indeed, using neutron scattering down to 2 K Fortes et al. (2006) found that, below 250 K, the unit cell parameter exhibits negative thermal expansion (see next section for our results obtained on the thermal expansion of epsomite).

Fig. 8.7 shows the Raman spectra collected as a function of temperature. The figure shows some clear differences as the temperature is decreased; this effect is most prominent on the H₂O stretching modes at around 3400 cm⁻¹ (see Fig. 8.8) – at room temperature we see two small bumps on the peak, as we approach 90 K these bumps become more distinguishable and increase in quantity until at 90 K there are seven identifiable peaks present. This same effect was also observed by Wang et al.

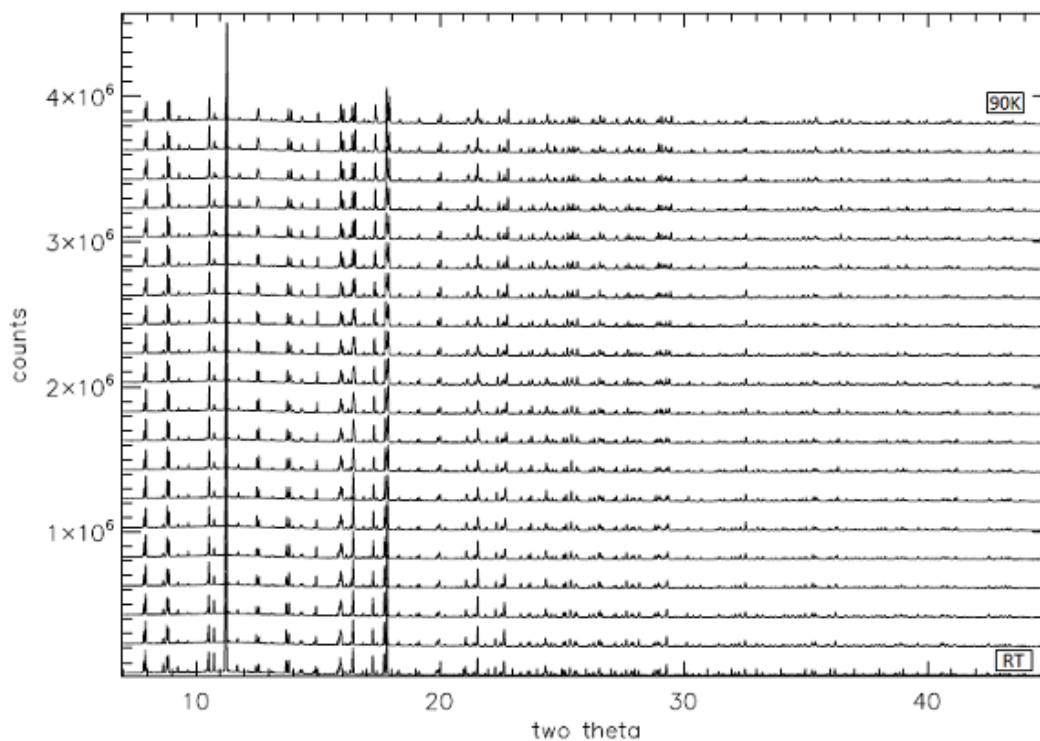


Figure 8.2: XRD pattern of epsomite. Between each successive pattern there is a temperature step of 10 K. RT is room temperature.

(2011), which they interpreted as further evidence that there is a low-temperature phase of epsomite. Since no phase change is observed in the XRD data, the effect of peak sharpening observed in the Raman spectra is unlikely to be due to a low-temperature phase; it most likely occurs due to changes to the overlapping of the distribution of modes and overtones of the molecular vibrations within the mineral. At high temperatures the distribution is more pronounced at lower temperatures leading to a smearing out of the features (Dalton et al. 2005).

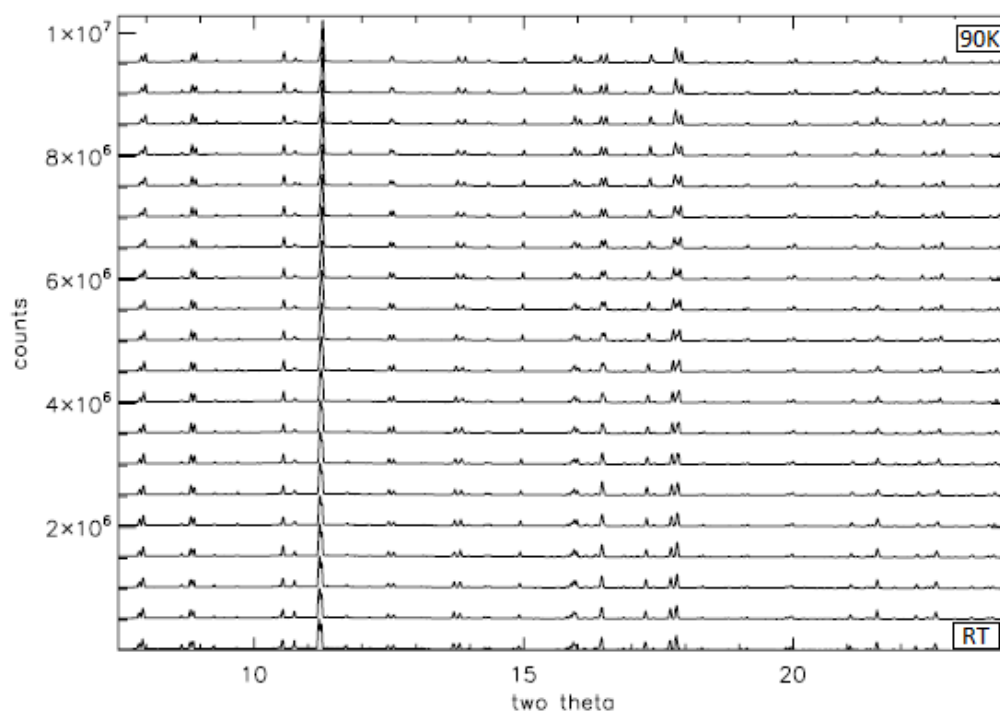


Figure 8.3: Zoomed pattern of XRD pattern of epsomite ($5^\circ < 2\theta < 30^\circ$). Between each successive pattern there is a temperature step of 10 K. RT is room temperature.

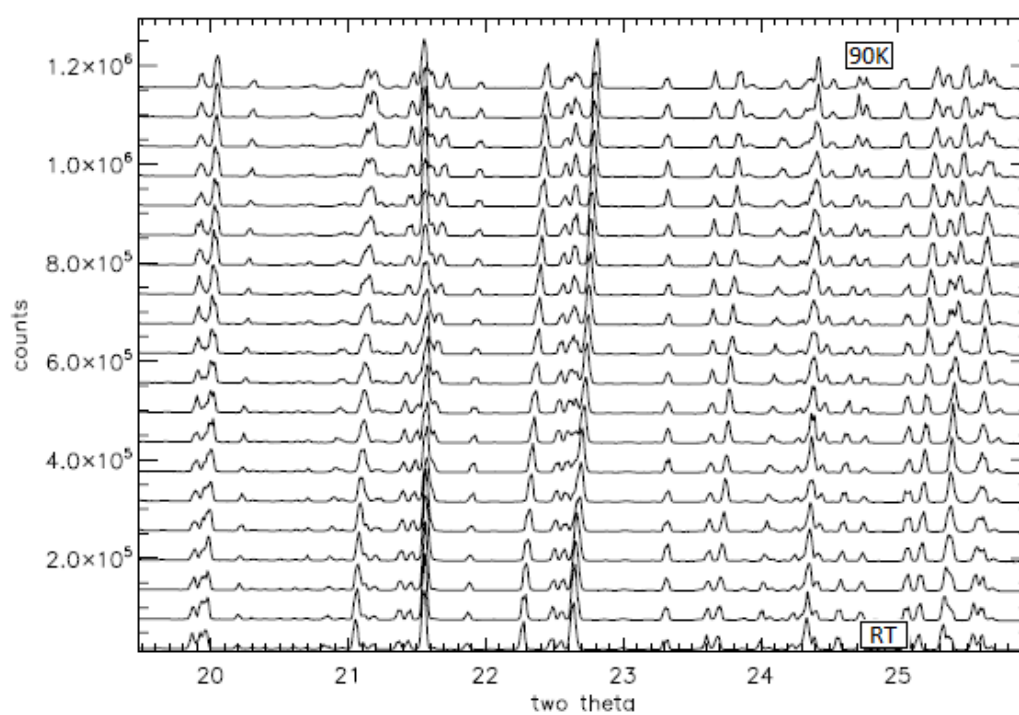


Figure 8.4: Zoomed pattern of XRD pattern of epsomite ($19^\circ < 2\theta < 26^\circ$). Between each successive pattern there is a temperature step of 10 K. RT is room temperature.

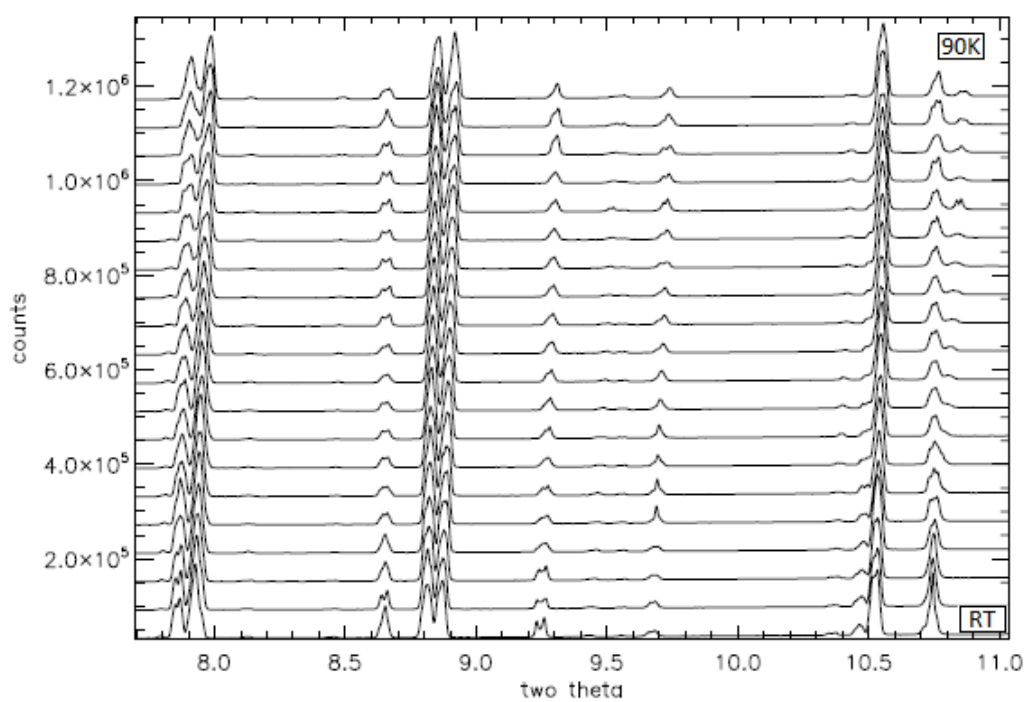


Figure 8.5: Zoomed pattern of XRD pattern of epsomite ($7.7^\circ < 2\theta < 11^\circ$). Between each successive pattern there is a temperature step of 10 K. RT is room temperature.

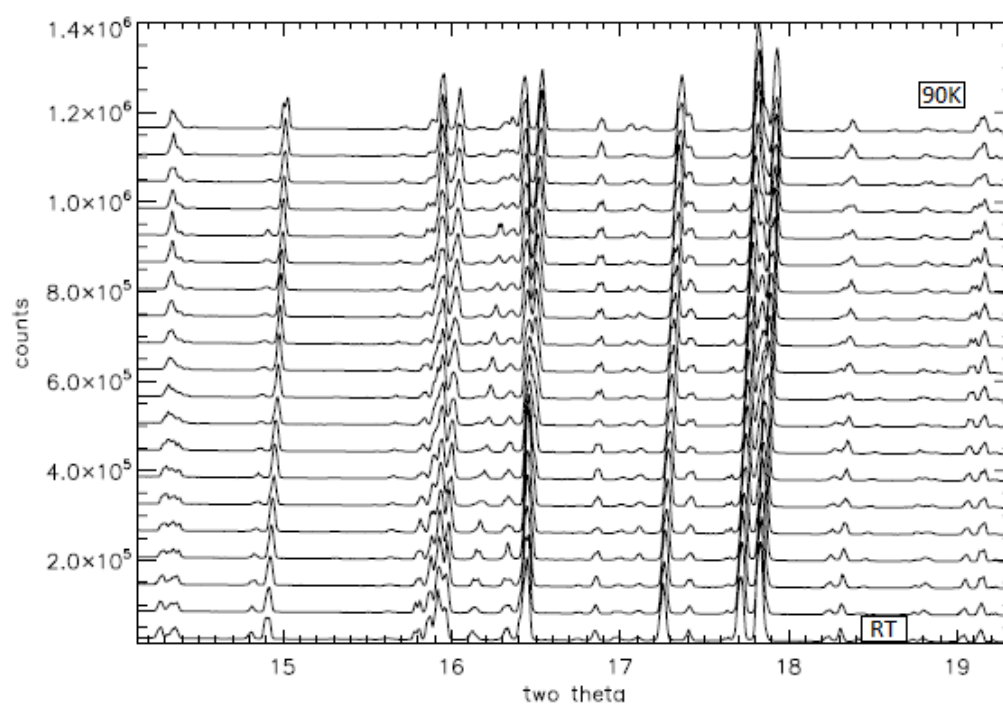


Figure 8.6: Zoomed pattern of XRD pattern of epsomite ($14^\circ < 2\theta < 19.3^\circ$). Between each successive pattern there is a temperature step of 10 K. RT is room temperature.

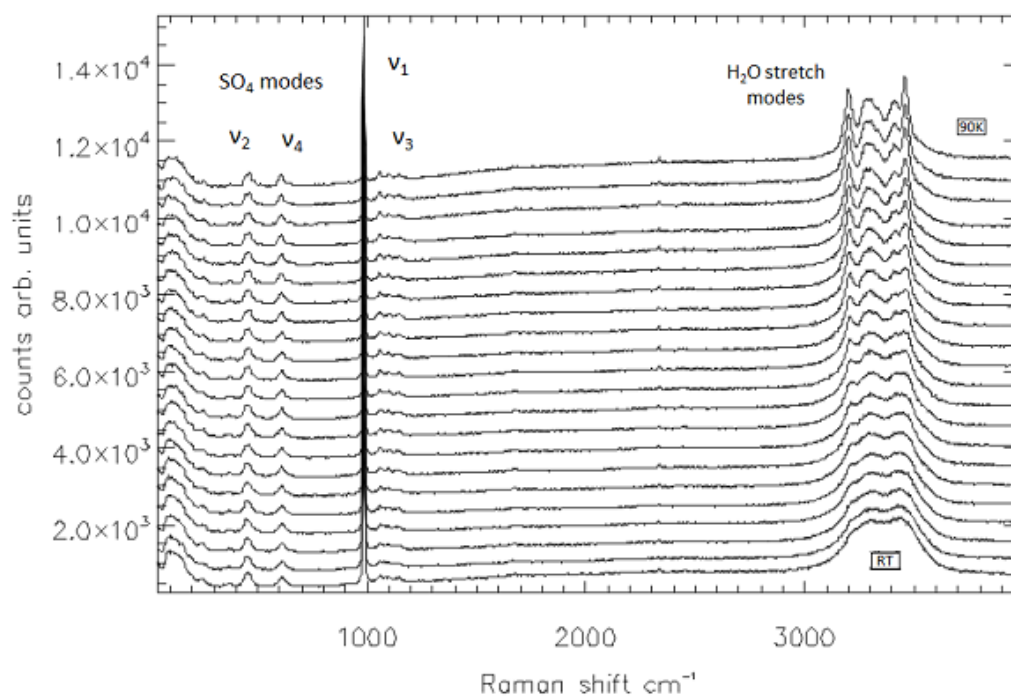


Figure 8.7: Raman pattern obtained from epsomite. Between each successive pattern there is a temperature step of 10 K. RT is room temperature.

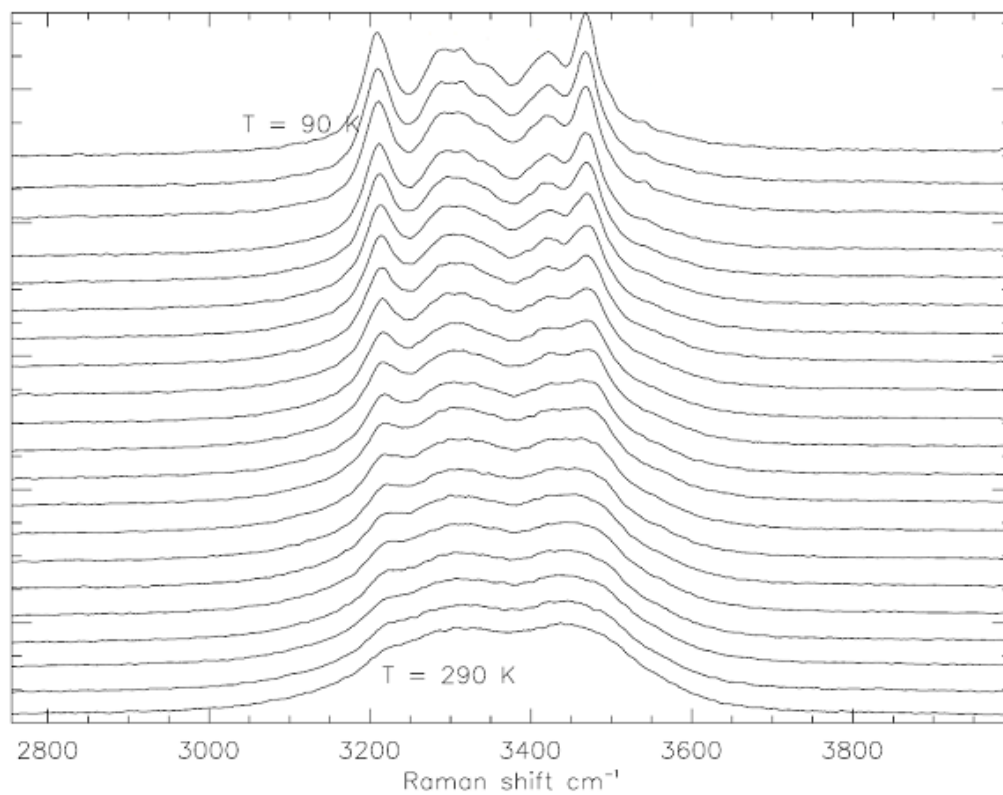


Figure 8.8: Zoomed hydration band of Raman obtained from epsomite. Between each successive pattern there is a temperature step of 10 K.

8.6.2 Thermal expansion of epsomite

If geophysical models are to be made of icy planetary satellites that include epsomite as a significant rock-forming mineral, then we need to know its bulk physical properties under the low temperatures and high pressures that are characteristic of these satellites.

With the results obtained from our Raman and XRD experiments on epsomite, we were able to determine the nature of the thermal expansion curves of this mineral. The data were refined using a Pawley whole pattern refinement (see Fig. 8.9) on TOPAS academic, with initial values of the a -, b -, and c -axis set at 11.86Å, 11.99Å and 6.858Å respectively (Fortes et al. 2006). When the refined lattice parameters were plotted against temperature the curves produced provide a good match when compared to previously published work by Fortes et al. (2006). For this work we have used a polynomial approach to describe the temperature dependency of the lattice parameter using the function:

$$a = a_0 + a_1T + a_2T^2 \quad (8.1)$$

Fitting Figs. 8.10 to 8.13 we can obtain the coefficients a_0 , a_1 and a_2 for each axis and the volumetric expansion as shown in Table 8.1.

Table 8.1: Coefficients of a_0 , a_1 and a_2 for each axis and the volumetric expansion, obtained from fitting Eq.(8.1).

	a_0 (\AA)	a_1 (\AA K^{-1})	a_2 (\AA K^{-2})
a -axis	11.9262 ± 0.0011	-0.0005 $\pm 1.3050 \times 10^{-5}$	9.7971×10^{-7} $\pm 3.4630 \times 10^{-8}$
b -axis	11.8968 ± 0.0009	0.0003 $\pm 1.1050 \times 10^{-5}$	2.9243×10^{-4} $\pm 2.9310 \times 10^{-8}$
c -axis	6.7909 ± 0.0005	3.0130×10^{-5} $\pm 5.4950 \times 10^{-6}$	6.6127×10^{-7} $\pm 1.4580 \times 10^{-8}$
Volume expansion	963.5510 ± 0.1764	-0.0143 ± 0.0021	0.0002 $\pm 5.4450 \times 10^{-6}$

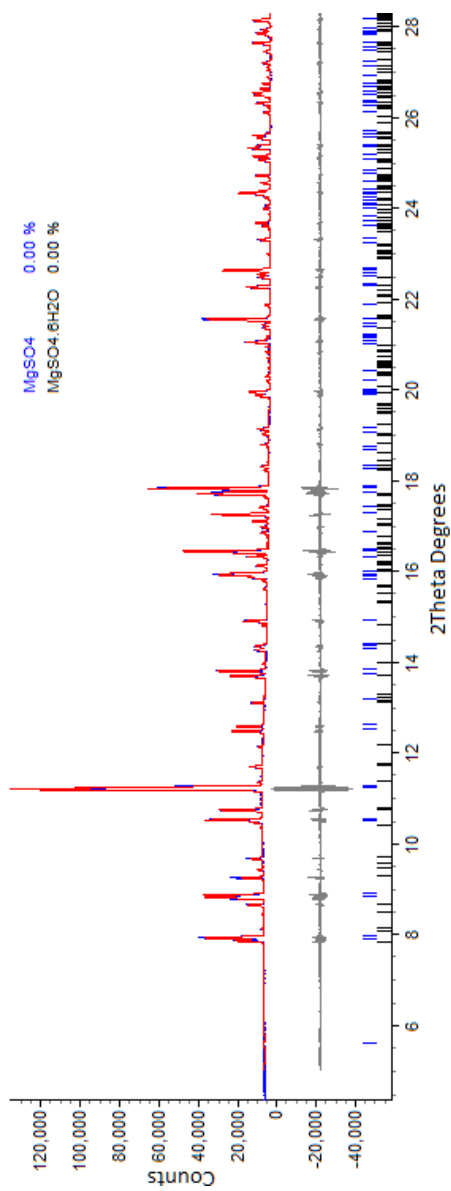


Figure 8.9: Pawley whole pattern refinement of the experimental data. The experimental are shown in blue, the calculated fit in red and the residuals in grey below.

From looking at Figs. 8.10 to 8.13 it is possible to assess the thermal behaviour of epsomite. At lower temperatures the a -axis seems to exhibit negative thermal expansion; as the temperature reaches approximately 250 K, the a -axis shows positive thermal expansion. The b -axis shows near linear behaviour (note the small value of a_1 in Table 8.1). The temperature at which the negative thermal expansion behaviour stops is lower for this axis than for the a -axis. The temperature at which negative thermal expansion – if any – behaviour stops is also lower for the c -axis by comparison with the a -axis. Also, from the present data it is possible to establish that, at lower temperatures, the c -axis expands at a slower rate than the b -axis due to the shallower gradient. In addition, from Fig. 8.13 it is possible to deduce that the total overall volume occupied by epsomite expands as temperature is increased, which is what we would expect.

8.7 Conclusion

From the work presented in this section we conclude that the existence of a low temperature structural phase change in epsomite is unlikely. However, the possible existence of a second polymorph of epsomite cannot be definitively ruled out. Fortes (2005) noted that solubility curves of epsomite are usually presented for two phases. However, more recent attempts to replicate crystals with triangular or hexagonal plates were not successful, and hence in current literature, there are no studies of this polymorph. In addition to this, given that the historical observations were close to room temperature on Earth, the existence of crystals with triangular, or hexagonal, plates on cold extra-terrestrial bodies seems unlikely.

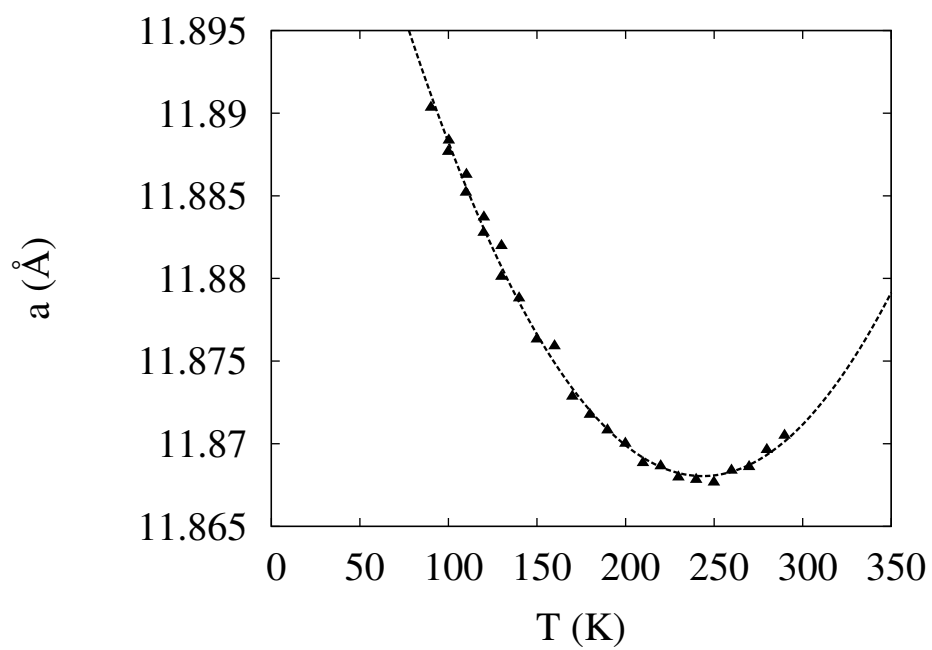


Figure 8.10: Thermal expansion curves of epsomite along the a -axis.

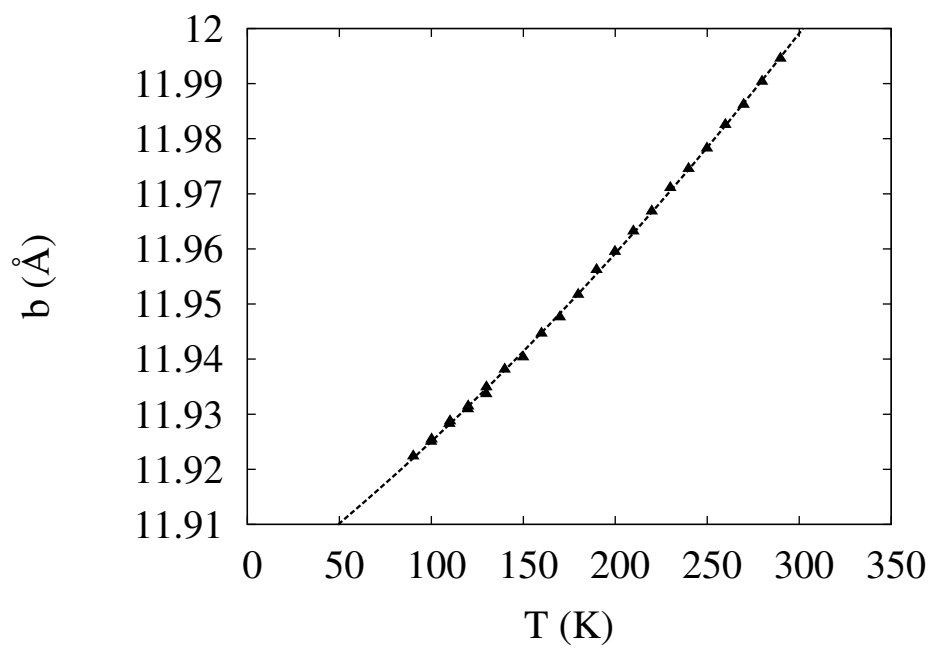


Figure 8.11: Thermal expansion curves of epsomite along the b -axis.

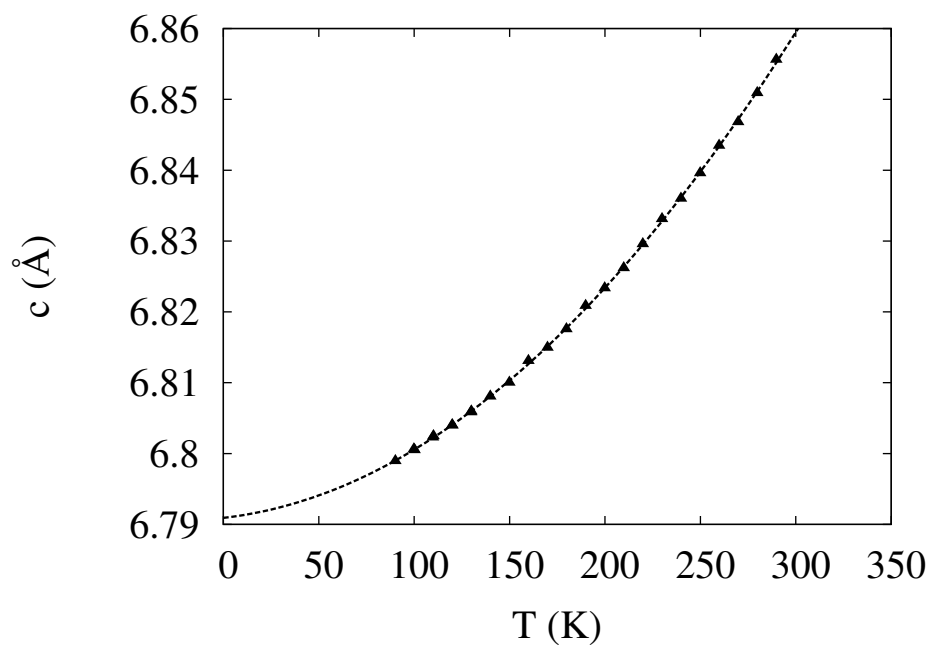


Figure 8.12: Thermal expansion curves of epsomite along the c -axis.

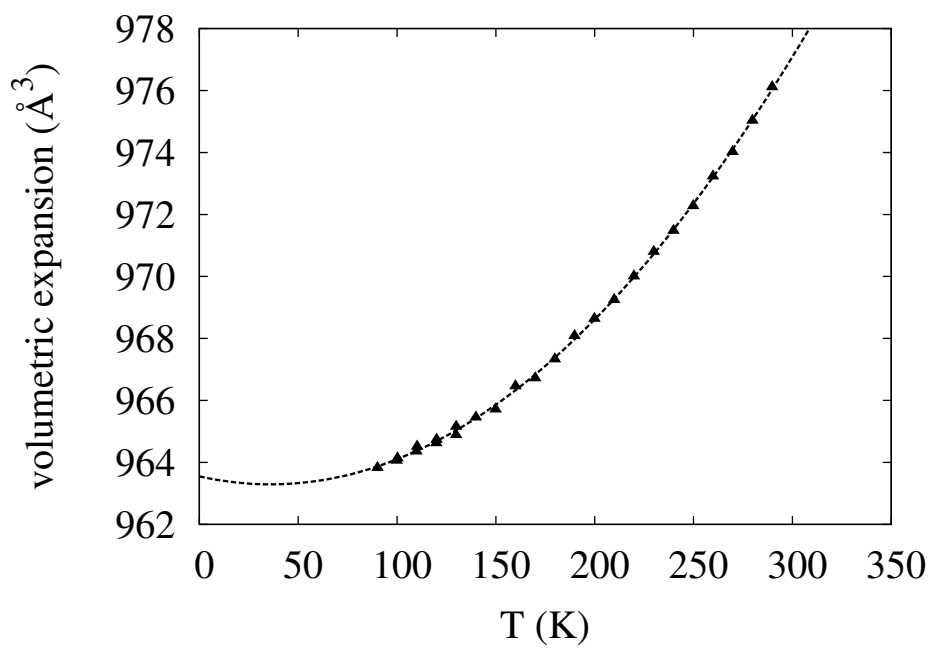


Figure 8.13: Volumetric expansion of epsomite.

9 A slow cooling study of hydrated minerals using the LDE

In this chapter results are presented on a slow cooling study of meridianiite and a saline solution representative of Europa's ocean composition using the LDE. The experimental work completed in this chapter was done in conjunction with Dr. Stephen Thompson (DLS).

9.1 Introduction

The hydrated sulphate mineral meridianiite ($\text{MgSO}_4 \cdot 11\text{H}_2\text{O}$, MS11) is believed to be wide spread on Mars, deriving its name from the Opportunity Rover landing site in Meridiani Planum. The mineral can only be formed from low concentration solution by slow cooling.

The study of meridianiite formation is fundamental for the interpretation of data from current exploration of Mars and other planetary bodies. The images from NASA Opportunity Rover in Meridiani Planum has indicated the existence of needle-shaped cavities throughout the deposit. The empty cavities are interpreted as once being likely filled by a highly soluble minerals such as magnesium sulphate, since they are closely matched to the morphology of meridianiite.

As the mineral decomposes to 70% epsomite and 30% water, it has been proposed that meridianiite may represent a wet period on the Martian surface. During warmer periods, the meridianiite crystals would have melted which may help to explain the occurrence of some of the chaotic and short lived, surface-water episodes. The results from our study of the slow formation of the hydrated magnesium sulphate should aid our understanding of the Martian surface as well as other planetary bodies (e.g. Europa and Ganymede).

9.2 Experimental

To use the LDE facility on beamline I11 at DLS (see Section 4.1.3) in order to investigate slow mineral precipitation in cold aqueous environments, a transmission geometry cold cell was designed at DLS which is able to achieve significantly slow cooling ramp-rates. For details on the cold cell see Section 4.1.3.1 and Fig 4.6. In this section results for low temperature precipitation from a MgSO_4 rich solution of the mineral phase MS11 are reported.

The sample of meridianiite was prepared using 5 g of reagent grade $\text{MgSO}_4 \cdot 7\text{H}_2\text{O}$ mixed in 24 g of 18 M Ω deionised water. This resulted in a aqueous solution of 36 wt% concentration of MgSO_4 which was then loaded into the cold cell using a pipette. The cell was sealed and assembled and then mounted on the beamline.

The I11 LDE beamline facility houses multiple long running experiments, each mounted on an individual motorised *xyz*-stage, which is itself mounted on an individual linear stage that runs across a large granite sample table (the LDE setup is shown in Fig. 4.5, see Section 4.1.3). This enables each experiment to be brought into the beam, such that the samples can be cooled via a large area detector, which is itself mounted on a linear drive that runs along the length of the sample table, allowing a predefined sample-detector distance to be specified.

Meridianiite data are collected on a weekly basis when the synchrotron is in operational mode. The wavelength and detector-sample distance is refined each week using a standard CeO_2 calibrant that is embedded on the cold cell. Before the beginning of the experiment, the optimal beam sample position is found by scanning the cell chamber horizontally and vertically across the beam. The chamber can be returned to this optimal position weekly by entering it into a control script. Diffraction data for meridianiite can then be collected at this position and at ± 2 vertical positions offset from the centre by 1 mm. The beamsize used in this experiment was 200 μm^2 , which was achieved by slitting down the incident 25 keV undulator X-ray beam.

9.3 Results and discussion

Fig. 9.1 shows the pattern of data collection from October 2015 to August 2016. Periods marked “shutdown” on Fig. 9.1 are when data collection halted due to the synchrotron not being operational. Fig. 9.2 shows the diffraction patterns collected in the first 7 weeks of the experiment. In weeks 1 and 2 the aqueous solution starts to crystallise and ice forms, identified by peaks at approximately 7.25° , 8.25° and 10.5° 2θ in week 2. A network failure then occurred where the chiller ceased to function and no data were collected. When cooling once again commenced during week 3 ice was still forming, as was the case in week 4. During weeks 5 and 6, the ice began to break up, as indicated by the broadening of the peaks (see Section 3.3.3). This was followed by a shutdown of the synchrotron so no data were collected. Data collected during week 7 still show the weaker ice peaks, however this pattern also shows that MS11 has formed, identified by peaks at approximately 4.5° , 4.8° and 5.75° 2θ .

These results show an interesting pattern of behaviour of ice as MS11 forms. Amorphous ice is formed by rapid quenching of water, vapour deposition at low T (<120 K) or application of high pressure (1.6 GPa below 140K). Therefore, the volume expansion caused by the formation of meridianiite could be forcing the ice to break up into smaller particles. This could indicate that the MS11 is forming in brine channels within the ice. The increase in density of brine channels within the ice could ultimately weaken the ice, hence affecting its mechanical properties by increasing the grain boundary slipping, decreasing the shear strength; this could reduce ice rheology and alter bulk flow properties.

After week 7, cooling continued down to approximately -25°C and both ice and MS11 remained present (see Fig. 9.3). However, in week 12 a coolant leak developed which meant the samples were not being cooled. Due to this the samples were reheated to approximately 3°C ; cooling was then restarted and data collection began again at about -6°C . This thermal cycling of the sample showed a surprising result in terms of ice formation; after heating and then re-cooling of the sample we seem to achieve the formation of more prominent ice peaks, as shown in Fig. 9.4. This could

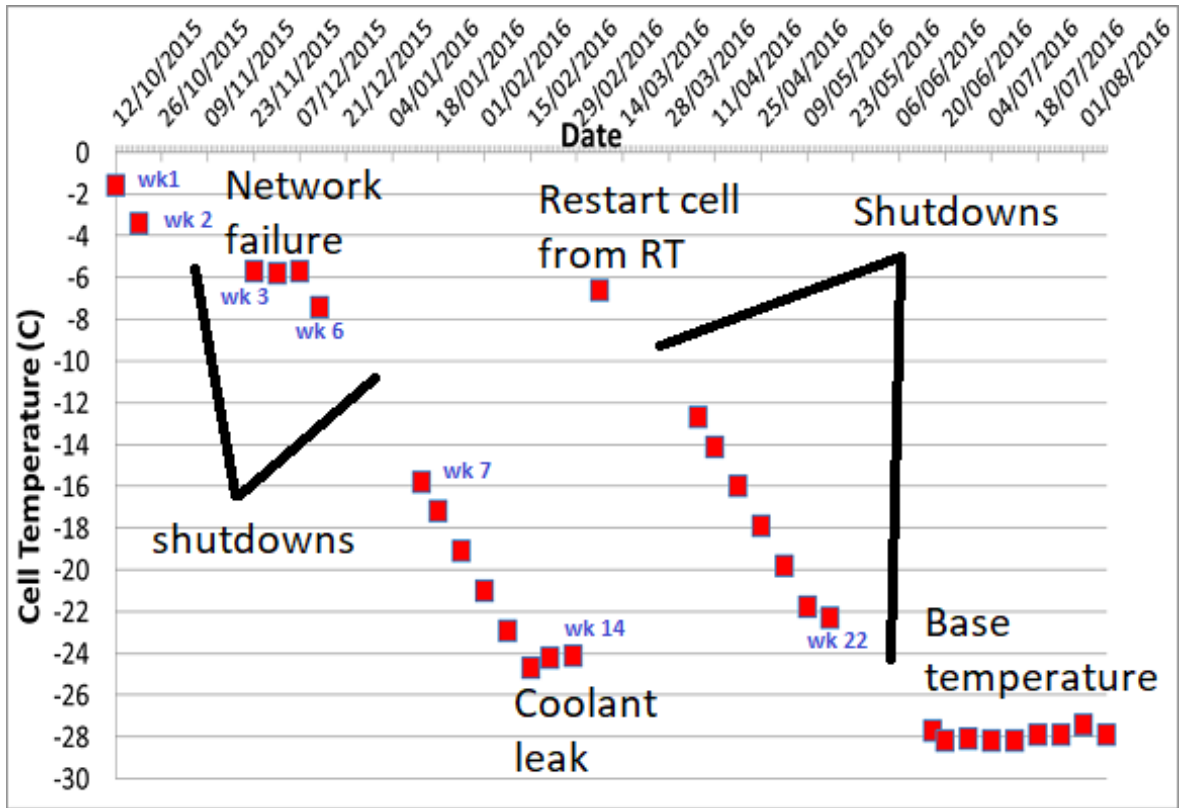


Figure 9.1: Meridianiite data collection from the LDE.

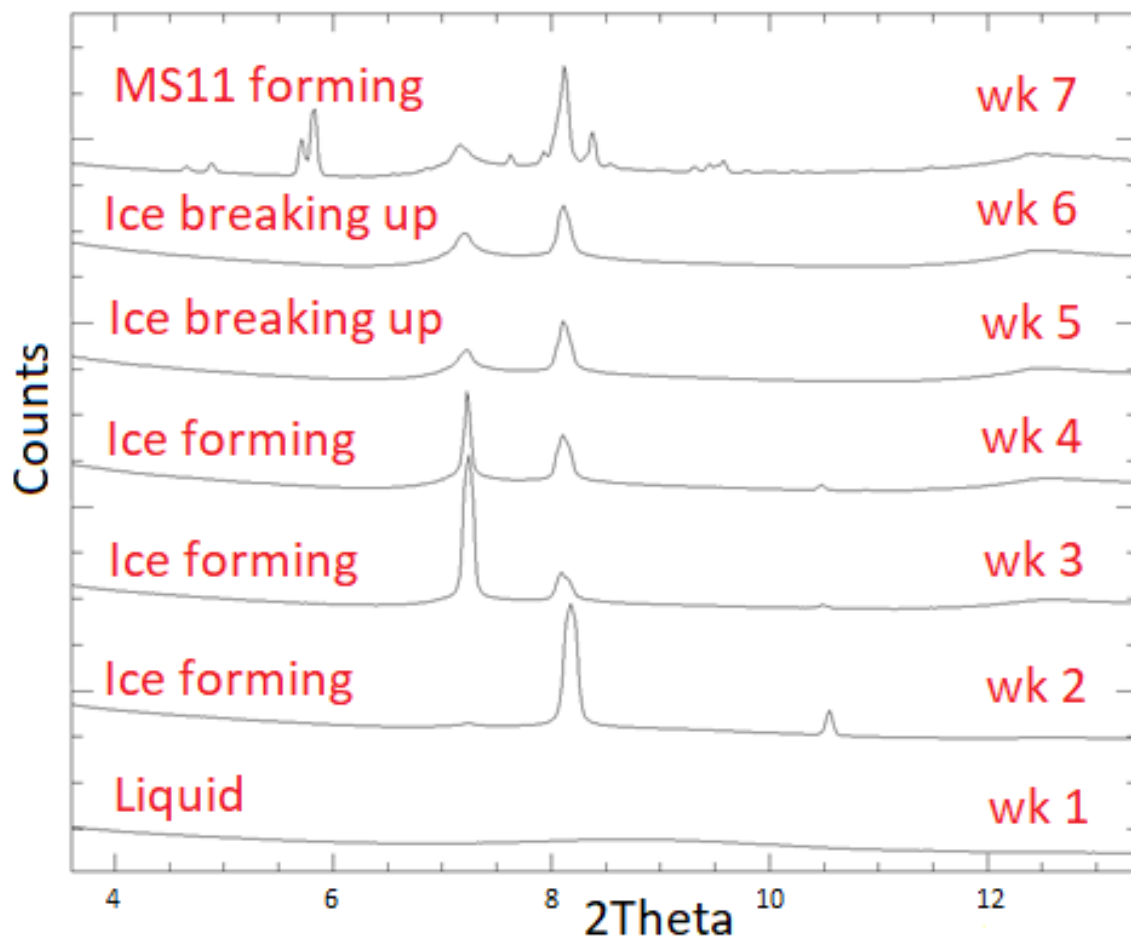


Figure 9.2: Evolution of ice and MS11 in the first 7 weeks of data collection on the LDE.

be due to the ice showing a so-called “memory effect” similar to that exhibited by clathrates (see Section 6.1). This could have implications for Solar System bodies (e.g. Martian polar ice caps) as this “memory effect” could result in more ice forming on these bodies as a result of thermal cycling from seasonal temperature changes.

As cooling continues down to approximately -23°C , we once again can witness the ice breaking up as more MS11 begins to form, this can be seen in Fig. 9.5. This is once again following by a shutdown of the synchrotron, before the base temperature of approximately -28°C is reached (see Fig. 9.6). As the base temperature on the LDE is reached, the ice peaks can be seen to become more prominent. However, this is due to ice forming on the outside of the cell.

From these results, it was possible to investigate in more detail the breaking up of the ice particles as MS11 forms. A solution of 30% MgSO_4 concentration was prepared and investigated using an in-situ time-resolved experiment in EH1. The sample was cooled at a rate of 50 K/h to 240 K and held at that temperature while a series of diffraction patterns were collected. These diffraction patterns (see Fig. 9.7) allowed a more in detailed view of the ice peaks broadening out, indicating disintegration of the ice, as MS11 formed. This served as a confirmation of the results from the LDE.

9.4 Conclusion

In this section, by the use of both in-situ time-resolved and long duration experiments, results are presented on the evolution of MS11 and ice as temperature is varied. Specifically, we have:

1. formed ice and MS11, hence shown that, in order for MS11 to grow, the ice particles which form initially must break up into smaller particles, as implied by the broadening of the ice peaks,. This phenomenon was seen in the results from both the LDE and later confirmed by a in-situ time-resolved experiment in EH1;

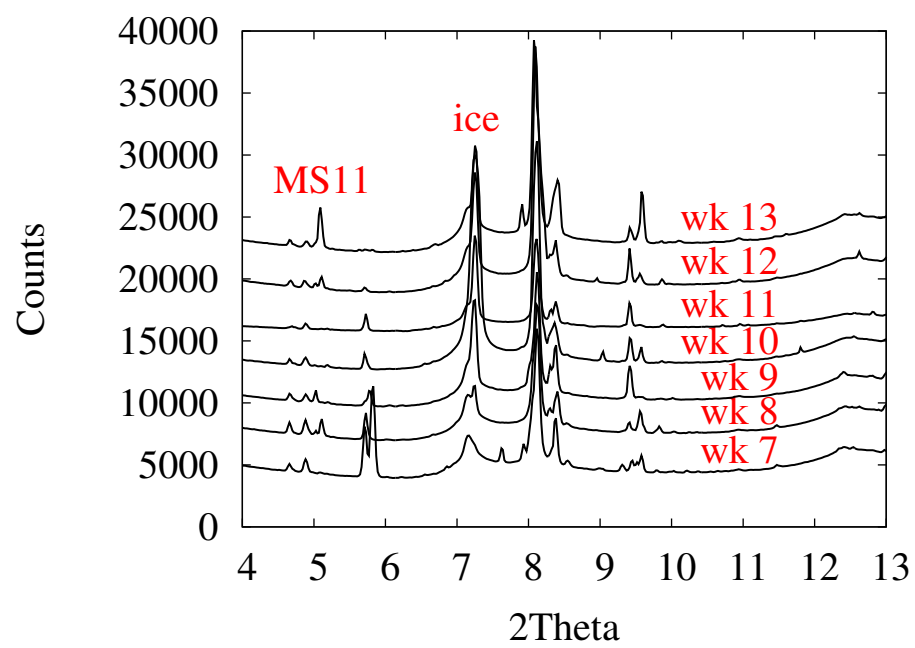


Figure 9.3: Evolution of ice and MS11 from week 7 to 13 of data collection on the LDE.

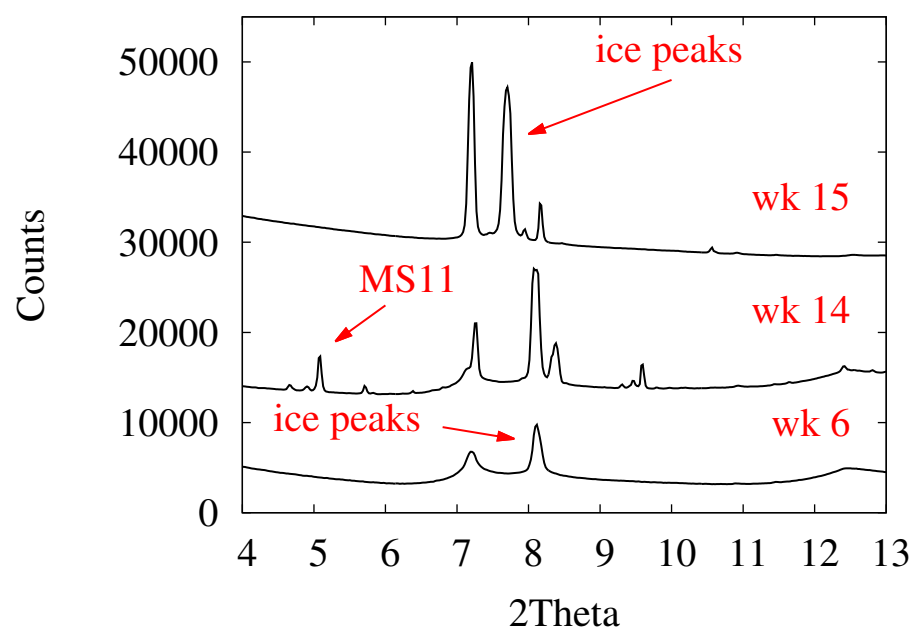


Figure 9.4: Changes in ice peaks after thermal cycling of the LDE sample.

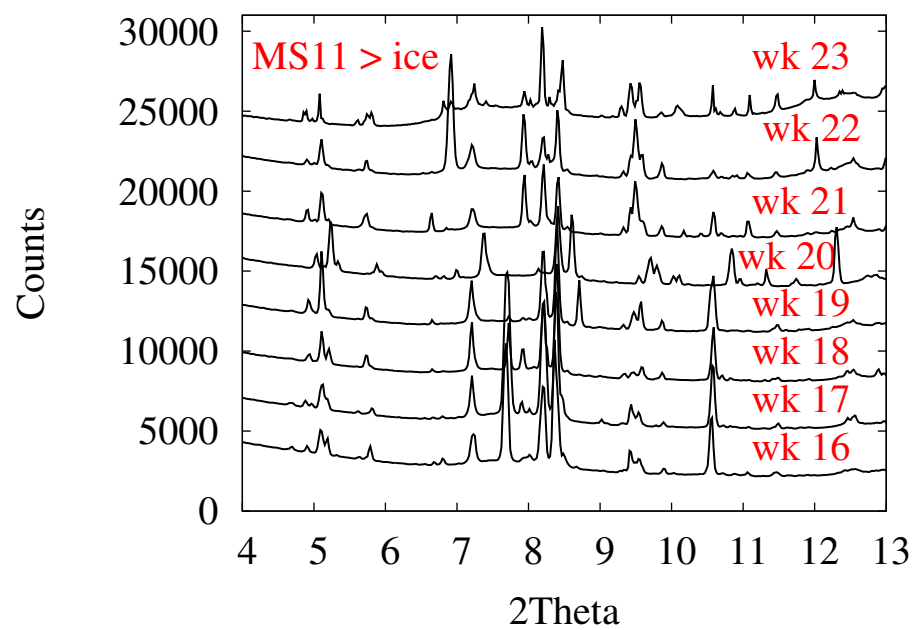


Figure 9.5: Evolution of ice peaks as MS11 forms.

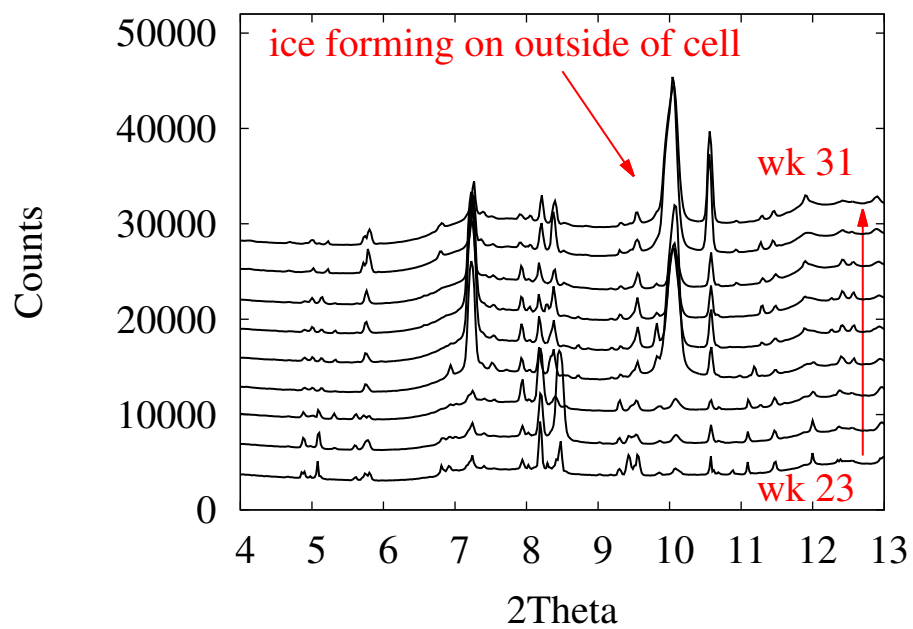


Figure 9.6: Ice forming on outside of the cell as base temperature on the LDE is reached.

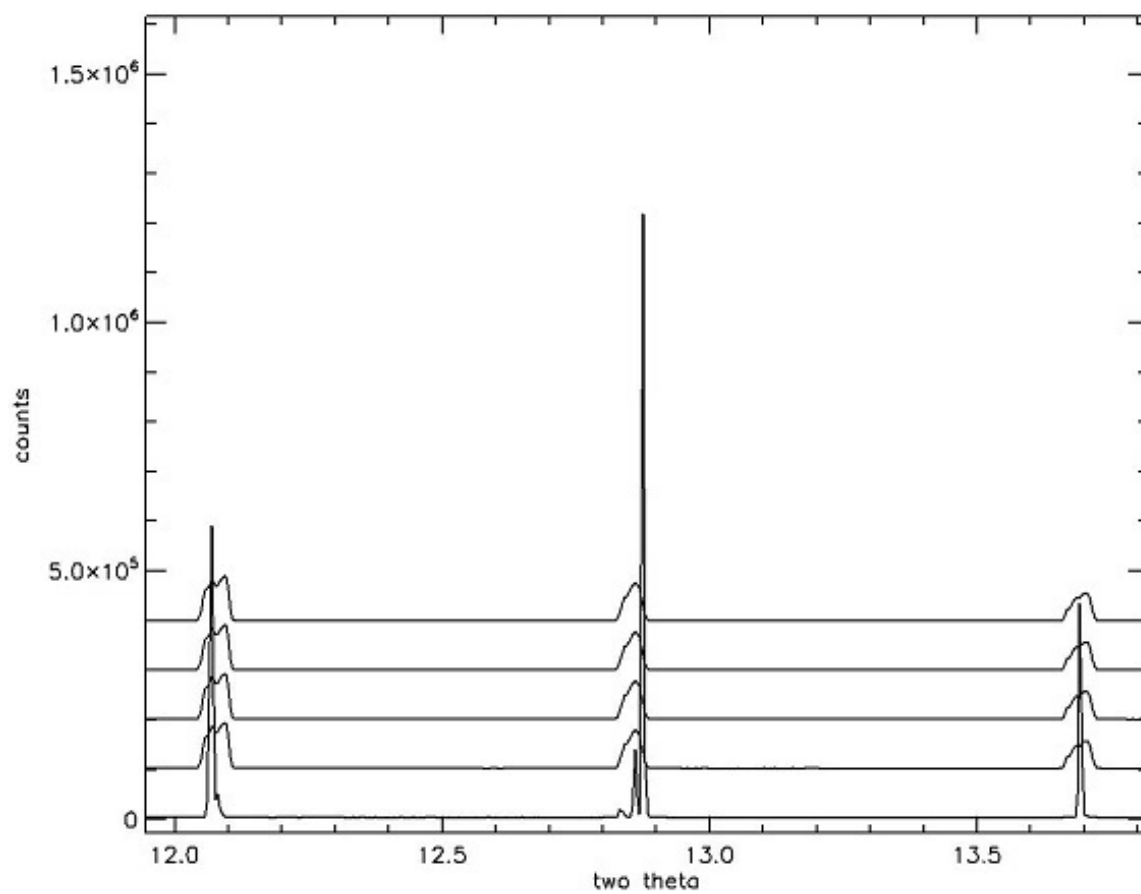


Figure 9.7: Zoomed in ice peaks formed in in-situ time-resolved experiment in EH1. Ice peaks are broadening indicating disintegration of the ice as MS11 forms.

2. suggested that this is due to MS11 forming brine channels in the ice. This implies that if the density of brine channels in the ice is high enough, the ice could ultimately weaken, hence affecting the mechanical properties of ice by increasing the grain boundary slipping, decreasing the shear strength and could reduce ice rheology and alter bulk flow properties;
3. found that thermal cycling of ice produces more intense ice peaks. This could be due to the ice showing the so-called “memory effect”. This could have implication for Solar System bodies (e.g. Martian polar ice caps) as this “memory effect” could imply that more ice than previously thought is forming on these bodies as a result of thermal cycling from seasonal temperature changes.

These results highlight the importance of future experiments of hydrated sulphates in the context of Solar System bodies, particularly in the case of quantifying the exact implications of the effect of thermal cycling of ice on these bodies.

9.5 LDE studies of the ocean composition on Europa

9.5.1 Introduction

It was concluded in the previous section that mineral precipitates (in this case MS11) could potentially affect the mechanical properties of ice. Therefore, it follows that understanding the chemical and physical properties of mineral precipitates, not only MS11 and other hydrated sulphates, will enable us to gain a better understanding of the aqueous environments present on Solar System bodies e.g. Europa, Enceladus and Mars. Indeed, the environments of Europa and Enceladus are considered potential habitats for life due to the likely presence of salts similar to those found on Earth. These terrestrial brine-channels house a wide range of micro-organisms (e.g. bacteria, viruses, fungi, etc.) under conditions where the pH and salinity are dependent on

the mineral precipitations of Na-K-Mg-Ca-Cl-SO₄-H₂O from the terrestrial oceans. Therefore, from this, it is possible that the mineral precipitations on planetary bodies such as Europa, Enceladus and Mars could also have played a role in sustaining putative life.

Europa is one of the main locations in the Solar System targeted for exploration due to its astro-biological potential. There is strong evidence that points to the existence of a briny global ocean situated between its icy surface and rocky interior (Hand & Carlson 2015). The Galileo spacecraft magnetometer has revealed a distortion of the magnetic field from Jupiter around Europa. This is consistent with the sub-surface saline ocean hypothesis. Indeed, Galileo NIMS data show numerous regions on Europa where highly distorted water absorptions indicate the presence of bound water and little or no ice where the deep interior has been exposed. Two classes of material are thought to be the origin of the non-ice material observed (Kargel et al. 2000):

1. hydrated magnesium and sodium sulfates and/or sodium carbonates (McCord et al. 1998);
2. hydrated sulphuric acid with traces of radiolytic sulphur impurities (Carlson et al. 1999).

The presence of the suggested hydrated sulphates are supported by theoretical observations from cosmochemistry, are water soluble, and are electrolytic in nature. Hence, these hydrated minerals could explain the electrically conductive nature of a near-surface liquid layer required by magnetic field data. Sodium carbonates are also a candidate for Europa, however they would require a more complex chemical evolution (Kargel et al. 2000). Additionally, the composition of Europa's surface salt minerals includes chloride salts. These are of interest due to their abundance throughout the Solar System and have been suggested to be present on Europa (Hand & Carlson 2015).

In this section we describe results obtained from the LDE facility at DLS. A sample was placed in one of the five holders situated the in cold cell on the same

Table 9.1: Initial composition of sample used to model mineral precipitates on Europa.

Mental/anion	Initial composition (mols/kg H ₂ O)
Na	1.630
Mg	2.929
Ca	0.0064
SO ₄	3.5964
Cl	0.308

experimental run described in Section 9.2. The sample analysed is a saline solution with similar initial salt concentrations thought to be present in the ocean on Europa.

9.5.2 Experimental set-up and results

This experimental set-up is identical to that described in Section 9.2, with the sample placed in one of the five aqueous sample holders. Data were collected on a weekly basis from March 2016 to June 2017.

The initial composition of the solution was based on a neutral environment described by Marion (2009) called FREZCHEM. FREZCHEM is a thermodynamic model parametrised for saline solutions for concentrations up to 20 moles/kg(H₂O) (molality). This model uses the Pitzer approach for the temperature range -70–25 °C and pressure range 1–1000 bars range. FREZCHEM has been widely used to explore cold geochemical processes and/or limits for life in the Arctic, Antarctica, Europa, and Mars (Marion 2009). Changes in the solution used during this experiment and associated mineral precipitates based on the output of FREZCHEM (provided by Benjamin Butler of Bangor University) were used and the initial composition is shown in Table 9.1.

From this initial composition, using the FREZCHEM software, the mineral precipitates produced in the temperature range 300–230 K could be modelled, this is shown in Fig. 9.8. From this model, the data from each week were refined using a Pawley whole pattern refinement on the TOPAS academic software package. The initial

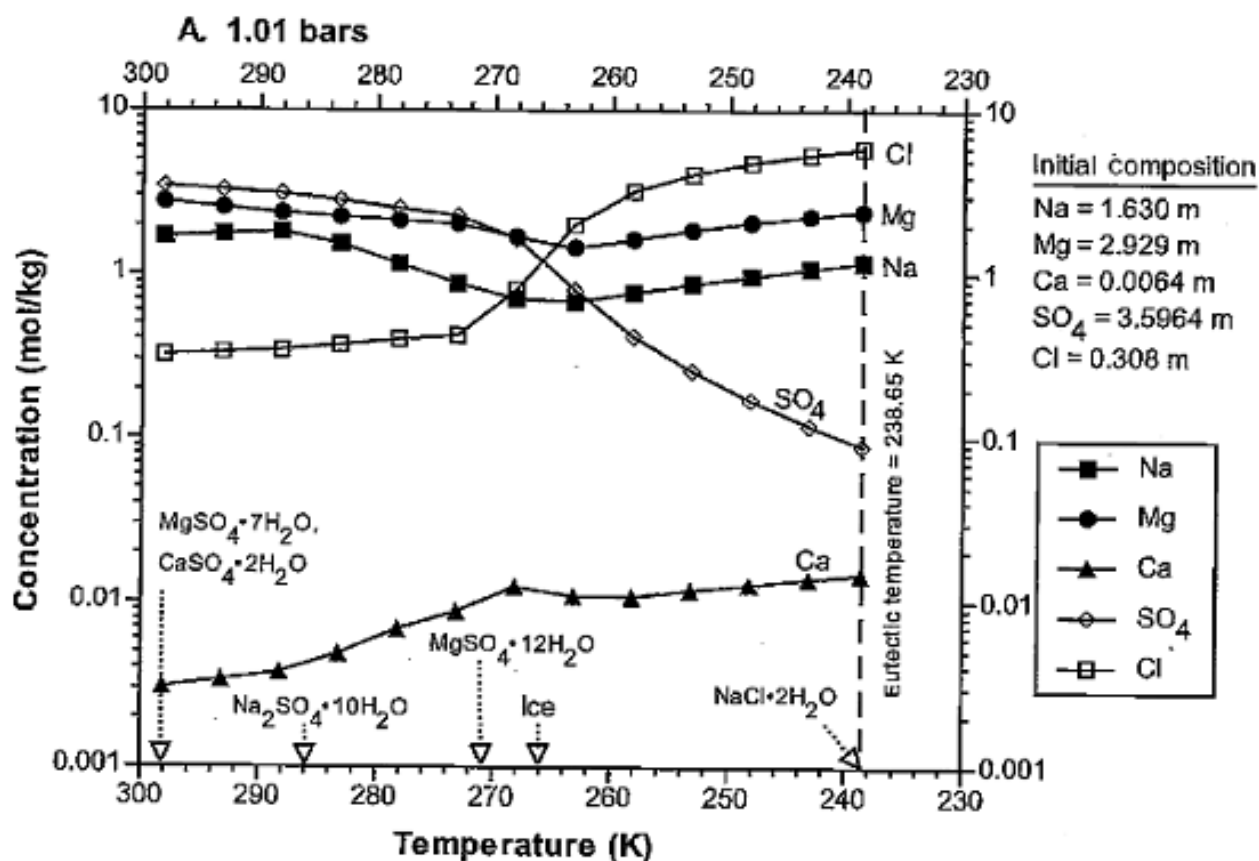


Figure 9.8: Modelled changes in solution composition and associated mineral precipitates based on the output of the thermodynamic model FREZCHEM (Courtesy of Benjamin Butler).

lattice parameters for each mineral used are shown in Table 9.2.

The Pawley whole pattern refinement allowed us to calculate the total crystalline area of each mineral present. These values were then normalised to a diamond peak from the diamond windows which cover the samples to allow for long-term changes in the beam intensity. From this the wt% of minerals present in each diffraction pattern from the weekly data collection could be determined. The results are shown in Figs. 9.9

Table 9.2: Initial lattice parameters used in Pawely refinement.

Salt	Lattice parameter (\AA)
$\text{NaSO}_4 \cdot 10\text{H}_2\text{O}$ (mirabilite)	$a = 12.82; b = 10.35; c = 11.48$
$\text{MgSO}_4 \cdot 7\text{H}_2\text{O}$ (epsomite)	$a = 11.86; b = 11.99; c = 6.858$
$\text{MgSO}_4 \cdot 11\text{H}_2\text{O}$ (meridianiite)	$a = 6.78; b = 6.733; c = 8.137$
$\text{CaSO}_4 \cdot 2\text{H}_2\text{O}$ (gypsum)	$a = 5.679; b = 15.202; c = 6.522$
Hexagonal ice	$a = 4.497479; b = 7.322382$

to 9.14. For this work we have used a linear approach to describe the evolution of the minerals during the LDE experimental run using the function:

$$wt\% = mt + c \quad (9.1)$$

Fitting Eq.(9.1) to the experimental data provided a correlation coefficient (R) parameter. The values of the coefficient m , the constant c and the correlation coefficient, R , are shown in Tables.9.3 and 9.4.

Table 9.3: The values of the coefficient m , the constant c and the correlation coefficient, R for the results obtained from the LDE experimental run for days 0–190.

Mineral	Days 0–190						
	m (Day ⁻¹)	c	R	n	z	σ	$ z/\sigma $
Evolution of MS7	0.0620 ±0.0335	16.96 ±3.52	0.4878	13	0.5332	0.3162	1.6860
Evolution of MS11	-0.1039 ±0.0431	53.70 ±4.53	-0.5879	13	-0.6745	0.3162	2.1330
Evolution of CS2	0.0799 ±0.0425	11.35 ±4.38	0.5312	11	0.5918	0.3536	1.6740

As can be seen from Fig. 9.12 to 9.14, a comparison of the mineral evolution was also plotted. These plots show that the only relationship that exist seems to be between that of meridaniite and gypsum (Fig. 9.12). The experimental data in Fig. 9.12 can also be fitted using a linear function. The value of these coefficients were $m = -0.7564 \pm 0.2433$ and $c = 57.7300 \pm 4.8350$, with $R = -0.6839$ and $|z/\sigma| = 2.6500$, which is not really significant.

According to the FREZCHEM model, we should be able to fit mirabilite to the diffraction patterns using TOPAS. However, fitting both meridaniite and mirabilite proved challenging as it was not possible to obtain crystalline fits for both minerals simultaneously. Therefore, the mineral which provided the overall best fit when fitted in conjunction with gypsum, epsomite and ice was assumed to be present, in this case meridaniite.

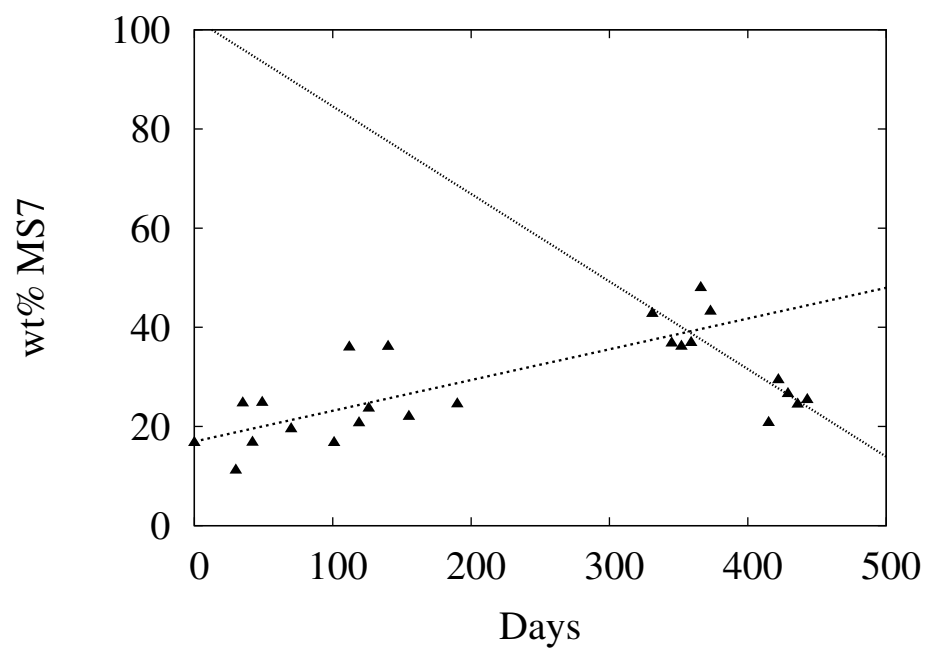


Figure 9.9: Evolution of epsomite during the LDE experimental run.

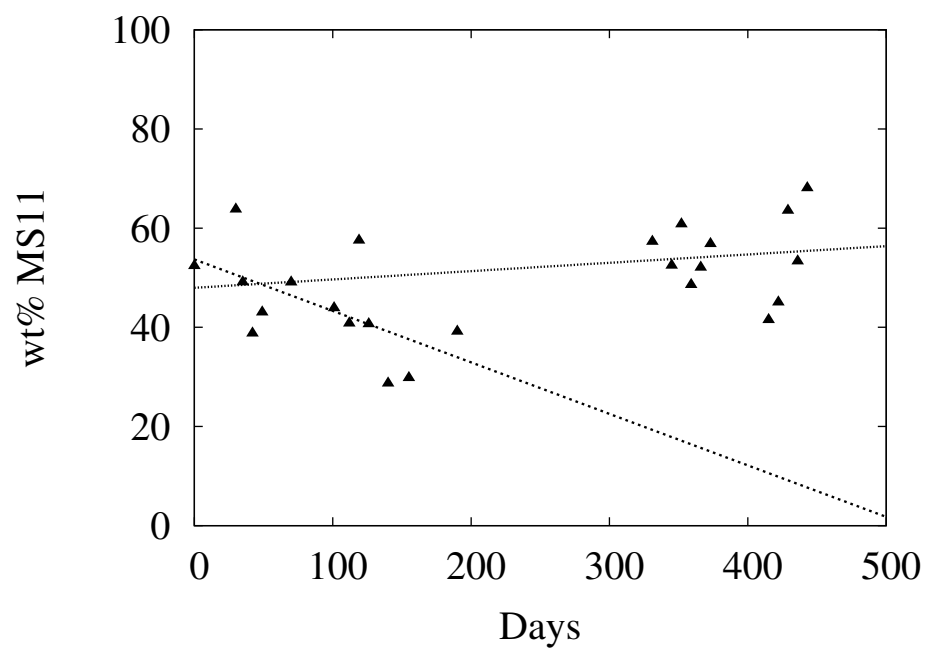


Figure 9.10: Evolution of meridianiite during the LDE experimental run.

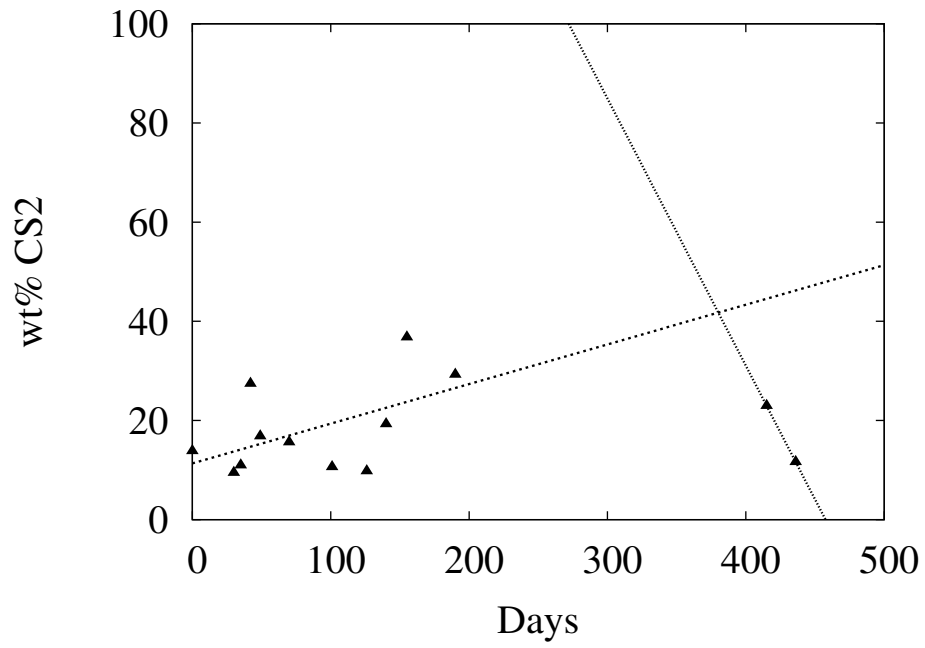


Figure 9.11: Evolution of gypsum during the LDE experimental run.

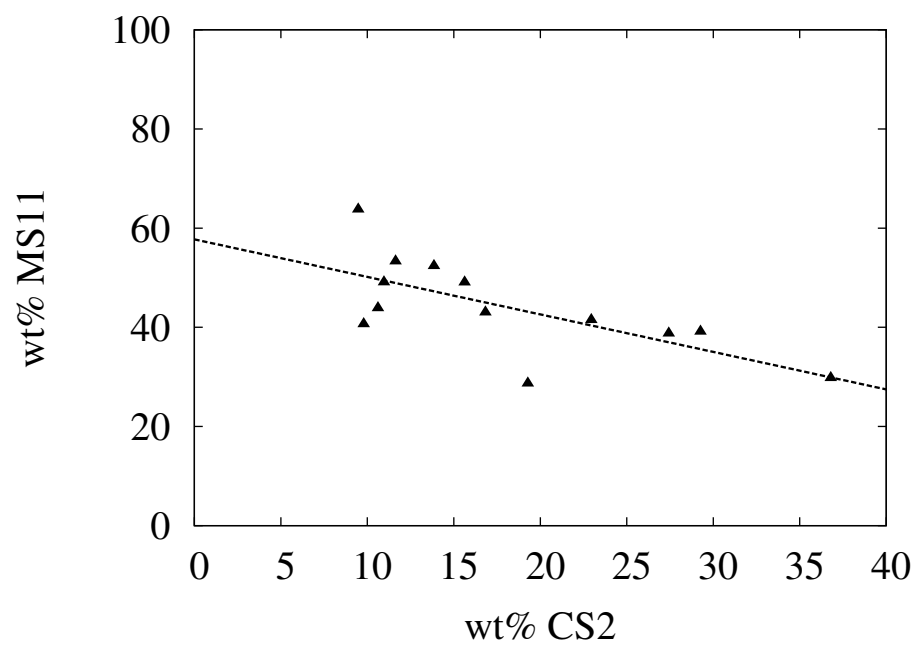


Figure 9.12: Comparison of the evolution of meridianiite versus gypsum during the LDE experimental run.

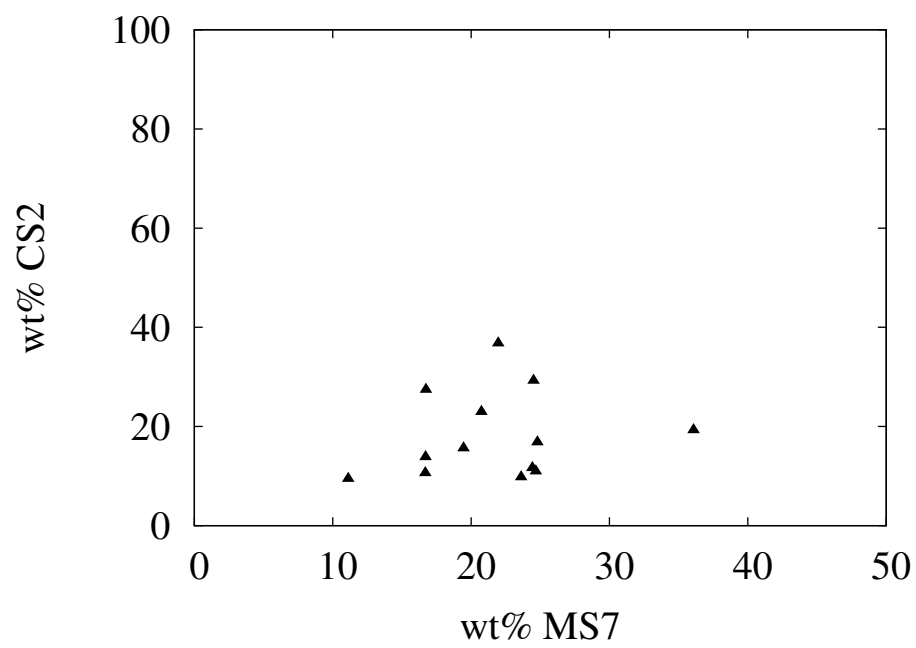


Figure 9.13: Comparison of the evolution of gypsum versus epsomite during the LDE experimental run.

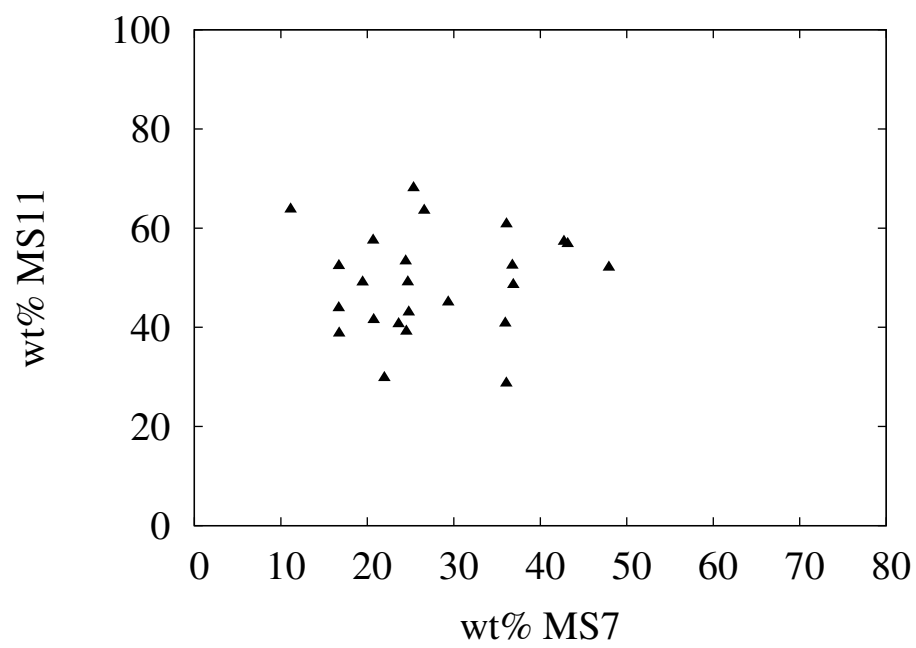


Figure 9.14: Comparison of the evolution of meridianiite versus epsomite during the LDE experimental run.

Table 9.4: The values of the coefficient m , the constant c and the correlation coefficient, R for the results obtained from the LDE experimental run for days 331–443.

Mineral	Days 331–443						
	m (Day ⁻¹)	c	R	n	z	σ	$ z/\sigma $
Evolution of MS7	-0.1767 ±0.0419	102.20 ±16.38	-0.8143	11	-1.1397	0.3536	-3.220
Evolution of MS11	0.0168 ±0.0639	47.97 ±24.95	0.08730	11	0.0875	0.3536	0.2470
Evolution of CS2	-0.5389	246.60	-1.0000	2.0000	-	-	-

The experimental data are split into two sections; days 0–190 and days 331–443. In the period 191–330, no data were collected due to shutdown of the beamline. During this shutdown the R value seems to change, indicating a change in the behaviour of the mineral evolution. When comparing the evolution of merdianiite to that of gypsum (Fig 9.12), we see the emergence of an approximately linear relationship as shown by the $R = -0.6839$ and $|z/\sigma| = 2.6500$. The same cannot be said for the evolution of the gypsum and epsomite (Fig. 9.13), and of the meridiannite and epsomite (Fig. 9.14). The clustering of the data indicates no correlation between these data.

9.5.3 Discussion

Of the mineral precipitates thought to be present in Europa's ocean, both epsomite and mirabilite are also suggested to be present on Europa's surface (Zolotov & Shock 2001), as indicated by reflectance spectroscopy from the Galileo spacecraft. This could suggest that the surface conditions favour the production of highly hydrated sodium sulphates as opposed to magnesium sulphate. However, Zolotov & Shock (2001) suggest that sulphur, magnesium, calcium and potassium may be some of the major elements constituting Europa's saline ocean. Indeed, Kargel et al. (1991, 2000) are in favour of an ocean composition of aqueous $\text{MgSO}_4\text{-H}_2\text{O}$ in equilibrium with crystalline ice and Mg sulphates. This, in contrast to Europa's surface, suggests that highly hydrated magnesium sulphates are more likely to form as opposed to sodium sulphates.

Zolotov & Shock (2001) performed freezing calculations on a European water composition. They found complete freezing occurred below -36°C and at -36°C , only 0.31% of the initial aqueous solution remained unfrozen. Table 9.5 shows the temperatures at which each mineral precipitated, obtained from their calculations.

If we compare the results obtained by Zolotov & Shock (2001) to those obtained during this experiment we see they do not anticipate the formation of epsomite whereas we do. The Zolotov & Shock (2001) observations of the formation of KCl cannot be compared to our results as its precipitation temperature according to these authors is -29.1°C , which is lower than our lowest freezing temperature (-28°C) and we do not

Table 9.5: Mineral precipitation temperatures obtained from calculations by Zolotov & Shock (2001).

Salt	Precipitation temperature (°C)
CaSO ₄ ·2H ₂ O (gypsum)	-0.3
ice	-0.3
NaSO ₄ ·10H ₂ O (mirabilite)	-3.5
MgSO ₄ ·11H ₂ O (meridianiite)	-6.2
KCl (sylvite)	-29.1
NaCl·2H ₂ O (hydrohalite)	-35.4

include it in our initial composition. In the case of hydrohalite, we also anticipate its formation and at a similar temperature to that predicated by Zolotov & Shock (2001) i.e. -35°C . However, as stated, we only freeze to -28°C . The difference in final mineral precipitates is due to difference in initial salt concentrations and compositions.

Additionally, the important point to note in the comparison of the results presented in this section to that of Zolotov & Shock (2001), is that their models predict the presence of both meridianiite and mirabilite, while we observe meridianiite alone. It is noted by Zolotov & Shock (2001), that the formation of mirabilite decreases the abundance of Na^+ in the solution. However, the concentration of SO_4^{2-} continues to increase until $\text{MgSO}_4\cdot 11\text{H}_2\text{O}$ precipitates. This suggests that the formation of $\text{MgSO}_4\cdot 11\text{H}_2\text{O}$ is the cause of the decreases in abundance of Mg^{2+} and sulphate as the solution is frozen, and is therefore the dominant sink for sulphate. In terms of the results presented in this section, this could be the explanation of why we cannot fit mirabilite to our diffraction data, i.e. it does not precipitate or its abundance may be negligible due to a possible preferred reaction of Mg^{2+} and SO_4^{2-} .

An alternative interpretation of the results can be reached if we take into consideration the observation in Section 9.3. The mineral precipitates could again be forming brine channels in the ice. Due to the limited sample area which is subjected to the beam during the experiment, and in addition to the supposed preferred reaction of Mg^{2+} and SO_4 , there could a limited number of mirabilite brine channels forming

compared to that of meridianiite. Hence, the probability of observing meridianiite as opposed to mirabilite in our experimental data is greater.

Fig. 9.1 shows the pattern in data collection during the LDE run. As mentioned, the results discussed in this section were collected on the same experiment as those discussed in Section 9.2. In the process of this data collection, a coolant leak occurred which meant the samples has to be re-heated and cooled again in order for the experiment to continue and reach its lowest temperature. After the coolant leak the first data recorded were at a temperature of -6.4°C , which represents the first data collected from our “Europa” sample, and hence the first data point on Figs. 9.9 to 9.14. Additionally, there is period of 139 days where no data were collected; this was due to shutdown of the beamline.

The primary result to note from our experiment is the change in the R and $|z/\sigma|$ values during the evolution of our mineral precipitates. Looking at Table. 9.3, we see both epsomite and gypsum start with positive R values of 0.4878 and 0.5312 respectively, showing their increase in concentration as the experiment continues. However, the $|z/\sigma|$ values are 1.6860 and 1.6740 for epsomite and gypsum respectively indicating the results are not very significant. Meanwhile meridianiite initially shows a negative R value of -0.5879 with $|z/\sigma| = 2.1330$, showing a decrease in wt% of meridianiite from days 0–190 which is more significant, but still only marginal, than the increase in epsomite and gypsum during this period. These results could indicate that, once formed, meridianiite accelerates the growth of both epsomite and gypsum due to the increase in concentration of the calcium and magnesium ions in solution, as indicated on Fig. 9.8. This is most likely due to the large concentration of water removal from solution due to the formation of meridianiite. However, after the 330th day, the wt% of meridianiite seems to increase, but there is no linear correlation ($R=0.0873$ and $|z/\sigma| = 0.2470$). Conversely, after the 330th day the wt% of epsomite decreases as indicated by $R=-0.8143$; here $|z/\sigma| = 3.220$ showing that this decrease is reasonably significant. Nothing, however, can be said of gypsum as there are only two data points in the period of days 331–443. This could be attributed to meridianiite becoming more stable as temperature is decreased, allowing epsomite to convert into meridianiite, which in

turn uses most of the water in solution possibly leading to less gypsum forming.

Figs. 9.12 to 9.14 show comparisons of the evolution of minerals formed during the LDE experimental run. It is immediately apparent from Figs. 9.13 and 9.14 that there is no correlation between the wt% of gypsum versus epsomite or meridianiite versus epsomite. However, from Fig. 9.12 we see that there is a negative correlation between the wt% of meridianiite versus gypsum, hence confirming the FREZCHEM model results and that the formation of meridianiite in this experiment could indeed be inhibiting the formation of gypsum. This suggests a potential seasonal change in the pH and salinity conditions in Europa's sub-surface ocean due to changes in the salts, which may have astro-biological implications.

There is a region in the Canadian High Arctic at the Borup Fiord pass that presents a unique glacial spring system (Gleeson et al. 2010). This system originates from a glacial surface and deposits gypsum, elemental sulphur and calcite (CaCO_3) in regions at the site. These deposits could provide a terrestrial analogue to non-ice surface material thought to be present on Europa as the simultaneous occurrence of sulphur springs and glacial ice is, terrestrially, extremely rare. Samples were collected from this site by Gleeson et al. (2010) with one of the objectives being to evaluate the possibility that the sulphur-rich deposits could contain biosignatures associated with the present microbial community. It is expected that pure sulphur will react with oxygen and water to form gypsum (Gleeson et al. 2010). Due to the fact that sulphur produced by the microbes exhibits a more complicated structure, Gleeson et al. (2010) was able to conclude that sulphur being taken up by oxygen was replenished by micro-organisms.

Sulphur-rich materials are present on the surface of Europa in cracks and ridges. Gleeson et al. (2010) speculate as to whether the origin of these sulphur-rich materials are from organic compounds in the ice in Europa's sub-surface ocean. From our results, however, it is possible that the presence of sulphur on Europa's surface is due to gypsum's apparent inability to form in the presence of meridianiite at low temperatures.

9.5.4 Conclusion

In this section, results are presented from subjecting an aqueous saline solution replicating that of Europa's ocean to long-duration freezing experiments. This was done using the LDE facility on Diamond's X-ray powder diffraction beamline I11. From the results, it is found that:

1. using novel experimental methods, Europa's oceans could indeed be Mg and SO_4 rich, suggesting the dominant sink of sulphates in the ocean is due to the presence of meridianiite and not mirabilite;
2. the mineral precipitates could be forming brine channels in the ice. Due to the limited sample area which is subjected to beam during the experiment, in addition to the supposed preferred reaction of Mg and SO_4 , there could be a limited number of mirabilite brine channels forming compared to that of meridianiite. Hence, the probability of observing meridianiite as opposed to mirabilite in our experimental data is greater;
3. initial formation of meridianiite accelerates the growth of both epsomite and gypsum due to the increase in concentration of the calcium and magnesium ions in solution;
4. as temperature decreases, meridianiite seems to become more stable. This suggests epsomite converts to meridianiite, which in turn uses most of the water in solution, inhibiting the formation of gypsum;
5. the presence of sulphur-rich material on the surface of Europa could be due to gypsum's inability to form at low temperatures in the presence of meridianiite, rather than the presence of organic compounds in the ice in Europa's subsurface ocean;
6. the change in salt concentrations suggests that thermal cycling could have a significant impact on ocean composition on Europa. This implies a poten-

tial change in the pH and salinity conditions in the ocean, which has astrobiological implications, hence highlighting the importance of future studies.

10 Conclusions and future work

The work presented in this thesis is a result of experimental investigations of clathrate hydrates and hydrated minerals. Investigations were carried out at DLS using SXPD to study the properties and behaviour of clathrates in presence of saline solutions, with relevance to icy Solar System bodies. SXPD was also used, and in some cases along with Raman spectroscopy, to investigate the structure and behaviour of hydrated minerals thought to be present on Mars and Europa. The novel features of this work include:

1. using SXPD to investigate the formation and dissociation mechanisms and temperatures of CO₂ and CH₄ clathrate hydrates in the presence of varying salt concentrations and pressures;
2. using SXPD and Raman spectroscopy in order to determine whether changes in the structure of hydrated magnesium sulphate are real at low temperatures;
3. investigating the behaviour of meridianiite and its interaction with ice using the LDE at DLS. This allowed the long-term behaviour (~ 8 months) of meridianiite to be studied for the first time;
4. the long-term behaviour of a sample representative of Europa's saline ocean were also studied for the first time using the LDE.

The motivation for this work is that clathrates are thought to support life (Prieto-Ballesteros & Muñoz-Iglesias 2014), and for life to occur one of the essential ingredients is water. The presence of clathrates could also be related to the (bio)geochemistry of planetary environments. Therefore, investigations into clathrates in the presence of saline solutions and the behaviour of hydrated minerals at low temperatures, while lacking in current literature, is essential to aid in our understanding of planetary environments and geology. This could lead us to establishing a greater understanding of the possible emergence of life in our Solar System.

10.1 Astrophysical implications of forming clathrate in saline solutions

By the use of in situ SXRPD we have:

1. studied the formation, dissociation and thermal expansion properties of CO₂ clathrate hydrates formed in MgSO₄ salt solutions at salinities, temperatures and pressures representative of the likely conditions on icy moons such as Europa and Enceladus;
2. studied the effect that different polymorphs of ice have on the formation of clathrate hydrates in the presence of aqueous chloride solutions;
3. investigated the formation, dissociation, buoyancy and thermal expansion properties of CH₄ clathrates formed in ammonium sulphate salt solutions.

From these experimental studies, it is concluded that the salt solutions used inhibit both CO₂ and CH₄ clathrate formation, by observing that clathrates form and dissociate at lower temperatures in the presence of the salt solutions. Additionally, we have computed the density of CO₂ and CH₄ clathrates formed in MgSO₄ and (NH₄)₂SO₄ salt solutions at various temperatures and pressures. A comparison of these densities were made to the density of the solution in which they were formed. While it was found that the density of the clathrate depends on temperature and pressure, when compared to the density of the salt solution in which they were formed CO₂ clathrates should in general sink, while CH₄ clathrates would float. This conclusion is irrespective of temperature and pressure as far as CO₂ clathrates relevant to Europa and Enceladus are concerned. However, there are varying suggestions in the literature as to the density of Titan's sub-surface ocean, but if the ocean density was less than 0.91 g cm⁻³ then the CH₄ clathrates would sink. This implies that the atmospheric source of methane on Titan may not originate from outgassing via cryovolcanoes as previously suggested (Fortes et al. 2007). Furthermore, we have shown that, in the presence of a low temperature phase of ice and/or ammonium sulphate precipitate,

we observe CH_4 clathrates dissociating more readily. This would further decrease the ability of the clathrates to rise to the surface of Titan, which is again consistent with the conclusion that cryovolcanoes may not be the source of atmospheric CH_4 .

10.2 Effects of ice polymorphs on clathrate dissociation

Polymorphs of the ice phases formed in conjunction with clathrates in the presence of chloride salt solution were also investigated. These results have relevance to the cryosphere of Mars, and we have shown for the first time that clathrate hydrates can form in the cryosphere of Mars despite the presence of salts. It was found that Ih ice was the dominant phase throughout the experiment, despite the expectation of Ic being the thermodynamically stable polymorph at lower temperatures. It is concluded that this may be due to the chloride salt solutions inhibiting the transformation from Ih to Ic. Alternatively, it is suggested that during the formation of clathrates in the chloride solutions, ice I could be forming, which embodies structural aspects of both Ih and Ic as opposed to pure phase Ic, implying the possibility of ice I being the dominant phase of ice within the Martian cryosphere. This would provide an explanation for unexpectedly small wt% of Ic formed even at the lowest temperatures (~ 90 K) reached in this investigation. Additionally, observations of features consistent with Ic at 170 K were made; however, this is hypothesised to be due to the ratio of Ih and Ic in ice I varying with temperature. It is also shown that when the low-temperature phase of ice does form its presence seems to provide an easier diffusion pathway for clathrate dissociation. Furthermore it is concluded that the cation present in the salts used (and their inhibiting effect) seems to have a more significant impact on the ice formed, and therefore clathrate formation, than the concentration of the salt used. We have also shown that, in the presence of a low temperature phase of ice and/or ammonium sulphate precipitate, CH_4 clathrates seem to dissociate more readily. This is another factor that could prevent the rising of clathrates to the surface of Titan,

again suggesting that cryovolcanoes may not be the source of atmospheric CH_4 .

10.3 Behaviour of hydrated minerals on planetary bodies

By the use of SXRPD and Raman spectroscopy it is concluded that the existence of a low temperature structural phase change in epsomite is unlikely. However, the possible existence of a second polymorph of epsomite cannot be definitively ruled out (see Chapter 8 and Fortes (2005)).

Formation of MS11 was achieved from freezing a highly concentrated solution of epsomite. From this it was deduced that, in order for MS11 to grow, the ice particles which form initially must break up into smaller particles, as shown in the experimental SXRPD data by the broadening of the ice peaks. This phenomenon was seen in the results from both the LDE, and later confirmed by a in-situ time-resolved experiment in EH1. This is suggested to arise due to MS11 forming brine channels in the ice. Hence, it is possible, if the density of brine channels in the ice is high enough, that the ice could weaken and this would affect the mechanical properties of ice by increasing the grain boundary slipping, hence decreasing the shear strength. This could reduce ice rheology and alter bulk flow properties. In addition to this it was found that thermal cycling of ice produces more intense ice peaks. It is thought that this could be due to the ice showing the so-called “memory effect”. This has implication for icy Solar System bodies (e.g. Martian polar ice caps) as this “memory effect” could suggest more ice than previously thought is forming as a result of thermal cycling from seasonal temperature changes.

Additionally, work was carried out on meridianiite by subjecting an aqueous saline solution replicating that of Europa’s ocean to long-duration freezing experiments. This was done using the LDE facility on beamline I11. From this study it was concluded that Europa’s oceans may be Mg^{2+} and SO_4^{2-} rich. This implies that the dominant sink of sulphates in the ocean is due to the presence of meridianiite and

not mirabilite. Furthermore, it is concluded that there could be a limited number of mirabilite brine channels forming compared to that of meridianiite, suggesting that the probability of observing meridianiite as opposed to mirabilite during the experimental run is greater. During the LDE run we also observed that, despite epsomite being the first hydrated mineral to form (along with gypsum), as temperature is lowered it converts to meridianiite. This causes most of the water in solution to be used up, hence inhibiting the formation of gypsum. This has implications for Europa's possible inhabitance as presence of sulphur-rich material is suggested to be due to the organic compounds in the ice of Europa's sub-surface ocean (Gleeson et al. 2010). However, due to the fact that gypsum is thought to form from the combination of sulphur and oxygen, our results indicate that the presence of sulphur-rich material could be due to gypsum's inability to form at low temperatures in the presence of meridianiite.

10.4 Future work

10.4.1 Low pressure clathrate formation

The work in this thesis presents results from the in situ formation of CO_2 and CH_4 clathrates by subjecting frozen aqueous salt solutions to gas pressures between 5–26 bar to replicate the likely sub-surface ocean compositions and pressures found on Enceladus, Europa and Titan. These results, whilst simulating the high pressure environments found in sub-surface oceans, do not give any indication of the formation mechanisms of clathrates in *low pressure* environments, such as those found in Titan's atmosphere and on comets (Iro et al. 2003; Mousis et al. 2011). Indeed, it is thought that clathrates in the early solar nebula are responsible for the depletion of N_2 on cometary bodies, and that clathrates on the surface of Titan are responsible for Kr and Xe depletion in its atmosphere. Therefore, a low pressure gas cell, which has been constructed at DLS, could be used to form N_2 , Kr and Xe clathrates under low pressure environments. This could provide SXRPD and Raman data which could be used as

references for future remote sensing missions.

10.4.2 Nature of ice

During the experimental investigations of clathrates in saline solutions, abnormal behaviour of ice was also observed i.e. the absence of Ic at low temperatures. We have suggested this may be due to the fact that the salts in solution are affecting ice transformation rates and/or we are forming a ice I, a hybrid polymorph of Ih and Ic. These hypotheses are not confirmed or disproven in this thesis. Future work on ice polymorphs in the context of icy Solar System bodies could include the formation of ice and clathrates individually and simultaneously in various saline solutions on I11 over longer time-scales than possible in this thesis work. With these data, a comparison of ice polymorphs formed could be made. In this way, the questions regarding ice polymorphs in this thesis could be answered. These results could enable us to determine the behaviour of ice on Solar System, bodies providing a greater insight to their surface geology.

10.4.3 Meridianiite

Meridianiite is thought to be widespread on Mars (Peterson & Wang 2006) and chemical models predict it to be the most abundant phase (Freeman et al. 2007). Therefore meridianiite could be the most likely source of water on the present day surface of Mars. Studies of the equilibrium stability of MgSO_4 reveal a possible cycling between meridianiite and other hydrated phases during the Martian day (120–293 K) (Peterson & Wang 2006). However, the hydration–dehydration pathway between these hydrated states is poorly understood due to strong contributions of kinetics over thermodynamics (Wang et al. 2009); therefore it is currently challenging to accurately predict phase transitions under Martian conditions. Also, data on meridianiite in current literature are lacking; systematic in situ SXRPD would fill this gap, and allow H_2O loss to be observed at both a structural and molecular level. Raman data are also useful as these

instruments are frequently placed aboard planetary landers. Therefore, by the use of SXRPD on I11, it is possible to observe in situ phase transitions between meridianiite and epsomite and its temperature dependence. Additionally, the use of SXRPD will allow the characterisation of thermal effects on the structure of meridianiite on Mars to be made. Hence, these data could serve as a reference to the XRD facility on CheMin aboard the Curiosity Mars Rover (Dehouck et al. 2014) and any other X-ray facilities on future landers.

10.4.4 Sulphur bearing materials on Europa

Sulphur is thought to be a component of some of the non-water ice materials thought to be present on the surface of Europa (e.g. SO_2 and H_2S), and is also one of the gases thought to be trapped in clathrate structures (Prieto-Ballesteros et al. 2005). In addition to this, sulphur-rich materials are present on the surface of Europa in crack and ridges (Gleeson et al. 2010), with suggestions it could arise from organic compounds in the ice of Europa's sub-surface ocean. Therefore future experiments on the formation, dissociation and density of sulphur-bearing clathrates formed in saline solution could provide an insight to the origin of the surface sulphur on Europa. Indeed, Prieto-Ballesteros et al. (2005) has shown by modelling, that in a eutectic composition of the system $\text{MgSO}_4\text{-H}_2\text{O}$, SO_2 clathrates would sink to the ocean floor, implying the source of the surface sulphur could not be of clathrate origin, and supporting the hypotheses of sulphur being of microbial origin. Conversely, Prieto-Ballesteros et al. (2005) also states that in a much lower salinity ocean, SO_2 clathrates would float, hence casting doubt on the microbial hypothesis. Furthermore these results arise from theoretical modelling data, which leaves the need for experimental data to confirm the sinking/floating scenarios of SO_2 clathrates.

The general objective of the Jupiter ICy moons Explorer (JUICE) is to explore the emergence of habitable worlds around gas giants (Lorente et al. 2017). Specifically for Europa, the focus of the JUICE mission is on a) identifying organic molecules and b) understanding how some of the surface features formed. This will aid in

understanding the composition of the chemistry thought to be essential to support life. It is also hoped that JUICE will provide the first estimation of the minimum ice thickness of the crust over the most active surface regions (Lorente et al. 2017). Therefore, experimental work on forming SO₂ clathrates in situ using beamline I11 could be used in conjunction with results obtained from various science payloads on JUICE (e.g. Moons And Jupiter Imaging Spectrometer (MAJIS), Submillimeter Wave Instrument (SWI) and Radar for Icy Moon Exploration (RIME)) to help confirm the origin of Europa's surface sulphur.

Bibliography

- Alibert, Y. & Mousis, O. 2007, *A&A*, 465, 1051
- Ambuehl, D. & Elwood Madden, M. 2014, *Icarus*, 234, 45
- Atreya, S. K., Donahue, T. M., & Kuhn, W. R. 1978, *Science*, 201, 611
- Baird, A. K., Toulmin, III, P., Rose, Jr., H. J., et al. 1976, *Science*, 194, 1288
- Baker, V. R. 2009, *Annual Review of Earth and Planetary Sciences*, 37, 393
- Bellucci, A., Sicardy, B., Drossart, P., et al. 2009, *Icarus*, 201, 198
- Bergin, E. A., Lellouch, E., Harwit, M., et al. 2000, *The Astrophysical Journal Letters*, 539, L147
- Beuthe, M. 2015, *Icarus*, 258, 239
- Bibring, J.-P., Arvidson, R. E., Gendrin, A., et al. 2007, *Science*, 317, 1206
- Bilderback, D. H., Elleaume, P., & Weckert, E. 2005, *Journal of Physics B Atomic Molecular Physics*, 38, S773
- Bouquet, A., Mousis, O., Waite, J. H., & Picaud, S. 2015, *Geophysical Research Letters*, 42, 1334
- Bragg, W. H. & Bragg, W. L. 1913, *Proc. R. Soc. Lond. A.*, 88, 428
- Burt, D. M. & Knauth, L. P. 2003, *Journal of Geophysical Research (Planets)*, 108, 8026
- Carlson, R., Smythe, W., Baines, K., et al. 1996, *Science*, 274, 385
- Carlson, R. W., Anderson, M. S., Johnson, R. E., et al. 1999, *Science*, 283, 2062
- Carr, M. H. 1986, *Icarus*, 68, 187

- Carr, M. H. 1996, *Water on Mars* (Oxford Uni. Press)
- Chassefière, E., Dartois, E., Herri, J.-M., et al. 2013, *Icarus*, 223, 878
- Chastain, B. K. & Chevrier, V. 2007, *Planetary and Space Science*, 55, 1246
- Chipera, S. J., Vaniman, D. T., Bish, D. L., Carey, J. W., & Feldman, W. C. 2005, in 36th Annual Lunar and Planetary Science Conference, Vol. 36
- Chou, I. M. & Seal, R. R. 2007, *Journal of Geophysical Research (Planets)*, 112, E11004
- Choukroun, M., Grasset, O., Tobie, G., & Sotin, C. 2010, *Icarus*, 205, 581
- Christensen, P. R., Wyatt, M. B., Glotch, T. D., et al. 2004, *Science*, 306, 1733
- Clark, B. C. 1993, *Geochimica et Cosmochimica Acta*, 57, 4575
- Clark, B. C. 1998, *Journal of Geophysical Research (Planets)*, 103, 28545
- Clark, B. C., Morris, R. V., McLennan, S. M., et al. 2005, *Earth and Planetary Science Letters*, 240, 73
- Clark, B. C. & van Hart, D. C. 1981, *Icarus*, 45, 370
- Clegg, S. L. & Wexler, A. S. 2011, *The Journal of Physical Chemistry A*, 115, 3393
- Clifford, S. M. 1993, *Journal of Geophysical Research*, 98, 10
- Clifford, S. M. 1998, in 29th Lunar and Planetary Science Conference, Vol. 29
- Clifford, S. M., Lasue, J., Heggy, E., et al. 2010, *Journal of Geophysical Research (Planets)*, 115, E07001
- Clifford, S. M. & Parker, T. J. 2001, *Icarus*, 154, 40
- Coelho, A. 2007, <http://www.topas-academic.net/>
- Cottin, H., Kotler, J. M., Bartik, K., et al. 2017, *Space Science Review*, 209, 1

- Coustenis, A., Lellouch, E., Maillard, J. P., & McKay, C. P. 1995, *Icarus*, 118, 87
- Craddock, R. A. & Greeley, R. 2009, *Icarus*, 204, 512
- Crystal Impact. 2003, Match!, phase identification from powder diffraction (computer software), version 1.11
- Culka, A., Košek, F., Drahotka, P., & Jehlička, J. 2014, *Icarus*, 243, 440
- Dalton, J. B., Prieto-Ballesteros, O., Kargel, J. S., et al. 2005, *Icarus*, 177, 472
- Dartois, E., Duret, P., Marboeuf, U., & Schmitt, B. 2012, *Icarus*, 220, 427
- Davy, H. 1811, *Philosophical Transactions of the Royal Society*, 101, 1
- Day, S. J., Thompson, S. P., Evans, A., & Parker, J. E. 2015, *Astronomy and Astrophysics*, 574, A91
- de Mooij, E. J. W., Brogi, M., de Kok, R. J., et al. 2012, *Astronomy and Astrophysics*, 538, A46
- Dehouck, E., McLennan, S. M., Meslin, P.-Y., & Cousin, A. 2014, *Journal of Geophysical Research (Planets)*, 119, 2640
- Dholabhai, P. D., Parent, J. S., & Bishnoi, P. R. 1996, *Industrial & Engineering Chemistry Research*, 35, 819
- Dowell, L., Moline, S., & Rinfret, A. 1962, *Biochimica et Biophysica Acta*, 59, 158
- Downes, D. & Genzel, R. 1980, in *Giant Molecular Clouds in the Galaxy*, ed. P. M. Solomon & M. G. Edmunds, 161–179
- Duan, Z. & Sun, R. 2006, *American Mineralogist*, 91, 1346
- Elder, F. R., Gurewitsch, A. M., Langmuir, R. V., & Pollock, H. C. 1947, *Physical Review*, 71, 829

- Elwood Madden, M. E. & Bodnar, R. J. 2002, in 33rd Lunar and Planetary Science Conference, Vol. 33
- Falenty, A., Hansen, T. C., & Kuhs, W. F. 2011, arXiv:1510.08004
- Fanale, F. P. 1976, *Icarus*, 28, 179
- Fawcett, T. G., Faber, J., Kabbekodu, S., McClune, F., & Rafaja, D. 2005, in *Misrostructure Analysis in material Science*, Freiberg
- Feldman, W. C., Mellon, M. T., Maurice, S., et al. 2004, *Geophysical Research Letters*, 31, L16702
- Fortes, A. D. 2005, *Axis*, 1, 1
- Fortes, A. D. 2007, *Icarus*, 191, 743
- Fortes, A. D., Grindrod, P. M., Trickett, S. K., & Vočadlo, L. 2007, *Icarus*, 188, 139
- Fortes, A. D., Wood, I. G., Alfredsson, M., Vocadlo, L., & Knight, K. S. 2006, *Eur. J. Mineral*, 18, 449
- Freeman, J. J., Wang, A., & Jolliff, B. L. 2007, in *Lunar and Planetary Science Conference*, Vol. 38, Lunar and Planetary Science Conference, 1197
- Gellert, R., Rieder, R., Anderson, R. C., et al. 2004, *Science*, 305, 829
- Gendrin, A., Mangold, N., Bibring, J.-P., et al. 2005, *Science*, 307, 1587
- Gibb, E. L., Whittet, D. C. B., Boogert, A. C. A., & Tielens, A. G. G. M. 2004, *The Astrophysical Journal Supplement Series*, 151, 35
- Gleeson, D. F., Pappalardo, R. T., Grasby, S. E., et al. 2010, *Remote Sensing of Environment*, 114, 1297
- Gough, R. V., Chevrier, V. F., & Tolbert, M. A. 2016, *Planetary and Space Science*, 131, 79

- Grazulis, S., Chateigner, D., Downs, R. T., et al. 2009, *J. Appl. Cryst.*, 42, 726
- Grindrod, P. M., Fortes, A. D., Nimmo, F., et al. 2008, *Icarus*, 197, 137
- Hammond, C. 2009, *The basics of crystallography and diffraction*, 3rd edn. (Oxford Science Publications)
- Hand, K. P. & Carlson, R. W. 2015, *Geophysical Research Letters*, 42, 3174
- Hand, K. P. & Chyba, C. F. 2007, *Icarus*, 189, 424
- Hansen, T. C., Falenty, A., & Kuhs, W. F. 2016, *The Journal of Chemical Physics*, 144, 054301
- Hansen, T. C., Koza, M. M., Lindner, P., & Kuhs, W. F. 2008, *Journal of Physics: Condensed Matter*, 20, 285105
- Haskin, L. A., Wang, A., Jolliff, B. L., et al. 2005, *Nature*, 436, 66
- Hecht, M. H., Kounaves, S. P., Quinn, R. C., et al. 2009, *Science*, 325, 64
- Helled, R. & Guillot, T. 2013, *The Astrophysical Journal*, 767, 113
- Helled, R. & Lunine, J. 2014, *MNRA*, 441, 2273
- Hoffman, N. 2000, *Icarus*, 146, 326
- Hogerheijde, M. R., Bergin, E. A., Brinch, C., et al. 2011, *Science*, 334, 338
- Hsu, H.-W., Postberg, F., Sekine, Y., et al. 2015, *Nature*, 519, 207
- Huang, Y., Zhu, C., Wang, L., et al. 2016, *Science Advances*, 2, e1501010
- Iro, N., Gautier, D., Hersant, F., Bockelée-Morvan, D., & Lunine, J. I. 2003, *Icarus*, 161, 511
- Jakosky, B. M., Grebowsky, J. M., Luhmann, J. G., & Brain, D. A. 2015, *Geophysical Research Letters*, 42, 8791

- Johnson, J. R., Phillips-Lander, C. M., & Elwood Madden, M. E. 2017, in Lunar and Planetary Science Conference, Vol. 48, Lunar and Planetary Science Conference, 2257
- Kang, S.-P., Chun, M.-K., & Lee, H. 1998, *Fluid Phase Equilibria*, 147, 229
- Kargel, J. S., Croft, S. K., Lunine, J. I., & Lewis, J. S. 1991, *Icarus*, 89, 93
- Kargel, J. S., Kaye, J. Z., Head, J. W., et al. 2000, *Icarus*, 148, 226
- Kawamura, T., Komai, T., Yamamoto, Y., et al. 2002, *Journal of Crystal Growth*, 234, 220
- Kereszturi, A., Vincendon, M., & Schmidt, F. 2011, *Planetary and Space Science*, 59, 26
- Kieffer, H. H. 2007, *Journal of Geophysical Research (Planets)*, 112, E08005
- Kieffer, S. W., Lu, X., Bethke, C. M., et al. 2006, *Science*, 314, 1764
- King, P. L., Lescinsky, D. T., & Nesbitt, H. W. 2004, *Geochimica et Cosmochimica Acta*, 68, 4993
- Kivelson, M. G., Khurana, K. K., Russell, C. T., et al. 2000, *Science*, 289, 1340
- Klingelhöfer, G., Morris, R. V., Bernhardt, B., et al. 2004, *Science*, 306, 1740
- Knauth, L. P. & Burt, D. M. 2002, *Icarus*, 158, 267
- Kohl, I., Mayer, E., & Hallbrucker, A. 2000, *Physical Chemistry Chemical Physics (Incorporating Faraday Transactions)*, 2, 1579
- Kuhs, W. F., Genov, G., Staykova, D. K., & Hansen, T. 2004, *Physical Chemistry Chemical Physics (Incorporating Faraday Transactions)*, 6, 4917
- Kuhs, W. F., Staykova, D. K., & Salamatina, A. N. 2006, *The Journal of Physical Chemistry B*, 110, 13283

- Kunz, D. 2001, *J. Phys.: Condens. Matter*, 13, 7499
- Kuzmin, R. O. 1983, *Priroda*, 79
- Langevin, Y., Poulet, F., Bibring, J.-P., & Gondet, B. 2005, *Science*, 307, 1584
- Le Bail, A. 2005, <http://www.cristal.org/iniref/lbm-story>
- Lewis, J. S. 1971, *Icarus*, 15, 174
- Light, B., Maykut, G. A., & Grenfell, T. C. 2003, *Journal of Geophysical Research (Oceans)*, 108, 33
- Ligier, N., Poulet, F., Carter, J., Brunetto, R., & Gourgeot, F. 2016, *The Astronomical Journal*, 151, 163
- Liu, D., Zhang, Y., Chen, C. C., et al. 2007, *PNAS*, 104, 9570
- Lorente, R., Altobelli, N., Vallat, C., et al. 2017, in *EGU General Assembly Conference Abstracts*, Vol. 19, 14611
- Lorenz, R. D., Wood, C. A., Lunine, J. I., et al. 2007, *Geophysical Research Letters*, 34, L07204
- Lunine, J. I., Stevenson, D. J., & Yung, Y. L. 1983, *Science*, 222, 1229
- Macfarlane, D. R. 1986, *Cryobiology*, 23, 230
- Makogon, Y. F. 1997, *Penwell Books*
- Malkin, T. L., Murray, B. J., Salzmann, C. G., et al. 2015, *Phys. Chem. Chem. Phys.*, 17, 60
- Marboeuf, U., Schmitt, B., Mousis, O., & Petit, J. 2010, in *Bulletin of the American Astronomical Society*, Vol. 42, AAS/Division for Planetary Sciences Meeting Abstracts #42, 973

- Marion, G. M. 2009, in LPI Contributions, Vol. 1482, Workshop on Modeling Martian Hydrous Environments, 40–41
- Martínez, G. M. & Renno, N. O. 2013, *Space Science Reviews*, 175, 29
- Martínez, G. M., Renno, N. O., & Elliott, H. M. 2012, *Icarus*, 221, 816
- Matson, D. L., Davies, A. G., Johnson, T. V., Castillo-Rogez, J. C., & Lunine, J. I. 2013, in AAS/Division for Planetary Sciences Meeting Abstracts, Vol. 45, AAS/Division for Planetary Sciences Meeting Abstracts, 416.03
- Max, M. D. & Clifford, S. M. 2000, in Lunar and Planetary Science Conference, Vol. 31, Lunar and Planetary Science Conference
- Mayer, E. & Hallbrucker, A. 1987, *Nature*, 325, 601
- McCord, T. B., Hansen, G. B., Fanale, F. P., et al. 1998, *Science*, 280, 1242
- McCord, T. B., Orlando, T. M., Teeter, G., et al. 2001, *Journal of Geophysical Research*, 106, 3311
- McCusker, L. B., Von Dreele, R. B., Cox, D. E., Louër, D., & Scardi, P. 1999, *Journal of Applied Crystallography*, 32, 36
- McKay, C. P., Hand, K. P., Doran, P. T., Andersen, D. T., & Priscu, J. C. 2003, *Geophysical Research Letters*, 30, 35
- McSween, H. Y., Taylor, G. J., & Wyatt, M. B. 2009, *Science*, 324, 736
- Mehta, M., Renno, N. O., Marshall, J., et al. 2011, *Icarus*, 211, 172
- Mellon, M. T., Feldman, W. C., & Prettyman, T. H. 2004, *Icarus*, 169, 324
- Miller, S. L. 1961, *PANS*, 47, 1798
- Möhlmann, D. T. F. 2010, *Icarus*, 207, 140

- Momma, K., Ikeda, T., Nishikubo, K., et al. 2011, *Nature Communications*, 2, 196
- Moore, E. B. & Molinero, V. 2011, *Phys. Chem. Chem. Phys.*, 13, 20008
- Motoi, K. 1968, *Journal of Glaciology*, 7, 95
- Mousis, O., Chassefière, E., Holm, N. G., et al. 2015, *Astrobiology*, 15, 308
- Mousis, O., Chassefière, E., Lasue, J., et al. 2013, *Sp. Sci. Rev.*, 174, 213
- Mousis, O., Choukroun, M., Lunine, J. I., & Sotin, C. 2014, *Icarus*, 239, 39
- Mousis, O., Lunine, J. I., Pasek, M., et al. 2009, *Icarus*, 204, 749
- Mousis, O., Lunine, J. I., Picaud, S., et al. 2011, *The Astrophysical Journal Letters*, 740, L9
- Muñoz-Iglesias, V., Prieto-Ballesteros, O., & Bonales, L. J. 2014, *Geochimica et Cosmochimica Acta*, 125, 466
- Mumma, M. J., Villanueva, G. L., Novak, R. E., et al. 2009, *Science*, 323, 1041
- Murchie, S. L., Mustard, J. F., Ehlmann, B. L., et al. 2009, *Journal of Geophysical Research: Planets*, 114, e00D06
- Murray, B. J. & Bertram, A. K. 2005, *Physical Chemistry Chemical Physics (Incorporating Faraday Transactions)*, 8, 186
- Murray, C. A., Potter, J., Day, S. J., et al. 2017, *Journal of Applied Crystallography*, 50, 172
- Nelson, R. M., Kamp, L. W., Matson, D. L., et al. 2009, *Icarus*, 199, 429
- Niemann, H. B., Atreya, S. K., Bauer, S. J., et al. 2005, *Nature*, 438, 779
- Ojha, L., Wilhelm, M. B., Murchie, S. L., et al. 2015, *Nature Geoscience*, 8, 829
- Onstott, T. C., McGown, D., Kessler, J., et al. 2006, *Astrobiology*, 6, 377

- Oort, J. H. & van de Hulst, H. C. 1946, *Bulletin of the Astronomical Institutes of the Netherlands*, 10, 187
- Osterloo, M. M., Hamilton, V. E., Bandfield, J. L., et al. 2008, *Science*, 319, 1651
- Pappalardo, R. T., Head, J. W., Greeley, R., et al. 1998, *Nature*, 391, 365
- Peterson, R. C., Nelson, W., Madu, B., & Shurvell, H. F. 2007, in *LPI Contributions*, Vol. 1353, *Seventh International Conference on Mars*, 3124
- Peterson, R. C. & Wang, R. 2006, *Geology*, 34, 957
- Pikuta, E. V. & Hoover, R. B. 2007, in *Proc. SPIE*, Vol. 6694, *Instruments, Methods, and Missions for Astrobiology X*, 66941C
- Porco, C. C., Helfenstein, P., Thomas, P. C., et al. 2006, *Science*, 311, 1393
- Prieto-Ballesteros, O., Kargel, J. S., Fernández-Sampedro, M., et al. 2005, *Icarus*, 177, 491
- Prieto-Ballesteros, O. & Muñoz-Iglesias, V. 2014, in *LPI Contributions*, Vol. 1774, *Workshop on the Habitability of Icy Worlds*, 4077
- Raman, C. V. 1928, *Indian J. Phys.*, 2, 387
- Ratcliffe, C. I. & Ripmeester, J. A. 1986, *J. Phys. Chem*, 90, 1259
- Renno, N. O., Bos, B. J., Catling, D., et al. 2009, in *Lunar and Planetary Science Conference*, Vol. 40, *Lunar and Planetary Science Conference*, 1440
- Rieder, R., Economou, T., Wanke, H., et al. 1997, *Science*, 278, 1771
- Rieder, R., Gellert, R., Anderson, R. C., et al. 2004, *Science*, 306, 1746
- Rietveld, H. M. 1969, *J. Appl. Cryst.*, 2, 65
- Roach, L. H., Mustard, J. F., Murchie, S. L., et al. 2009, *Journal of Geophysical Research (Planets)*, 114, E00D02

- Rossbacher, L. A. & Judson, S. 1981, *Icarus*, 45, 39
- Sabil, K. M. 2009, Phase behaviour, thermodynamics, and kinetics of clathrate hydrate systems of carbon dioxide in the presence of tetrahydrofuran and electrolytes (Ph.D. dissertation, Technische Universiteit Delft, Delft, The Netherlands)
- Safi, E., Thompson, S. P., Evans, A., et al. 2018, *Geochimica et Cosmochimica Acta*, submitted
- Safi, E., Thompson, S. P., Evans, A., et al. 2017, *Astronomy and Astrophysics*, 600, A88
- Shin, K., Kumar, R., Udachin, K. A., Alavi, S., & Ripmeester, J. A. 2012, *Proceedings of the National Academy of Science*, 109, 14785
- Shpakov, V. P., Tse, J. S., Tulk, C. A., Kvamme, B., & Belosludov, V. R. 1998, *Chemical Physics Letters*, 282, 107
- Siegert, M. J., Kwok, R., Mayer, C., & Hubbard, B. 2000, *Nature*, 403, 643
- Sloan, E. D. & Koh, C. A. 2007, *Clathrate hydrates of natural gas* (2nd edition, CRC Press, Florida)
- Soh, M. T. K., Thurn, J., Thomas, III, J. H., & Talghader, J. J. 2007, *Journal of Physics D Applied Physics*, 40, 2176
- Stanton, A. 1896, *Nature*, 53, 274
- Stephan, K., Jaumann, R., & Wagner, R. 2013, *Astrophysics and Space Science Library*, Springer, New York, NY, 356, 1340
- Stofan, E. R., Elachi, C., Lunine, J. I., et al. 2007, *Nature*, 445, 61
- Sun, R., Hu, W., & Duan, Z. 2001, *Journal of Solution Chemistry*, 30, 561
- Takeya, S., Kida, M., Minami, H., et al. 2006, *Chemical Engineering Science*, 61, 2670

- Thomas, C., Mousis, O., Ballenegger, V., & Picaud, S. 2007, *Astronomy and Astrophysics*, 474, L17
- Thompson, S. P., Parker, J. E., Marchal, J., et al. 2011, *Journal of Synchrotron Radiation*, 18, 637
- Thompson, S. P., Parker, J. E., Potter, J., et al. 2009, *Review of Scientific Instruments*, 80, 075107
- Tobie, G., Lunine, J. I., & Sotin, C. 2006, *Nature*, 440, 61
- Tokano, T. 2003, *International Journal of Astrobiology*, 2, 155
- Tomasko, M. G., Archinal, B., Becker, T., et al. 2005, *Nature*, 438, 765
- Toner, J. D., Catling, D. C., & Light, B. 2014, *Icarus*, 233, 36
- Tosca, N. J., McLennan, S. M., Clark, B. C., et al. 2005, *Earth and Planetary Science Letters*, 240, 122
- Tse, B. 1987, *Journal de Physique Colloques*, 48, 543
- Udachin, K. A., Ratcliffe, C. I., & Ripmeester, J. A. 2001, *J. Phys.*, 40, 2176
- Vaille, A., Bougher, S. W., Tenishev, V., Combi, M. R., & Nagy, A. F. 2010, *Icarus*, 206, 28
- Vaniman, D. T., Bish, D. L., Chipera, S. J., et al. 2004, *Nature*, 431, 663
- Wadsworth, J. & Cockell, C. S. 2017, *Scientific Reports*, 7
- Waite, J. H., Lewis, W. S., Kasprzak, W. T., et al. 2004, *Space Science Review*, 114, 113
- Waite, J. H., Magee, B. A., Gell, D. A., et al. 2006, *AGU Fall Meeting Abstracts*
- Wang, A., Feldman, W. C., Mellon, M. T., & Zheng, M. 2013, *Icarus*, 226, 980

- Wang, A., Freeman, J. J., Chou, I.-M., & Jolliff, B. L. 2011, *Journal of Geophysical Research (Planets)*, 116, E12006
- Wang, A., Freeman, J. J., & Jolliff, B. L. 2009, *Journal of Geophysical Research (Planets)*, 114, E04010
- Wang, A., Haskin, L. A., Squyres, S. W., et al. 2006, *Journal of Geophysical Research (Planets)*, 111, E02S17
- Wänke, H., Brückner, J., Dreibus, G., Rieder, R., & Ryabchikov, I. 2001, *Space Science Reviews*, 96, 317
- Williams, T. & Kelley, C. 2015, An interactive plotting program, Version 5.0., <http://gnuplot.sourceforge.net/>
- Zimmer, C., Khurana, K. K., & Kivelson, M. G. 2000, *Icarus*, 147, 329
- Zolotov, M. Y. 2007, *Geophysical Research Letters*, 34, L23203
- Zolotov, M. Y. & Shock, E. L. 2001, *Journal of Geophys. Res.*, 106, 32815

A Publication List

A.1 Peer-reviewed journal papers

Safi, E., Thompson, S. P., Evans, A., Day, S. J., Murray, C. A., Parker, J. E., Baker, A. R., Oliveira, J. M., van Loon, J. T. 2017. Properties of CO₂ clathrate hydrates formed in the presence of MgSO₄ solutions with implications for icy moons. *Astronomy and Astrophysics* 600, A88.

A.2 Submitted journal papers

Safi, E., Thompson, S. P., Evans, A., Day, S. J., Murray, C. A., Baker, A. R., Oliveira, J. M., van Loon, J. T. 2018. Effects of ice polymorphs and chloride salts on clathrate hydrate evolution in the Martian cryosphere. *Geochimica et Cosmochimica Acta*. Submitted.

A.3 Journal papers in preparation

Safi, E., Thompson, S. P., Evans, A., Day, S. J., Baker, A. R., Murray, C. A. 2018. Clathrate buoyancy and the source of atmospheric methane on Titan. *Icarus*. In preparation.

Thompson, S. P., **Safi, E.**, Evans, A. 2017. Structure and spectroscopic behaviour of epsomite (MgSO₄·7H₂O) in the range T = 293 to 90 K relevant to Solar System bodies.

2017. Icarus. In preparation.

Thompson, S. P., Kennedy, H., **Safi, E.**, Day, S. J., Baker, A. R., Murray, C. A., Kelley, J., Potter, J., Cobb, T., Tang, C., Evans, A., Butler, B. M. 2018. A slow cooling rate sample cell for long duration studies of cold aqueous mineral precipitation using synchrotron powder diffraction—cell design and results for $\text{MgSO}_4 \cdot 11\text{H}_2\text{O}$ (meridianiite). *Journal of Applied Crystallography*. In preparation.

B List of abbreviations and acronyms

COD – Crystallography Open Database

CRISM – Compact Reconnaissance Imaging Spectrometer for Mars

DCM – Double Crystal Monochromator

DLS – Diamond Light Source

EH1 – Experimental Hutch 1

EH2 – Experimental Hutch 2

GCMS – Gas Chromatograph and Mass Spectrometer

GDA – Generic Data Acquisition

GoF – Goodness of Fit

HRM – Harmonic Rejection Mirrors

HiRise – High Resolution Imaging Science Experiment

ICDD – International Centre for Diffraction Data

INMS – Ion and Neutral Mass Spectrometer

JUICE – Jupiter Icy Moons Explorer

LDE – Long Duration Experiment

MAC – Multi-Analysing Crystals

MAJIS – Moons And Jupiter Imaging Spectrometer

MAC – Multi-Analysing Crystals

MER – Mars Exploration Rover

MS1 – Kieserite

MS6 – Hexahydrite

MS7 – Epsomite

MS11/MS12 – Meridianiite

NIMS – Near Infrared Mapping Spectrometer

OMEGA – Infrared Mineralogical Mapping Spectrometer

PSD – Position Sensitive Detector

RH – Relative Humidity

RIME – Radar for Icy Moon Exploration

RSL – Recurring Slope Lineae

RT – Room Temperature

SWI – Submillimeter Wave Instrument

SXRPD – Synchrotron X-ray Powder Diffraction

WEH – Water Equivalent Hydrogen

XRD – X-ray Diffraction